AD688164

AD

USAAVLABS TECHNICAL REPORT 68-69

DESIGN AND EVALUATION OF A HIGH-TEMPERATURE RADIAL TURBINE

PHASE I - FINAL REPORT

By

Glenn S. Calvert

Ulo Okapuu

January 1969

U. S. ARMY AVIATION MATERIEL LABORATORIES
FORT EUSTIS, VIRGINIA

CONTRACT DAAJ02-68-C-0003
PRATT & WHITNEY AIRCRAFT
FLORIDA RESEARCH AND DEVELOPMENT CENTER
WEST PALM BEACH, FLORIDA

279

Disclaimers

The findings in this report are not to be construed as an official Department of the Army position unless so designated by other authorized documents.

When Government drawings, specifications, or other data are used for any purpose other than in connection with a definitely related Government procurement operation, the United States Government thereby incurs no responsibility nor any obligation whatsoever; and the fact that the Government may have formulated, furnished, or in any way supplied the said drawings, specifications, or other data is not to be regarded by implication or otherwise as in any manner licensing the holder or any other person or corporation, or conveying any rights or permission, to manufacture, use, or sell any patented invention that may in any way be related thereto.

Disposition Instructions

Destroy this report when no longer needed. Do not return it to the originator.

DEPARTMENT OF THE ARMY
U. S. ARMY AVIATION MATERIEL LABORATORIES
FORT EUSTIS, VIRGINIA 23604

U. S. Army Aviation Materiel Laboratories technical personnel have reviewed this report and concur with the conclusions contained herein.

The findings and recommendations outlined herein have been and will be taken into consideration in Phase II final turbine design and tests.

Task IG162203D14413
Contract DAAJ02-68-C-0003
USAAVLABS Technical Report 68-69
January 1969

DESIGN AND EVALUATION OF A HIGH-TEMPERATURE RADIAL TURBINE

Phase I
Final Report

By

Glenn S. Calvert

Ulo Okapuu

Prepared by

Pratt & Whitney Aircraft
Florida Research and Development Center
West Palm Beach, Florida

for

U. S. ARMY AVIATION MATERIEL LABORATORIES
FORT EUSTIS, VIRGINIA

ABSTRACT

This report describes the work accomplished in the first phase of a two-phase, two-year program that involves the design and testing of a single-stage, high-work radial inflow turbine. This turbine will be typical of one required for advanced gas turbine engines employing high cycle pressure ratios and high turbine inlet temperatures.

The objectives of Phase I were to establish a preliminary turbine design, to confirm the preliminary design through cold-flow tests, and to conduct a fabrication study. The objectives of Phase II will be to develop a final turbine design and, finally, to fabricate and test the design.

The Phase I final preliminary turbine design is the result of iterative aerodynamic-structural-heat transfer analyses. The final selections of number of nozzle vanes, number of rotor blades, and rotor cooling air ejection method were confirmed and supported by cold-flow tests. The fabrication study showed some material property problems which require additional investigation.

FOREWORD

The work described in this report was accomplished under U. S. Army Aviation Materiel Laboratories Contract DAAJ02-68-C-0003 during the period 18 July 1967 to 30 May 1968. This report covers Phase I of a two-phase program. Phase II will be the subject of a similar document.

This program is being conducted by three elements of United Aircraft Corporation: The Florida Research and Development Center of Pratt and Whitney Aircraft (FRDC); the Connecticut Operations of Pratt and Whitney Aircraft (Connecticut Operations); and United Aircraft of Canada, Ltd. (UACL), formerly Pratt and Whitney Aircraft of Canada, Ltd. FRDC is the prime contractor for the program, and both Connecticut Operations and UACL have major supporting roles.

In Phase I, UACL performed the preliminary design of the USAAVLABS turbine and conducted cold-flow tests to verify the preliminary design. Connecticut Operations performed the heat transfer analyses of the cooled airfoils and assisted FRDC in the fabrication study. FRDC coordinated the overall program and conducted the fabrication study.

In Phase II, UACL will finalize the turbine design. FRDC will fabricate the turbine rig and the hot turbine components and will test the turbine at its West Palm Beach, Florida, facility. UACL will assist FRDC in both of the latter functions as required.

BLANK PAGE

TABLE OF CONTENTS

LIST OF ILLUSTRATIONS

LIST OF ILLUSTRATIONS (Continued)

LIST OF ILLUSTRATIONS (Continued)

LIST OF ILLUSTRATIONS (Continued)

LIST OF ILLUSTRATIONS (Continued)

LIST OF ILLUSTRATIONS (Continued)

LIST OF ILLUSTRATIONS (Continued)

LIST OF ILLUSTRATIONS (Continued)

LIST OF ILLUSTRATIONS (Continued)

LIST OF ILLUSTRATIONS (Continued)

LIST OF ILLUSTRATIONS (Continued)

LIST OF TABLES

LIST OF SYMBOLS

Symbol		Units
C	Absolute gas velocity	ft/sec
C_p	Specific heat at constant pressure	Btu/lb_m -^oR
C'_o	Isentropic spouting velocity $C'_o = \sqrt{2gJ\Delta H'}$	
C_v	Specific heat at constant volume	
g	Gravitational constant	ft-lb_m/lb_f-sec^2
J	Mechanical equivalent of heat	ft-lb_f/Btu
M	Mach number	
M_r	Relative Mach number	
N	Speed	rpm
N_s	Specific speed $= \dfrac{N\sqrt{Q_6}}{(\Delta H')^{3/4}}$	
P	Total pressure	psia
p	Static pressure	psia
PR	Pressure Ratio	
Q	Volumetric flow	ft^3/sec
R	Gas constant	ft-lb_f/lb_m-^oR
T	Stagnation temperature	^oR
t	Static temperature	^oR
TET	Nozzle vane trailing-edge thickness	in.
TIT	Turbine inlet stagnation temperature	^oR
U	Rotor tip speed	ft/sec
V	Relative gas velocity	ft/sec
W	Flowrate	lb/sec
α	Absolute gas angle	deg
γ	Ratio of specific heats, C_p/C_v	
ΔH	Actual enthalpy drop	Btu/lb or ft-lb/lb
$\Delta H/\theta$	ΔH = actual enthalpy change of 1 lb of combustion products across the turbine from nozzle vane inlet to rotor exhaust (Btu/lb) θ = ratio of turbine inlet temperature (^oR) $\div$ standard temperature (519.7^oR)	
$\Delta H'$	Isentropic enthalpy drop $= C_p\, T_o \left[1 - \left(\dfrac{P_6}{P_o}\right)^{\frac{\gamma-1}{\gamma}}\right]$ (Total-total conditions)	Btu/lb
$\Delta m/m$	Nondimensional distance from tip	
δ	Normalized pressure = P/standard atmosphere pressure (14.7 psia)	

Symbol		Units
η_R	Rotor efficiency = actual work removed from gas $\div$ isentropic work available between rotor inlet stagnation pressure and rotor exhaust stagnation pressure.	
θ_N	Nozzle velocity ratio = absolute velocity at rotor leading edge $\div$ isentropic absolute velocity at rotor leading edge	

$$\eta_R = \frac{(1 - T_{6R}/T_{3R})}{\left[1 - (P_{6R}/P_{3R})^{\frac{\gamma-1}{\gamma}}\right]}$$

SUBSCRIPTS

T-T	Total-to-total conditions
T-S	Total-to-static conditions
R	Rotor
AV	Average
INLET	Same as station 0
MECH	Mechanical
ACTUAL	Measured
N	Nozzle
0	At nozzle inlet
3	At rotor inlet
6	At rotor trailing edge

BLANK PAGE

INTRODUCTION

Radial turbines can offer greater stage-work capacity than axial turbines and at higher efficiencies. If this advantage can be coupled with a capability to accommodate high turbine inlet temperatures, radial turbines will permit appreciable simplification of small gas turbine engines for use in future Army vehicles. The objective of this contract is to develop the technology for high-temperature radial turbines to a level that will permit a potential small-engine manufacturer to make a choice between the radial and axial turbine.

A two-year, two-phase program is being conducted involving the design and testing of a cooled, single-stage, radial-inflow turbine with the following design conditions: turbine inlet temperature of 2300°F, total-to-total aerodynamic efficiency of 87.5%, gas flow of approximately 5 pounds per second, and stage work parameter ($\Delta H/\theta$) greater than 40.0 Btu per pound. The first phase of the program involves a preliminary design of the cooled radial turbine including development of cold-flow data to verify the preliminary turbine design. In the second phase, the design will be finalized and the cooled radial turbine will be fabricated and tested.

This report documents the tasks undertaken in Phase I only and it presents the final configurations and conclusions resulting from these tasks. It was the objective of this first phase to evolve, through iterative aerodynamic-structural-heat transfer analyses, a preliminary turbine design to meet performance objectives. Cold-flow tests were conducted to verify the selected numbers of nozzle vanes and rotor blades and to help in assessing the effect of cooling air ejection at the rotor leading edge.

Finally, a fabrication study was conducted to establish the existing state of the art for casting radial turbines and to uncover any potential fabrication problem areas.

TASK 1 - CONTROL LAYOUT

OBJECTIVE

The Control Layout was conceived as a program management tool that shows the latest design configuration of the high-temperature turbine rig. During Phase I of this program, the Control Layout was updated four times as the results of aerodynamic, structural and mechanical, and heat transfer analyses indicated that modifications were desirable.

INTERIM CHANGES

Control Layout 1, shown in Figure 1, was a simple rig design that consisted of a radially bladed brake (compressor), a bleed air system, a combustor, and a turbine assembly. This early configuration represents the originally proposed design and was necessarily based on rather limited study. Once this configuration came under detailed study, it became apparent that the simple brake design could not supply the desired range of test data, and that a more sophisticated shaft/bearing assembly would be required to solve critical-speed and high-temperature problems in the bearing compartment.

The most notable changes in the evolution of the final rig configuration took place between Control Layouts 1 and 2 (Figures 1 and 2). These changes resulted from detailed studies conducted under other Phase I tasks, which are described later.

Control Layout 2 is essentially the same basic design as the Phase I final configuration, and will be described under four general headings: compressor section, burner assembly, bearing compartment, and turbine section.

In the compressor section, the simple configuration previously shown was replaced by an annular air inlet that is supplied by two inlet lines 180 degrees apart. The compressor inlet is a bellmouth with adjustable inlet guide vanes (IGV's). A more efficient compressor (or brake) impeller design replaced the earlier radial-bladed design. Pipe diffusers accept the impeller discharge and diffuse it to burner pressure. Two pipe diffuser designs will be used in conjunction with the variable IGV's to extend the available range of test data. The pressure in the cavity behind the impeller will be adjusted to control the axial thrust of the rotating assembly.

The burner assembly of Control Layout 2 shows an additional sheet-metal duct around the burner that was not present in the previous design. This duct establishes the same reverse flowpath as the PT6 burner, and the pressure drop across the holes (at the downstream end) should have a smoothing effect on the air entering the burner.

The bearing compartment in Control Layout 2 is oil cooled and lubricated. Cooling is achieved by enveloping the outside of the compartment with cool oil flowing in a spiral-type path. Lubrication is achieved by directing a stream of oil against the inside diameter of the cage. Both cooling and lubricating oil are scavenged from the compartment between the bearings. The bearings are the spring-loaded angular contact type with oil-film damping on the compressor bearing. Axial thrust is monitored by strain gages mounted on the cylindrical part that seats on the Outer Diameter (OD) of the turbine bearing. Pressure-balanced labyrinth seals at the compressor and turbine ends of the compartment keep hot gases from flowing into the bearing area; maximum bearing temperatures will be limited to 350°F.

In the turbine section of the Control Layout 2, the segmented backplate was replaced by a single-piece design. The cooling air flowpath was also modified so that the backplate coolant contributes to cooling the nozzle vanes. Likewise, the shroud coolant is also used for cooling the nozzle vanes. The rotor cooling airflow was also modified, so that it enters the rotor from a downstream location. This change required the addition of an exhaust centerbody to route the cooling air to the rotor. The vane cooling design in Control Layout 2 was changed to indicate the cooling configuration as it existed at that time.

Figure 3 shows Control Layout 3. Changes in the mechanical design between Control Layouts 2, 3, and 4 are minor. The most important feature to be noted on the third Control Layout is the initial appearance of the two-pass rotor cooling configuration. This marks the point in the aerodynamic and heat transfer analyses that the two-pass rotor cooling design became the preferred configuration.

PHASE I FINAL CONFIGURATION

Control Layout 4, shown in Figure 4, was the final configuration evolved in Phase I. The turbine test rig shown in Figure 4 is a supercharged gas generator that creates a turbine environment typical of advanced engines designed for high pressure ratio (18:1) and high turbine inlet temperature (2300°F). In the turbine test configuration, pressurized inlet air is supplied by compressor bleed air taken from a slave gas turbine engine. Key design features of the turbine test rig include the following:

1. Adjustable brake (compressor) IGV's
2. Single-stage centrifugal compressor
3. Pipe diffusers (two designs with different numbers of diffusers)
4. Bleed air discharge
5. High-temperature burner
6. Oil cooled and lubricated bearing package with film damping

7. Integrally cast, air-cooled nozzle vanes
8. Integrally cast, air-cooled turbine rotor
9. Cast, air-cooled shroud and backplate

In operation, the brake serves two purposes: it absorbs the power generated by the turbine, and it raises the pressure of the inlet air (90 psia) to the turbine design inlet pressure (257.5 psia). It is designed to accept approximately twice as much air as the turbine design flow (nominally 5 pounds per second). The excess air is discharged through the bleed air line. This feature of the rig design affords an increased range of turbine test data as compared to a design in which the compressor and turbine airflow rates are equal.

The adjustable brake IGV's and the two pipe diffuser designs are required to utilize the wide range of test conditions (made possible by the bleed air system) without operating the brake in surge conditions.

The heart of the burner design is the UACL PT6 flame tube and fuel system. To this have been added a sheet-metal duct that establishes the proper gas flowpath for efficient burner operation, and a transition piece to turn the hot gases in a radially inward direction. The outer shell of the rig supports the entire test assembly.

To operate the high-speed (67,000 rpm) bearing system in a high-temperature environment, it was necessary to provide appreciable cooling within the bearing package. This was accomplished by designing a cylindrical flowpath for cooling oil that envelops the bearing assembly and maintains acceptable temperatures in this area. Oil-film damping has been provided at the brake bearing to damp out the first two critical speeds (10,000 and 25,000 rpm) which must be passed through in accelerating to design speed.

The four main turbine parts (rotor, nozzle assembly, shroud, and backplate) have been designed as air-cooled IN 100 (PWA 658) castings. The preliminary design of these parts was accomplished in Phase I, and the detail design will be completed during Phase II.

Primary control of the rig is achieved with the PT6 fuel control and the bleed air control valve. Secondary control points are the adjustable brake IGV's and a turbine back-pressure control valve. Turbine power is determined by measuring the compressor work, and correcting it for bearing, seal, and windage losses. This value is verified by the total temperature drop across the turbine.

In the burner test configuration (Figure 5), the rotating turbine assembly is replaced by a temperature/pressure traversing assembly. This configuration will be used to measure total temperature and total pressure at the nozzle leading edge. An indexing gearbox will be used to advance the probes in equal circumferential increments, and multipie probes located at different axial positions will provide spanwise data.

TASK 2 - AERODYNAMIC DESIGN

OBJECTIVES

This task involved design studies in the following four categories:

1. High-temperature hardware
2. Cold-flow hardware
3. Water visualization rig
4. Rig brake (compressor)

The objective of the high-temperature hardware study was to produce a preliminary aerodynamic design of a turbine rotor and nozzle that would be suitable for the gas generator turbine in the following hypothetical cycle:

- Type of engine - twin-spool turboshaft
- Airflow rate - approximately 5.0 pounds per second
- Turbine inlet temperature - 2300°F
- Engine pressure ratio - 18:1

In the aerodynamic design of the cold-flow hardware, an existing turbine design was used as the basis of new hardware configurations. The objective of this effort was to design hardware that could be compared with existing data to show the effect on performance of:

- Different number of rotor blades
- Different number of nozzle vanes
- Thickened vane trailing edges

The objective of the water visualization rig study was to produce a design for an inexpensive, yet useful, water analogy rig. This rig was used to study flow characteristics near the rotor leading edge.

Although not originally scheduled, the aerodynamic design of the rig brake became necessary when studies showed that the original type of brake was unsuitable. The objective of the brake aerodynamic study was to produce designs for a brake configuration (including IGV's, rotor, and diffuser) that would be suitable for loading the turbine over a wide range of operating conditions.

The following paragraphs describe the basic aerodynamic design philosophy and the results of the analyses in each of the aforementioned categories.

DESIGN PHILOSOPHY

In designing the cooled rotor and nozzles, the overall objective was to arrive at the lowest loss design while accommodating the necessary geometric compromises required for satisfactory stress and temperature levels. In the case of the cooled rotor, these compromises were found to be comparatively severe due to its small size and high temperature, which made proportionately large running clearances mandatory. In the case of the cooled nozzles, the aerodynamic compromise appears in the form of thickened trailing edges, which are required for adequate heat conduction from the vanes to the sidewalls.

GENERAL DESIGN PROCEDURE

The general shape of the USAAVLABS turbine was evolved as follows:

- Rotor exit swirl was first chosen to be zero, and
- Rotor exit annulus area was chosen such that the absolute Mach number at rotor exit came to a reasonably low value, 0.427. This was done to minimize the exhaust duct losses in a single-shaft engine application, and inter-turbine duct losses in a free-turbine engine application of the turbine.
- Rotor exit radius was chosen as a compromise between the two most likely exhaust configurations (straight or annular exhaust ducts) to make the design equally suitable for a range of applications.
- Rotor tip width was chosen next. For a given relative flow angle at the tip, a wide tip corresponds to a rotor design having high mean line acceleration relative to the rotor (and hence lower separation losses), but it also requires a high absolute velocity at rotor tip, and a more highly stressed blade. The tip width finally chosen was a compromise between performance and stress requirements and corresponds to an absolute flow angle at the rotor tip of 75 degrees.
- Rotor tip radius is, for a given combination of enthalpy drop, rotational speed and exit swirl, a function only of the rotor tip relative flow angle. Since for stress reasons the USAAVLABS rotor blades had to be radial, the relative flow angle at the rotor tip was equal to the tip incidence. A high positive incidence corresponds to a reduced blade length, which in turn reduces blade and hub stresses. However, a high positive incidence produces turning losses at rotor tip. The tip radius finally chosen was a compromise between performance and stress requirements, and it corresponds to a positive incidence of 6.5 degrees. Past test results indicate that this will result in a drop of 1/2 point in turbine efficiency.

HIGH-TEMPERATURE HARDWARE

Mean-Line Design History

The first mean-line design that was extensively analyzed is presented in Figure 6. The numbers of nozzle vanes and rotor blades shown are 20 and 12, respectively. These original choices were considered to be the best compromise between higher and lower numbers of vanes and blades on the basis of the previous Canadian Defence Research Board tests. In these tests, a rotor with 14 blades was tested with a nozzle section of 25 vanes, and the measured turbine efficiency was acceptable (89.8%, verified by tests conducted under this program in Task 6 - Cold-Flow Tests). The original vane and blade numbers were selected to reduce the number of airfoils that required cooling air, without incurring a great performance penalty. These original selections were later confirmed by the cold-flow tests.

When the number of nozzle vanes was originally chosen at 20, it was anticipated that this selection would be verified by using results from the cold-flow tests (with different numbers of vanes) and trading off performance for cooling air. For example, more vanes might improve turbine performance, but they would also require more total coolant. However, the Phase I final hot turbine design uses the backplate and shroud coolant to cool the vanes also, and the total cooling air flowed through the vanes is more than that required to cool the airfoils alone. Therefore, the originally planned trade-off study is irrelevant. The cold-flow tests showed only a slight change in performance with number of vanes greater than and less than 20, and the original choice of vane number was maintained on the basis of a somewhat different rationale (see Task 6 - Cold-Flow Tests).

Likewise, the selection of 12 rotor blades was expected to be verified by the results of the cold-flow tests (using different numbers of blades) and another cooling/aerodynamic trade-off study. This trade-off study would be similar to that for nozzles in that more rotor blades might improve performance, but additional rotor blades would require more total coolant. Cold-flow tests showed that the 12-bladed rotor was slightly less efficient than the 14-bladed rotor, even when the increased coolant required for the 14-bladed rotor was taken into account. However, the applicability of these data was influenced by other considerations (see Task 6 - Cold-Flow Tests) and the original selection of 12 blades for the rotor was retained in the Phase I final aerodynamic design.

The rotor tip absolute flow angle in Figure 6 is 75 degrees. As previously stated, this value was chosen as a compromise between a lower flow angle (shown in Figure 7, desirable for low rotor blade centrifugal stresses) and a higher flow angle (shown in Figure 8, desirable for high flow acceleration within the rotor). The preliminary (proposal) nozzle angle had been selected at 70 degrees with a nozzle span of 0.250 inch and a flow rate of 5 pounds per second. Changing the flow angle to 75 degrees required a span increase to 0.339 inch to pass the nominal design flow of 5 pounds per second.

The hot turbine mean-line design was modified twice during Phase I, both times as a result of cooling air effects. The first modification is shown on Figure 9, and the most significant change is in the flowrate at the nozzle inlet (W_{inlet}). In this design, W_{inlet} has been decreased to 4.75 pounds per second from the 5.00 pounds per second shown in the previous mean-line design. This is the result of discharging the backplate and shroud cooling air through the vane trailing edge, which increases the gas flow through the rotor relative to the gas flow at the nozzle inlet. To allow for this difference with a minimum of geometry changes, the rotor flowrate was held constant, and the nozzle inlet flowrate was reduced by the amount of shroud and backplate coolant.

The second modification to the mean-line design resulted in the Phase I final configuration (see Figure 10). This configuration reflects the temperature-reduction effect of mixing the shroud and backplate coolant with the 2300°F main gas stream. This is predicted to reduce the main stream stagnation temperature from 2300°F (TIT) at the nozzle inlet to 2225°F at the rotor leading edge, which will reduce the work extraction from 226.0 Btu per pound to 219.6 Btu per pound. Changes to the mean-line design were again chosen to minimize the geometry modification required as follows:

- Rotor tip incidence was reduced from 15 degrees (positive) to 6.5 degrees (positive). This was desirable for improved aerodynamic performance. To achieve this incidence with the corrected leading edge temperature, the rotor tip diameter was increased by 0.028 inch.
- Mass flow at the vane inlet was increased from 4.75 pounds per second to 4.90 pounds per second to restore the desired air angle at rotor inlet.

Hot Nozzle Velocity Distribution

The velocity distributions for the cooled nozzle and rotor were calculated with previously formulated computer programs, which use a potential flow analysis to predict internal flow conditions.

The vane that has been designed for the USAAVLABS turbine is of the reflex type (i.e., the suction surface downstream of the throat is a streamline in a compressible, adiabatic, free vortex with sidewall and vane profile friction). Calculated incidence at the leading edge is zero. Figure 11 is a schematic of this type of nozzle.

The calculated velocity distribution for the USAAVLABS nozzle is shown in Figure 12. This figure shows that the flow is accelerating on both the pressure and suction surfaces, with increased acceleration on the suction surface near the throat. This is noteworthy because it is not uncommon in nozzle design practice to have local diffusion at the throat on the suction surface, even though the flow is accelerating overall. The velocity distribution shown is desirable to reduce boundary layer buildup and thus improve nozzle efficiency.

Hot Rotor Velocity Distribution

Figures 13, 14, and 15 present the velocity distributions for the Phase I final rotor design. These velocity distributions were calculated by the method of Katsanis*, and they correspond to the Phase I final mean-line design shown in Figure 10.

In evaluating calculated velocity distributions, there are four velocity distribution features that should be noted: (1) the diffusion on the exducer suction surface near the shroud, (2) diffusion on the geometric mean streamline near the shroud, (3) the extent of calculated flow reversal at the rotor tip, and (4) the smoothness of the calculated velocity distributions. These features can be used for a qualitative comparison of a new rotor design with another rotor of known performance to arrive at a qualitative conclusion regarding the new rotor's performance.

Diffusion is generally undesirable in a turbine rotor because it results in unfavorable pressure gradients, thickening of the boundary layer, and in some cases, flow separation. In the case of the radial turbine, diffusion is especially undesirable near the shroud in general, and on the suction surface of the exducer near the shroud in particular. This conclusion results from previous experience with the Canadian Defence Research Board (DRB) turbine, which indicated lower efficiency near the exducer blade tips compared to the efficiency at the exducer blade root**. The calculated velocity distribution for the DRB turbine showed some diffusion in the exducer, especially on the suction side of the blade near the tip, and some separation from the blade tips was indicated by exit traverses.

Flow separation is always undesirable in a turbine, because it results in turbulent flow patterns and some energy loss. Most radial turbines have some leading edge separation and flow reversal at the design point; the calculated flow reversal can be used as a measure of the extent of flow separation.

The smoothness of the calculated velocity distributions is another indicator of rotor efficiency. A smooth velocity distribution is desirable because it means that the gas is accelerated evenly throughout the gas path, and losses associated with abrupt velocity changes and/or local diffusion are minimized.

Some qualitative conclusions can be drawn from a comparison of the calculated velocity distributions for the USAAVLABS rotor with those calculated for the 10-, 12-, and 14-bladed cold-flow rotors (Figures 16 and 17).

---

* "The Use of Quasi-Orthogonals for Calculating Flow Distribution in a Turbomachine," Katsanis, T., ASME 65-WA/GTP-2.

** UACL Engineering Report No. 458, "Phase III Interim Report No. 6, 90 degree Inward Flow Radial Turbine Research Program," Project P3.

Figure 13 indicates a relatively low suction side diffusion (220 feet per second in the exducer near the shroud. Only one of the cold-flow rotors (14-bladed) showed a lower value, 200 feet per second. Considering the diffusion along the geometric mean streamline near the shroud, the USAAVLABS turbine has only 50 feet per second diffusion compared to 270 feet per second for the best cold-flow rotor.

The calculated flow reversal at the rotor leading edge for the USAAVLABS turbine is 670 feet per second which is higher than either the 14-bladed (400 feet per second) or the 12-bladed (570 feet per second) cold-flow rotors. However, the velocity distribution of the USAAVLABS rotor is smoother than any of the cold-flow rotors.

Table I summarizes the comparative evaluation of the turbine rotors; on the basis of this comparison, the aerodynamic performance of the USAAVLABS turbine should be as good as the 12-bladed cold-flow rotor.

TABLE I. COMPARATIVE EVALUATION OF TURBINE ROTOR SUMMARY

Turbine Rotor	Exducer Diffusion (ft/sec)	Mean Streamline Diffusion (ft/sec)	Flow Reversal (ft/sec)	Smoothness of Velocity Distribution
Cold-Flow (14-Bladed)	200	270	400	Poor
Cold-Flow (12-Bladed)	340	280	570	Poor
Cold-Flow (10-Bladed)	480	290	800	Poor
USAAVLABS Rotor (12-Bladed)	220	50	670	Good

Hot Turbine Predicted Performance

Figures 18 and 19 present the predicted performance of the AVLABS turbine. The off-design characteristics were estimated from the results of the previous DRB tests*; these turbine performance data were used in the design of the control system, the rig brake, IGV's and pipe diffusers.

* UACL Engineering Report No. 463, "Final Report, 90 degree Inward Flow Radial Turbine Research Program," Project P3.

COLD-FLOW HARDWARE

Cold-Flow Rotors

In this segment of the aerodynamic design task, two new cold-flow rotors were designed with 12 and 10 blades to provide data for comparison with existing data from the DRB 14-bladed rotor. These two new rotors used the same blade design as the existing 14-bladed rotor. Although this meant that the 12-bladed and 10-bladed designs would not be aerodynamically optimized, it was desirable from an economic and scheduling viewpoint since the tooling was already available. Figure 20 shows the new rotor designs.

Effect of Blade Number on Efficiency

Flow analyses of the 10- and 12-bladed rotors were completed using the potential flow analysis. Figures 16 and 17 (previously discussed) compare the calculated velocity distributions for these rotors with the distribution of the basic 14-bladed rotor.

Figure 16 describes the calculated velocity distributions along the rotor shroud at the suction surface, the pressure surface, and the geometric mean. It is evident that the blade loading (i.e., the velocity difference between the suction and pressure surfaces) increases as the number of blades is reduced. As a corollary, reducing the number of blades increases local diffusion, as well as the extent of the flow reversal region at the leading edge of the pressure surface. On the basis of earlier DRB test results, the calculated pressure-surface flow reversal and the suction-surface diffusion in the exducer are believed to be governing parameters for rotor losses. Therefore, the implication of these calculated velocity distributions is that a reduction of the number of blades is accompanied by a loss of turbine efficiency, with a wider efficiency increment between 10 and 12 blades than between 12 and 14 blades. This has been verified by the cold-flow tests of Builds 1, 2, and 3 (see Task 6-Cold-Flow Tests).

Figure 17 shows the calculated velocity distributions along the hub of the rotor. The negative loading indicated between the nondimensional distance from tip ($\Delta m/m$) of 0.55 and 0.65 is very small in the radial direction and may well be due to peculiarities in the analysis method. Results of the cold-flow tests indicate that the local efficiency at the hub is very high; therefore, the negative loading, if it does exist, does not have much effect on turbine efficiency. The high measured hub efficiency also suggests that the large calculated suction surface diffusion in the star portion (between $\Delta m/m$ of 0.15 and 0.55) does not have a strong effect on rotor efficiency. The very low blade loading in the exducer (between $\Delta m/m$ of 0.65 and 1.00) is caused by the requirement for radial blade elements and is unavoidable.

Cold-Flow Nozzles

Three new cold-flow nozzle sections were designed which, in conjunction with existing data from a 25-vaned nozzle section, would show these two effects:

1. Increased nozzle vane trailing-edge thickness (TET)
2. Reduced number of vanes

The effect of trailing-edge thickness was of interest in this program because the USAAVLABS turbine was designed with thicker-than-usual trailing edges to conduct heat from the vane to the platforms. The effect of reduced number of vanes was also of interest because the original design studies were based on 20 vanes for the USAAVLABS turbine. This was considered to be the best compromise between a higher number of vanes (which may perform better, but require more coolant) and a lower number of vanes (which may have lower performance, but require less coolant).

The existing 25-vaned nozzle section had a throat dimension of 0.354-inch and a TET of 0.017-inch which is typical of the minimum castable TET (0.020 inch). The USAAVLABS turbine was designed with a 0.040-inch TET, the minimum dimension for adequate heat conduction. Since the significant aerodynamic design parameter associated with vane trailing-edge thickness is the ratio of TET to throat opening, the new 25-vaned cold-flow nozzle was designed with a TET of 0.050-inch (giving a ratio of TET/throat opening = 0.141) to cover a range of data that would include the USAAVLABS turbine TET-to-throat opening ratio (0.40/0.313 = 0.128). Thus, comparison of the performance of the two 25-vaned nozzle sections with otherwise identical hardware shows the efficiency penalty associated with heat conduction requirements of the USAAVLABS turbine vane (see Task 6 - Cold-Flow Tests).

The other two cold-flow nozzle sections were designed with 20 and 15 nozzle vanes. These two sections were designed along with the new 25-vaned section to be members of a consistent design "family," with the following parameters held constant:

- Vane span (i.e., the axial dimension for a radial vane)
- Radius to trailing-edge center
- Total throat area
- Trailing-edge thickness
- Angle between inlet stagnation streamline and line tangent to suction surface at intersection of suction surface with leading-edge radius

The following parameters were varied (by necessity) for the new designs:

- Wetted wall area per nozzle passage
- Throat aspect ratio, defined as the span divided by the throat dimension
- Trailing-edge wedge angle

Thus, comparison of the performances of the three new cold-flow nozzle sections with otherwise identical hardware indicates the effect of reducing the number of nozzle vanes below 25.

It is noteworthy that the new cold-flow nozzles were designed to have velocity distributions identical to each other and similar to the USAAVLABS turbine nozzle (previously shown in Figure 12). The test data generated by the cold-flow tests should be applicable to the USAAVLABS design.

Figures 21, 22, and 23 present the designs of the 15-, 20-, and 25-vaned cold-flow nozzle rings.

Nozzle Potential Flow Streamlines

Figures 24, 25, and 26 present calculated potential flow streamlines for the three new cold-flow nozzle sections. These figures show that the three sections were designed to have similar leading-edge flow conditions, (i.e., the leading edge is aligned with the anticipated incident flow direction).

To illustrate the importance of correct leading-edge orientation, potential flow streamlines were calculated for the basic 25-vaned nozzle with a progressively reduced (cutback) chord. If the vane chord were reduced by a moderate cutback on the leading edge, leaving the rest of the vane untouched, the streamline pattern would look like that shown in Figure 27. Part of the flow in passing around the leading edge would feel a rather high local curvature that would produce a high local velocity. This high velocity at the leading edge cannot be maintained, since the suction surface curvature decreases toward the throat (i.e., local diffusion takes place). When this diffusion becomes sufficiently high, a real gas would separate from the suction surface. While the flow would probably reattach ahead of the throat due to the high overall acceleration in the channel, the total pressure loss would be increased and flow would become unsteady. Figure 28 shows the calculated streamlines with a severe leading-edge cutback. Now the circulation imposed by the vane moves the leading-edge stagnation streamline farther away from the leading edge, and the flow next to the suction surface would certainly separate. While this vane design might be suitable for a turbine having a nonradial inlet flow direction, it is clearly not adequate for the USAAVLABS design.

WATER VISUALIZATION RIG

Figure 29 shows the final configuration of the water visualization rig. This rig incorporates a rotating mirror optical system and a high-speed movie camera to record the movement of water flow relative to a turbine blade. A transparent viewing port will permit the photographic system to follow a single rotor blade through approximately one-fourth of a revolution.

To record the relative flow, a fixed camera is aimed at a mirror located on the centerline and above the turbine wheel. This mirror rotates at one-half turbine speed, and the effective line of sight thus rotates at turbine speed along a single radial line on the turbine rotor. At the rim, another mirror mounted on this radial line (i.e., rotating with the turbine) deflects the line of sight down through the blades so that the camera sees an image in which the rotor blades are fixed and the nozzle vanes rotate. During the period in which the central mirror is at a usable angle, the view is the same as that of a camera mounted approximately 4 feet above the turbine rim, looking down through the blades and rotating with the turbine wheel. Surface-aluminized mirrors are used to eliminate multiple secondary images.

By the use of a system in which the final viewing device is fixed, there are no restrictions on camera type, other than the minimum focal distance requirement of approximately 4 feet. The image could in fact be viewed by eye, although the intermittent presentation would make interpretation difficult.

The camera that was used with this rig is a Wollensak WF4 16-mm Fastax that is capable of speeds up to 9000 frames per second. Usable speed was limited by light intensity (from a 1 kw lamp) to about 1000 frames per second. At a normal projection speed of 16 frames per second, this gives a time magnification of more than 60. Assuming 12 blades and 30 rpm, a rotor blade channel passes a fixed point in about 1/6 second, and this event will thus be expanded to 10 seconds on projection.

Water streamlines, both for the primary (driving) flow and the secondary (cooling) flow, were initially to be made visible through the generation of tiny hydrogen bubbles. These hydrogen bubbles were to be generated by electrolysis of water. Electrodes were located both in the nozzles (for primary flow streamlines) and at the rotor leading edge (for secondary flow streamlines). During our pre-proposal studies, dyed water was considered for the coolant flow, but this system was discarded in favor of the simpler hydrogen-bubble design. However, operational problems (described in Task 6 - Cold-Flow Tests) made the hydrogen system unfeasible for this program, and the original dyed water scheme was used to distinguish the rotor cooling flow from the main flow.

Results (discussed in Task 6-Cold-Flow Tests) from the water rig were influential in finally selecting a two-pass rotor cooling design with exducer ejection over the original single-pass design with tip ejection (see Task 6-Cold-Flow Tests).

RIG BRAKE DESIGN

The original conceptual design of the rig brake impeller is shown in Figure 30. During the pre-proposal design studies, it was assumed that an adiabatic efficiency of 60% could be achieved with the simple radial-bladed impeller. However, during the detailed design of the rig, one of the reference works in the literature* indicated that this efficiency estimate was high, and that efficiencies below 50% should be expected. This would severely limit the available range of test data, and it was decided to design a more sophisticated, more efficient compressor impeller.

The impeller that was finally designed (shown schematically in Figure 31) is a scaled-up version of one that was designed for a Canadian DRB-funded compressor research program. The scaled-up version of the DRB compressor was selected instead of a new impeller design for two reasons: (1) the tooling required to machine this impeller was available, and the cost of new tooling was thus avoided; and (2) prediction of the brake performance could be made with a high degree of accuracy, using the extensive test data that have been generated with the DRB impeller.

Variable IGV's were chosen because of the desired range in power absorption that extends from 660 Btu per second to 1225 Btu per second at design speed. The alternative of throttling the flow upstream of the impeller was also considered. This, however, resulted in an excessively low brake inlet pressure with a correspondingly low and unacceptable pressure at the turbine inlet.

Axial IGV's were selected instead of radial IGV's for three principal reasons. First, extensive test data are available for this type IGV. Secondly, axial guide vanes can be designed by simply scaling an existing design that is known to perform satisfactorily. Last, the choice of axial IGV's facilitates the aerodynamic design of the intake, which would be difficult with radial-type IGV's for impeller inlet swirls ranging from 0 to 55 degrees.

A diffusing system is required to deliver the design static pressure to the combustor. A vaneless diffuser was first considered, but was judged inadequate; it was decided to use a pipe diffuser. Cost-wise a pipe diffuser is competitive with a vaned diffuser, and extensive testing has already been accomplished with pipe diffusers. However, a single diffuser could not be designed to cover the complete range of data, and a second one was designed for the lower end of the power absorption curve.

---

* "Development of Some Unconventional Centrifugal Pumps," U. M. Barske, Institute of Mechanical Engineers (London) Paper No. 21/59, 1960.

Figures 32 through 36 show calculated part-load maps of the brake. For a given pipe diffuser and IGV setting, the range of data shown on the performance maps will be accessible through different combinations of bleed-valve settings and turbine inlet temperatures. Figures 32 through 35 show the brake equipped with a 26-pipe diffuser at IGV swirl settings of 0, 10, 25, and 35 degrees, respectively. Figure 36 shows the same impeller, but with a 36-pipe diffuser, at an IGV setting of 0 degrees. Although it is predicted that only a single IGV setting will be required with the 36-pipe diffuser, all of the previously-used IGV settings will be available for use if necessary. These part-load maps were used in conjunction with predicted turbine performance to calculate the turbine part-load range available during hot testing (shown in Figure 37).

TASK 3 - STRUCTURAL AND MECHANICAL DESIGN

OBJECTIVE

The objective of this task was to evolve a hot turbine design that is mechanically feasible and structurally adequate to achieve the turbine operational goals.

Task activity was concentrated in two main categories:

1. Mechanical design of hot section
2. Mechanical design and structural analyses of rotor, nozzles, backplate, and shroud.

The hot section is defined roughly as the area from the nozzle vane inlet to the turbine exhaust, including the exhaust center body. In the axial direction, the hot section encompasses the turbine rotor, nozzles, backplate, and shroud, their respective cooling air passages, and all attachments involving hot parts. The mechanical design of the rest of the test rig was furnished by the contractor.

STRESS ANALYSIS

Extensive stress analyses were required on four parts: the turbine rotor, nozzles, shroud, and backplate. Of these four parts, the nozzles, shroud, and backplate are primarily structural nonrotating members subject only to static loads and thermal gradients. Conventional stress analyses are sufficient to design these parts. The rotor, however, is a highly stressed rotating member, and the design criteria for this part might be less well established than design criteria for the static parts. The following paragraphs describe the procedure followed in the structural design of the USAAVLABS rotor.

The structural design of the rotor is initiated by calculating the thickness distributions of two random blade sections, shown in Figure 38 as sections A and B.

Each of the two reference sections is first designed as an independent strip element. The radial variation of metal temperature and the corresponding allowable stress criteria for the strip are known from heat transfer analyses and material property data. The tip of the element must have a certain minimum thickness and minimum taper angle for manufacturing reasons. This taper angle is continued radially inward (Figure 39) until the allowable stress is reached. In the design of the USAAVLABS rotor, the allowable stress in the hub was defined as the ultimate tensile strength; in the blades, the allowable stress was defined as the lower value of either (1) ultimate tensile strength divided by 1.3 squared (corresponding to a design overspeed of 30%) or (2) the stress that gives 1% creep in

100 hours. At lower metal temperatures, it is the former value that determines the allowable stress, and at higher metal temperatures (roughly, above 1400°F) it is the latter value that determines the allowable stress.

The radial location where the allowable stress first occurs is defined as the transition point between the tip portion of the element and the hub portion, which has a thickness distribution that keeps the blade stress always within the maximum allowable. The thickness distribution of the hub portion is described by a polynomial of the form:

$$T = a + b\cdot z + c\cdot z^2 + d\cdot z^3 \tag{1}$$

The transition points of the two reference sections can be joined by any arbitrary curve (Figure 40) that describes the locus of transition points of all interpolated and extrapolated sections. In the structural design of the USAAVLABS turbine rotor, a parabola was used to join the transition points of the radial sections. Each interpolated (and extrapolated) section has its thickness distribution below the transition point described by a polynomial which has coefficients obtained by linear interpolation between (or extrapolation from) coefficients of the reference sections. For instance, in Figure 40, the thickness T at the transition point of section C is:

$$T_C = a_C + b_C z + c_C z^2 + d_C z^3 \tag{2}$$

where the coefficients a_C, b_C, c_C, etc. are obtained by linear interpolation of the similar coefficients in sections A and B as:

$$a_C = \frac{(C-B)}{(A-B)} a_A + \frac{(A-C)}{(A-B)} a_B \tag{3}$$

The rotor blade design thus consists of (1) choosing the reference planes A and B, (2) choosing the shape of the transition point locus curve, (3) calculating the complete blade thickness distribution, and then (4) carrying out a complete two-dimensional stress analysis. Depending on the results of this analysis, either the reference plane location or the locus of transition points is modified and the process is repeated until the blade stress distribution is satisfactory.

MATERIAL SELECTION

The material originally selected for the turbine rotor, shroud, and backplate was IN 100 (PWA 658), and that selected for the nozzle was WI52 (PWA 653). PWA 658 is a cast nickel-base alloy with excellent high-temperature properties. Figures 41 and 42 show the minimum properties for PWA 658; these properties were used in determining the allowable stress for the cast parts. PWA 653 is a cast cobalt-base alloy that is used in nonrotating parts. It was originally selected as the vane material to take advantage of its high melting temperature (nearly 100°F higher than PWA 658). Figure 43 compares the melting points, yield strengths, and 150-hour

stress-rupture properties of PWA 658 and PWA 653. During the vane stress analysis, it became obvious that the stresses in the nozzle vane were too high for PWA 653; the vane material was changed to PWA 658.

MECHANICAL DESIGN HISTORY

Preliminary Design

Figure 44 shows the initial configuration of the hot section, designated as the first-iteration mechanical design. This mechanical design was based on preliminary nozzle and rotor analyses, and earlier engine design studies. The rotor cooling configuration was a one-pass design with tip ejection. The backplate was formed by three concentric sections which could accommodate an expected high thermal gradient in the radial direction. Leading-edge impingement cooling without the use of an impingement tube was a unique feature of this configuration. This was possible because of the unusually short vane span (only 0.250 inches in this configuration). In this design, the backplate and shroud cooling air was taken from the air that flowed axially along the burner Inner Diameter (ID).

Second-Iteration Mechanical Design

The second-iteration mechanical design is shown in Figure 45. In this design the nozzle leading edge was cooled by injection of cooling air from the rear shroud into the vane cavity by a small impingement tube welded into the nozzle vane casting. The addition of the impingement tube was required when the vane span increased from 0.250 inches in the first-iteration design to 0.339 inches in this design. The vane span increase was required to maintain the design air flowrate (5.0 pounds per second) when the nozzle angle increased from 70 degrees (in the preliminary design) to 75 degrees (in this design). Because there are no experimental data on the span limitations of the previous cooling configuration, the better-known impingement tube design (for which data exist) was adopted. This impingement tube had a series of small holes that directed the cooling air onto the inner surface of the vane leading edge. The air then passed around the outside of the tube and exhausted through a slot adjacent to the trailing edge, as in the previous design. From a fabrication standpoint, this approach to cooling the nozzle vane facilitated production of the nozzle casting because the core of the vane was open on one side. This would permit more accuracy in positioning the ceramic core used in the production of the hollow nozzle vane.

In this and all succeeding designs, the cooling air is taken from an area ahead of the combustion chamber to obtain cooler initial temperatures. Cooling air from the front shroud was directed to the mid-chord region of the nozzle vanes, where it mixed with the air from the impingement tube. The combined airstream then exhausted near the vane trailing edge.

Third-Iteration Mechanical Design

The third-iteration mechanical design (Figure 46) showed four changes from the previous configuration. These changes appeared at the turbine backplate, nozzle vane interior, front shroud, and at the turbine rotor.

The first change that is noted in Figure 46 is the one-piece backplate that replaced the more complicated three-piece backplate shown in earlier designs. A preliminary heat transfer assessment had indicated that the thermal gradient in the aircooled backplate was not as severe as originally anticipated, and that the segmented backplate (that allows for more differential thermal growth) would not be required.

The second change to the turbine design was the addition of a hollow cooling-air deflector inside the nozzle vanes. Figure 46 shows this cooling-air deflector located just downstream of the impingement tube. This deflector was a sheet metal part that increased the velocity of the cooling air passing between the nozzle vane inner surface and the deflector outer surface. Increased cooling-air velocity in this region promotes better convective cooling of the nozzle vane. The deflector also provided an outlet for the front shroud cooling air, which exhausted at the deflector trailing edge.

The third change to the turbine design was the addition of a piston that is rigidly attached to the downstream end of the front shroud. This was the result of a stress analysis (see Figure 47) of the second-iteration design that indicated high shroud stresses in the rotor tip region. To reduce these stresses, the piston was exposed to atmospheric pressure on the downstream side and cooling-air supply pressure on the upstream side. This pressure differential resulted in an axial force on the shroud that reduced the shroud deflection.

The fourth change shown in Figure 46 was the addition of rotor balance rings. The balancing problem with radial turbine rotors is relatively severe because of the large rotor mass and the lack of balancing locations at a large radius. In this instance, a balance ring can be effective because weights can be added to the ring on the light side of the rotor and metal can be removed from the ring on the heavy side.

Fourth-Iteration Mechanical Design

In the fourth-iteration mechanical design (Figure 48), the backplate and shroud designs were simplified as much as possible. The backplate was a one-piece disk of constant thickness, with constant-depth fins covering the OD portion. The shroud was also a one-piece design with a constant thickness, but with tapered fins covering the OD portion. These basic designs have not been changed in the Phase I final configuration.

The backplate (shown in Figure 49) was designed as a PWA 658 casting of constant 0.15-inch thickness from 2.10- to 3.92-inch radius. It has 280 fins 0.017-inch high with constant-width 0.040-inch slots extending from 3.30- to 3.92-inch radius on the cool-side surface. The backplate is coated on the hot side with PWA 58 (an aluminum-tungsten coating) or a similar coating. A cover plate maintains a 0.020-inch deep cooling air passage from 2.70-inch radius to the outer radius. Cooling air is fed through four sets of circumferentially located holes.

The backplate is supported at both the OD and the ID. The ID support is designed to give nearly zero axial deflection of the plate ID with respect to the OD. The resulting axial forces are 2880 pounds at 3.92-inch radius and 2890 pounds at 2.10-inch radius. No radial forces or bending moments should be transmitted at the backplate-vane platform junction. A convolution was added to the backplate cover at 2.80-inch radius to accommodate radial expansion. The structure supporting the ID of the backplate was also modified to provide a better seal between the rotor cooling air and the backplate cooling air.

The shroud (shown in Figure 50) was also designed as a PWA 658 casting, of constant 0.15-inch thickness that is profiled from 2.40- to 3.92-inch radius and coated on the hot side with PWA 58 or a similar coating. Three hundred tapered radial fins extend from 3.26-inch radius (0.040-inch high) to 3.92-inch radius (0.020-inch high). Slots between the fins are a constant 0.040-inch width.

The shroud cover plate, which forms the cooling air passage, sits on controlled-height lands. The cover plate extends from 2.50-inch radius to 3.92-inch radius, where it is extended in an axial direction to deliver the shroud cooling air to the vanes.

The shroud is supported at the OD by the vane platform and at the ID by a piston-like arrangement. The calculated axial forces are 2100 pounds at 3.92-inch radius and 2540 pounds at 2.40-inch radius. No radial forces or bending moments will be transmitted at the shroud-vane platform junction.

<u>Fifth-Iteration Mechanical Design</u>

Progressive refinement of the turbine design resulted in the fifth-iteration mechanical design shown in Figure 51. In this configuration, entry duct attachment to the nozzle was modified to obtain better control of film cooling air entering at that point. The previous series of dogs on the nozzle casting and mating slots in the entry duct was eliminated. The entry duct was located by two circumferential grooves, the depth of groove being designed to seal on the sheet metal duct ID when differential expansion takes place.

Another change in the fifth-iteration structural design simplified the nozzle design shown in the previous configurations. An enlarged sketch of the vanes is presented in Figure 52. A single impingement tube receives an equal amount of cooling air from both ends, and the second insert

(called a deflector) of previous designs was deleted. The vane platforms received additional film cooling from circumferential slots in the platforms.

Detailed studies of the rotor cooling system of the fourth-iteration design showed that there was a high differential pressure existing across the labyrinth seal on the rear balancing ring. To overcome this problem, the rotor cooling air in the fifth-iteration design was introduced through the center of the rotor from a downstream direction and into the blades by a series of slots in the mounting flange. This change in the rotor cooling-air configuration required the addition of an exhaust fairing with cooling air being introduced through one of the supporting struts, and a carbon face seal installed at the rotor downstream face. The small anticipated air leak past the carbon seal combines with air from the downstream side of the rotor and exhausts through another one of the struts.

Sixth-Iteration Mechanical Design

Figure 53 shows the sixth-iteration mechanical design. This design differs from the previous configurations in two areas: the rotor attachment flange was redesigned, and the carbon face seal of the previous design was replaced by a "controlled gap" carbon seal that has a lower (one-half) rubbing velocity than the face seal. However, this rotor attachment design failed to match the centrifugal and thermal growths of the shaft and rotor, and had to be abandoned in favor of the seventh-iteration mechanical design, which eliminated the troublesome sealing problem.

Seventh-Iteration Mechanical Design

In the seventh-iteration design (Figure 54), the problem of the rotor-shaft attachment was eliminated by a modification to the rotor cooling-air delivery system. The rotor cooling air was introduced into the rotor at the downstream end by a series of machined holes that intersect the cored passages in the rotor; a matched shaft/roror seal was no longer required. To ensure proper intersection of the cooling-air inlet passages, the cored passage in the blade was increased in cross-sectional area at the point of intersection (see rotor section at Station 1.20 in Figure 54).

This configuration also used the two-pass rotor cooling design for the first time in the succession of mechanical designs. The adoption of the two-pass design in preference to the single-pass cooling design was the aggregate result of heat transfer analyses, aerodynamic studies, and cold-flow tests (see discussions of the two-pass design under sections entitled Heat Transfer Analysis and Cold-Flow Tests).

Eighth-Iteration (Phase I - Final) Mechanical Design

During the eighth and final iteration, the mechanical configuration showed minor modifications in five areas: (1) rotor cooling system, (2) backplate, (3) shroud, (4) exhaust duct and exhaust fairing, and (5) carbon ring seal mounting. The Phase I final mechanical design is shown in Figure 55.

The rotor cooling passage has the enlarged section (at intersection of drilled holes) relocated at a smaller diameter. This change was required to increase the wall thickness between the core and the primary gas passage.

The backplate and the shroud have increased outside diameters. This ensures that the pressure load is applied within the vane area rather than downstream of the vane trailing edge where there is no spanwise support. In addition, the shroud has been extended in the downstream direction to ease a stress problem in mounting the exhaust duct to the rig outer casing.

The exhaust duct has a redesigned attachment flange and an elongated exhaust fairing or center body. The center body was elongated to reestablish adequate spacing between the traversing probes and the exhaust struts.

Inside the exhaust fairing, the method of mounting the controlled gap carbon seal was modified to facilitate the fabrication of the exhaust duct center body and the cooling air passage in this region. Also, the carbon ring cross section was modified in accordance with the manufacturer's recommendation.

RESULTS OF STRUCTURAL ANALYSES

This section presents the results of detailed structural analyses on the four most critical members designed under the contract: (1) the nozzles, (2) the rotor, (3) the backplate, and (4) the shroud. All data presented in this section are applicable to the Phase I final configurations.

Temperature distributions for the backplate and shroud were calculated under this task and therefore are presented in this section; the temperature distributions for the nozzles and the rotor are presented in Task 4 - Heat Transfer Analysis.

TURBINE NOZZLES

The calculated stresses for the nozzle vane assembly are shown in Figure 56. The effective stress shown at the inside diameter of the inner platform just satisfies the 300-hour stress-rupture criteria. In the other locations, the effective stress is well below the maximum allowable stress. In Phase II, stress analysis of the vane will continue with the objective of reducing the effective stress at the inner platform ID and optimizing the stress distribution throughout the vane assembly.

TURBINE ROTOR

The Phase I final blade thickness distribution for the double-pass rotor is presented in Figure 57. The corresponding steady-state stress distributions are shown in Figure 58 (for design point), and Figure 59 shows the ratio of effective stress to allowable stress in the rotor at a 130% overspeed condition.

BACKPLATE

The temperature distributions and the corresponding stresses in the backplate are shown in Figures 60 and 61. It should be noted that the tangential stress shown in Figure 61 does not quite meet the 300-hour stress-rupture criteria at the outer radius. However, the magnitude of this discrepancy is small and the design is adequate for a preliminary design. In the Phase II detailed design, the backplate design will be refined to correct this condition.

SHROUD

The metal temperatures and differential pressures acting on the shroud at the design point are presented in Figure 62. The stress distribution corresponding to these conditions is shown in Figure 63. In this part, the maximum stresses meet the 300-hour stress-rupture criteria throughout.

TASK 4 - HEAT TRANSFER ANALYSIS

OBJECTIVE

Analyses under this task were concentrated in two areas:

1. High-temperature nozzles
2. High-temperature rotor

In both of these areas, it was the objective of the heat transfer analyses to evolve a simple yet effective cooling design that would meet the requirements of both aerodynamic and stress analysis.

Because heat transfer analyses constituted a basic portion of the aerodynamic-structural-heat transfer design iteration, both the nozzle and the rotor cooling configurations experienced a progressive development. Following is a description of the evolution of the Phase I final configurations.

GENERAL

Calculation of the heat transfer characteristics of cooled turbine airfoils requires complex analysis aided by empirical input from experimental data. An accurate knowledge of internal and external heat transfer coefficients is important in establishing an efficient cooling design. The system that was used to design the cooled airfoils for the USAAVLABS turbine is the result of established analytical procedures and experimental data accumulated through many years of testing air-cooled engine components. Pertinent factors considered in the design analysis and the method used to calculate metal temperatures are presented in the following paragraphs:

HEAT TRANSFER DESIGN PHILOSOPHY AND ASSUMPTIONS

Airfoil metal temperatures were determined by the classical relations for convective heat transfer. However, the calculated metal temperatures are influenced by the boundary layer assumptions that are used to calculate film coefficients, and the assumptions used in the analysis deserve more detailed description.

In the vane heat transfer calculations, the internal boundary layer was assumed to be fully turbulent. The external boundary layer was assumed to be laminar over a region of 120 degrees (60 degrees in both directions from the inlet stagnation streamline). The remainder of the external boundary layer was assumed to be fully turbulent.

In the rotor heat transfer calculations, the internal boundary layer was assumed to be fully turbulent. On the external sides of the blades, the boundary layer was assumed to be laminar for 0.100 inch downstream of the stagnation streamline. Downstream of this point, the boundary layer was assumed to be in a transition state until a Reynolds number of 7.5×10^5

was reached, at which point the boundary layer was assumed to be fully turbulent. The analysis was based on work published by G. S. Ambrok.*

Film cooling introduces a secondary airstream which alters the normal behavior of the boundary layer; film cooling is used on both the vanes and the rotor in the USAAVLABS design. The altered boundary layer is not well defined analytically, and in these analyses, a previously-generated data corrrelation was used to predict the effect of the secondary airstream.

Thermal stresses are minimized by reducing thermal gradients in the airfoil surface. This is accomplished by matching the coolant distribution and internal heat transfer coefficients with the external heat flux distribution to achieve the desired metal temperatures.

NOZZLE COOLING DESIGNS

Preliminary Nozzle Cooling Design

Figure 64 shows the nozzle cooling configuration as originally conceived. This design used three forced convection schemes to cool the vane. The leading edge was cooled by two impingement streams, the midchord region used pedestals for improved convective cooling, and the vane trailing edge was film cooled. Calculated metal temperatures for this configuration with 1.5% cooling air are shown in Figure 65.

First-Iteration Nozzle Cooling Design

The first-iteration nozzle cooling design is presented in Figure 66. Compared to the original configuration, the nozzle design was simplified by reducing the number of pedestal rows from seven to three.

As part of the initial heat transfer analysis, the cooling air required for the shroud and backplate was calculated. This analysis showed that 3% airflow would be required for each, or that a total of 6% airflow would be required for both. Since there was appreciable cooling air pressure loss across the shroud and backplate, it was not feasible to exhaust the cooling air to the high-pressure region ahead of the nozzle vanes. A more logical location for the shroud cooling air exhaust, which was chosen for the first-iteration nozzle heat transfer design, is near the vane trailing edge where the static pressure is reduced. With this flowpath, the shroud coolant can also be used to cool the nozzle vane without additional nozzle coolant. However, this flowpath increases the temperature of the cooling

*"Approximate Solution of Equations for the Thermal Boundary Layer With Variations in Boundary Layer Structure," By G. S. Ambrok, Soviet Physics, Technical Physics, Volume II, No. 9, 1957.

air entering the vanes. Since it was desirable to obtain the cooling air from the coolest possible location, the shroud/backplate cooling air in this and all later configurations was taken directly from the compressor discharge, bypassing the combustion chamber. The estimated metal temperature distributions for this design are shown in Figure 67.

Second-Iteration Nozzle Cooling Design

Figure 68 shows the second-iteration nozzle cooling design which differs from the previous design in two respects; an impingement tube has been added, and the trailing edge pedestals have been removed.

The impingement tube is used instead of the drilled holes shown in the previous design for two reasons: the vane span was increased from 0.250 inch to 0.339 inch, and the inlet temperature of the vane coolant was increased from 875°F in the original design to 1050°F with the new coolant gas path. The increased span reduces the effectiveness of the former design because it requires a longer distance between impingement streams and possibly a less-effective impingement angle. The higher coolant temperature reduces the heat transfer capacity of the cooling air, and makes the more efficient normal (i.e., 90-degree) impingement angle desirable.

The pedestals in the trailing-edge region were removed in the second-iteration design because the 6% airflow through the vanes did not require increased turbulence in this region.

As previously stated, the 6% airflow exhausting at the vane trailing edge was more than the 1.5% required to cool the airfoil alone; therefore, the originally planned trade-off between vane coolant and trailing-edge thickness was no longer pertinent to this program. In this case, the trailing-edge thickness was determined by the larger value of either the minimum fabricable thickness, or the minimum thickness required to conduct the heat from the vane to the sidewalls. According to the casting vendors contacted during the fabrication study, the minimum thickness for a casting is 0.020 to 0.025 inch. For heat transfer purposes a minimum trailing-edge thickness of 0.040 inch was required to maintain acceptable vane metal temperatures through conduction to the sidewalls; this value was therefore selected as the trailing-edge thickness.

Before this design was analyzed in detail, a different internal configuration was considered desirable (see third-iteration nozzle design) and metal temperatures were not calculated for the second-iteration nozzle configuration.

Third-Iteration Nozzle Cooling Design

A preliminary assessment of the second-iteration vane design indicated that another insert inside the cooled vane would be desirable. This second insert would perform the dual functions of (1) increasing the heat transfer in the mid-chord portion of the vane (by increasing the velocity of the

cooling air), and (2) promoting good mixing of the shroud coolant with the backplate coolant. This two-insert configuration was designated as the third-iteration heat transfer design, and it is shown in Figure 69. This figure shows the computer-calculated steady-state temperatures for the hot test vane (T_{gas} = 2600°F). This design showed a local hot spot of 2111°F on the suction surface near the leading edge, and a redesign was necessary.

Fourth-Iteration Nozzle Cooling Design

Figure 70 shows the cooling configuration that was considered to be the fourth-iteration cooling design. This vane used cross-flow impingement to direct some of the backplate cooling air toward the suction surface hot spot. However, preliminary calculations indicated that this design would create an undesirable temperature gradient in the vane between the two impingement streams, and a detailed analysis was not performed on this configuration.

Fifth-Iteration Nozzle Cooling Design

The fifth-iteration heat transfer design, shown in Figure 71, used a grid of 0.010-inch diameter impingement holes and a spanwise slot in the forward insert to smooth out the vane temperature gradient of the previous design. Calculated vane metal temperatures were acceptable for this fifth vane configuration, but an unacceptable radial temperature gradient (400°F) existed in the vane platforms.

Sixth-Iteration Nozzle Cooling Design

In the sixth heat transfer design, the thermal gradient in the platforms was reduced by injecting 1.5% cooling air (formerly used in the downstream insert) through circumferential slots in each platform, as shown schematically in Figure 72. The sixth-iteration vane used only a single insert to cool the leading edge because the downstream insert had to be removed to achieve platform cooling. This required the reinstallation of pedestals in the trailing-edge region. Similar to the previous design, a spanwise slot in the insert directed an impingement stream against the vane leading edge, and the grid of 0.010-inch diameter impingement holes in the insert smoothed out of the temperature gradient in the vane suction surface. Calculated steady-state metal temperatures for this vane are shown in Figure 73.

Although the vane metal temperatures and stresses for this configuration were acceptable, there was a problem with the endwall effective stress which exceeded the allowable stress at the inner radii (see Figure 74).

This stress problem was the cumulative result of two thermal gradients; one in the endwalls, and the other between the endwalls and the vane itself. The radial gradient in the endwall was the result of overcooling the larger diameters (i.e., the inlet portion) relative to the smaller diameters, which induced high tangential compressive stresses at the inner diameters. The

axial thermal gradient between the endwalls and the vane was the result of the endwalls operating at lower temperatures than the vane, which induced shear stresses at the vane/endwall junction.

Seventh-Iteration Nozzle Cooling Design (Phase I Final Configuration)

In the seventh (and final) nozzle cooling design, the thermal gradients of the previous design have been decreased to a tolerable level. Figure 75 shows schematically how this was accomplished. The circumferential slots that formerly exhausted 3% cooling air were eliminated, allowing the downstream portion of the endwalls to operate at higher metal temperatures. At the same time, heat shields were attached to the upstream portion of the endwalls. The heat shields insulate the endwalls from the cooling air films ejected ahead of the nozzle vane inlet, thus raising metal temperatures in this portion of the endwalls.

With this endwall design, it was necessary to find another way to pass the 3% cooling air that was formerly exhausted through the circumferential slots into the main gas stream. The simplest solution would be to double the flow area of the vane trailing-edge slot on the pressure surface and exhaust all of the 6% cooling air through this slot. However, aerodynamics and the required wall thickness limited the increase in slot opening to about 30%, which will pass 4% cooling-air flow.

The remaining 2% cooling air (total of 6% still required for backplate and shroud) will now be exhausted through a second slot that is on the vane suction surface upstream of the throat, as shown in Figure 76. Downstream of the injection point, the flow is accelerating, and the cooling-air film is expected to remain attached to the vane all the way to the trailing edge. This minimizes aerodynamic losses and reduces the trailing-edge metal temperatures significantly. Figure 76 also shows the vane midspan temperatures with the corresponding local endwall temperatures. These temperatures correspond to 2300°F at the nozzle vane inlet. In the case of a 2600°F hot spot, the vane midspan temperatures will increase by approximately 100°F, and the endwall temperatures will increase by approximately 30°F.

The final temperature and stress distributions for the nozzle endwalls are presented in Figure 77.

ROTOR COOLING DESIGNS

Original Rotor Cooling Design

The original rotor cooling design is shown in Figure 78. This configuration, referred to as the single-pass design, had the cooling-air inlet near the OD of the hub on the backface. The cooling air passed through the blade and exhausted at the rotor tip (i.e., at the leading edge). Pedestals inside the cooling passage increased the effectiveness of the convective heat transfer system; calculated metal temperatures are presented in Figure 79.

First-Iteration, Single-Pass Rotor Cooling Design

The first-iteration, single-pass rotor cooling design (shown in Figure 80) came as a result of an attempt to simplify the original cooling scheme. The number of pedestals in the cooling passage was reduced from 20 small ones and 4 elongated ones to 13 small pedestals. Steady-state temperatures calculated for 3% cooling air are shown in Figures 81 and 82.

In the early analyses of the single-pass rotor, it was assumed that the heat transferred through the blade endwall (i.e., the backside of the blade) was negligible. This assumption is valid at the OD because the blade thickness is small in that region. However, at the lower diameters, the blade thickness at the endwall increases significantly, and the heat transferred through this portion of the blade is enough to raise the previously calculated metal temperatures by approximately 50°F. This temperature increase in the first-iteration design was unacceptable from a stress point of view, and a design modification was required to restore lower rotor temperatures.

Second-Iteration Single-Pass Rotor Cooling Design

The second-iteration rotor cooling design is shown in Figure 83. In this configuration, a center rib was added to the cooling passage to increase cooling-air velocity along the blade endwall. Coolant flow was increased to 3.5%, with a flow split of 2.5% along the endwall, and 1.0% along the shroud side; the flow was choked in the two throat areas. Metal temperatures (shown in Figures 84 and 85) were calculated for the assumed environmental conditions; relative temperature at rotor leading edge = 2225°F, and cooling-air temperature = 850°F. The calculated metal temperatures were approximately 35°F above the allowable limit in the critical area of the blade endwall near the hub. At this point, the single-pass rotor was replaced by the double-pass rotor as the preferred design for the USAAVLABS cooled turbine.

First-Iteration Double-Pass Rotor Cooling Design

While the single-pass design was being analyzed in detail, work was started on an alternative design called the double-pass (or two-pass) cooling design shown in Figure 86. In this scheme, the blade passage is divided into two channels, one along the endwall and the other along the shroud side of the blade. Cooling air enters the rotor as before, and flows along the endwall to the closed tip. Here the cooling air is turned 180 degrees and flows along the shroud side of the blade. Cooling air ejection takes place at a slot on the suction surface near the beginning of the exducer section.

Figure 87 shows the temperature distribution for the first-iteration double-pass design. This analysis, like that for the early single-pass design, assumed that endwall heating was negligible; therefore, calculated temperatures shown were low in the endwall area.

Second-Iteration Double-Pass Rotor Design

When the endwall heating effects were calculated for the double-pass design, metal temperatures became excessive, and the second-iteration cooling design was evolved. In this configuration (Figure 88) endwall cooling was achieved by relocating the center rib closer to the backwall to increase cooling air velocity in that critical region. It was also necessary to increase the rotor cooling airflow to 3%. This change required that 0.5% cooling air be ejected at the tip to allow the 3% cooling air to pass along the rear cavity (i.e., the forward cavity will choke when passing approximately 2.5% cooling air). This 0.5% cooling air exhausting at the tip also serves to reduce the high metal temperatures at the leading edge, and it should not significantly affect the main gas stream. This design shows acceptable metal temperatures at 2225°F rotor leading-edge temperature and 850°F cooling air inlet temperature. Metal temperatures for this configuration are presented in Figures 89, 90 and 91.

Third-Iteration Double-Pass Design (Phase I Final)

Figure 92 shows the Phase I final rotor cooling design, which has been designated as the third-iteration, double-pass design. Differences between this and the previous configuration stem mainly from manufacturing considerations rather than heat transfer requirements. During the Phase II Fabrication (Task 2), cooling passages will be cast in the same manner as before, with core prints for each blade at the rear of the rotor at the leading edge and at the exducer exhaust slot. After casting, the holes at the rear will be brazed closed, and plugs will be brazed into position at the leading edges. Cooling air will be introduced into the cooling passages that intersect the hollow core from a downstream direction.

The final metal temperature distributions for the Phase I Final rotor configuration are presented in Figures 93, 94, and 95.

TASK 5 - FABRICATION STUDY

OBJECTIVES

This task involved work in the following areas:

1. Vendor contact and liaison
2. Metallurgical evaluation
3. Vibration testing

The overall objectives of this task were to establish the level of difficulty in casting the turbine nozzles and rotor, and to evaluate the material properties that can be anticipated in parts cast with present state-of-the art techniques. To accomplish these objectives, leading investment casting vendors were contacted and invited to submit sample parts. The sample rotors were tested to establish both tensile and creep-rupture properties.

Although not originally planned as part of the fabrication study, it was convenient to conduct vibration tests under this task. These tests determined the natural frequencies and vibration modes of the turbine blades. These data will be used in the detail design of the hot turbine (Phase II).

SAMPLE ROTOR DESIGNS

In our original approach to this task, it was planned to obtain sample nozzle and rotor castings that looked like the parts sketched in Figure 96. Metallurgical tests were planned for the rotor only, since it was the more difficult part to fabricate. Ideally, the sample rotor specimen would be designed to have all of the features that could be found in the actual part, such as cored "blades" and thin wall sections. However, further consideration of the program convinced us that a more informative rotor study could be devised if an actual radial turbine rotor could be cast instead of a simplified replica. This would eliminate any doubt as to the applicability of the metallurgical results. When existing tooling for an 11-inch-diameter rotor was found to be available at one of our other facilities, the fabrication study was modified by the substitution of rotors cast with this tooling for the originally planned rotor specimens. Expansion of the original plan uncovered problem areas that otherwise would have gone undetected.

METALLURGICAL PROGRAM

Three leading investment casting vendors (identified as Vendors A, B, and C) agreed to participate in the fabrication study by submitting the following parts:

- Two 11-inch-diameter, 14-bladed rotors, with hollow blade tips and curved exducer blades (designated as parts Nos. 1 and 2).

- One 11-inch-diameter, 14-bladed rotor, with hollow blade tips, but straight exducer blades (designated as part No. 3).
- One typical segment of a nozzle section having cooled vanes (designated as part No. 4).

All three rotors were to be cast in PWA 658 (IN 100), and the vane segment was requested in PWA 653 (WI 52), the original vane material. Part No. 3 was cast with radial blades in the exducer to facilitate the machining of test specimens from that area of the rotor.

Structural tests were conducted in three areas of the rotor: in the hub, in the hub/blade interface (or blade root), and in the blades. These tests consisted of two types, tensile and creep-rupture. The tensile tests are the conventional type, conducted both at room temperature and at elevated temperature. The creep-rupture test is essentially a creep test that is extended to failure; it yields the information usually obtained from separate creep and stress tests. These tests were conducted at elevated temperatures (1400°F). The first test plan is shown in Table II.

TABLE II. ORIGINAL METALLURGICAL TEST PROGRAM

Specimen Location	Test Type	Specimen Orientation
Hub	High Temperature Tensile	1 Radial 1 Tangential
-	High Temperature Creep-Rupture	2 Radial 2 Tangential
Star Root	High Temperature Tensile	2 Radial
-	High Temperature Creep-Rupture	4 Radial
Exducer Root	High Temperature Tensile	2 Radial
-	High Temperature Creep-Rupture	2 Radial
Star Tip	High Temperature Tensile	4 Radial
-	High Temperature Creep-Rupture	4 Radial

The specimens located at the "star tip" were later deleted from the program because blade curvature in this area made the machining of test specimens difficult. Figure 97 shows the general locations of the test specimens within a sample rotor.

The test specimens were of two basic types: a cylindrical specimen taken from the hub area, and a thin flat specimen taken from the blade area. Figures 98 and 99 define the geometry of these two types of specimens.

The tensile specimens were tested with a 60,000-pound capacity Young Universal Testing Machine, shown in Figure 100. This machine was equipped with an autographic recorder, strain pacer, crosshead rate indicator, load pacer, 6-unit rotary electric furnace with a temperature capability to 2200°F, electronic temperature controller, and extensometers for room and elevated temperature testing. The creep-rupture specimens were tested with a Satec model JE testing machine, shown in Figure 101. This machine has a load capability of 12,000 pounds and a temperature capability to 2000°F.

The remainder of Task 5 describes the sample castings that were received and the results of the test programs.

VENDOR A RESULTS

Vendor A experienced some difficulties in casting the hollow-bladed rotors. These difficulties included:

- Failure to fill the blade tips in the star region
- Core breakthrough
- Shrinkage at the rear face of the hub

On the other hand, the grain structure throughout appeared to be excellent.

Figures 102 through 108 show the sample castings as received from the vendor. Figure 101 is an overall view of part No. A-1. The casting deficiencies evident in this photograph include core breakthrough and failure to fill the blade tips; Figures 103 and 104 show typical closeups of these two types of deficiencies. Figure 105 is an overall view of part No. A-2, which is a rotor casting of the same design as part No. A-1. The blade-tip fill problem seems to have been solved in this casting but core breakthrough is still present as shown by the closeup in Figure 106. This figure also shows columnar grains at the blade root as contrasted to the equiaxed grains at the tip area. Columnar grains can give good mechanical properties in the direction of the major axis of the grain, and columnar grains oriented radially would not be objectionable from this standpoint. If the grains are oriented in the axial direction, mechanical strength would be lost due to stresses acting normal to the grain boundary which is weaker than the grain itself, and this is undesirable.

Figure 107 is an overall view of part No. A-3, which is the flat-bladed rotor used for exducer specimens. This part was submitted with solid blades because the vendor had used all of his cores and the core tooling was no longer available to him. Figure 108 shows the nozzle vane segment, part No. A-4, which was cast with vendor-furnished tooling. This part was not structurally tested.

Vendor A Casting Test Results

Results from metallurgical tests for the Vendor A castings are presented in Table III. Some slight deviations from the original test plan can be noted. For instance, there are extra specimens in the star root and hub/tangential categories; and in the exducer root series only one of the two tensile tests was accomplished at high temperatures. The temperature deviation is insignificant because these and later tests showed no difference between room temperature and 1400°F tensile properties.

In general, the results shown in Table III indicate that both tensile and creep-rupture properties are low; ductility in both cases was also low. The average elongations were 3.7% in tension and 1% in creep-rupture, as compared to 5% and 2% respectively that is required for PWA 658.

VENDOR C RESULTS

Figures 109 through 114 show the castings submitted by Vendor C. These castings presented a better overall appearance than the Vendor A castings; only a slight tip-fill problem is evident and some porosity in the blades was observed. Gross shrinkage was not observed in the hub area, and core alignment was good (Figure 110). Grain size in the hub and blades was generally fine and equiaxed (Figures 111, 112, 113), although some columnar formation was observed near the blade root.

Vendor C Specimen Tests

Vendor C metallurgical tests were approximately one-half completed at the time Vendor A results were being analyzed. Two of the Vendor A specimens that had previously been rejected from X-ray inspection were etched and examined. Figures 115 and 116 show that the specimens were small enough to allow a single grain boundary to completely span the test section. Since the grain boundary is weaker than the grain itself, the implication was that the test results might not be representative of larger and more homogeneous sections. It was therefore decided to test three new types of specimens:

1. Wider flat specimens containing only blade material.
2. Wider flat specimens containing both blade and hub material.
3. Original-size flat specimens containing only blade material.

Results from these specimens, when compared to the previously acquired data, should indicate:

- If the previous data were representative of larger sections
- If there was any degradation of properties at the blade/hub junction, where there may be an abrupt change in grain size.

TABLE III. METALLURGICAL TEST RESULTS FROM VENDOR A CASTINGS

				Tensile				Creep-Rupture			
Specimen Location	Code No.	Temp (°F)	Stress (ksi)	Ult (ksi)	Y.S. (ksi)	Elong (%)	R.A. (%)	Life (hr)	Elong Prior (%)	Elong Final (%)	Remarks
Star Root	A22-11	RT	-	78.0	None	3.0	-	-	-	-	Some shrink
	A22-9	1400	-	98.4	None	4.0	-	-	-	-	Some shrink
	A22-1	1400	-	109.3	108.2	4.0	-	-	-	-	-
	A22-3	1400	85.0	-	-	-	-	12.8	2.4	5.1	-
	A22-6	1400	85.0	-	-	-	-	0.1	-	1.6	-
	A22-7	1400	85.0	-	-	-	-	8.9	1.33	4.9	-
	A22-8	1400	85.0	-	-	-	-	0	-	2.1	-
Exducer Root	A33-9	RT	-	118.7	113.7	7.0	-	-	-	-	-
	A33-4	1400	-	109.6	108.5	5.0	-	-	-	-	-
	A33-2	1400	85.0	-	-	-	-	16.9	0.86	3.8	-
	A33-8	1400	85.0	-	-	-	-	36.2	1.53	3.1	As cast
Hub/Radial	A24-1	RT	-	103.0	None	-	-	-	-	-	-
	A24-2	1400	-	97.3	None	-	-	-	-	-	-
	A24-5	1400	85.0	-	-	-	-	1.9	0.50	2.1	-
Hub/Tangential	A25-2	RT	-	106.8	106.4	2.0	4.0	-	-	-	-
	A25-1	1400	-	128.0	117.5	4.0	6.5	-	-	-	-
	A25-3	1400	85.0	-	-	-	-	7.8	0.5	1.9	-
	A25-6	1400	85.0	-	-	-	-	104	1.86	4.2	-
	A25-8	RT	-	106.8	101.4	4.0	-	-	-	-	-
PWA 658 Spec	-	-	-	115.0	95.0	5.0	-	23	2.0	-	-

The width of the modified flat specimens was increased from the original dimension of 0.200 inch to 0.350 inch. Figure 17 shows the modified specimen geometry.

Results from the Vendor C metallurgical tests are presented in Table IV. All of the 0.350-inch flat specimens exceeded the PWA 658-specified ultimate tensile strength of 115,000 psi. All but one of them (code No. C336) exceeded the specification yield strength of 95,000 psi. However, this one part failed outside the test section, which precludes any conclusions relative to yield strength and elongation. Elongation ranged from 11% to 3.3%; the average tensile elongation (8%) exceeded that of the specification (5%). Thus, the general conclusion is that these wider specimens showed acceptable tensile properties.

In attempting to compare the tensile properties of the 0.350-inch specimens with those of the 0.200-inch specimens, there is only one tensile specimen shown in the smaller size (code No. C121). This specimen exceeded the specified tensile properties. However, part No. C122 was a creep-rupture specimen that ruptured on loading, or at a stress less than 85,000 psi. It can therefore be regarded as a 0.200-inch tensile specimen that failed to meet the ultimate tensile properties. Specimens C145 and C152 are 0.188-inch diameter cylindrical specimens that were given tensile tests; both specimens failed to meet the tensile specifications. Although these two specimens were of different geometry than the 0.200-inch flat specimens, results from Vendor A rotors showed no discernible difference in tensile properties between the two types of specimens. If the premise is accepted that specimens C145 and C152 gave results typical of 0.200-inch flat specimens, then these conclusions are valid:

- Wider flat specimens show improved tensile properties; therefore, the results from the 0.200-inch specimens show lower tensile properties than actually exist in the part
- The Vendor C rotors have acceptable tensile properties
- The Vendor A tensile properties are somewhat better than those shown in Table I.

Creep-Rupture Test Results

Creep-rupture results from the 0.350-inch flat specimens (Table IV) show no increase in life as compared to the original size specimens. Admittedly, there are only three (0.350-inch) data points available for comparison (C333, C335, C34), and one of these (C333) failed outside the test section. Assuming that the other two 0.350-inch test specimens show an average creep-rupture life typical of the part, the following conclusions are valid:

- The 0.200-inch flat specimens and the 0.188-inch diameter cylindrical specimens (which show creep-rupture lives comparable to the 0.350-inch specimens) show the actual creep-rupture life of the part

- The creep-rupture lives of both the Vendor A and the Vendor C castings are below PWA 658 specification.

Experimental Heat Treatment Results

In an attempt to improve material properties through heat treatment, five 0.188-inch diameter specimens from the Vendor C rotors were given five different experimental heat treatments. These heat treatments were designed to improve the material homogeneity which would improve material properties if unusual segregation of the alloying elements was present. Results showed no improvement in creep-rupture life and it was concluded that segregation of alloying elements was not responsible for the foreshortened stress-rupture life.

VENDOR B TEST PROGRAM

Vendor B submitted the standard number of 11-inch diameter rotors and a nozzle section in PWA 658; in addition, two rotors were submitted in PWA 658 that were close to the USAAVLABS turbine size in overall dimensions (approximately 8-inch diameter). Figures 118 through 125 show these parts, all of which had a good overall appearance. There appeared to be no evidence of a tip-fill problem nor of excessive core shift. However, these rotors showed somewhat more axially-oriented columnar grain structure in the blades than was observed in the Vendor A and Vendor C castings. The two small rotors are shown in Figures 124 and 125. Part No. B-5 (Figure 124) had solid blades, while part No. B-6 had cored blades.

At the time that the Vendor B test program was about to start, the results from the Vendor A and Vendor C tests were available. It was concluded that if the Vendor B castings were similar to the previous castings, nothing would be accomplished by completing the originally-planned test program. Four specimens each (0.188-inch diameter hub specimens) were taken from rotors B-1 and B-5. One specimen from each rotor was given a tensile test, and the remaining six were given creep-rupture tests. Test results, presented in Table V, show results similar to the previous rotors (i.e., tensile properties are generally acceptable but creep-rupture life and ductility are low). At this point, the test program on the Vendor B rotors was suspended.

SUPPLEMENTAL METALLURGICAL DATA

After the formal completion of the Fabrication Study, supplemental metallurgical data were generated from two sources: (1) additional creep-rupture tests from rotors previously submitted by Vendors B and C, and (2) tensile and creep-rupture tests of a newly-submitted rotor from Vendor B.

TABLE IV. RESULTS OF METALLURGICAL TESTS ON VENDOR C ROTORS

Specimen Location	Code No.	Temp (°F)	Stress (ksi)	Ultimate Tensile Strength (ksi)	Yield Strength (ksi)	Elongation (%)	Creep-Rupture Life (hr)	Prior Elongation (%)	Final Elongation (%)	Remarks
Star Root	C121	1400		117.0	106.8	7.0	-	-	-	-
(0.200 in. wide)	C122	1400	85.0	-	-		-	-	-	Ruptured on loading
	C123	1400	85.0	-	-	-	14.0	1.10	3.2	-
	C124	1400	85.0	-	-	-	2.7	0.62	2.8	-
	C126	1400	85.0	-	-	-	11.3	1.01	2.8	-
Exducer Root	C331	RT	-	121.9	112.1	10.0	-	-	-	-
(0.350 in. wide)	C333	1400	85.0	-	-	-	7.7	1.5	7.1	Broke in radius
	C334	1400	-	132.1	110.7	11.0	-	-	-	-
	C335	1400	85.0	-	-	-	15.8	3.3	3.7	-
	C336	1400	-	129.0	-	-	-	-	-	Broke in pin hole
Blade Only	C31	1800	29.0	-	-	-	17.8	3.9	7.0	-
(0.200 in. wide)	C32	1400	85.0	-	-	-	4.7	0.6	3.4	-
	C33	1400	85.0	-	-	-	20.6	1.1	3.8	-
(0.350 in. wide)	C34	1400	85.0	-	-	-	13.4	2.1	3.3	-
	C35	RT	-	122.3	106.8	6.7	-	-	-	-
	C36	1400	-	129.8	110.9	3.3	-	-	-	-
Hub/Radial	C141	1400	85.0	-	-	-	10.4	0.76	2.7	-
(0.188 in. dia)	C144	1400	85.0	-	-	-	2.3	0.2	0.98	-
	C145	1400	-	107.5	-	-	-	-	-	No elongation
Hub/Tangential	C151	1400	85.0	-	-	-	2.3	0.29	1.1	-
(0.188 in. dia)	C152	1400	-	106.0	-	-	-	-	-	No elongation
	C156	1400	85.0	-	-	-	8.2	1.6	3.5	-
Hub/Rad/Tang.	C11	1400	85.0	-	-	-	3.1	-	1.2	Experimental heat treat
(0.188 in. dia)	C12	1400	85.0	-	-	-	2.0	-	4.5	Experimental heat treat
	C13	1400	85.0	-	-	-	-	-	3.5	Experimental heat treat ruptured on loading
	C141	1400	85.0	-	-	-	14.5	1.9	2.8	Experimental heat treat
	C142	1400	85.0	-	-	-	2.1	0.14	1.4	Experimental heat treat
PWA 658 Spec	-	1400	85.0	-	-	-	23.0	2.0	-	-
	-	1800	29.0	-	-	-	23.0	-	-	-
	-	1400	-	115.0	95.0	5.0	-	-	-	-

TABLE V. RESULTS OF METALLURGICAL TESTS ON VENDOR B ROTORS

Specimen Location	Code No.	Temp (°F)	Stress (ksi)	Ultimate Tensile Strength (ksi)	Yield Strength (ksi)	Elon-gation (%)	Creep Rupture Life (hr)	Prior Elon-gation (%)	Final Elon-gation (%)	Remarks
Hub/Tangential	BS1	1400	-	127.2	116.5	2.7	-	-	-	8-in. dia rotor
(0.188 in. dia)	BS2	1400	85.0	-	-	-	3.1	0.9	2.2	8-in. dia rotor
	BS3	1400	85.0	-	-	-	3.7	1.1	2.4	8-in. dia rotor
	BS4	1400	85.0	-	-	-	15.1	-	0.98	8-in. dia rotor
Hub/Tangential	BL1	1400	85.0	127.2	118.8	4.0	-	-	-	11-in. dia rotor
(0.188 in. dia)	BL2	1400	85.0	-	-	-	21.3	2.7	5.3	11-in. dia rotor
	BL3	1400	85.0	-	-	-	12.8	1.6	2.4	11-in. dia rotor
	BL4	-	-	-	-	-	9.9	1.6	2.4	11-in. dia rotor
PWA 658 Spec	-	1400	-	115.0	95.0	5.0	-	-	-	-
	-	1400	85.0	-	-	-	23.0	2.0	-	-

The supplemental creep-rupture tests used different test conditions (1400°F/70,000 psi) than were used earlier (1400°F/85,000 psi). The new test conditions were representative of the worst operating condition in the blade. Results are shown in Table VI. Cast bar specimen properties are included for comparison.

TABLE VI. TEST RESULTS FROM 1400°F/70,000 PSI CREEP-RUPTURE TESTS

Specimen	Hours To Rupture	Prior Elongation	Remarks
Vendor B-1	568	2.90	11-in. dia rotor
Vendor B-2	124	0.89	11-in. dia rotor
Vendor B-3	142	3.98	11-in. dia rotor
Vendor B-4	158	1.40	8-in. dia rotor
Vendor B-5	35	3.78	8-in. dia rotor
Vendor B-6	166	1.10	8-in. dia rotor
Vendor B-7	215	1.0	8-in. dia rotor
Vendor C-1	91.8	0.41	11-in. dia rotor
Vendor C-2	300.0	0.70	11-in. dia rotor
Vendor C-3	261.0	2.57	11-in. dia rotor
Vendor C-4	239.0	0.74	11-in. dia rotor
PWA 658	175.0*	Exact value not established, but greater than 2%	-

*Minimum life established from cast bar specimens.

Although the average life of the 8-inch diameter Vendor B rotor (143 hours) was less than the cast bar specimen minimum life of 175 hours, the average lives of the 11-inch diameter Vendor B and Vendor C rotors (278 and 223 hours, respectively) exceeded the minimum life. Even so, there were some specimens from each rotor that did not meet the minimum life, and this variation in material properties is considered unsatisfactory. In addition, at least one specimen from each rotor showed unacceptable creep elongation (i.e., below 2% elongation).

The 8-inch diameter supplemental rotor casting submitted by Vendor B was poured under different conditions than the earlier rotors. The new casting parameters were chosen in an attempt to improve ductility, creep elongation, and creep-rupture life, all of which were low in the earlier Vendor B rotors. Results are presented in Tables VII and VIII.

TABLE VII. RESULTS FROM VENDOR B SUPPLEMENTAL ROTOR - TENSILE PROPERTIES					
Specimen No.	Temperature (°F)	Ultimate Strength (kpsi)	Yield Strength (kpsi)	Elongation (%)	Area Reduction (%)
B-100	Ambient	123.5	112.7	6.0	17.3
B-101	1400	139.7	116.3	6.0	8.0
PWA 658 Spec	Ambient & 1400	115.0	95.0	5.0	-

TABLE VIII. RESULTS FROM VENDOR B SUPPLEMENTAL ROTOR - CREEP-RUPTURE PROPERTIES (1400°F/85,000 psi)			
Specimen No.	Hours To Rupture	Prior Elongation	Remarks
B-102	14.5	1.25	-
B-103	33.7	2.25	-
B-104	10.1	1.10	-
B-105	10.4	1.04	-
B-106	20.5	1.48	Broke outside gage length
PWA 658 Spec	23.0	2.00 min	-

Although the tensile elongation (6%) observed in these tests was improved compared to the previously-submitted parts (2.7 to 4.0%), the creep-rupture lives showed no significant improvement.

General Observations on Metallurgical Program

Based on the physical appearance of the sample castings and the results of the metallurgical tests, we have formulated the following observations:

- In the final vendor selection, Vendors B and C are preferred over Vendor A on the basis of the overall quality of the castings delivered. Final vendor selection has been deferred until Phase II.
- All castings (i.e., from Vendors A, B, and C) showed these similar material properties:

  1. Generally acceptable tensile properties
  2. Unacceptable creep-rupture life
  3. Generally low ductility

- Improvements in the material properties must come as a result of changes to the casting process or changes to the rotor geometry. Geometry modifications are severely limited by aerodynamic and stress requirements.
- A casting development program will be required to produce satisfactory castings for Phase II turbine testing.

TIP CLOSURE

At the time that the two-pass rotor became the preferred design for the USAAVLABS turbine, it was assumed that the tip could be closed after casting by brazing or welding. However, PWA 658 is not considered to be a weldable alloy and there was some concern regarding the validity of the initial assumption. A qualitative answer to the brazeability question was obtained with a blade taken from one of the Vendor C rotors. A nickel-base braze was used to close the end of the blade, which was then sectioned to determine the depth of penetration. Figure 126 shows the sectioned blade. The braze depth appears to be approximately twice the wall thickness (0.020 inch) at the tip, or about 0.040 inch. This demonstration was considered to be confirmation of the initial assumption regarding brazeability, but the specimen was not tested for structural integrity. The Phase I final configuration of the USAAVLABS rotor would require such a brazing procedure in two areas; at the tip and at the turbine backface. The latter passage is required to allow for a core print to be used during casting.

VIBRATION TESTS

The vibration test program was defined for a given rotor as follows:

1. Establish blade geometry through inspection methods and drawings, where available
2. Determine fundamental frequency of all sound blades on one rotor
3. Determine the frequency and nodal patterns of higher order resonance modes for:

- The blade having the lowest fundamental frequency.
- The blade having the highest fundamental frequency.
- The blade having a fundamental frequency nearest the mean value.

Vibration tests were completed for two rotors:

- 11-inch-diameter cored rotor (Vendor C)
- 8-inch-diameter cored rotor (Vendor B)

The experimentally determined natural frequencies are shown in Tables IX and X. No attempt was made to analytically predict these natural frequencies in Phase I. This will be done in Phase II to determine if the existing computer program can be used for hollow-bladed rotors.

The nodal patterns for the highest, lowest, and mean-frequency blade on each rotor are shown in Figures 127 through 132. These data will contribute to the final turbine design in Phase II by pinpointing potentially dangerous frequencies that should be avoided in the primary sources of blade excitation.

TABLE IX. RESULTS OF VIBRATION TESTS - 11-INCH DIAMETER ROTOR (PART NO. C-1)

Blade No.	Star Natural Frequency (cycles/sec)	Exducer Natural Frequency (cycles/sec)
1	2444	1859
2	2411	1860
3	2616	1857
4	2458	1845
5	2624	1925
6	2490	1826
7	2391	1825
8	2493	1857
9	2448	1853
10	2416	1855
11	2443	1953
12	2433	1857
13	2418	1936
14	2433	1954

TABLE X. RESULTS OF VIBRATION TESTS - 8-INCH DIAMETER ROTOR (PART NO. B-6)

Blade No.	Star Natural Frequency (cycles/sec)	Exducer Natural Frequency (cycles/sec)
1	4572	6810
2	4610	6650
3	4671	6698
4	4497	6720
5	4905	6768
6	4713	6853

TABLE X - Continued		
Blade No.	Star Natural Frequency (cycles/sec)	Exducer Natural Frequency (cycles/sec)
7	4574	6857
8	4898	6858
9	4639	6856
10	4529	6856
11	4713	6754
12	5227	6854

TASK 6 - COLD-FLOW TESTS

OBJECTIVES

Testing under this task was conducted in two areas:

1. Water-rig testing
2. Cold-flow turbine testing.

Water-rig testing was conducted with the water visualization rig that was designed under Task 2 - Aerodynamic Design. The objective of these tests was to qualitatively assess the effect of cooling-air exhaust at the rotor tip.

Cold-flow testing was accomplished with an existing test rig at UACL, shown in Figure 133. The objectives of the cold-flow tests were to show:

- Effect of increased vane trailing-edge thickness (TET)
- Effect of different numbers of nozzle vanes
- Effect of different numbers of rotor blades

The following hardware from another program was available for test at the beginning of the program:

- 25-vaned nozzle section with thin trailing edges (0.017 inch TET), hereafter referred to as "standard 25-vaned nozzle"
- 14-bladed rotor

The following new hardware was designed, fabricated and tested under this program:

- 25-vaned nozzle section with thickened trailing edges (0.050 inch TET)
- 20-vaned nozzle section with thickened trailing edges (0.050 inch TET)
- 15-vaned nozzle section with thickened trailing edges (0.050 inch TET)
- 12-bladed rotor
- 10-bladed rotor

The following paragraphs describe the water-visualization and cold-flow tests, the results, and the conclusions.

WATER VISUALIZATION TESTS

Shakedown tests of the water rig revealed several operational problems, the most troublesome of which was the hydrogen-bubble system. Initial attempts at high speed photography were disappointing; resolution was poor, the hydrogen bubbles could not be observed at all, and the slit-light output was inadequate. Eventually, the hydrogen-bubble system was replaced by a

hypodermic tube which injected air into the nozzle channel at mid-span. This did not prove to be completely satisfactory either because the relatively large bubbles tended to rise (toward the turbine shroud) as they flowed to the center of the rotor. As these bubbles approached the shroud, they tended to indicate secondary flow instead of primary flow. Ultimately, the very small air bubbles resulting from entrained air were used to trace the main stream flow, and dyed water was used to trace the cooling airflow.

Figure 134 shows the relative streamline patterns that were reconstructed from a large number of high-speed movie frames for three turbine operating conditions both with and without cooling air ejection. These pictures show the effect of tip ejection of cooling flow on the primary flow patterns. The streamlines shown here were formed by faint background traces produced by random aeration of the rig rather than by the injected bubbles. The spacing of the streamlines in Figure 134, therefore, does not indicate velocity; the streamtubes shown do not pass equal amounts of flow per unit time.

The three pairs of sketches show the rotor tip at a large negative incidence (N = 30 rpm), at a near-zero incidence (N = 22 rpm), and at a small positive incidence (N = 19 rpm). At the near-zero incidence case the primary streamline pattern appears to be little affected by the cooling air stream, but in both of the other cases where separation is already present due to tip incidences, the jet of cooling air increases the region of separation.

As the blade loading is increased by reducing the number of blades, the stagnation streamline assumes a direction of increasingly positive tip incidence and eventually moves down the pressure surface toward the hub. This results in a region of flow reversal on the pressure surface and a region of separation on the suction surface. Since the USAAVLABS turbine rotor has relatively few rotor blades (12) and since these blades are designed for some positive nominal incidence (6.5 degrees), it can be expected to operate at a condition of significant pressure surface flow reversal (like that shown for 18.9 rpm) at the design point. Tip ejection of cooling air is shown to increase the region of suction surface separation at this condition. While no quantitative results are available from the water tests, previous experience has shown that increasing the region of separation in a flow channel is generally accompanied by an increase in losses. The logical conclusions that must be drawn are that the use of tip ejection for the USAAVLABS turbine design will result in lower aerodynamic performance, and that the two-pass cooling design (see Task 4 - Heat Transfer Design) will show improved overall efficiency. The small amount of cooling air ejected at the tip in the two-pass design is not expected to alter the mainstream flow significantly.

It should also be pointed out that the two-pass rotor cooling design, in addition to reducing the losses at the rotor tip, might improve aerodynamic performance in the exducer. A performance gain will result if the

injection of the rotor cooling air can energize the suction surface boundary layer enough to delay or eliminate separation in the exducer.*

There is one tip ejection design configuration that offers the possibility of improving aerodynamic performance. In this design, the cooling air is turned nearly 180 degrees at the tip and it is injected in the same direction as the primary flow (radially inward). Injection of the cooling air in this manner could energize the boundary layer, thus reducing the separation that is ordinarily present. Such a design was studied for this turbine rotor, but the stress problems inherent in this configuration precluded its use.

COLD-FLOW TURBINE TEST PROGRAM

To accomplish the original cold-flow objectives, the following hardware configurations were assembled and tested:

- Build 1, standard 25-vaned nozzle, 14-bladed rotor
- Build 2, standard 25-vaned nozzle, 10-bladed rotor
- Build 3, standard 25-vaned nozzle, 12-bladed rotor
- Build 4, 25-vaned nozzle with thickened TET, 14-bladed rotor
- Build 5, 20-vaned nozzle with thickened TET, 14-bladed rotor
- Build 6, 15-vaned nozzle with thickened TET, 14-bladed rotor

In addition, an extra build was tested with the following configurations:

- Build 7, 15-vaned nozzle with thickened TET, 14-bladed rotor exhaust center body

Results from Builds 1, 2, and 3 showed the effect of reducing the number of rotor blades; the reduction was required in the USAAVLABS rotor to reduce stresses. Results from Builds 1 and 4 showed the effect of increasing the usual vane trailing-edge thickness; this increase was necessary for heat transfer in the USAAVLABS design. Results from Builds 4, 5, and 6 showed the effect of reducing the number of nozzle vanes; the reduction was required in the USAAVLABS design to reduce the number of cooled airfoils and to achieve a more favorable TET/throat opening ratio. Build 7 was tested to verify the applicability of the preceding six builds to the USAAVLABS turbine.

* "Phase III Interim Report No. 6, 90-degree Inward Flow Radial Turbine Research Program," UACL Engineering Report No. 458, DRB File 4720-10.

Cold-Flow Test Results

Test results from all builds are presented in curve form in Appendix I, (Figures 146 through 207), and in tabular form in Appendix II, (Tables XI through XVII).

Universal performance maps for Builds 1, 2, and 3 are presented (in order of increasing number of blades) as Figures 135, 136, and 137. However, to study the effect of reduced numbers of rotor blades, it is more convenient to plot the efficiency at a nominal "design point" as a function of the number of rotor blades, as in Figure 138. This Figure shows turbine efficiencies at $N/\sqrt{\theta}$ = 22,950 and a pressure ratio (PR) of 6.0, which is the nominal "design point" for the DRB 14-bladed rotor. On this basis, the turbine efficiency decreases as the number of rotor blades is decreased. The efficiency decrement between 10 and 12 blades is larger than that between 12 and 14 blades, as predicted by the calculated velocity distributions (see Task 2 - Aerodynamic Design). However, the efficiency losses shown in Figure 138 should be interpreted with the realization that the 10- and 12-bladed rotors were machined with the same blade tooling that was designed for the 14-bladed rotor. Thus, the 10- and 12-bladed rotors have been penalized to some extent with a nonoptimum blade geometry.

In evaluating the desirability of a given number of rotor blades, the cooling air required to cool the part must also be considered in addition to the aerodynamic performance of the rotor. Thus, the improved efficiency of a high number of blades tends to be offset by a higher cooling air requirement, which affects the overall cycle efficiency. To evaluate the desirability of a 12-bladed rotor for the USAAVLABS design, the following hypothetical cycle was analyzed:

- Type of engine - twin-spool turboshaft
- Airflow rate - 4.9 pounds per second
- TIT - 2300°F
- Engine pressure ratio - 18:1
- Operating conditions - sea level, standard day
- 12-bladed turbine efficiency - 87.5%

The following assumptions were applied to the hypothetical cycle:

- Efficiency variation for 10- and 14-bladed rotors would be the same as the test data shown in Figure 138.
- Coolant flowrate - 0.0104 pound of air per second per blade.

Figure 139 compares the cycle performance on the basis of specific fuel consumption (SFC) and "total power." Total power was calculated as the output horsepower, plus the estimated power required for the auxiliaries, plus the power required for disk friction. It was assumed that the auxiliary horsepower and disk friction remained constant, and that the shaft horsepower varied with a change in turbine design.

Figure 139 shows that the SFC increases from 0.4210 pound of fuel per horsepower-hour for the 14-bladed rotor to 0.4213 pound of fuel per horsepower-hour for the 12-bladed rotor. In spite of a slight improvement shown for the 14-bladed rotor, we are still planning to use a 12-bladed rotor for the USAAVLABS program for the following reasons:

- The results shown in Figure 139 are somewhat pessimistic for the 12-bladed rotor; it has been penalized with a nonoptimum blade shape.
- The results shown in Figure 139 are somewhat optimistic for the 14-bladed rotor. This follows from the fact that stresses in the 14-bladed rotor would be higher than in the 12-bladed rotor, which already operates at the maximum allowable stress; stresses in the 14-bladed rotor could be reduced by either operating at a lower tip speed (and lower velocity ratio) or increasing the blade root thickness, either of which would result in lowered performance.

Trade-Off Studies

In our original approach to the design of the USAAVLABS turbine, we had anticipated that two trade-off studies could be conducted. The first study would trade off vane coolant for trailing-edge thickness; for example, a thicker TET would require a thinner cooling air film. The second study would trade off total vane coolant for the number of vanes; for example, more vanes would require more total coolant, but turbine performance might be improved. However, these studies are no longer pertinent to the design, since the backplate and shroud coolant are also used to cool the vanes, and the total cooling air flowed through the vanes is more than that required to cool the airfoils alone.

Effect of Increased TET

Builds 1 and 4 used identical hardware except for the thickness of the nozzle vane trailing edge. Build 1 nozzles had a 0.017-inch TET, while the Build 4 nozzles had a 0.050-inch TET. Although the USAAVLABS turbine nozzles have a 0.040-inch TET, the significant parameter in nozzle design is the ratio of TET/Throat Opening, and Build 4 approximates this ratio for the USAAVLABS design (0.141 cold flow, 0.132 USAAVLABS).

A comparison of Builds 1 and 4 at the DRB turbine design point (PR = 6, $N/\sqrt{\theta}$ = 22,950) shows a total-to-total efficiency of 88.8% for Build 1 and 88.5% for Build 4. Figure 140 shows the measured change in efficiency as a function of the TET/Throat Opening ratio. Between these two data points, the loss is believed to be a linear function of TET/Throat Opening. Although those data are no longer required for a trade-off study, they can be used to assess the penalty imposed by the thickened TET of the USAAVLABS nozzle. The minimum TET/Throat Opening ratio shown for the USAAVLABS turbine is based on an assumed value of 0.017 inch for TET, which is typical of a minimum value for structural requirements. Thus, the 0.040 inch TET required for heat conduction results in a performance penalty of about 0.24 percentage points. However, this penalty is more than offset by the advantages derived from high cycle pressure ratio and high turbine inlet temperature.

Effect of Vane Reduction

Builds 4, 5, and 6 show the effect of reducing the number of nozzle vanes. A comparison of the performance of these three configurations is presented in Figure 141; the comparison gives the total-to-total efficiency of the three configurations as a function of reduced speed, $N/\sqrt{\theta}$. The design point of the DRB turbine is located at PR = 6, $N/\sqrt{\theta}$ = 22,950, which corresponds to an isentropic velocity ratio of 0.68. At this point, there is only a small variation in turbine performance with the 15-, 20-, and 25-vaned nozzle sections. The 15-vaned configuration shows the highest efficiency, and the 25-vaned configuration shows the lowest; however, there is less than 0.2 percentage points difference between the two extremes.

The USAAVLABS turbine has been designed for a pressure ratio of 5.165 and an isentropic velocity ratio of about 0.65. This corresponds approximately to a value of $N/\sqrt{\theta}$ = 21,000. Therefore, the test data shown for a pressure ratio of 5 and U/C_0 = 0.65 in Figure 141 might be more representative of the USAAVLABS turbine nozzle performance. Under these conditions, the 20-vaned nozzle configuration shows better performance than either the 15- or 25-vaned configurations. Again, the total variation in performance is very small, with only about 0.4 percentage points separating the two extremes.

Conclusion From Test Results

On the basis of these data, there appears to be no aerodynamically "optimum" number of vanes that shows a marked improvement in performance at design point. The rationale for selecting the number of nozzle vanes for the USAAVLABS turbine might then be based on other considerations, such as off-design performance, stress problems, or vibrational requirements. One of these considerations, off-design performance, can be evaluated from the current data. Figure 142 shows the variation in turbine performance as a function of pressure ratio and speed. Again, the results show that there is no clear-cut choice for the best number of vanes for off-design operation.

In view of these test results, we have concluded that our original selection of 20 vanes should be retained for the USAAVLABS design. If final stress and vibration studies show that the 20-vaned design is acceptable from their respective viewpoints, then the design will probably give slightly better performance at design point. If, however, a slightly different number of nozzle vanes appears desirable from the final stress/vibration studies, then this design affords the flexibility of either adding or subtracting nozzle vanes while staying within the range of acceptable and known performance.

Build 7 Test Results

Build 7 was an unscheduled test with the same hardware as Build 6 except that a center body (or bullet) was added downstream of the turbine rotor. The USAAVLABS turbine has been designed as a gas generator turbine for a hypothetical twin-spool engine which would have an annular duct between the gas generator turbine and the power turbine. However, the previous cold-flow tests used a single-shaft-engine type turbine configuration that exhausts directly into a conical diffuser. Since the meridional streamlines in the exducer are affected by the downstream duct geometry, a test indicating the effect of the center body was considered to be desirable.

Figures 200 through 207 in Appendix I compare the performance of Builds 6 and 7, and Table XVII in Appendix II presents Build 7 test data. At the DRB turbine design point, interpolation of the test data shows that Build 7 has a total-to-total efficiency 0.3 percentage points higher than Build 6. This performance improvement takes place over the outer half of the exducer exhaust annulus (Figure 143). Apparently, the addition of a center body alters the radial equilibrium at the rotor exit in such a way that the flow near the exducer tip is accelerated (Figures 144 and 145). This reduces the diffusion on the exducer suction surface which results in reduced flow separation in that area.

From these data, we have concluded that the results of Builds 1 through 6 are applicable to the USAAVLABS turbine (even somewhat conservative), since the difference in exit velocity triangles is slight with and without the center body. The data also indicate that for a given rotor geometry, an annular exhaust duct will give slightly better performance than a conical exhaust duct.

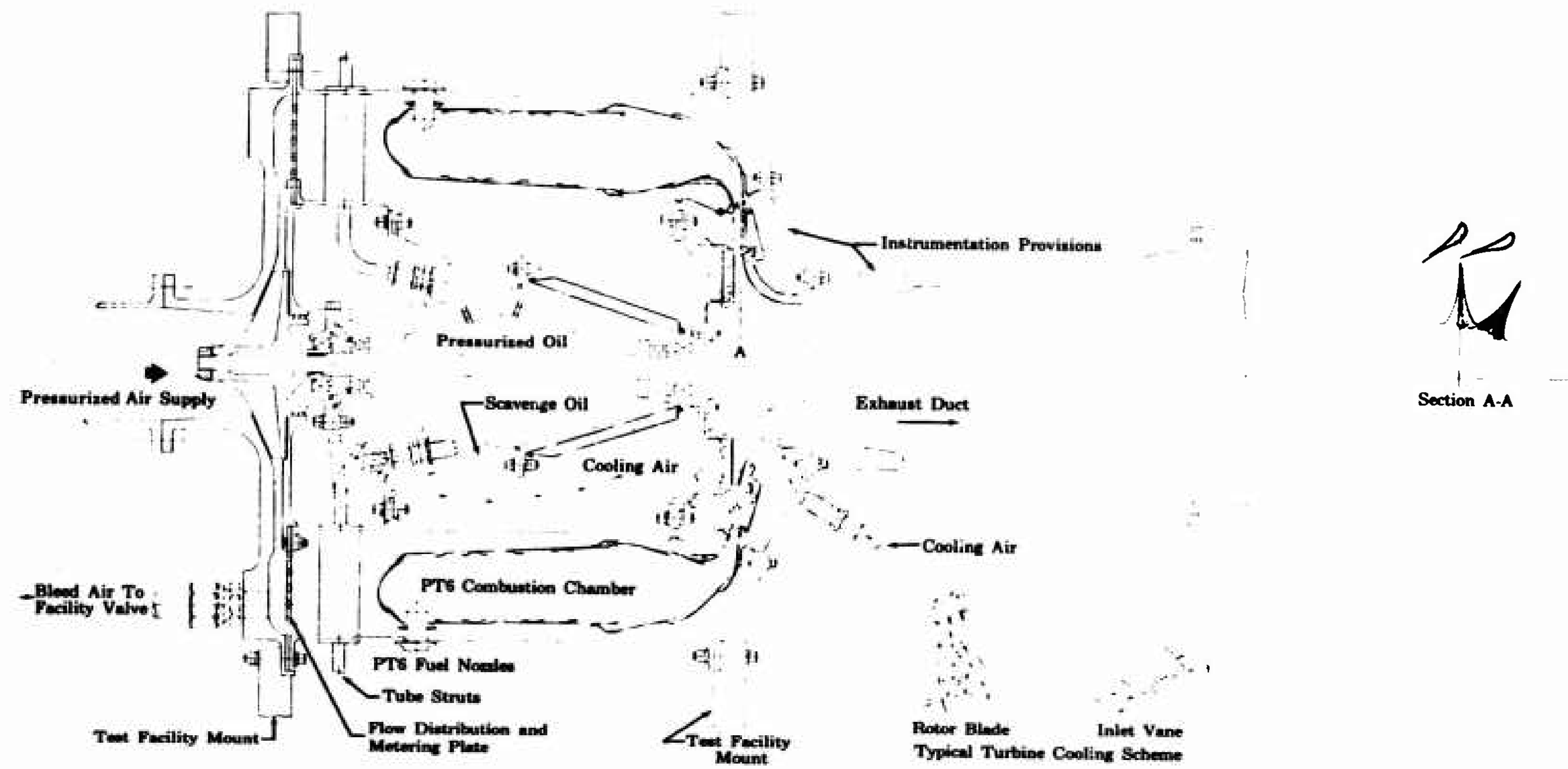

Figure 1. High-Temperature Radial Turbine Test Rig.

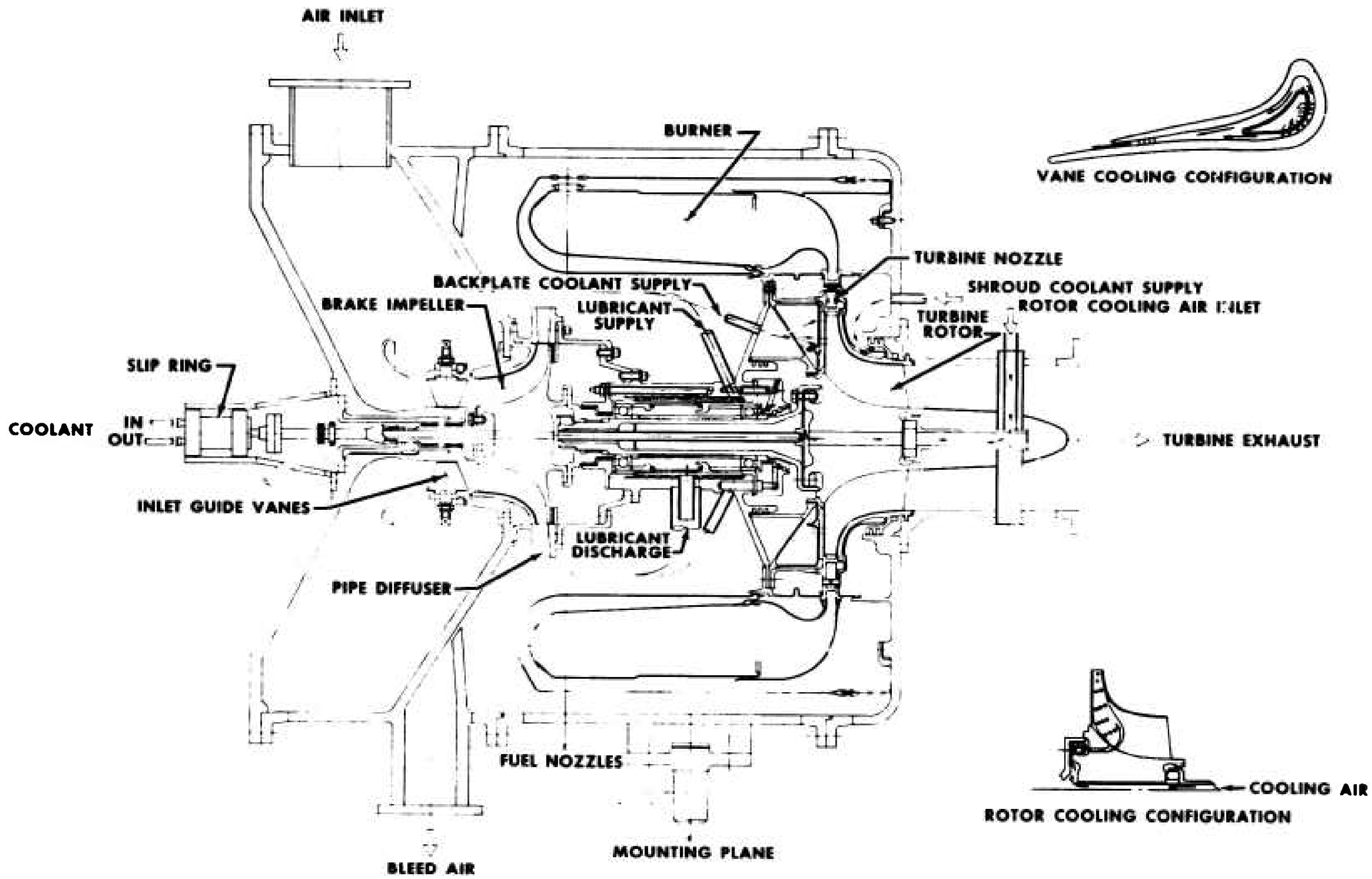

Figure 2. Control Layout No. 2.

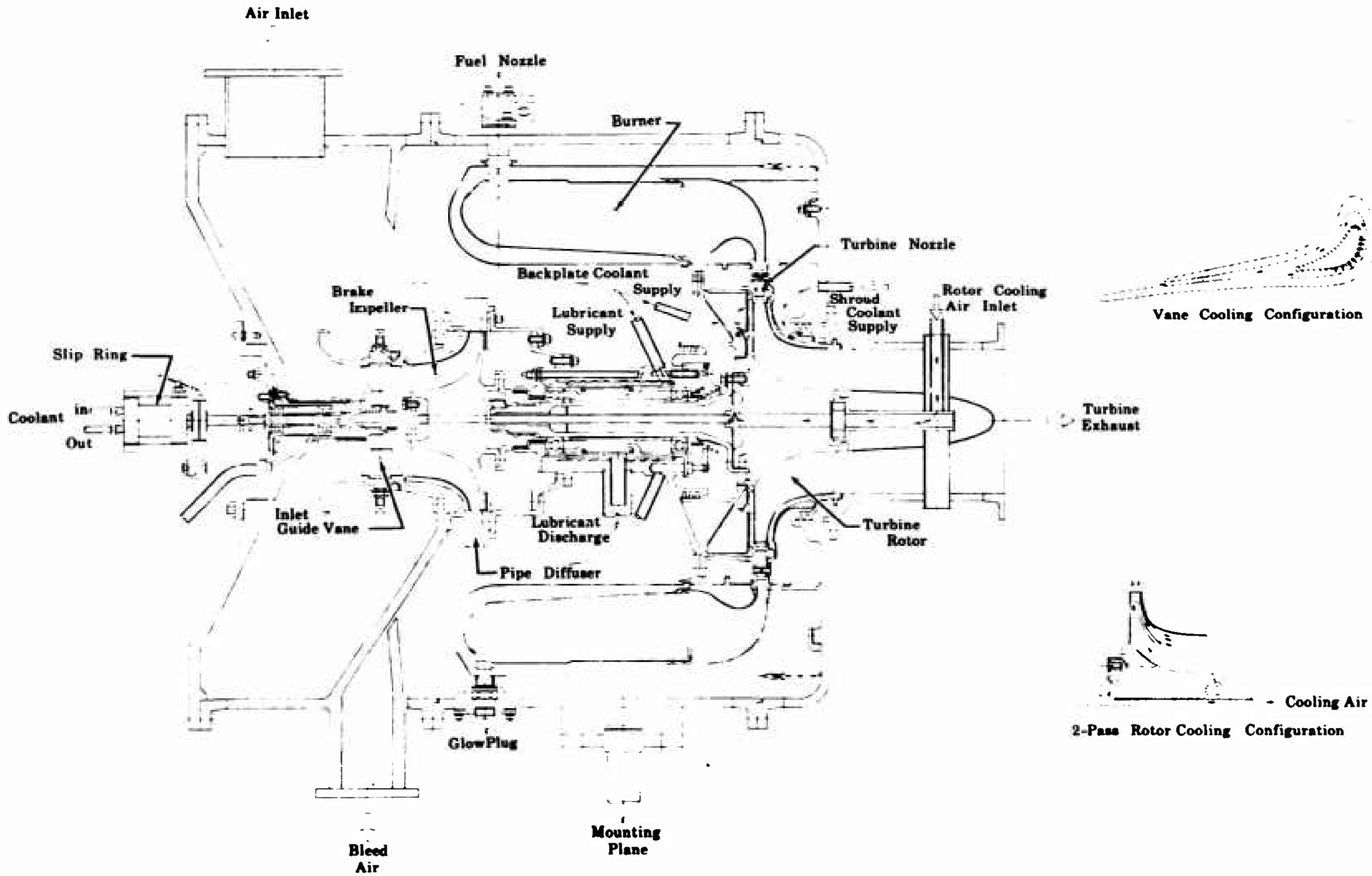

Figure 3. Control Layout No. 3.

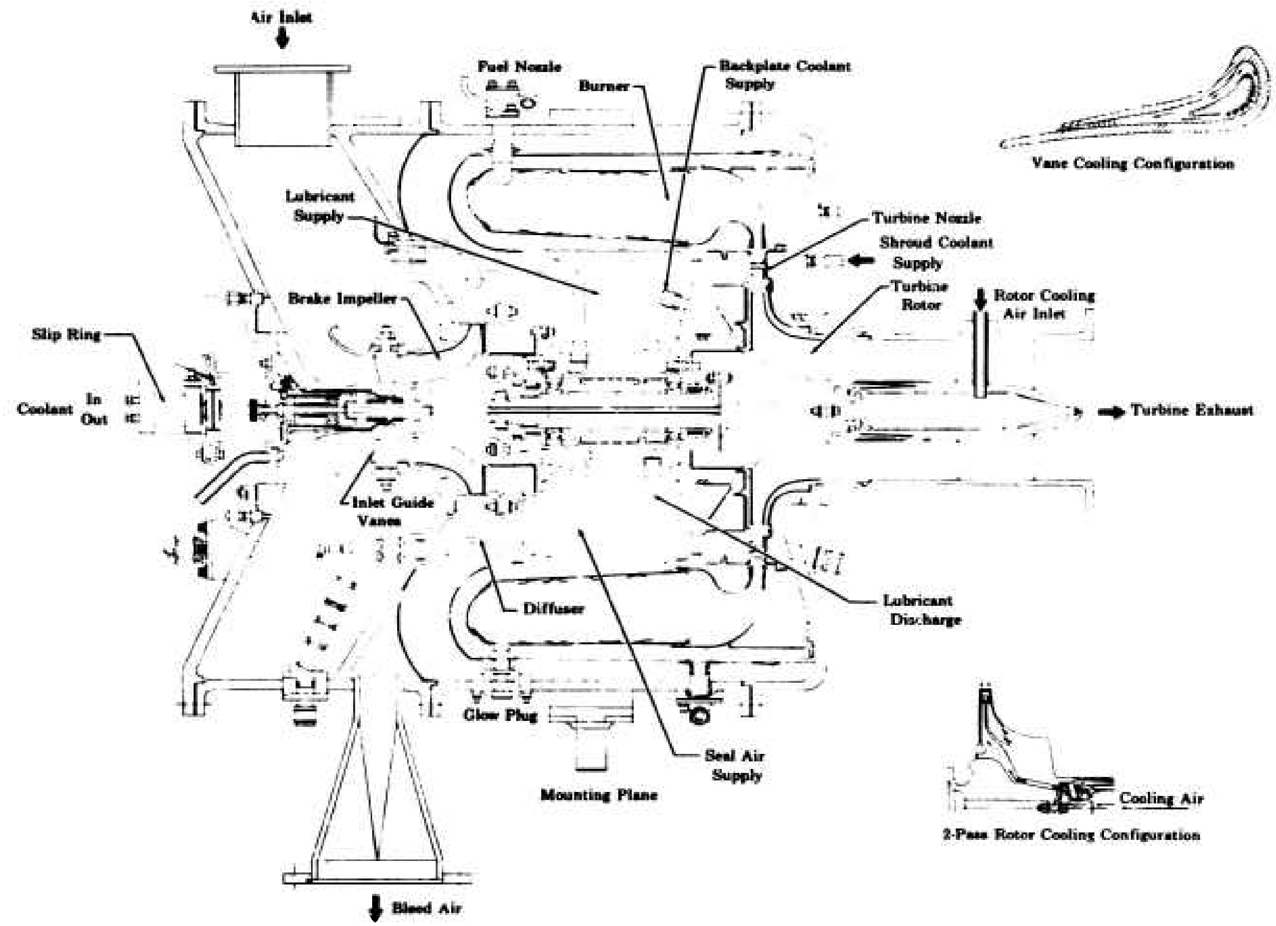

Figure 4. Control Layout No. 4.

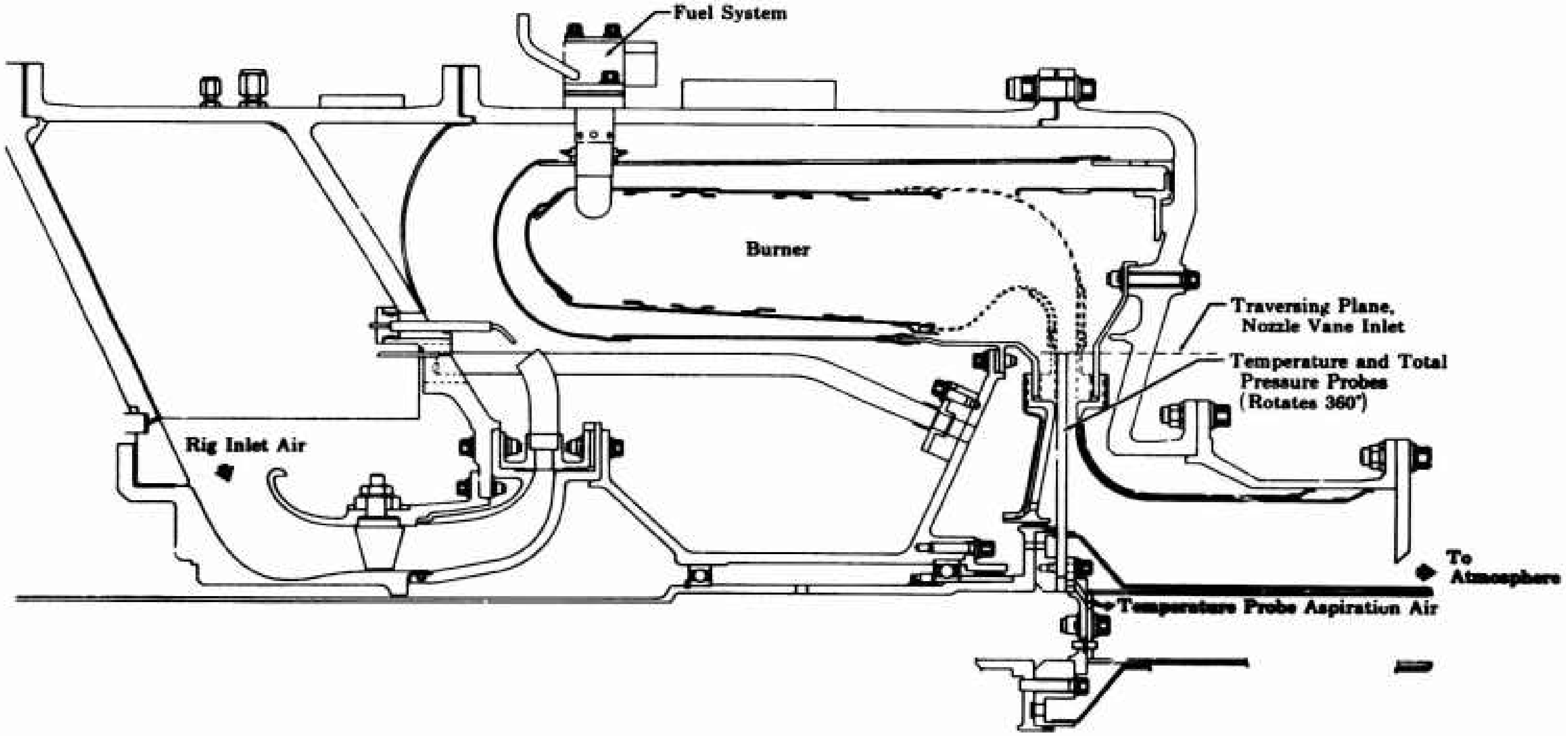

Figure 5. Control Layout No. 4.- Burner Test Configuration.

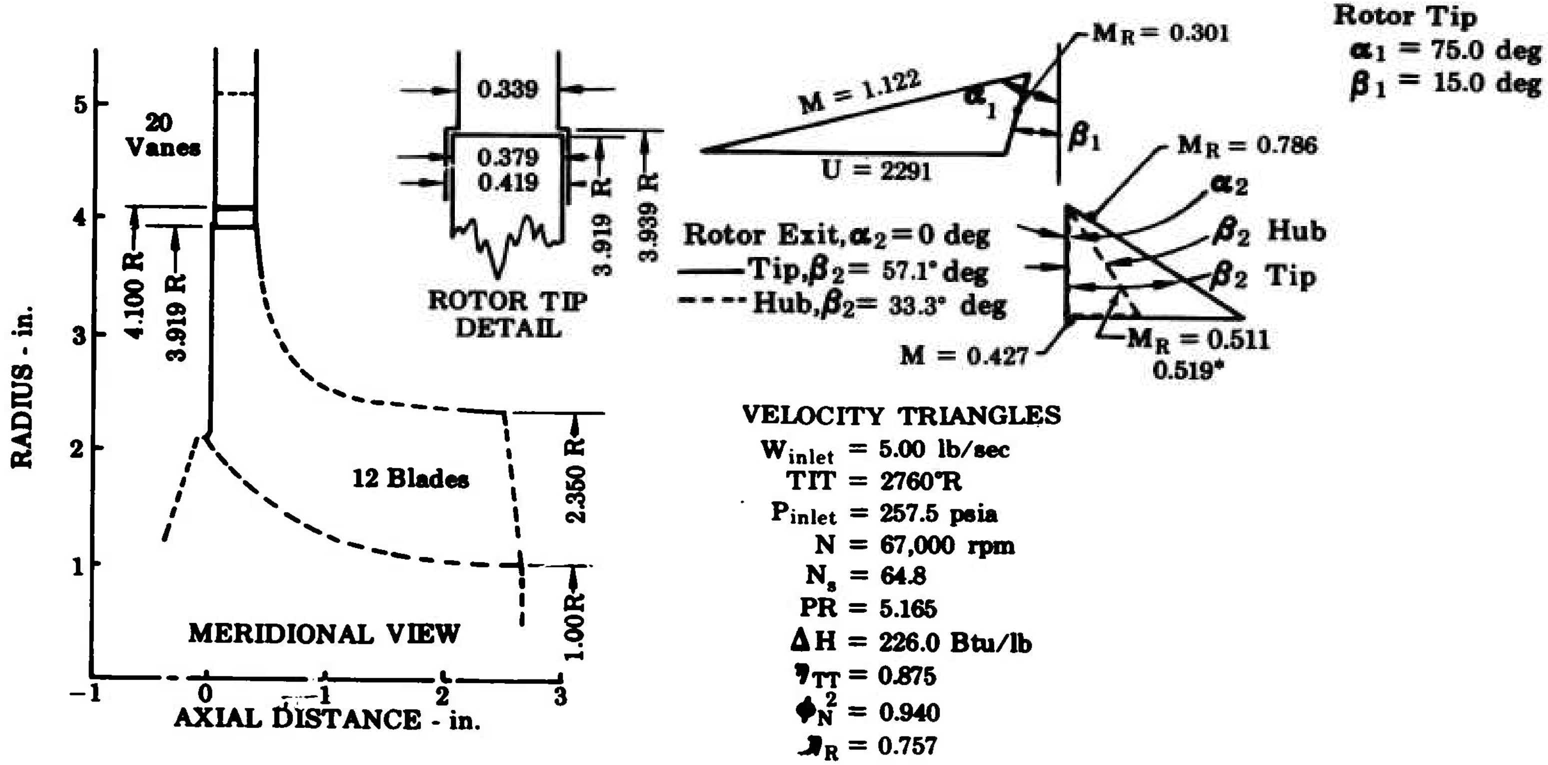

Figure 6. Cooled Turbine Mean-Line Design - 75-Degree Nozzle Angle.

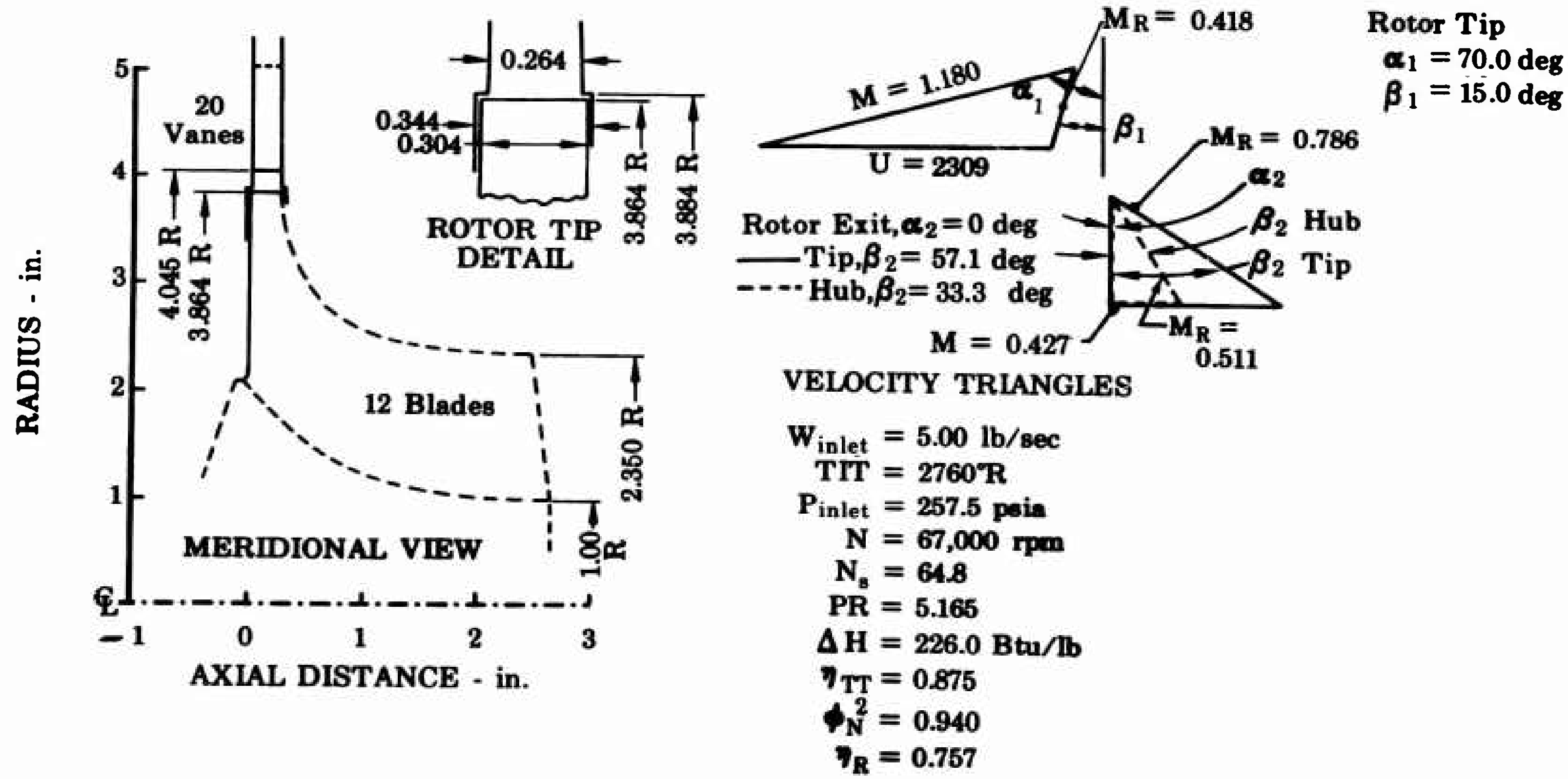

Figure 7. Cooled Turbine Mean-Line Design - 70-Degree Nozzle Angle.

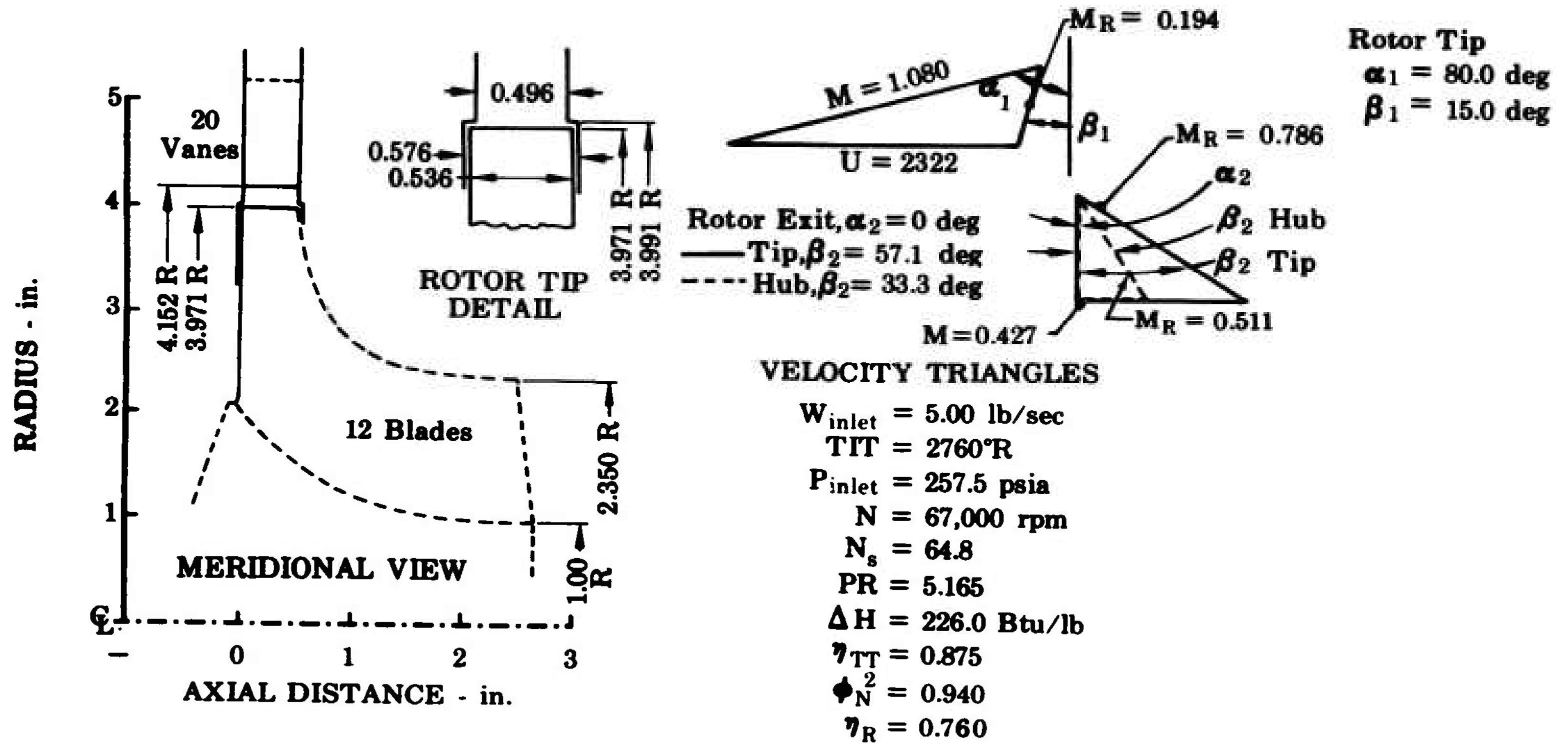

Figure 8. Cooled Turbine Mean-Line Design - 80-Degree Nozzle Angle.

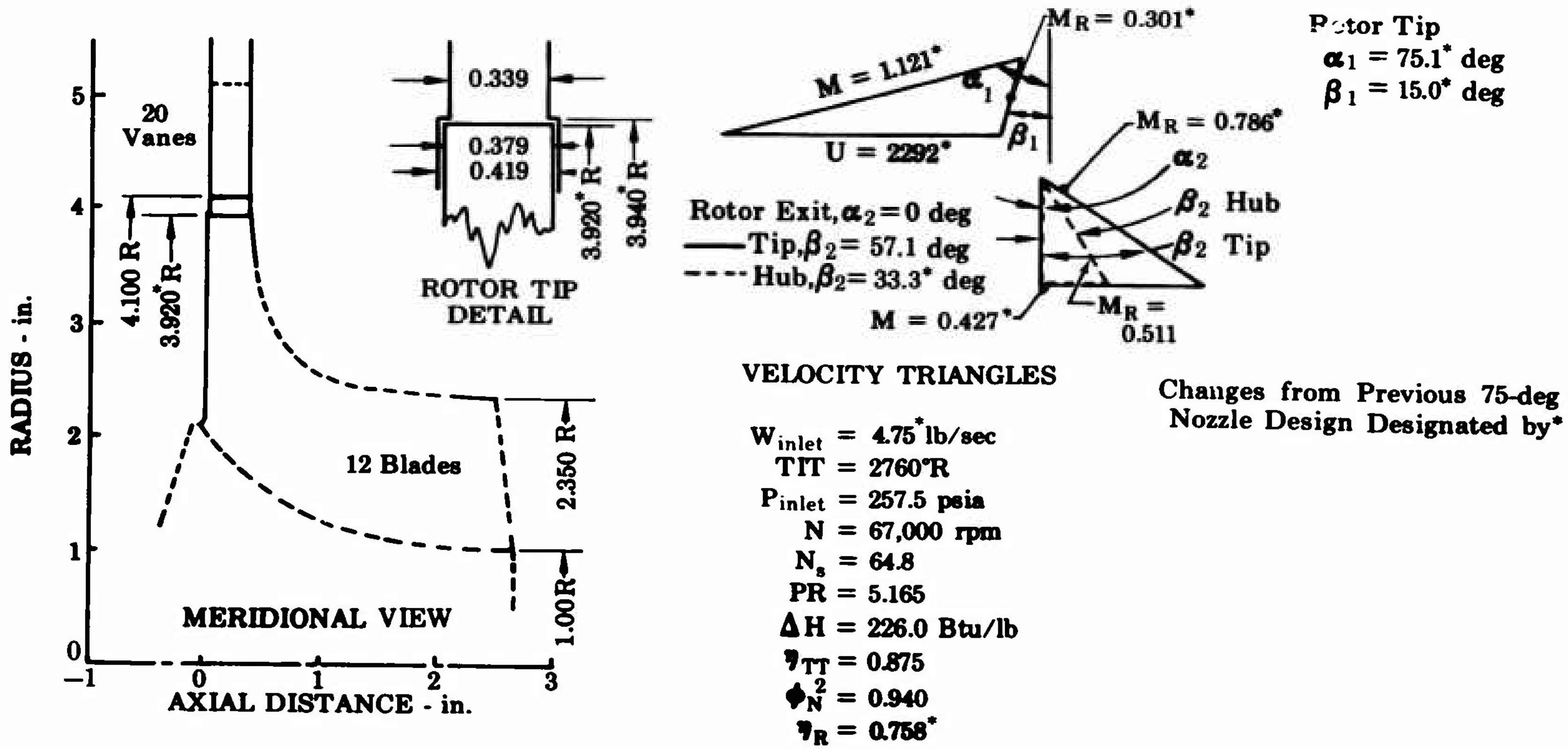

Figure 9. Cooled Turbine Mean-Line Design - Cooling Air Mass Effects Included.

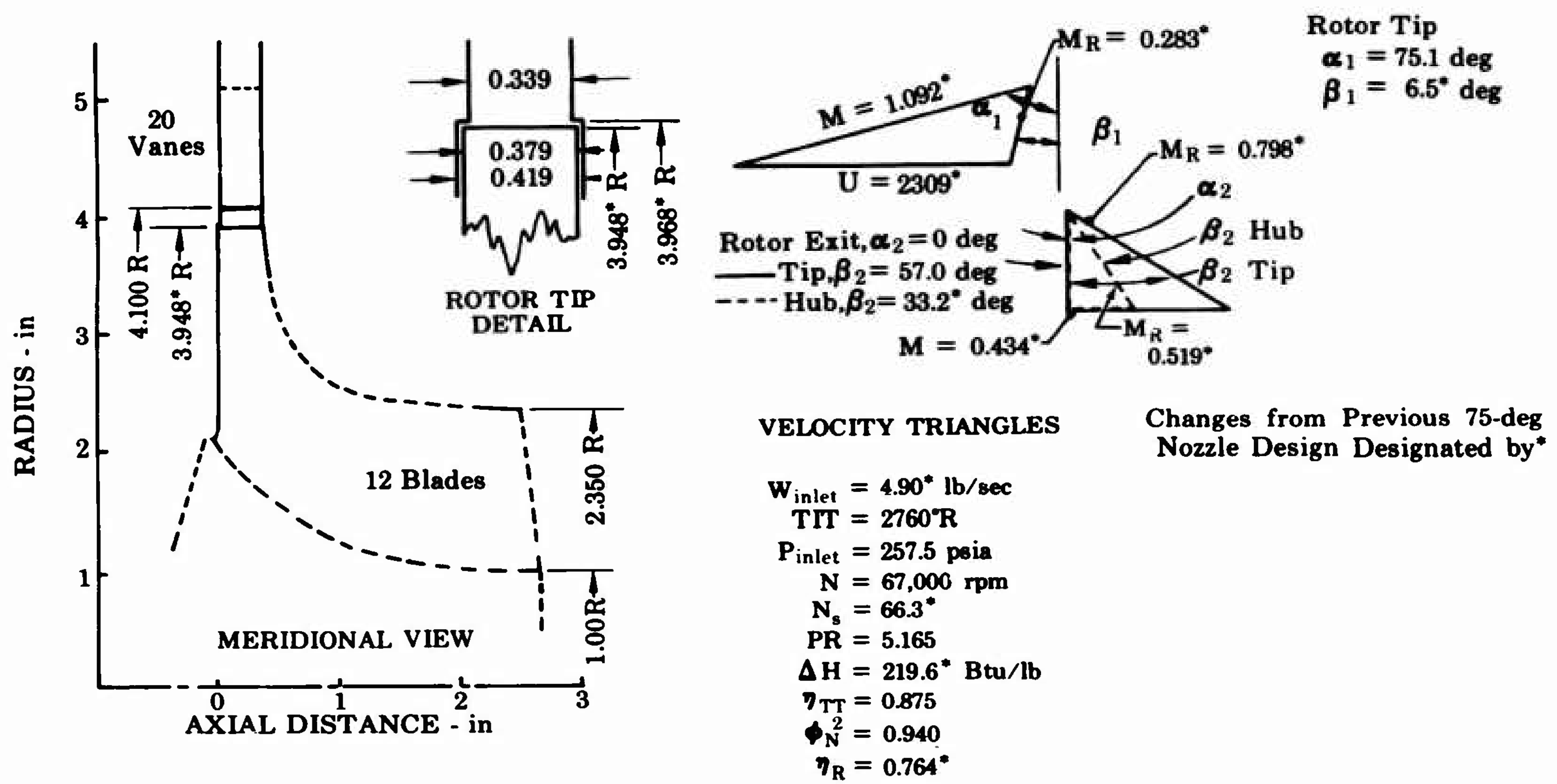

Figure 10. Cooled Turbine Phase I Final Mean-Line Design.

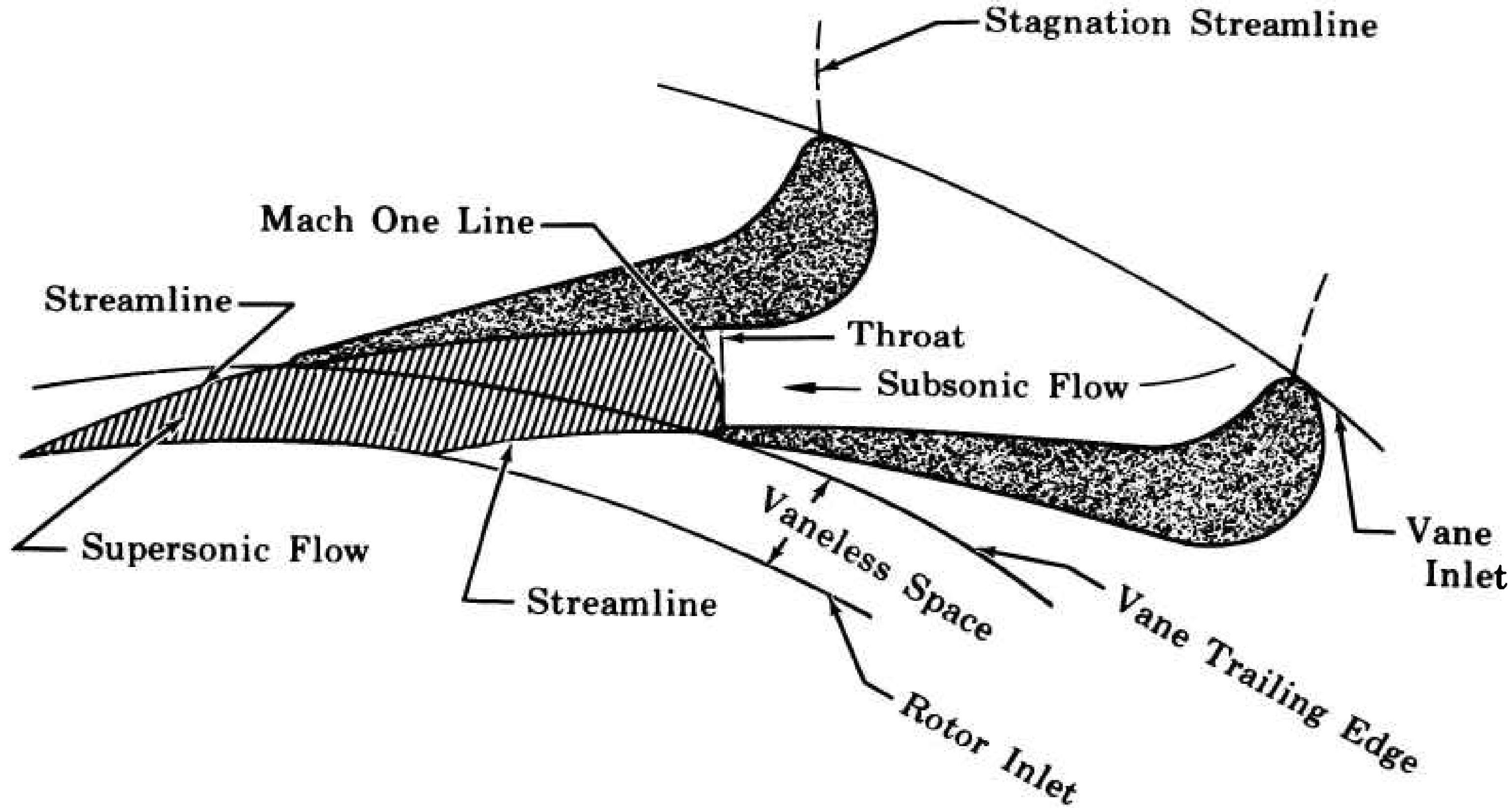

Figure 11. Reflex Vane Schematic.

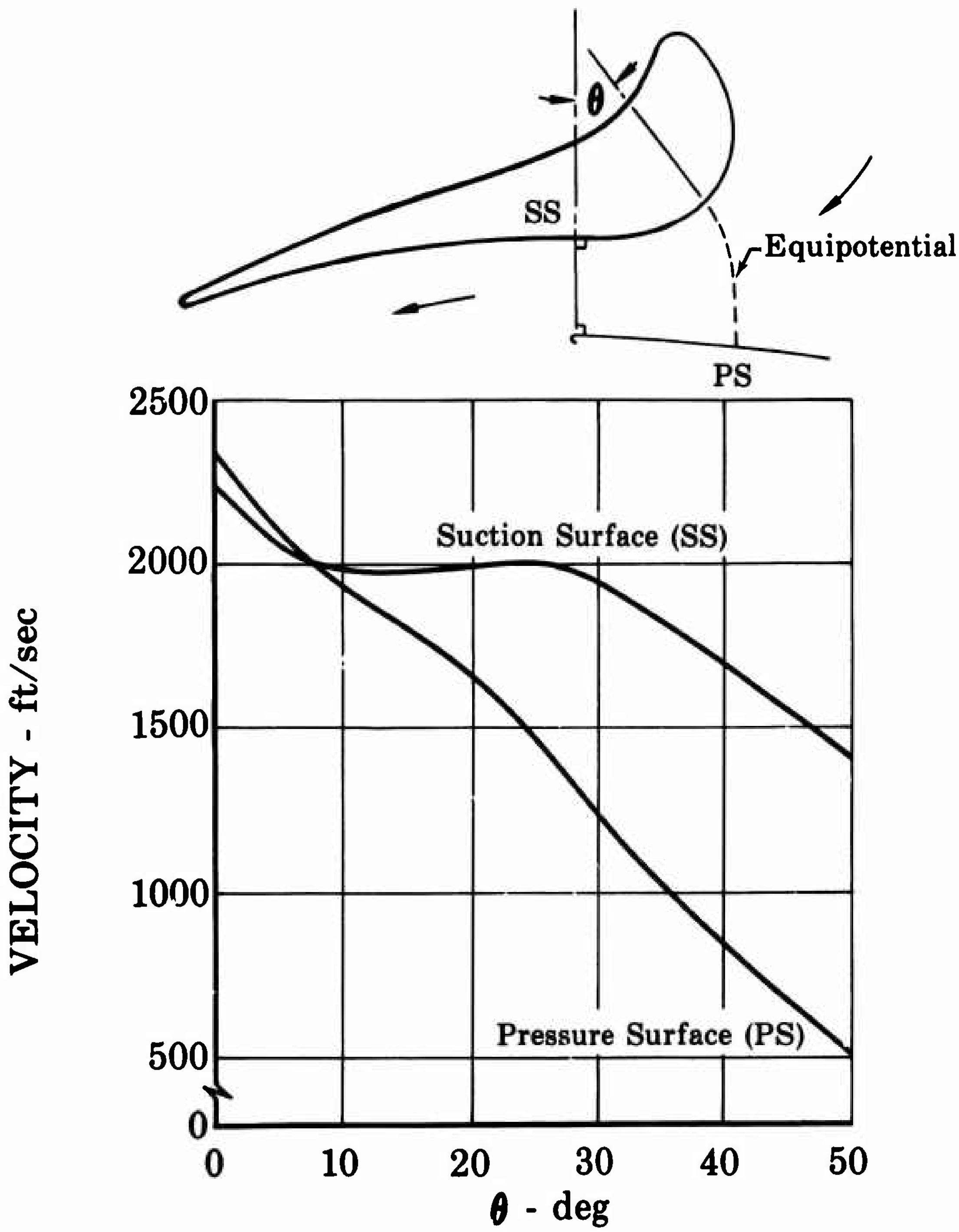

Figure 12. USAAVLABS Turbine Nozzle Velocity Distribution.

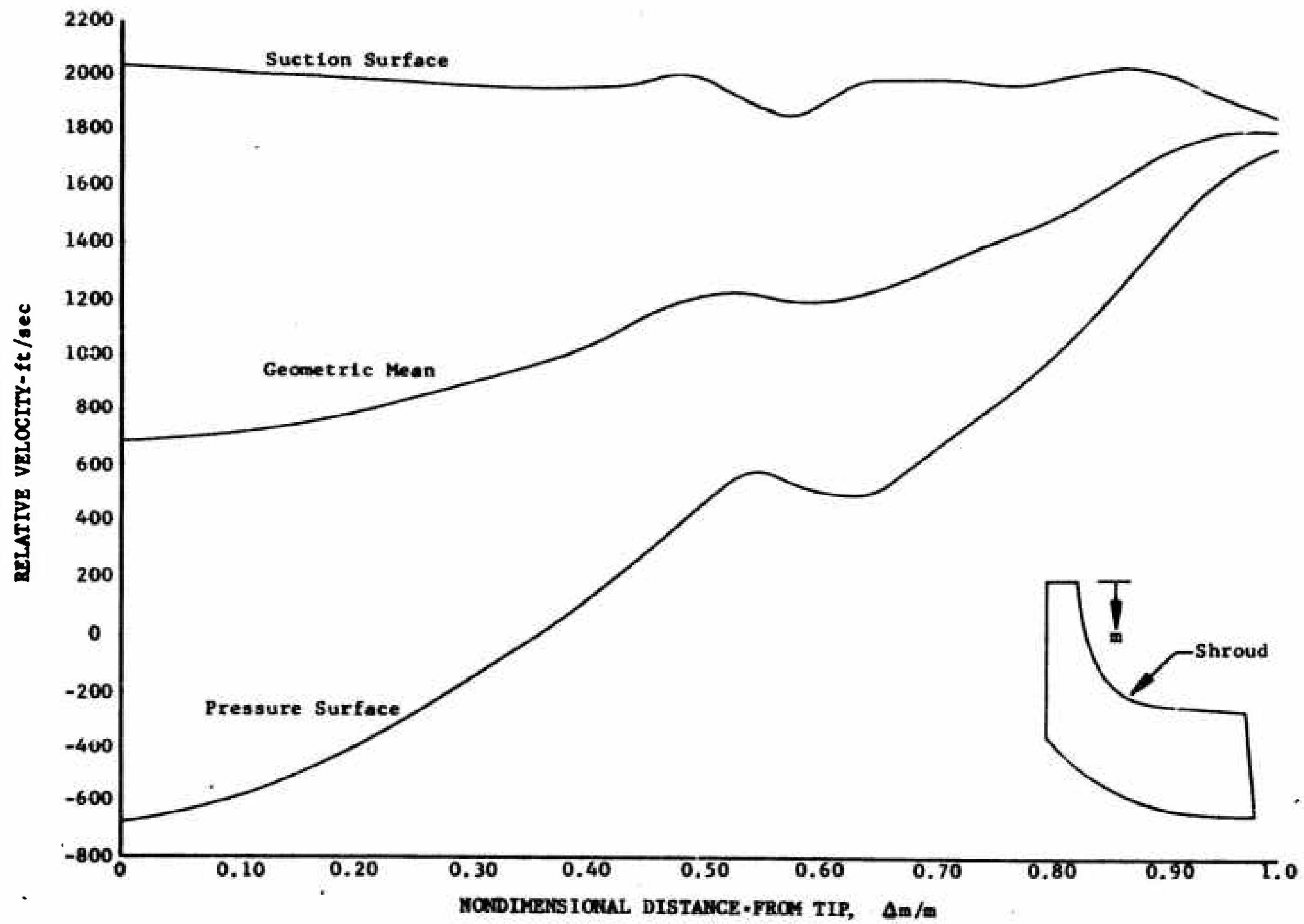

Figure 13. Cooled Turbine Velocity Distribution on Shroud.

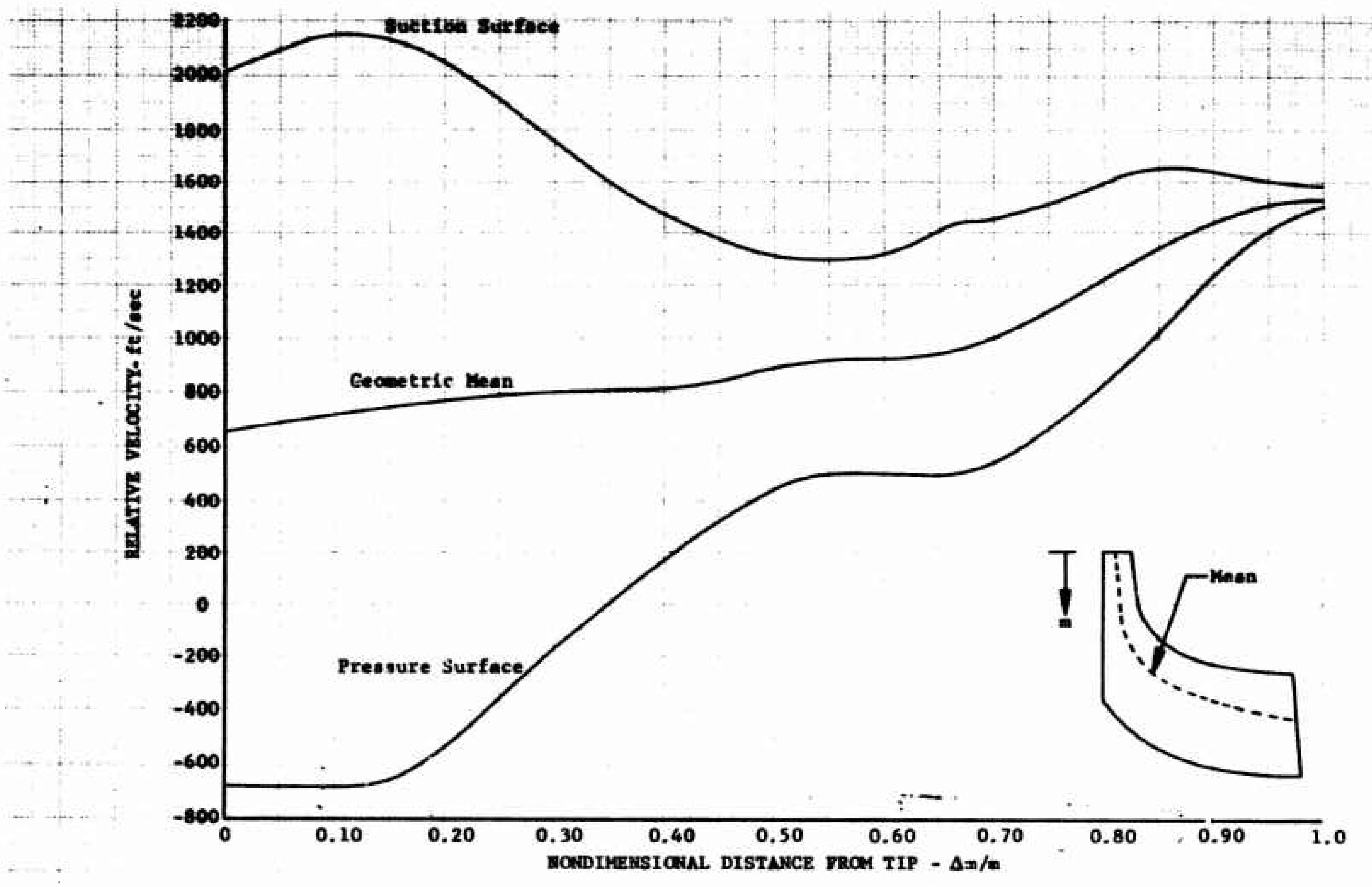

Figure 14. Cooled Turbine Velocity Distribution on Mean Line.

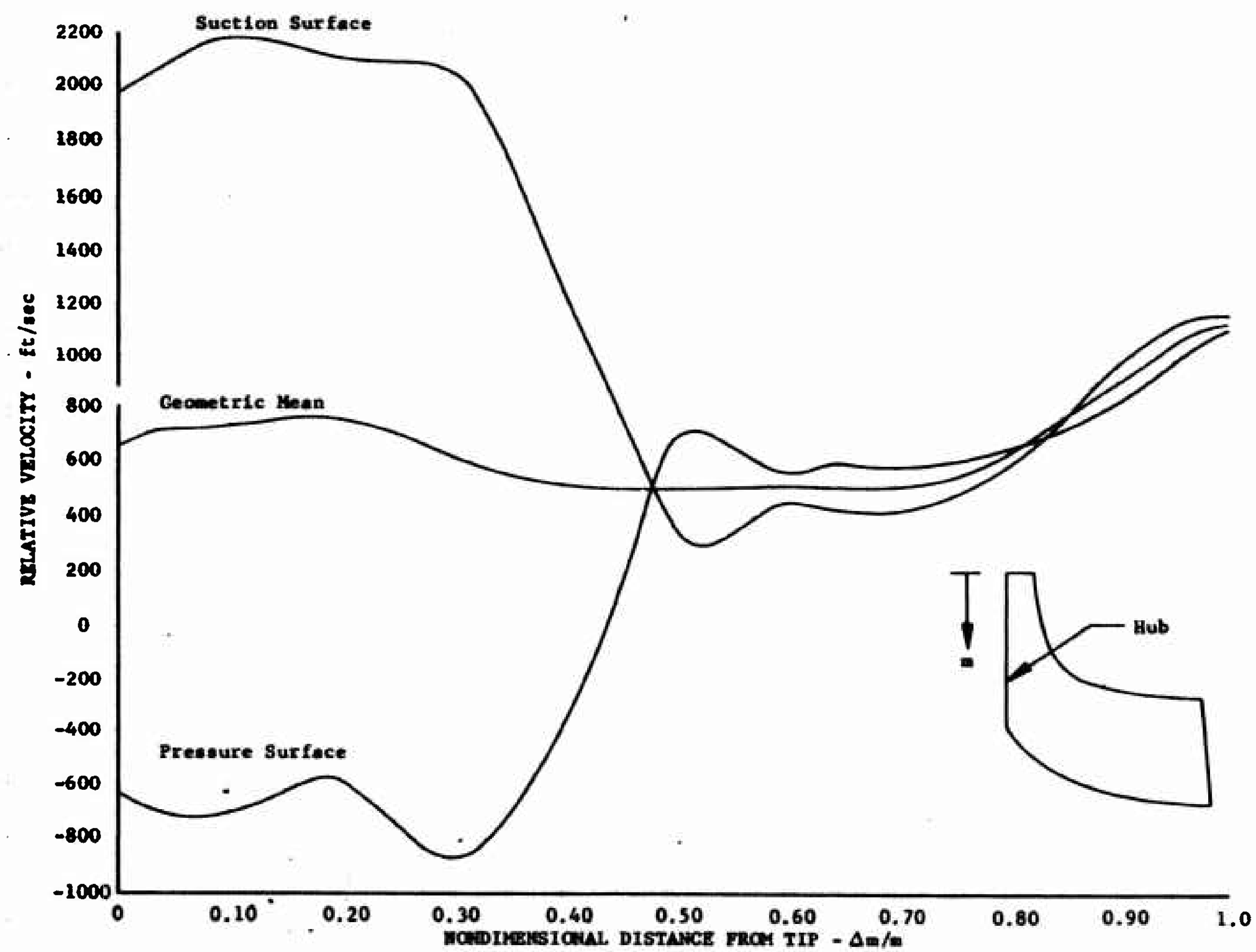

Figure 15. Cooled Turbine Velocity Distribution on Hub.

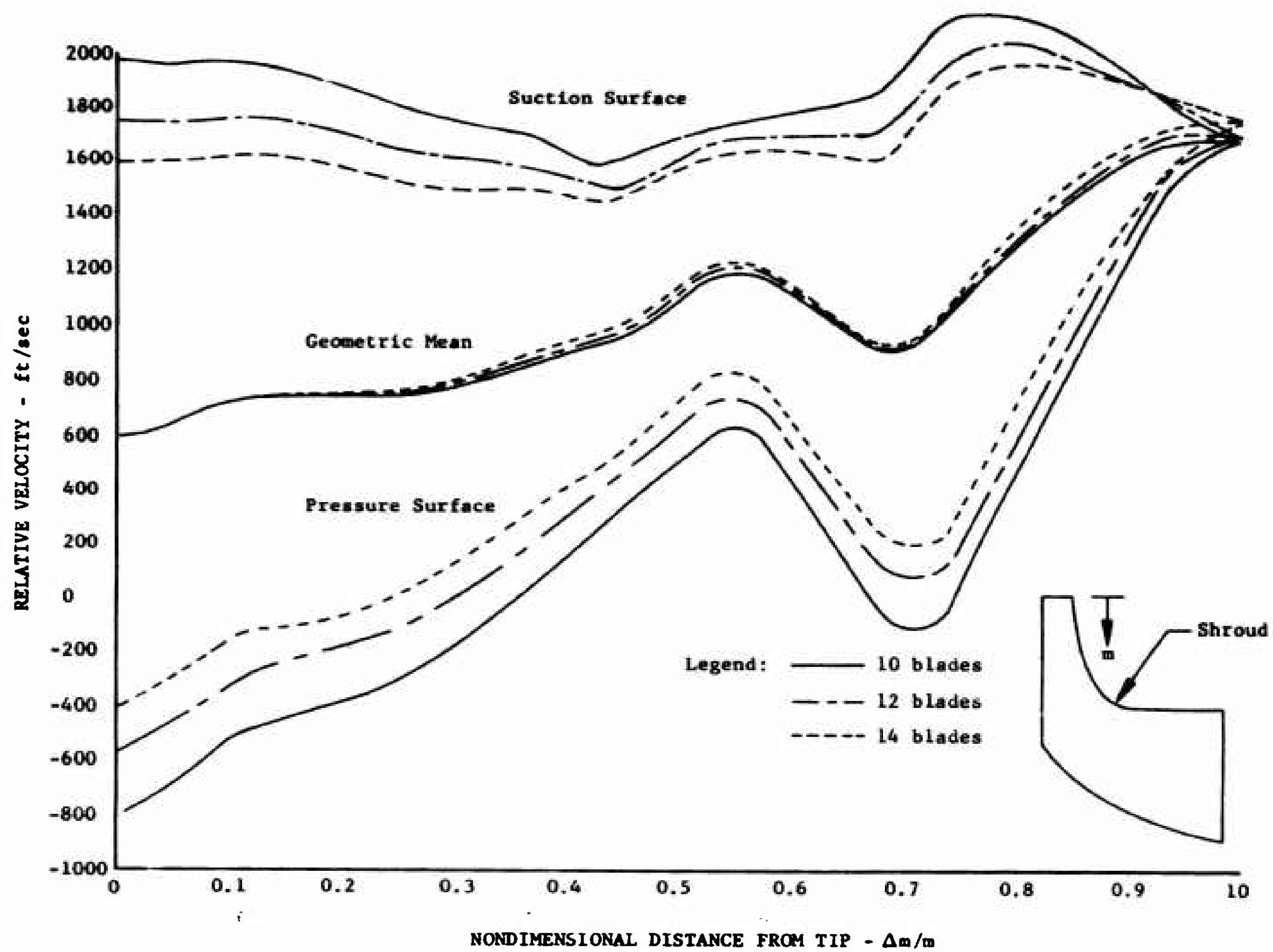

Figure 16. Velocity Distribution On Shroud.

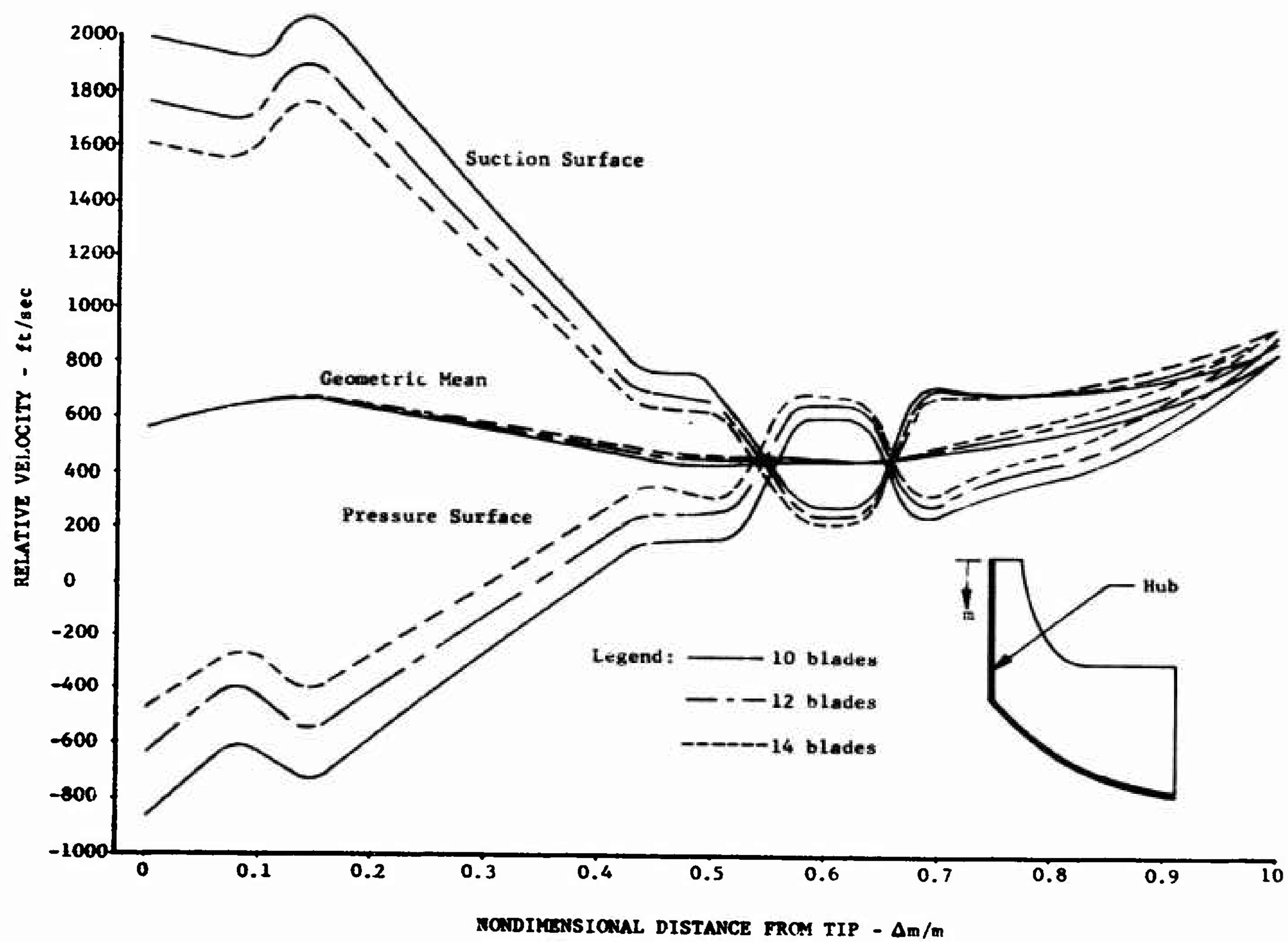

Figure 17. Velocity Distribution on Hub.

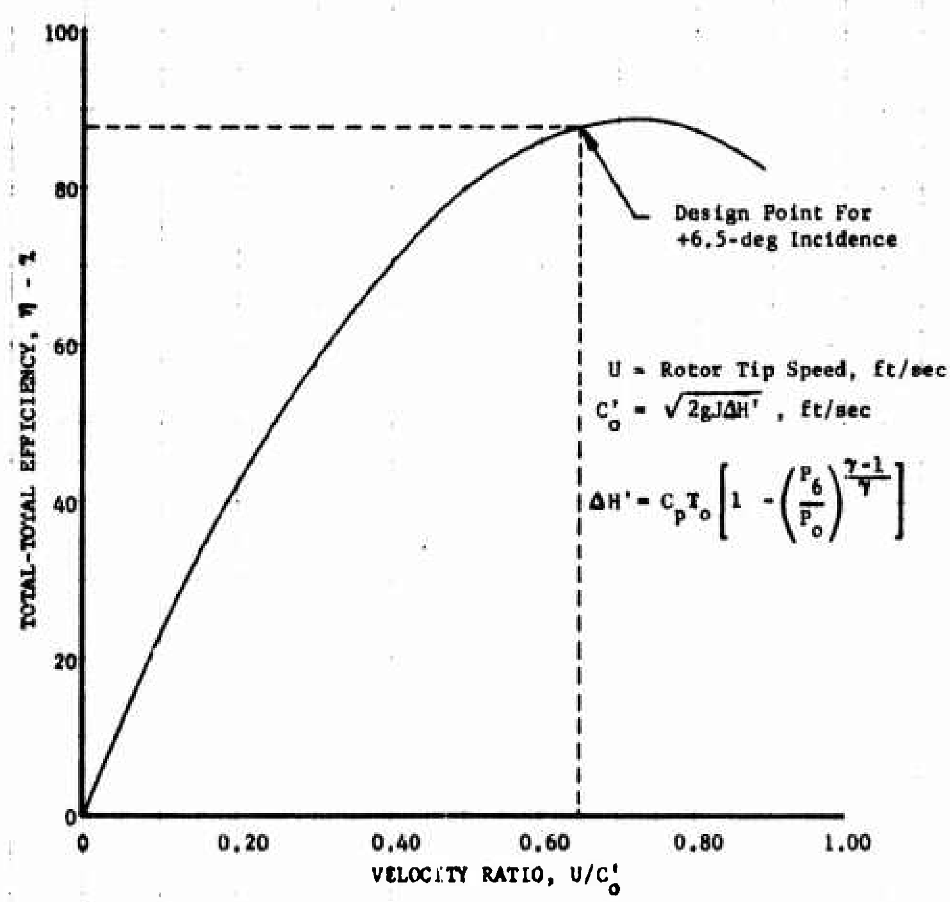

Figure 18. Cooled Turbine Part Load Efficiency (Estimated From Results of Previous Tests).

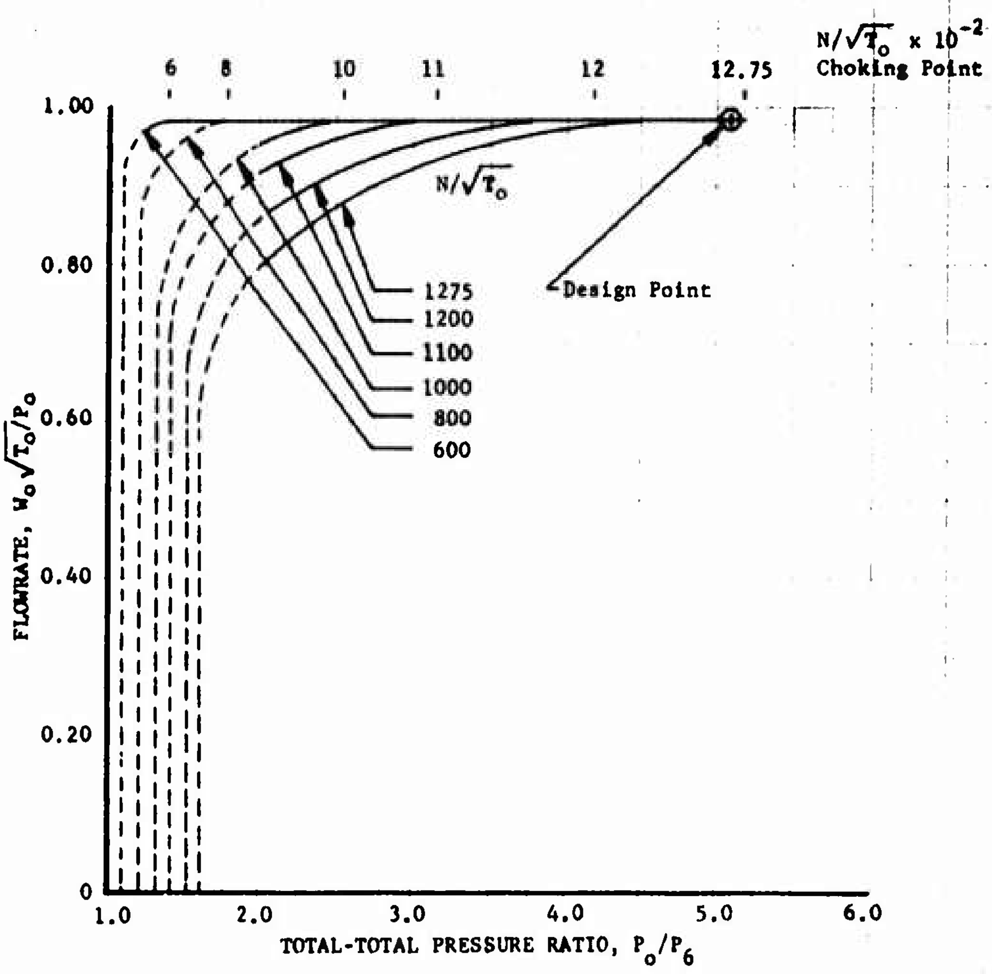

Figure 19. Cooled Turbine Swallowing Capacity (Estimated From Results of Previous Tests).

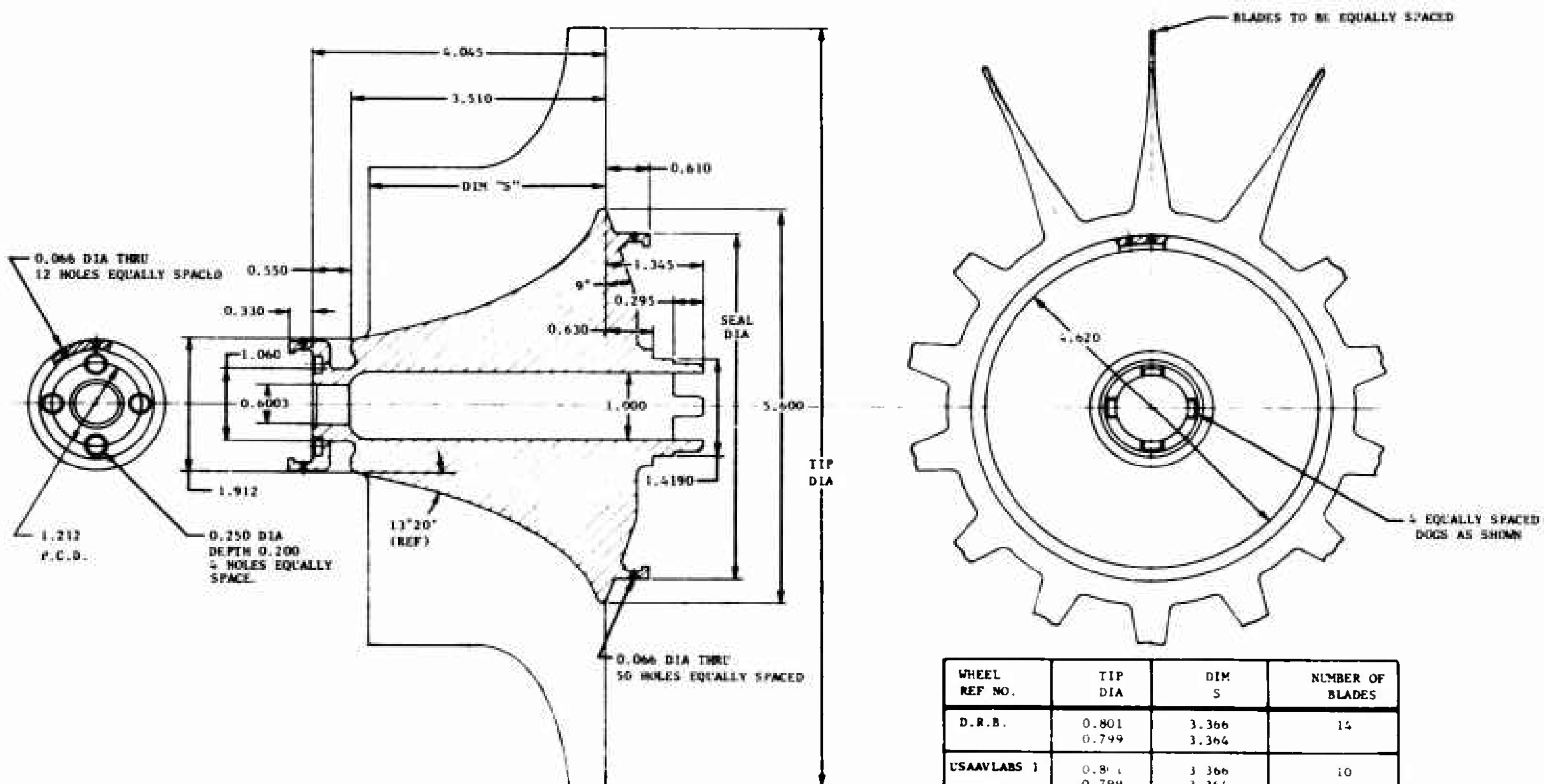

WHEEL REF NO.	TIP DIA	DIM S	NUMBER OF BLADES
D.R.B.	0.801 0.799	3.366 3.364	14
USAAVLABS 1	0.8[illegible] 0.799	3.366 3.364	10
USAAVLABS 2	0.801 0.799	3.366 3.364	12

Figure 20. Cold-Flow Radial Turbine Rotor.

BLANK PAGE

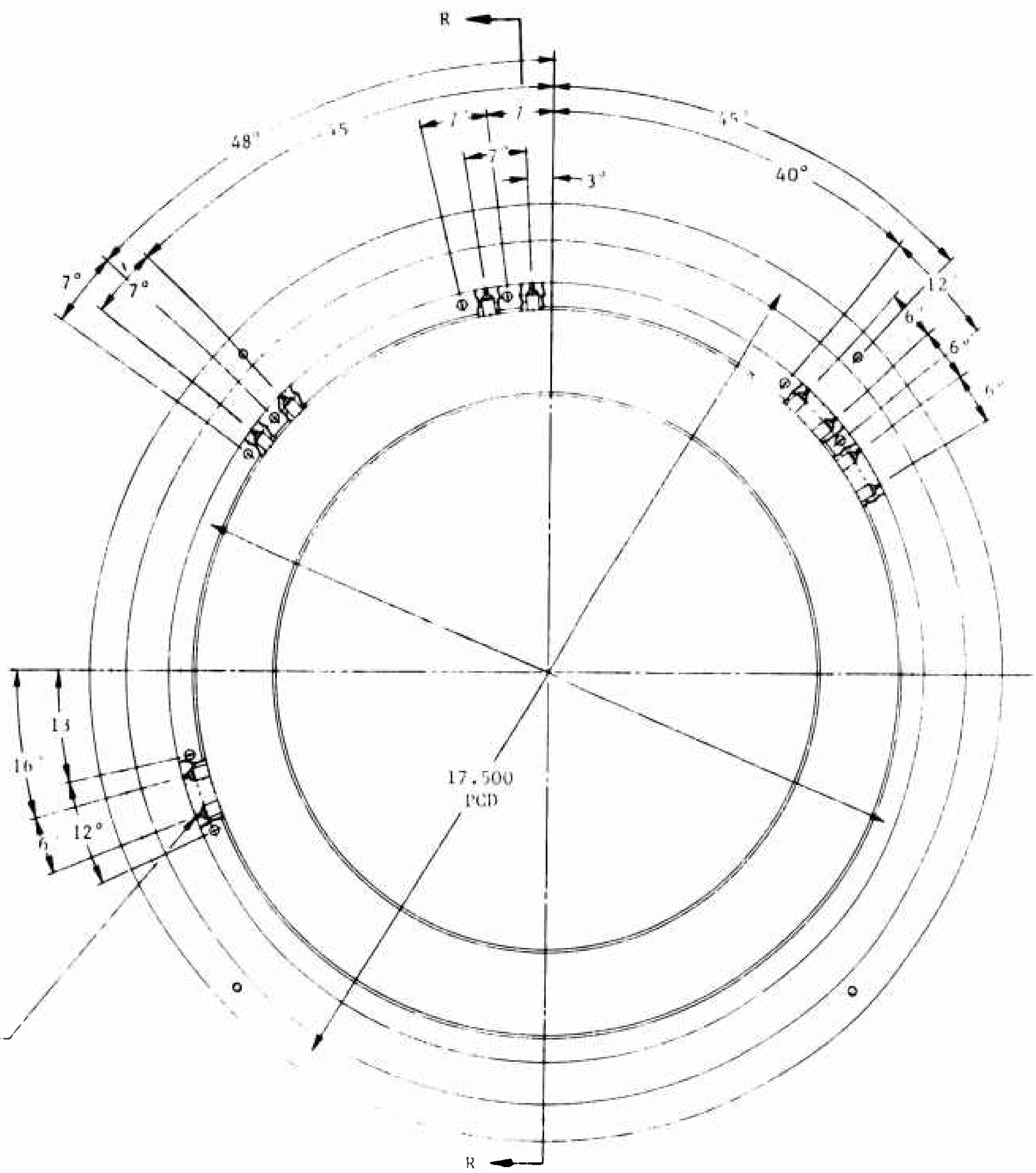

Figure 21. Fifteen-Vaned Cold-Flow Nozzle.

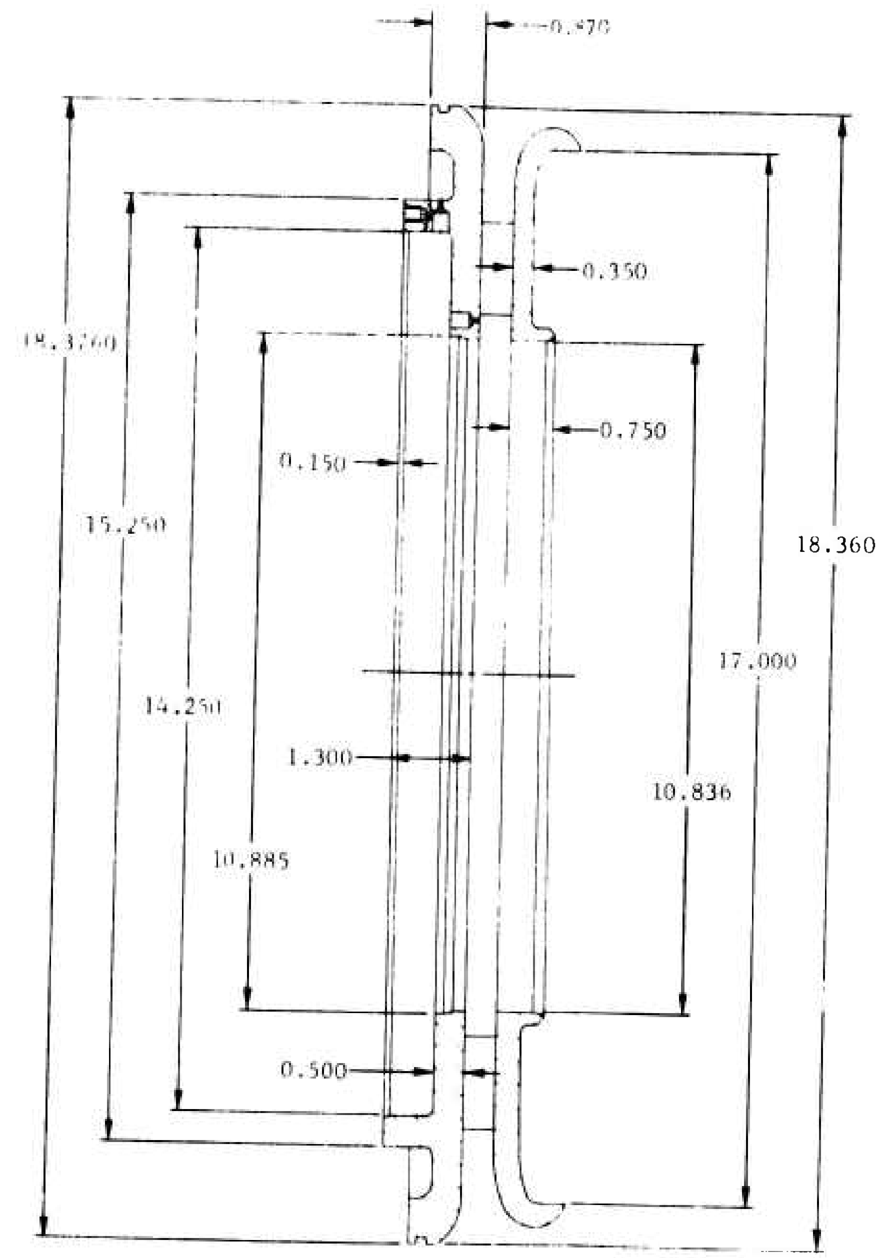
0.870
0.350
18.3760
0.750
0.150
15.250
18.360
17.000
14.250
1.300
10.836
10.885
0.500

SECTION R-R

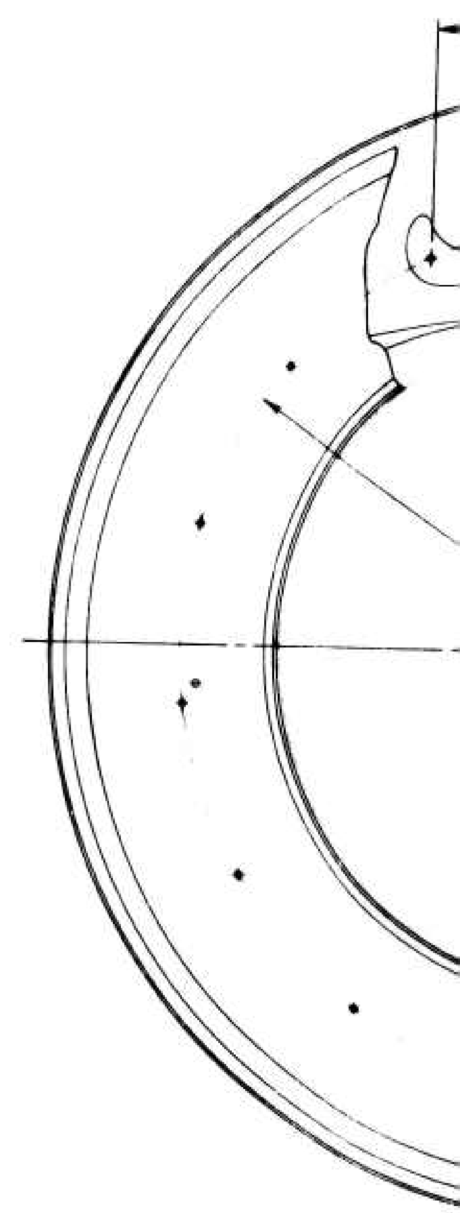

B

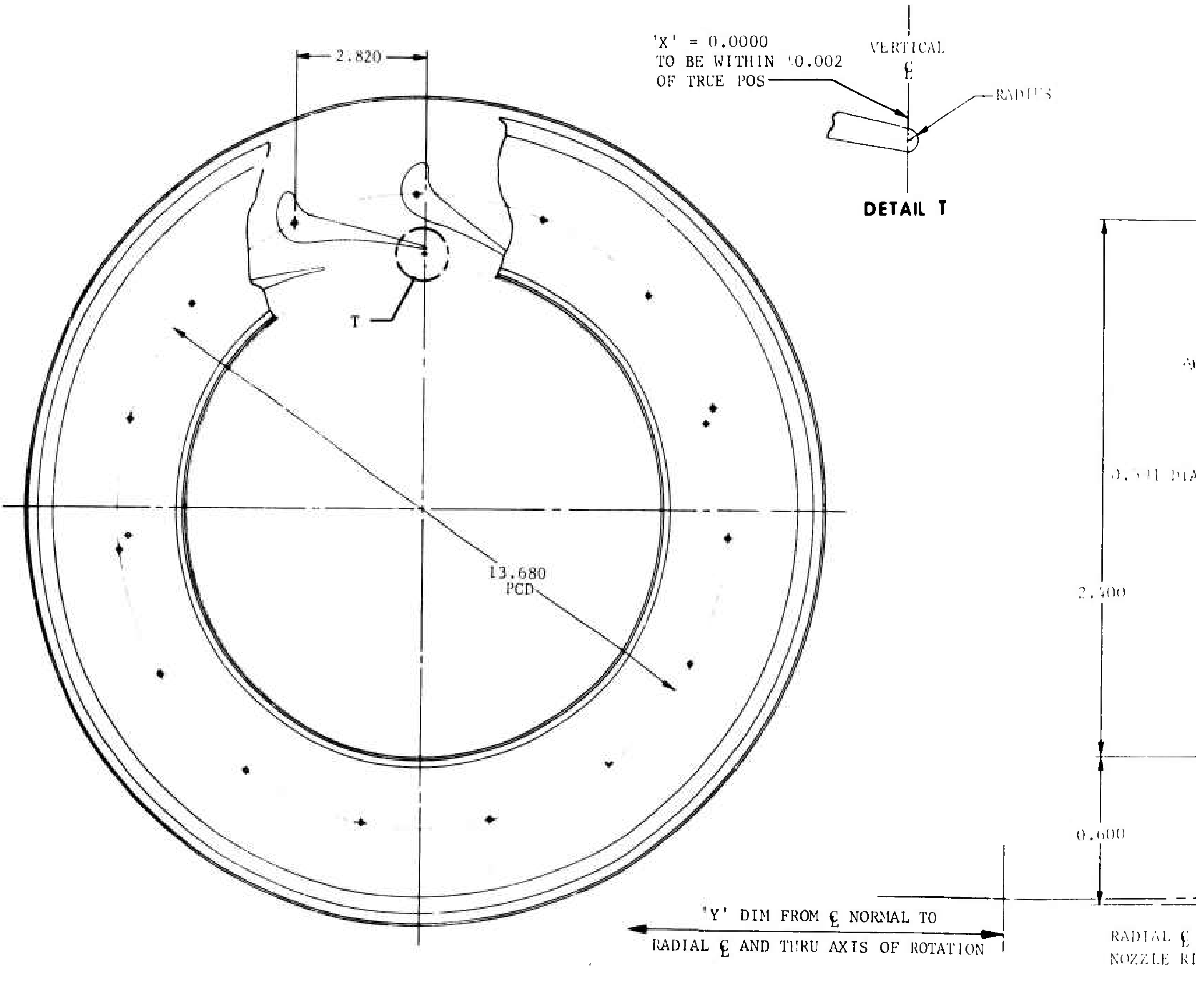
2.820
'X' = 0.0000
TO BE WITHIN ±0.002
OF TRUE POS
VERTICAL
℄
DETAIL T
T
13.680
PCD
0.600
'Y' DIM FROM ℄ NORMAL TO
RADIAL ℄ AND THRU AXIS OF ROTATION

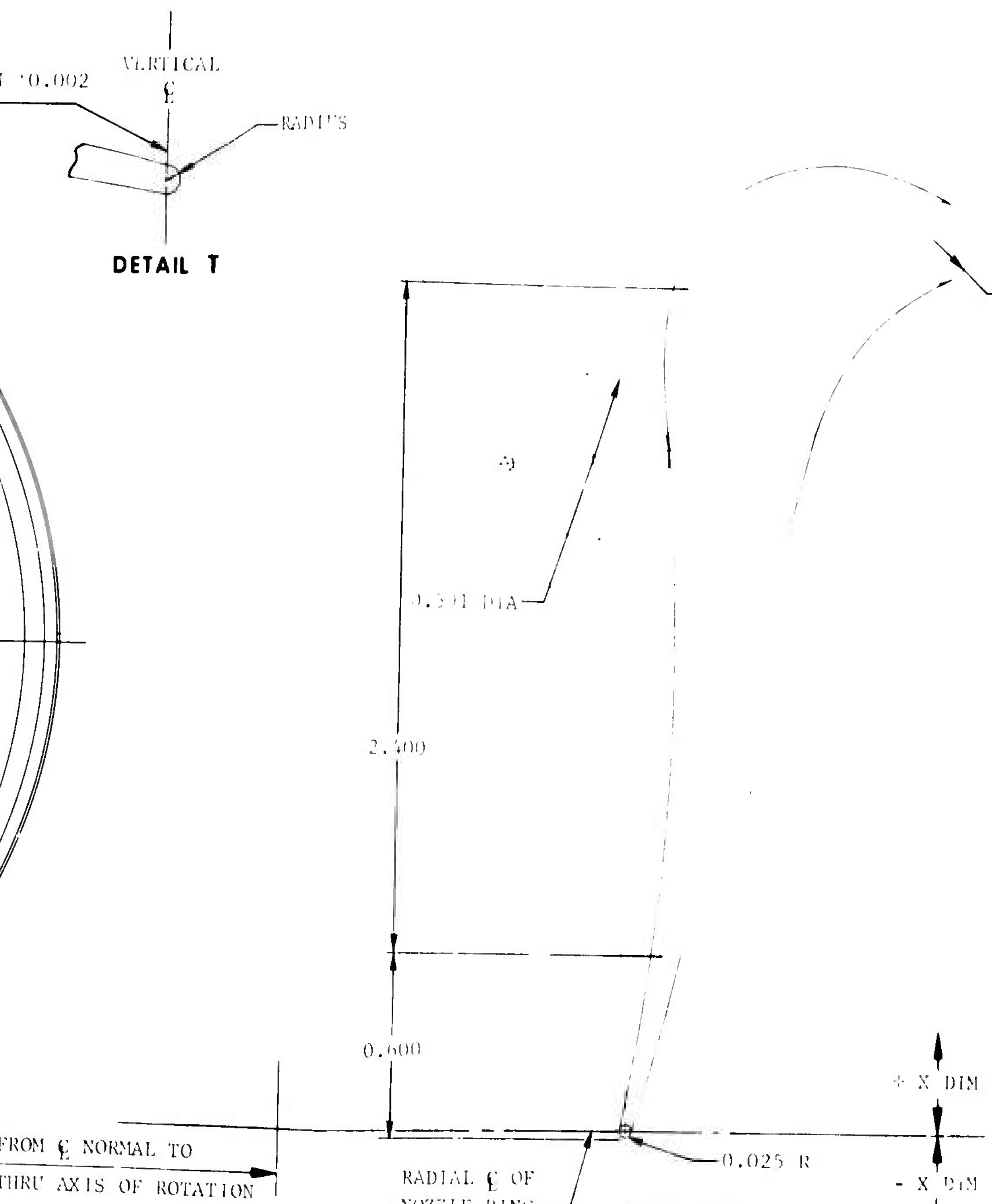

VANE SECTION
TYPICAL FOR 15 VANES

VANE COORDINATES		
X DIM	Y DIM	Y DIM
PROFILE DRAWING REF. ESK 3742		
TYPICAL FOR 15 EQUALLY SPACED VANES INDEXED FROM TOP VERTICAL CENTER AS SHOWN IN VANE SECTION AND DETAIL "T"		

D

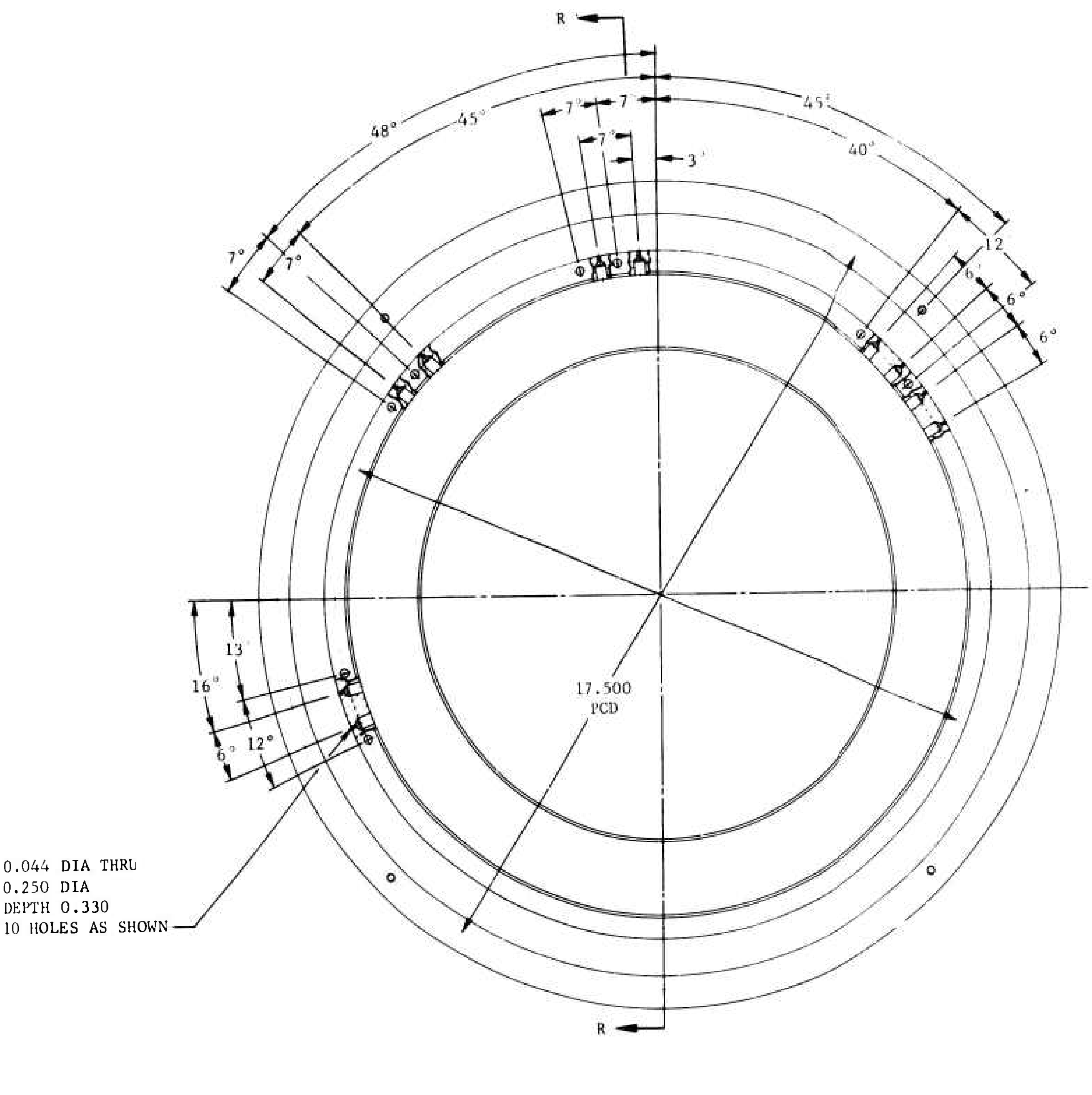

Figure 22. Twenty-Vaned Cold-Flow Nozzle.

A

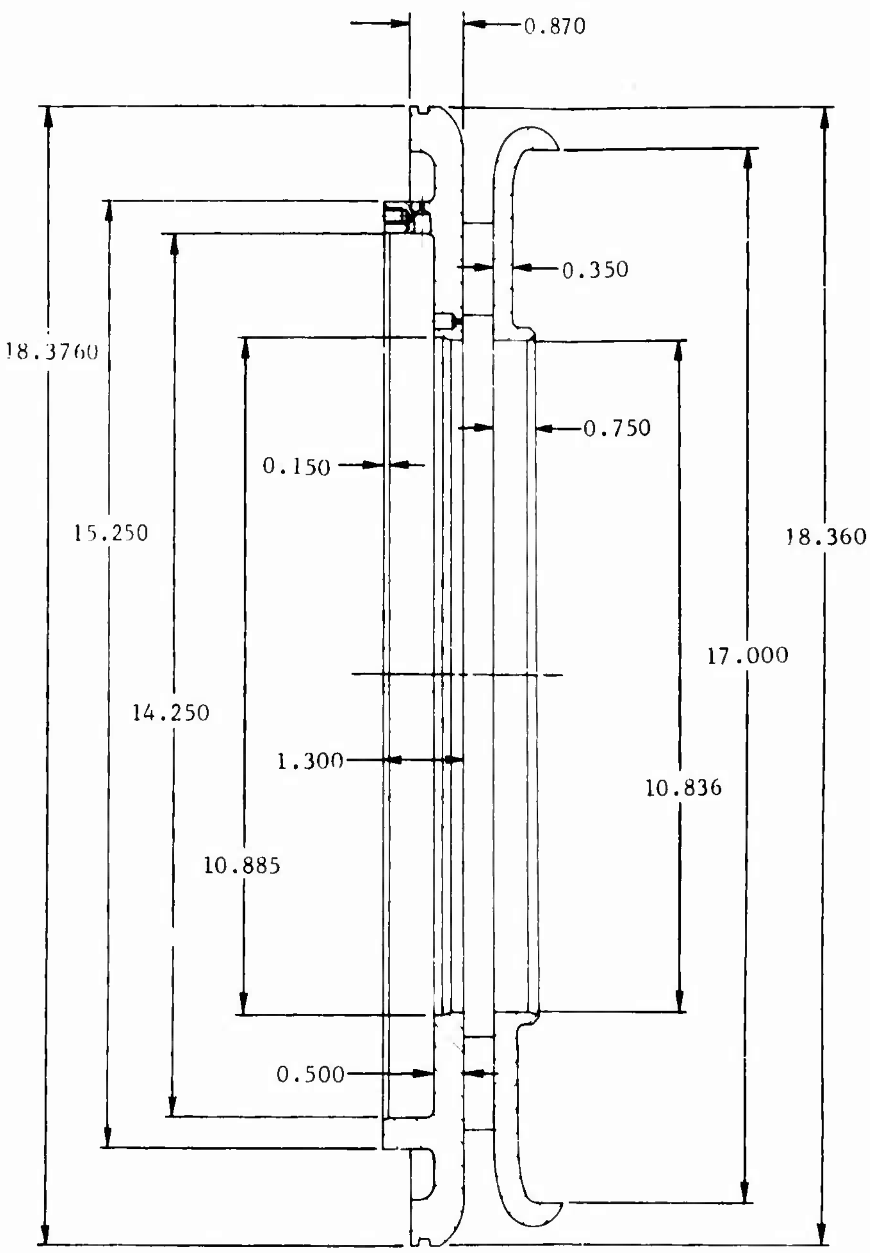
0.870
0.350
18.3760
0.750
0.150
15.250
18.360
17.000
14.250
1.300
10.836
10.885
0.500

SECTION R-R

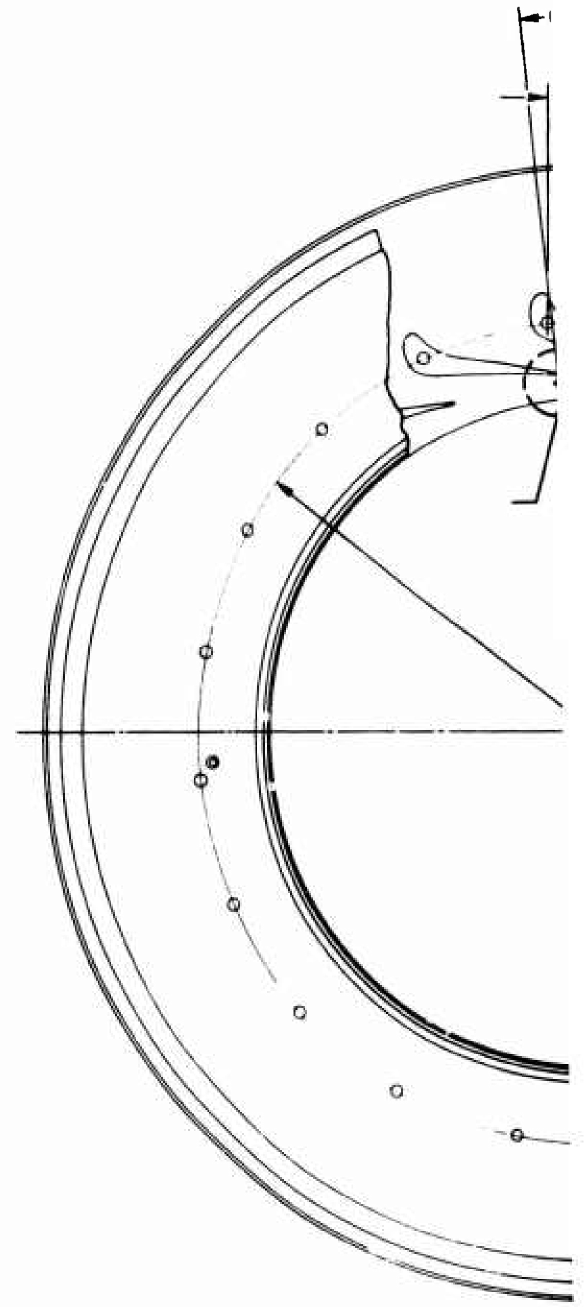

B

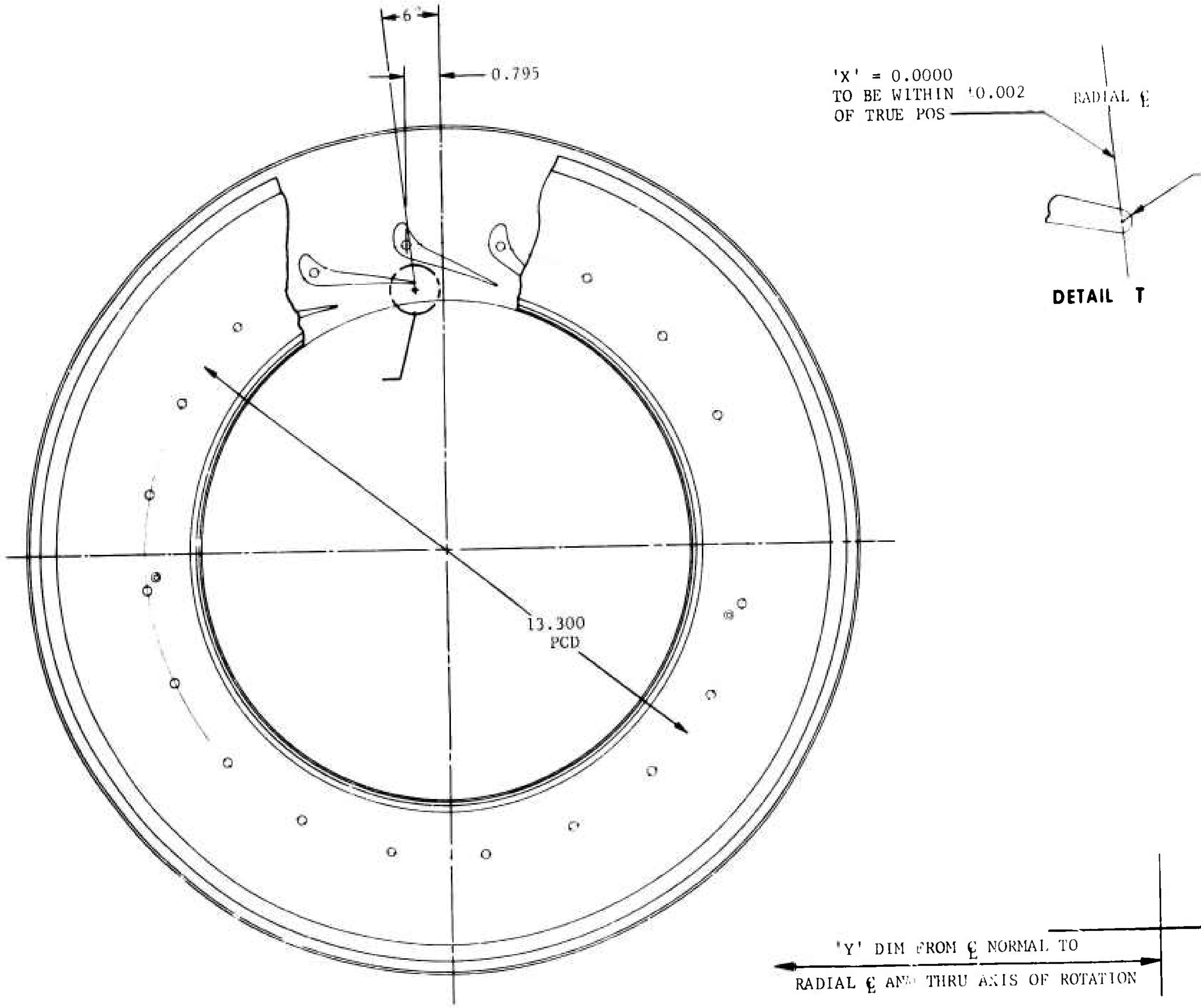
6°
0.795
'X' = 0.0000
TO BE WITHIN ±0.002
OF TRUE POS
RADIAL ℄
DETAIL T
13.300
PCD
'Y' DIM FROM ℄ NORMAL TO
RADIAL ℄ AND THRU AXIS OF ROTATION

C

VANE COORDINATES		
X DIM	Y DIM	Y DIM

FOR COLD VANE COORDINATES REFER TO ESK 3743 AND FOR THE PROFILE EMD REFER TO EFD 31778 THIS PROFILE IS TYPICAL FOR 20 EQUALLY SPACED VANES INDEXED FROM RADIAL CENTER LINE AS SHOWN IN DETAIL 'T'

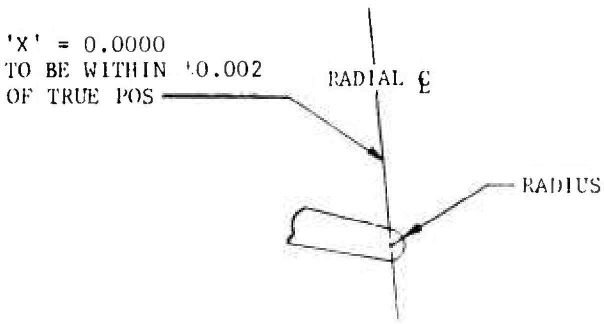

DETAIL T

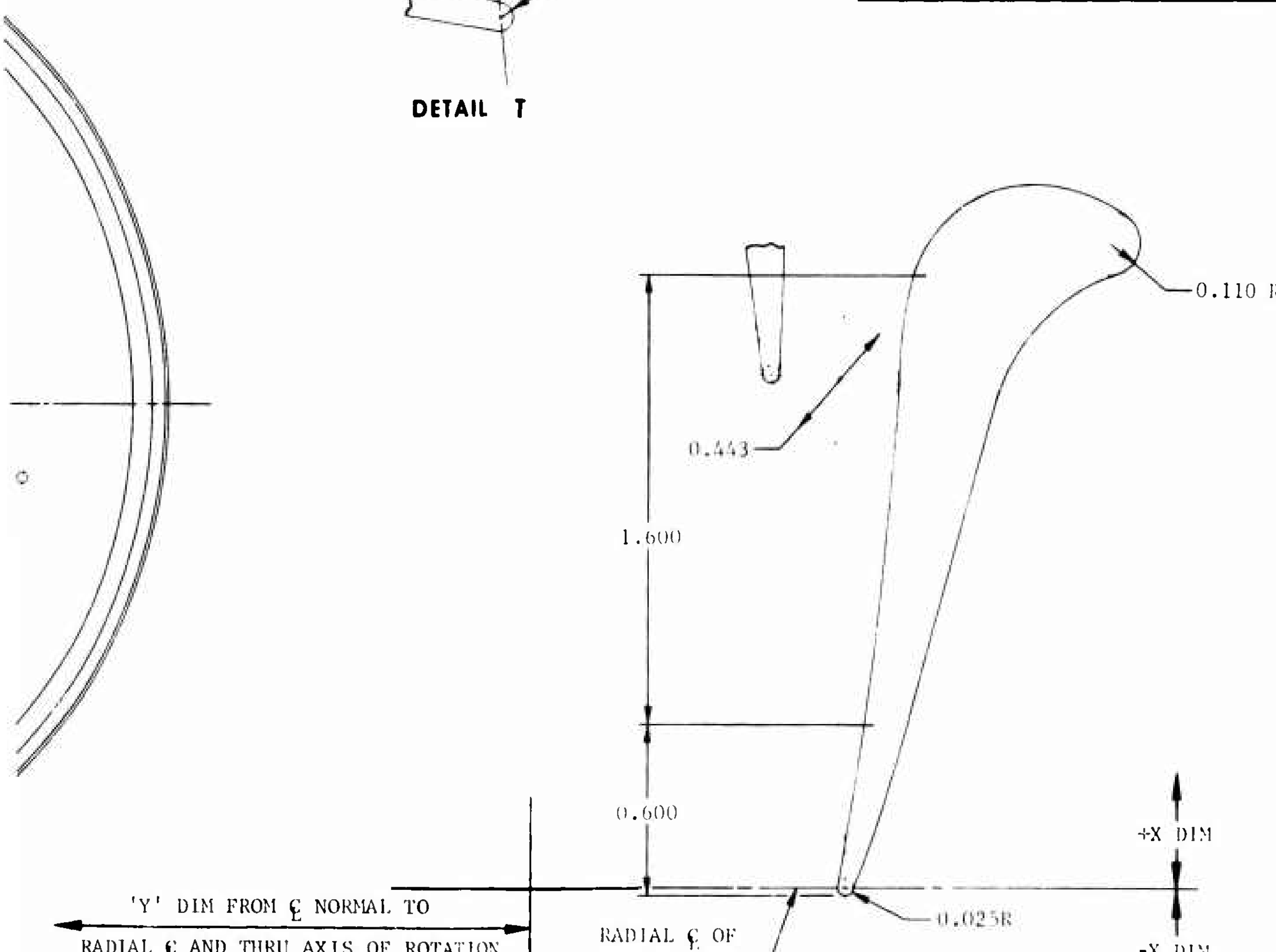

VANE SECTION
TYPICAL FOR 20 VANES

D

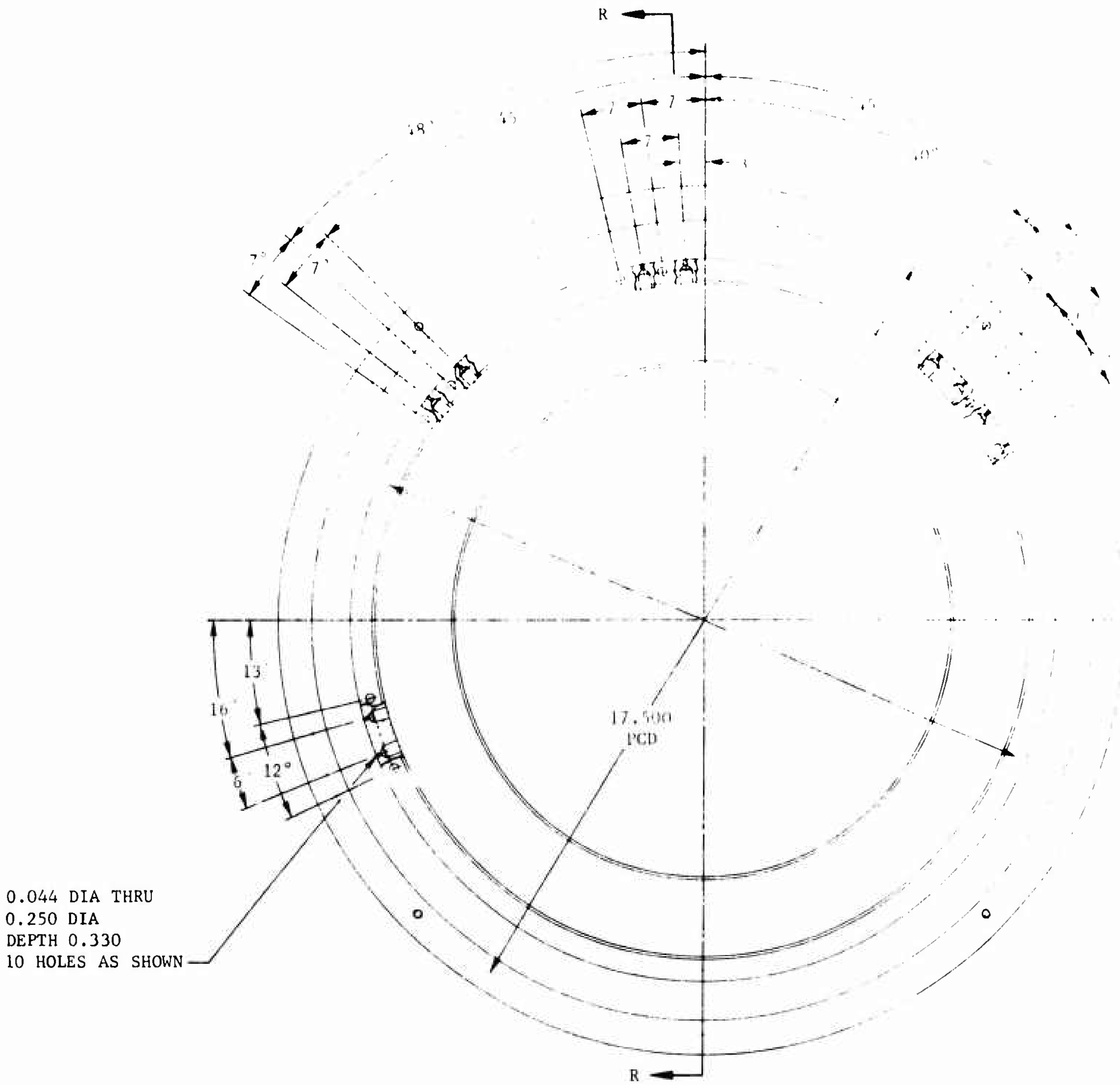

Figure 23. Twenty-Five-Vaned Cold-Flow Nozzle.

A

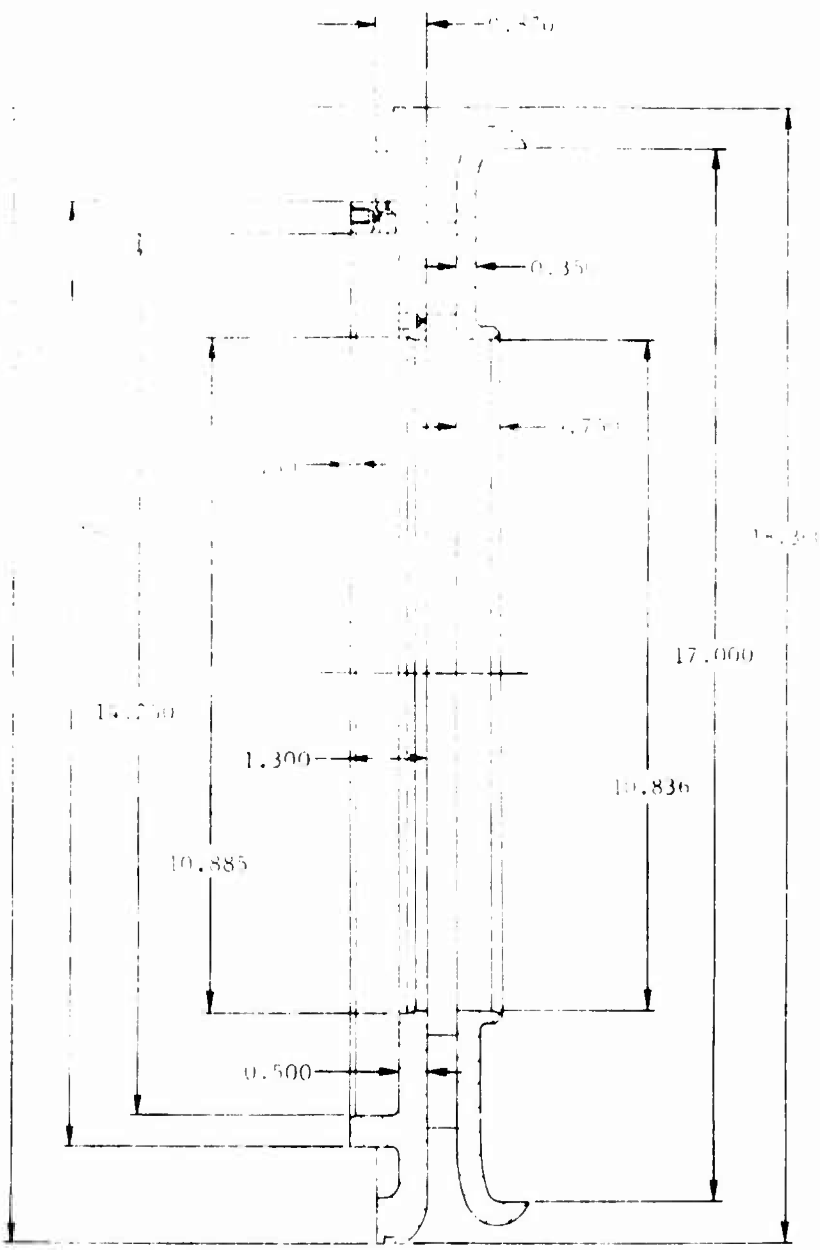

SECTION R-R

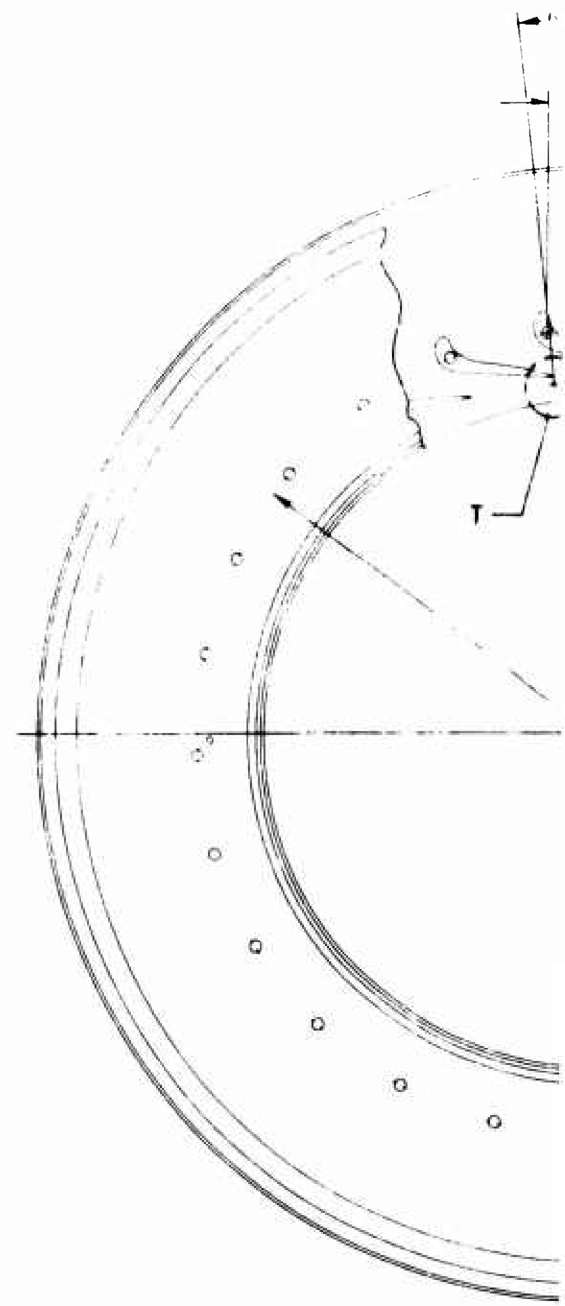

B

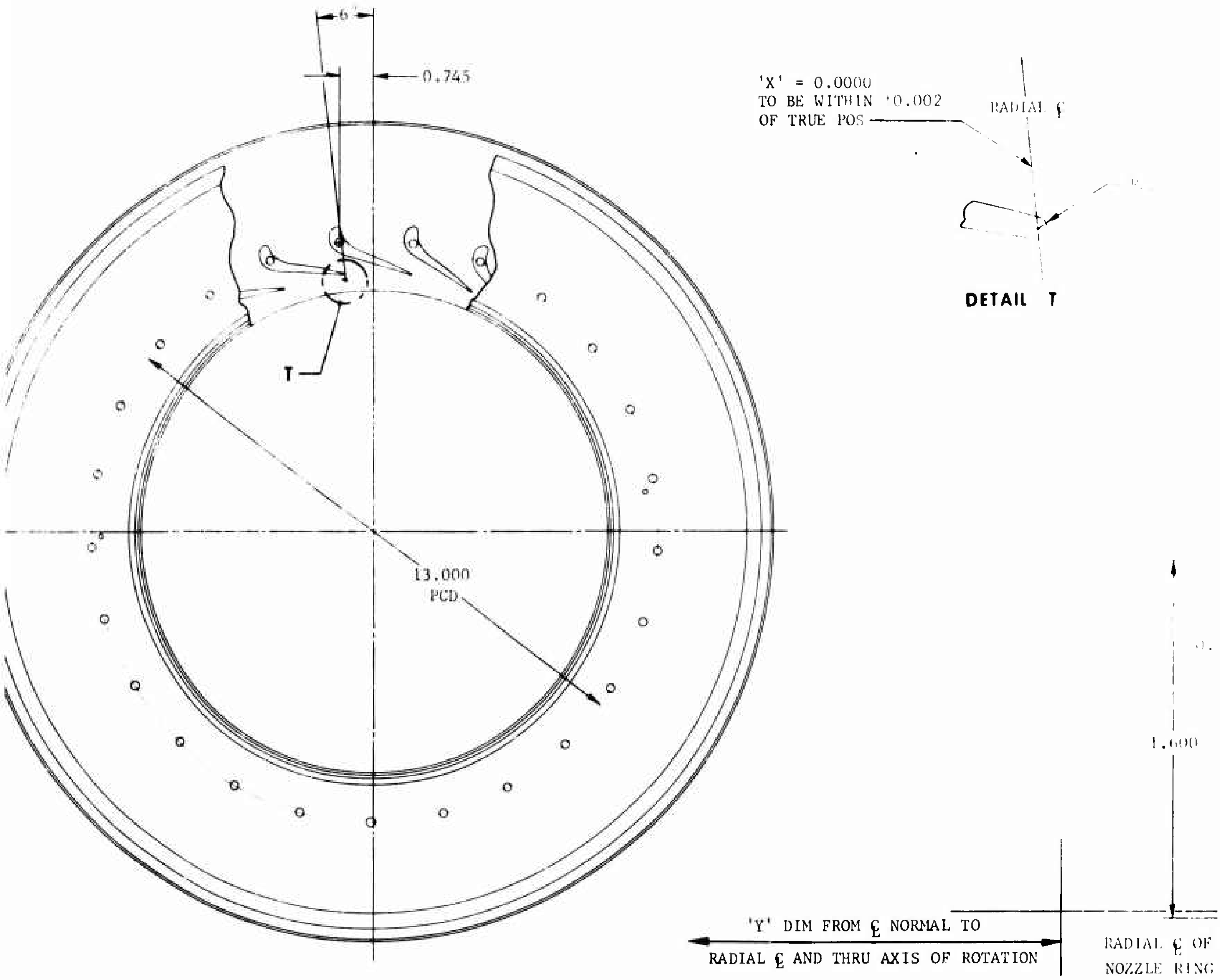
6°
0.745
'X' = 0.0000
TO BE WITHIN ±0.002
OF TRUE POS
RADIAL ℄
DETAIL T
T
13.000
PCD
1.600
'Y' DIM FROM ℄ NORMAL TO
RADIAL ℄ AND THRU AXIS OF ROTATION
RADIAL ℄ OF
NOZZLE RING

C

VANE COORDINATES		
X DIM	Y DIM	Y DIM

FOR COLD VANE COORDINATES REFER TO ESK 3744 AND FOR THE PROFILE EMD REFER TO EFD 31779. THIS PROFILE IS TYPICAL FOR 25 EQUALLY SPACED VANES INDEXED FROM RADIAL CENTER LINE AS SHOWN IN DETAIL 'T'

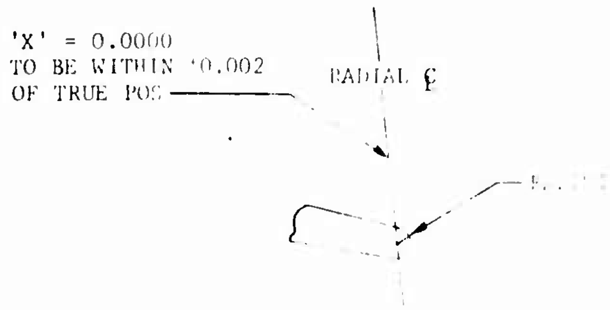

DETAIL T

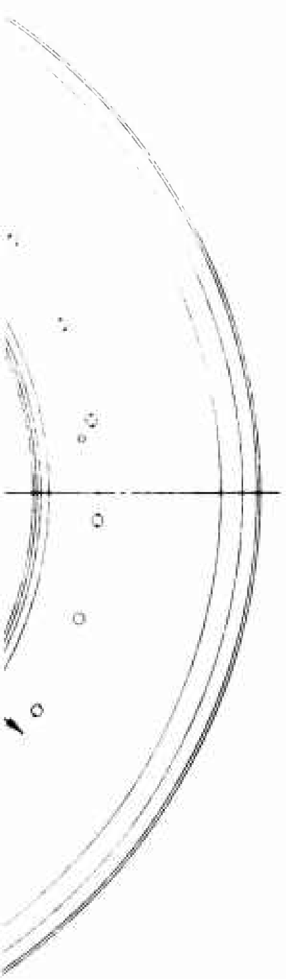

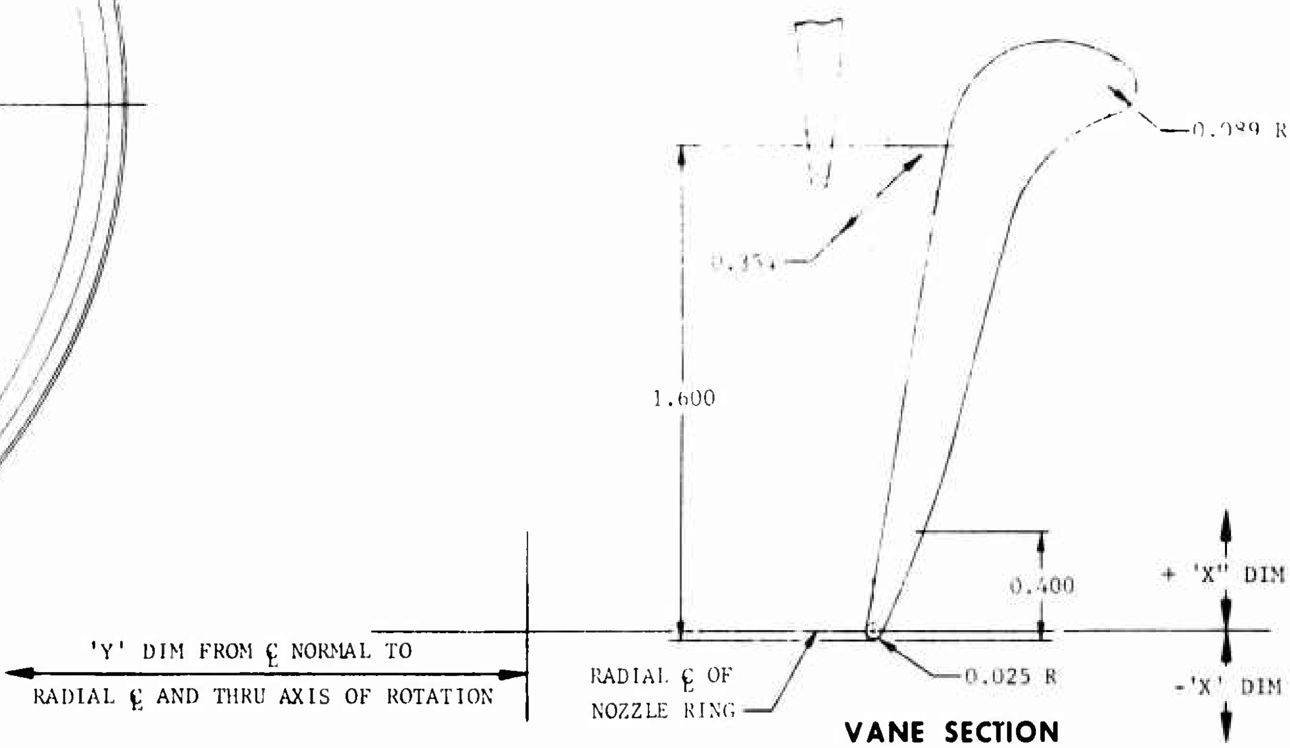

VANE SECTION
TYPICAL FOR 25 VANES

D

BLANK PAGE

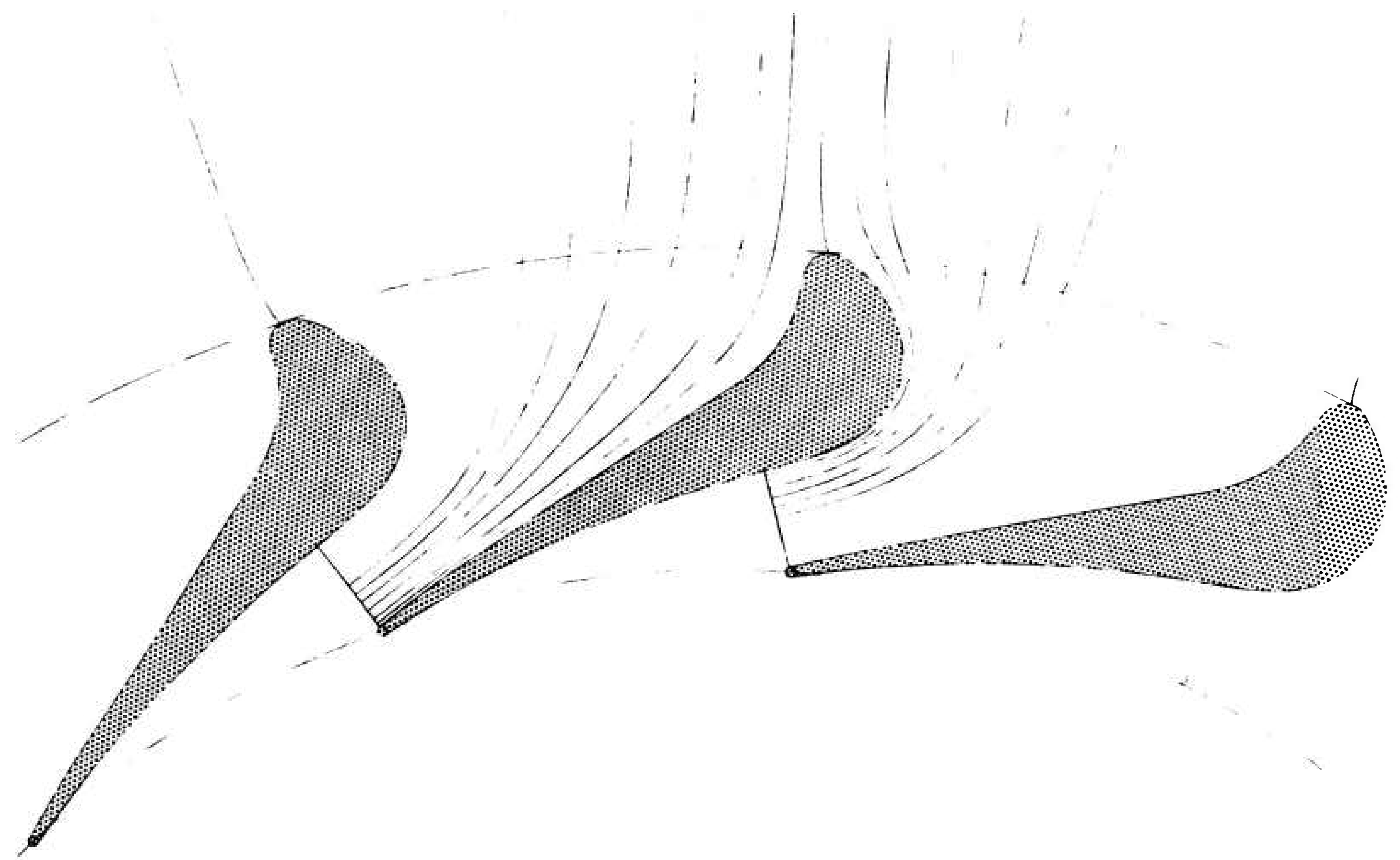

Figure 24. Fifteen-Vaned Nozzle Streamline Pattern.

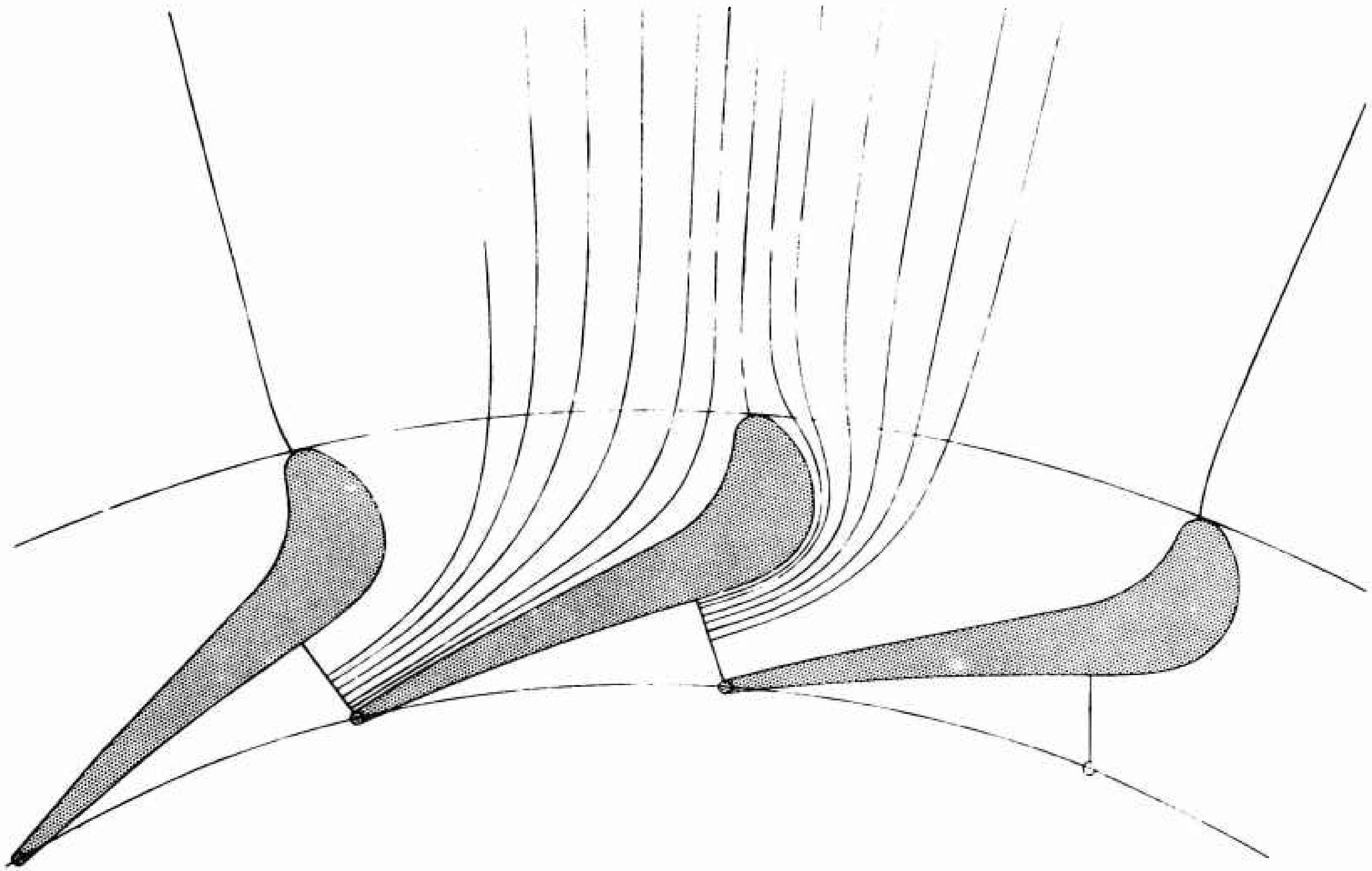

Figure 25. Twenty-Vaned Nozzle Streamline Pattern.

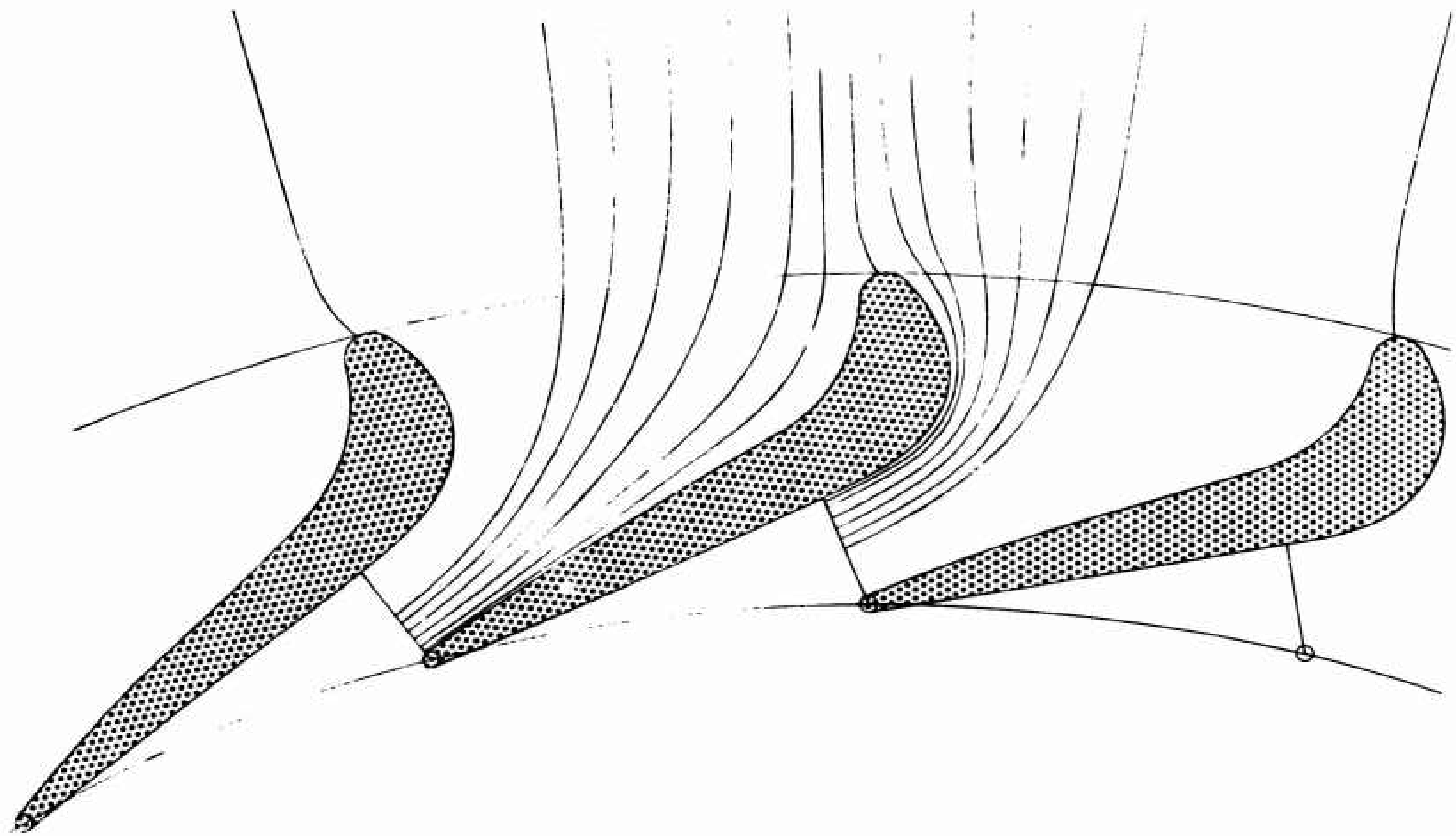

Figure 26. Twenty-Five-Vaned Nozzle Streamline Pattern.

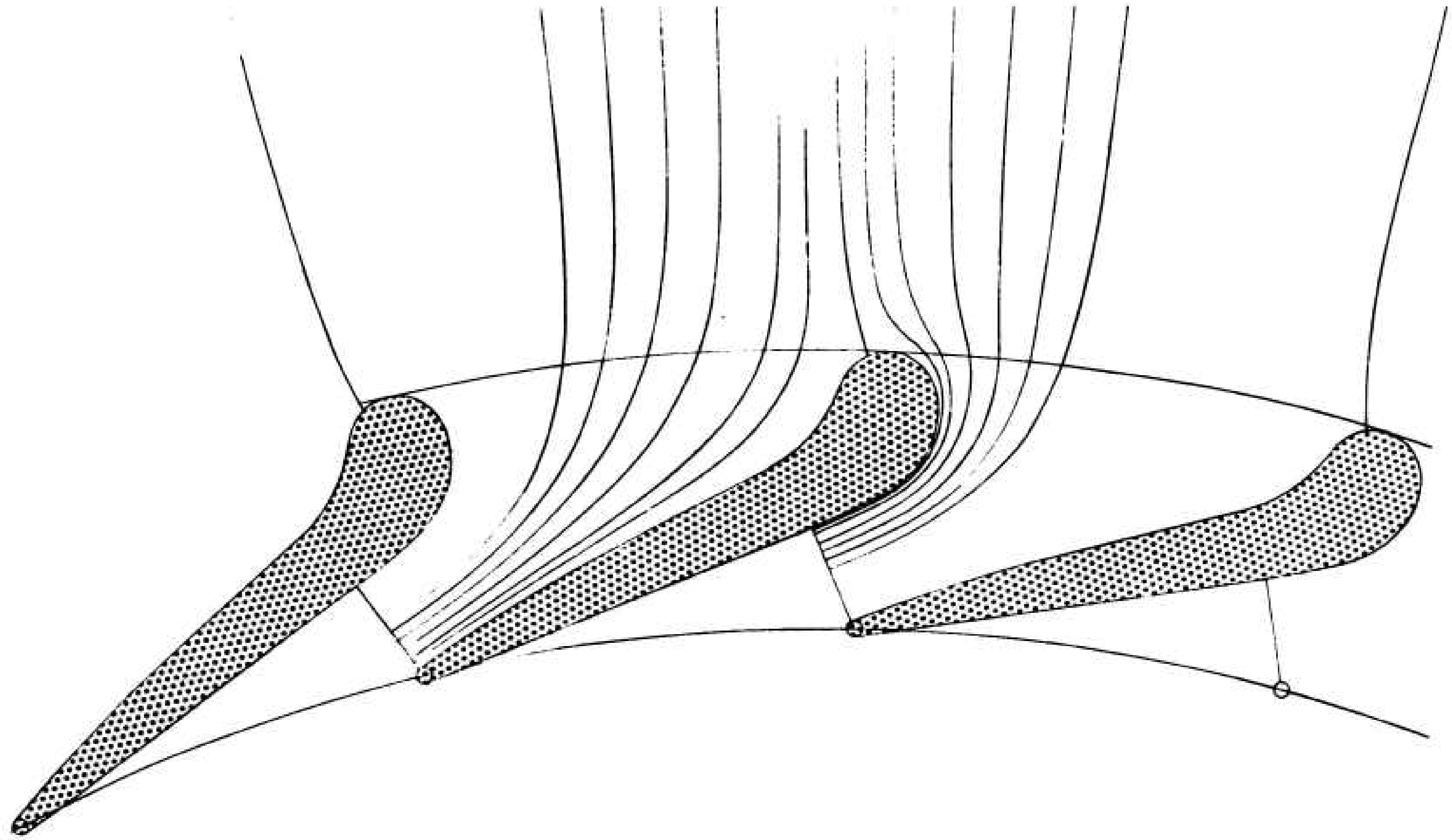

Figure 27. Twenty-Five-Modified-Vaned Streamline Pattern (Moderate Cut-Back).

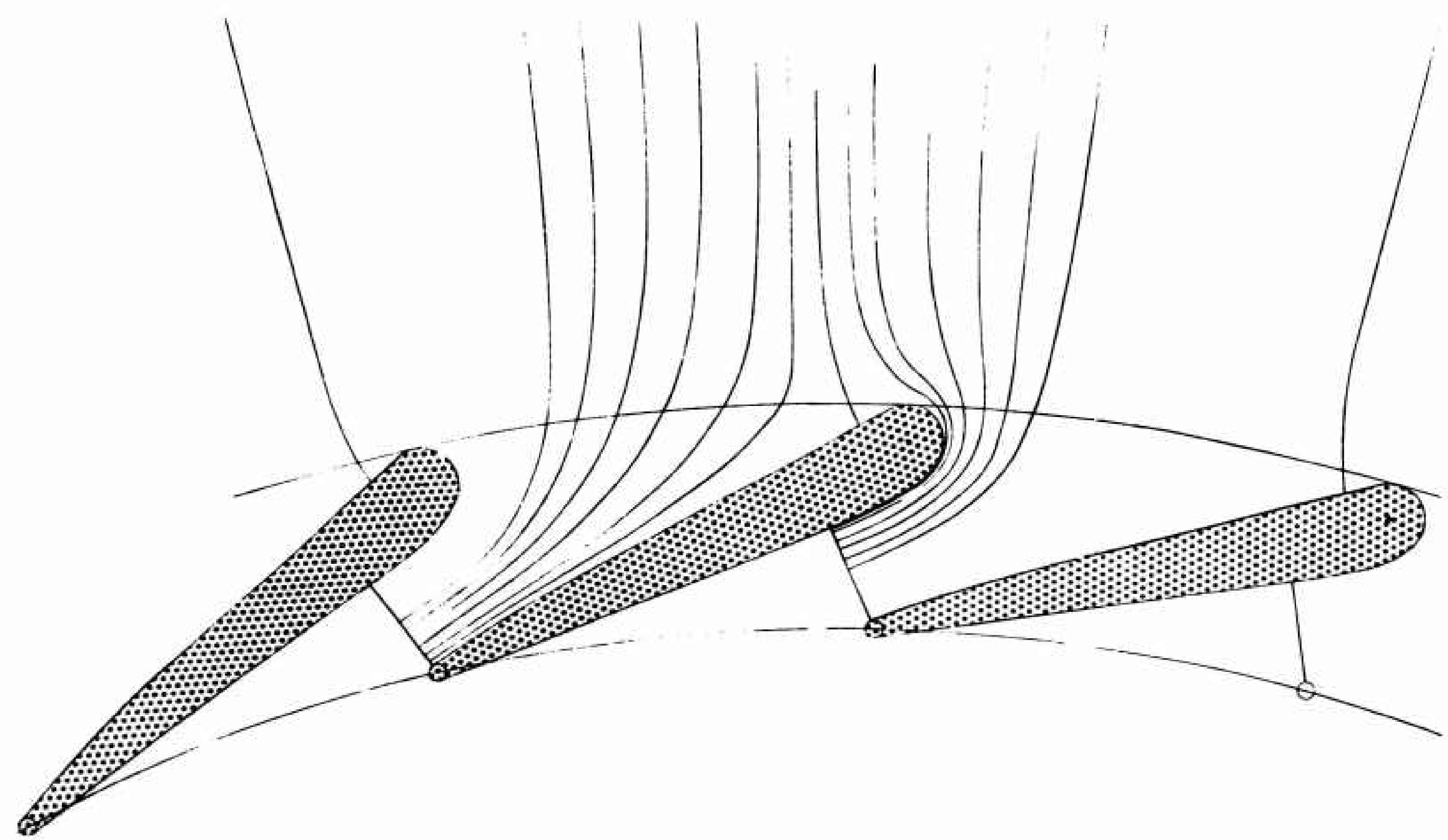

Figure 28. Twenty-Five-Modified-Vaned
Streamline Pattern (Severe Cut-Back).

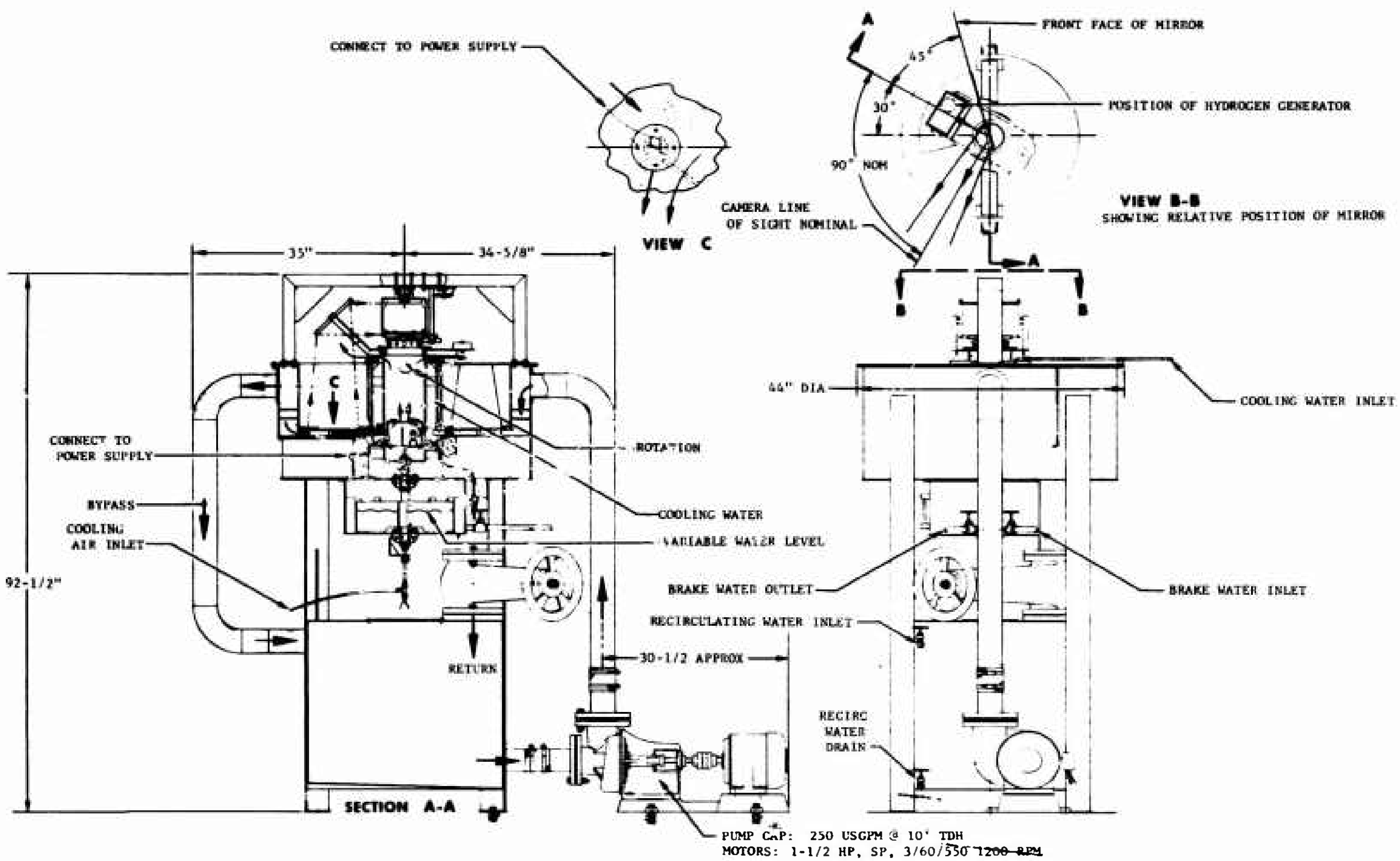

Figure 29. Water Visualization Rig.

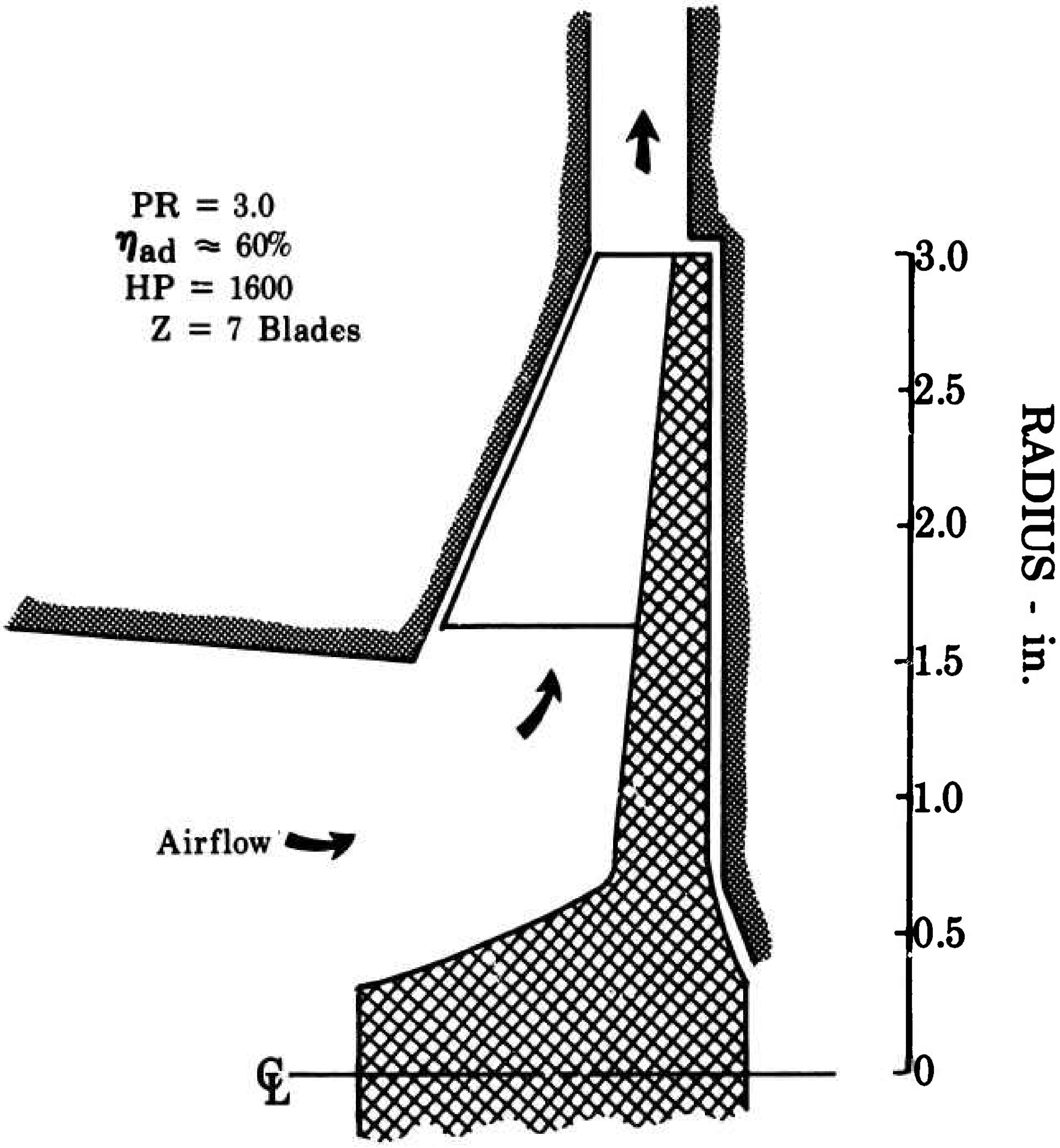

Figure 30. Original Rig Brake Design Schematic.

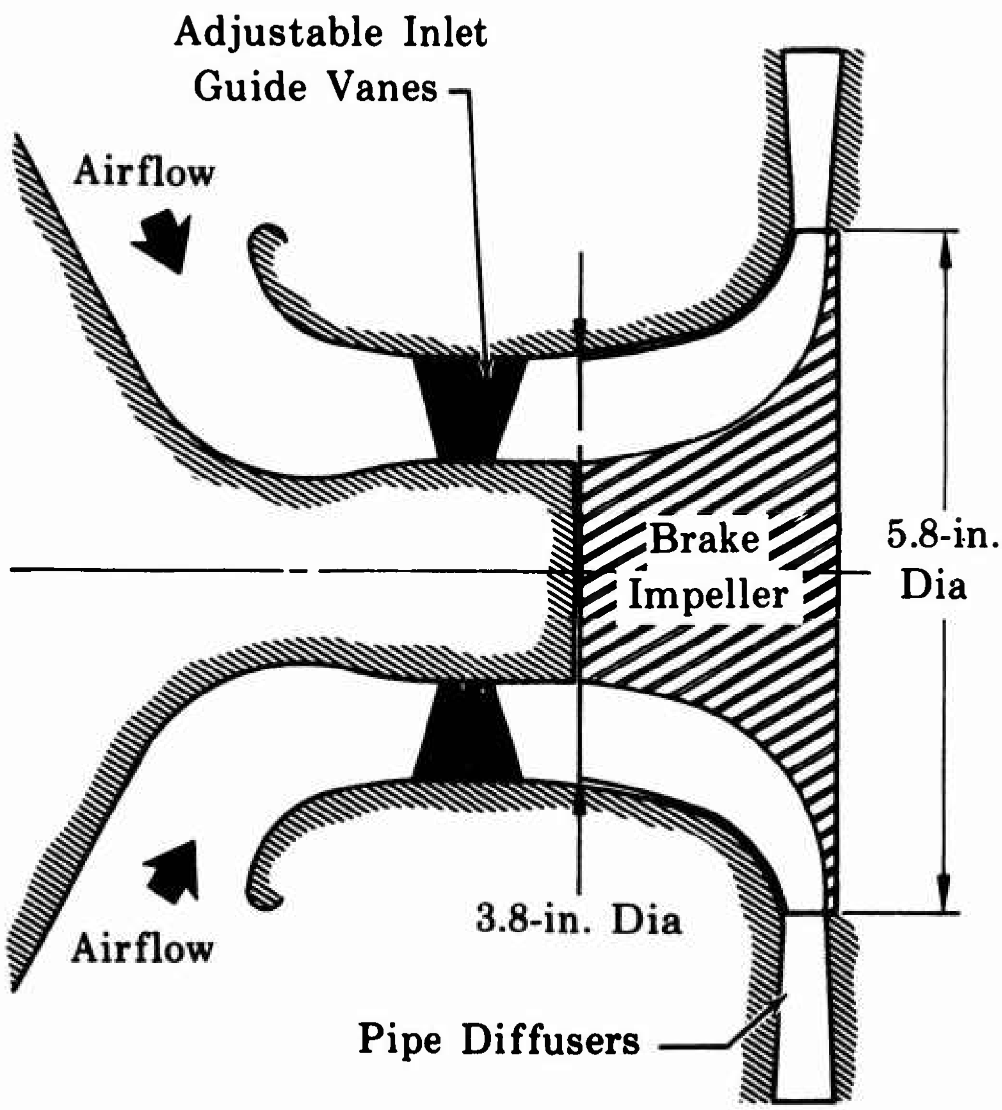

Figure 31. Aerodynamic Design of Rig Brake.

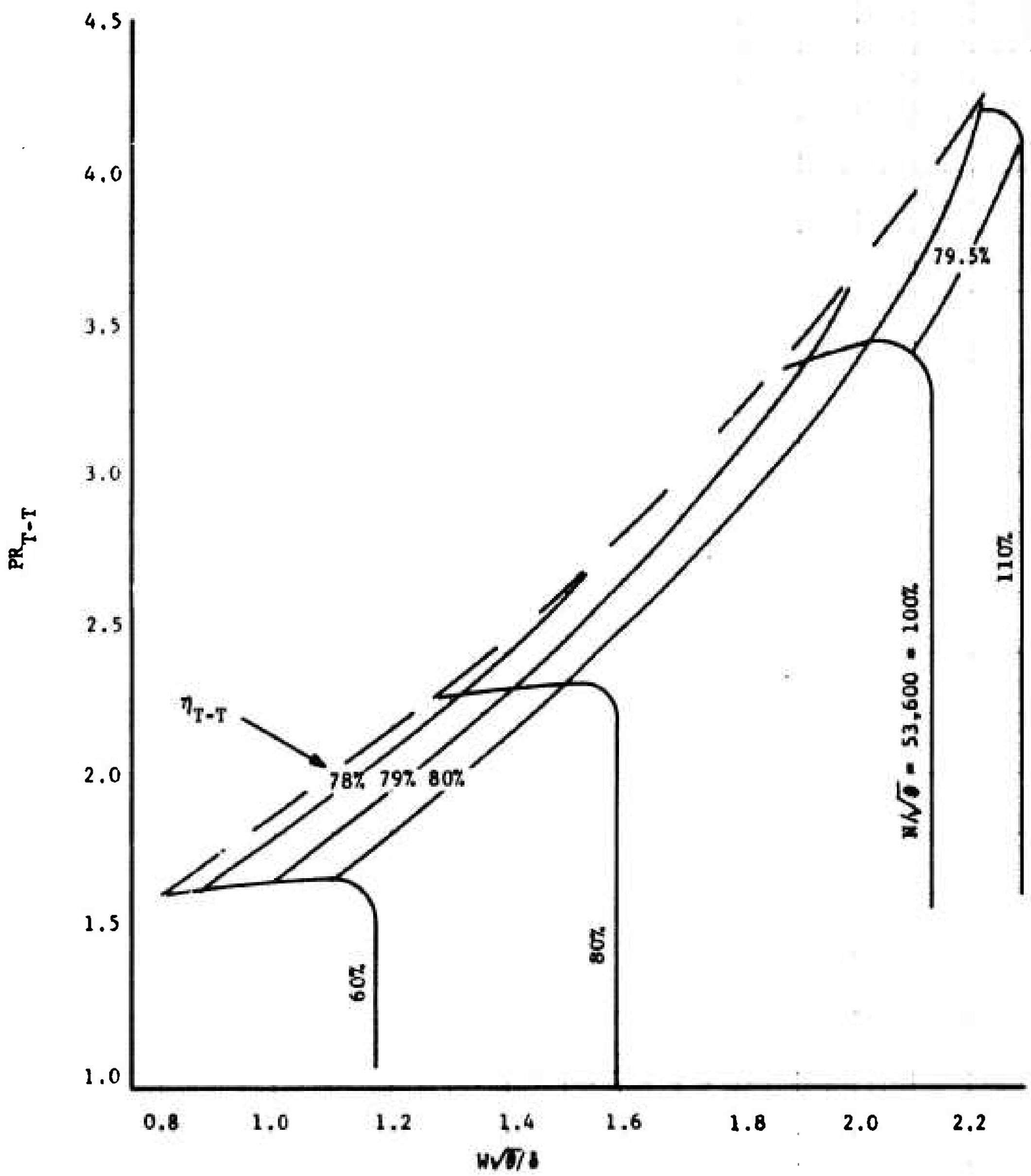

Figure 32. Brake Impeller - 26-Pipe Diffuser, 0-Degree Prewhirl.

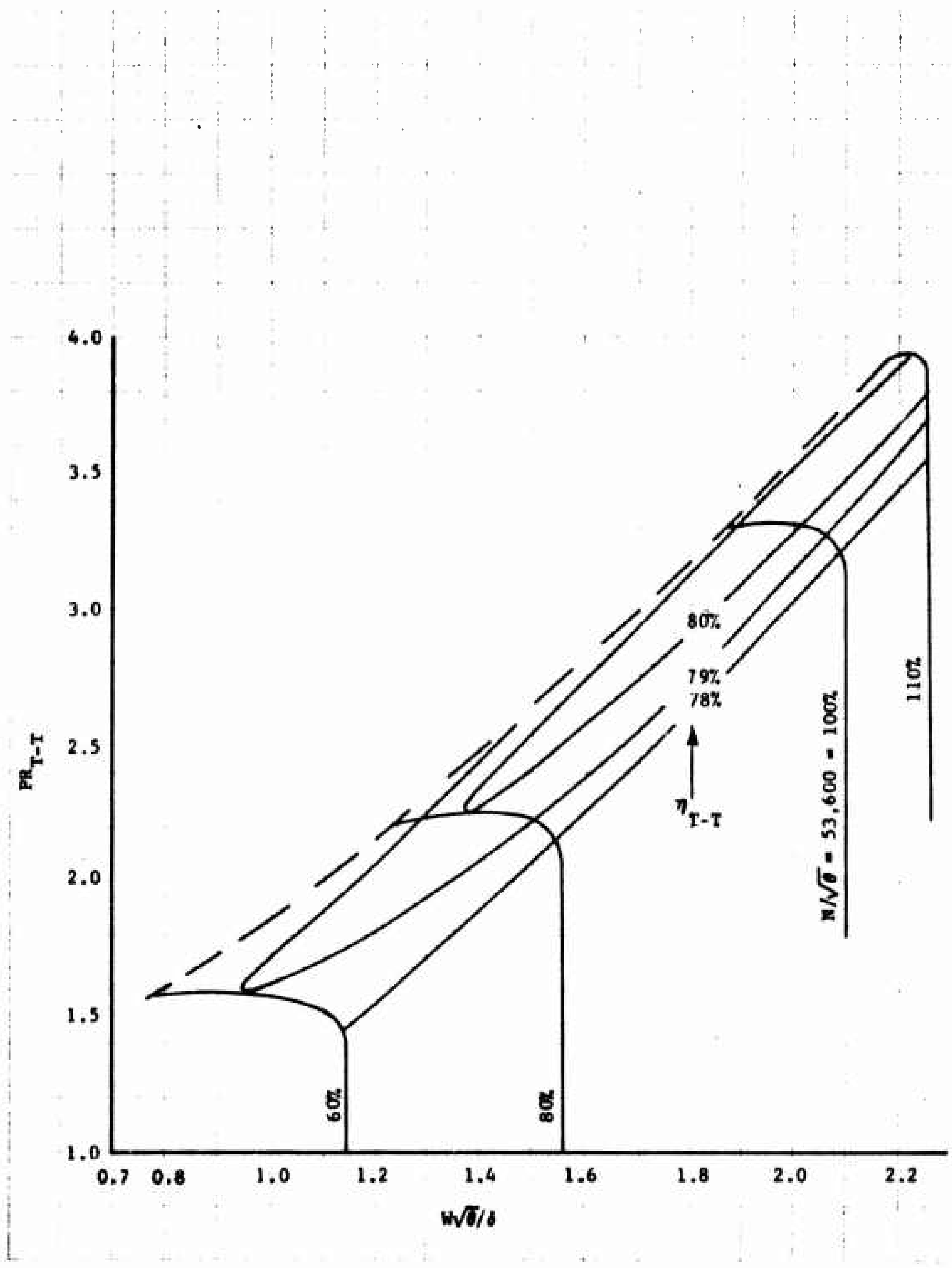

Figure 33. Brake Impeller - 26-Pipe Diffuser, 10-Degree Prewhirl.

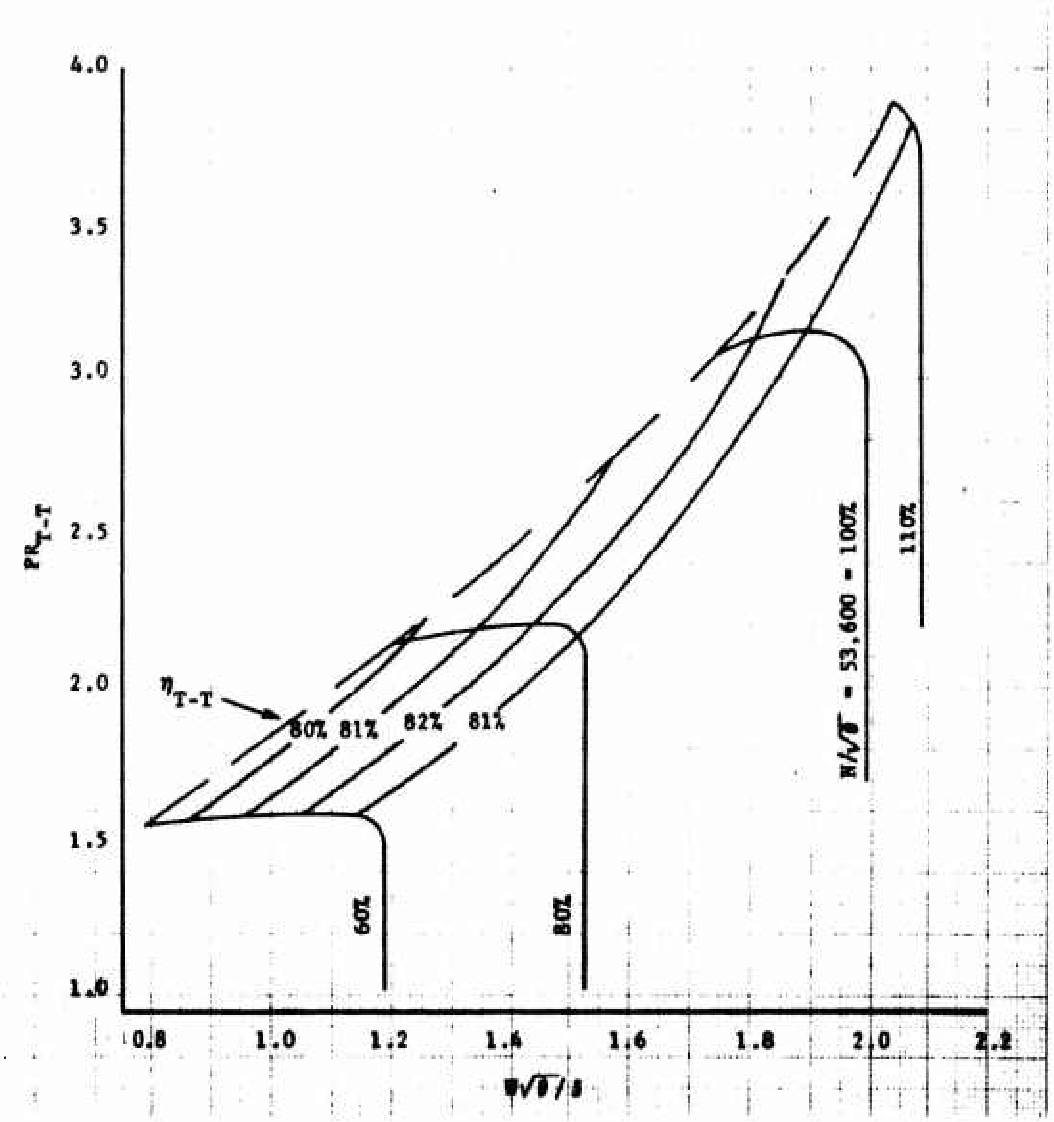

Figure 34. Brake Impeller - 26-Pipe Diffuser, 25-Degree Prewhirl.

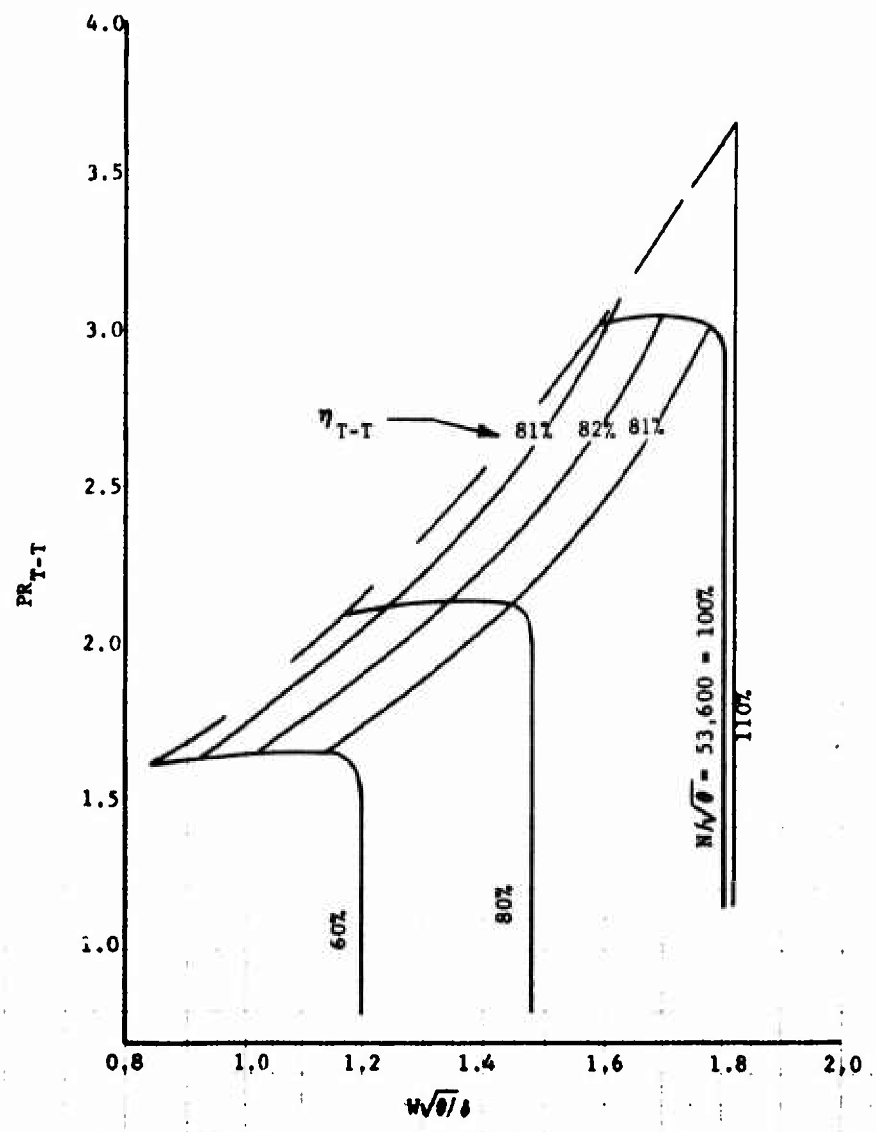

Figure 35. Brake Impeller - 26-Pipe Diffuser, 35-Degree Prewhirl.

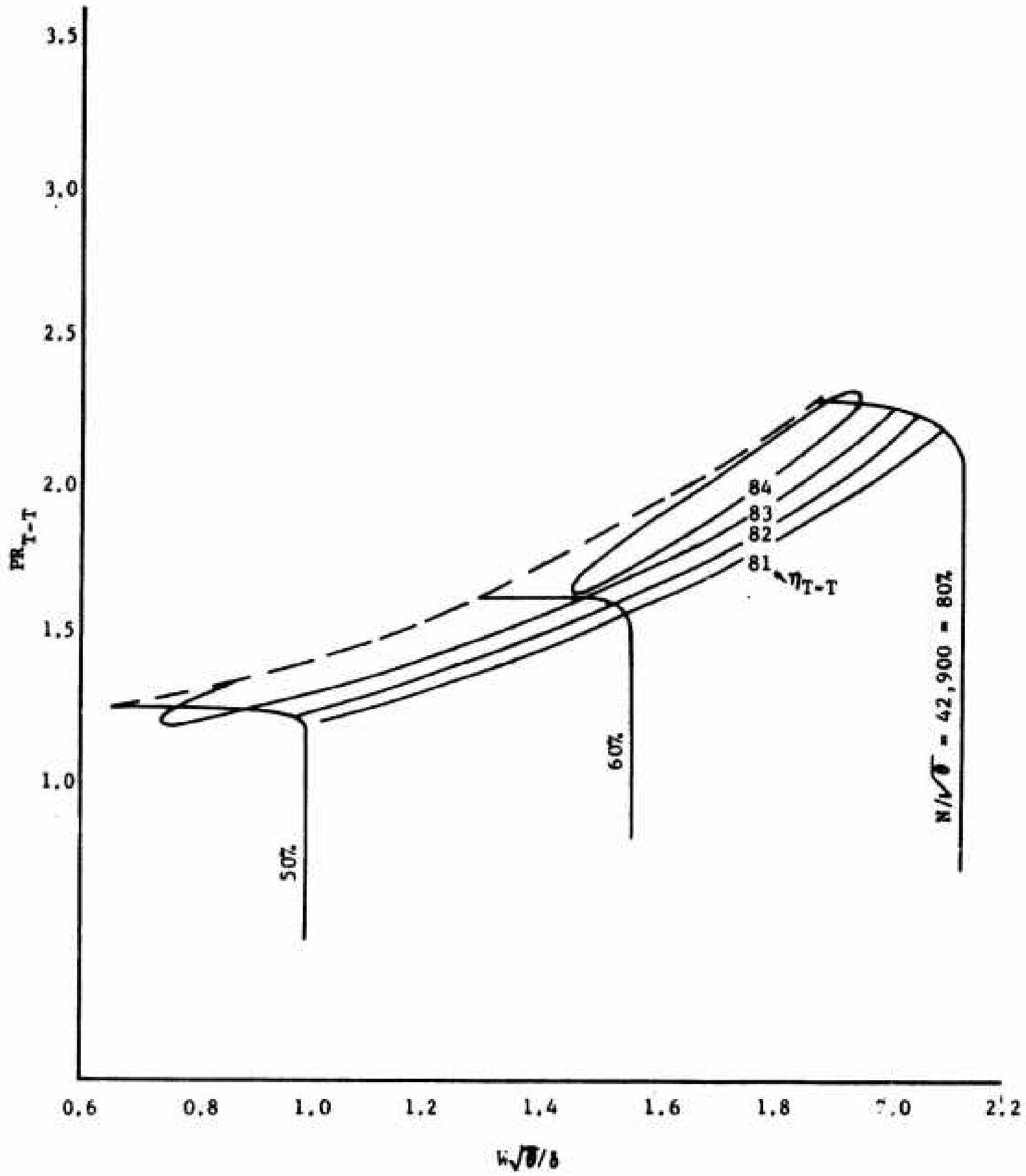

Figure 36. Brake Impeller - 32-Pipe Diffuser, 0-Degree Prewhirl.

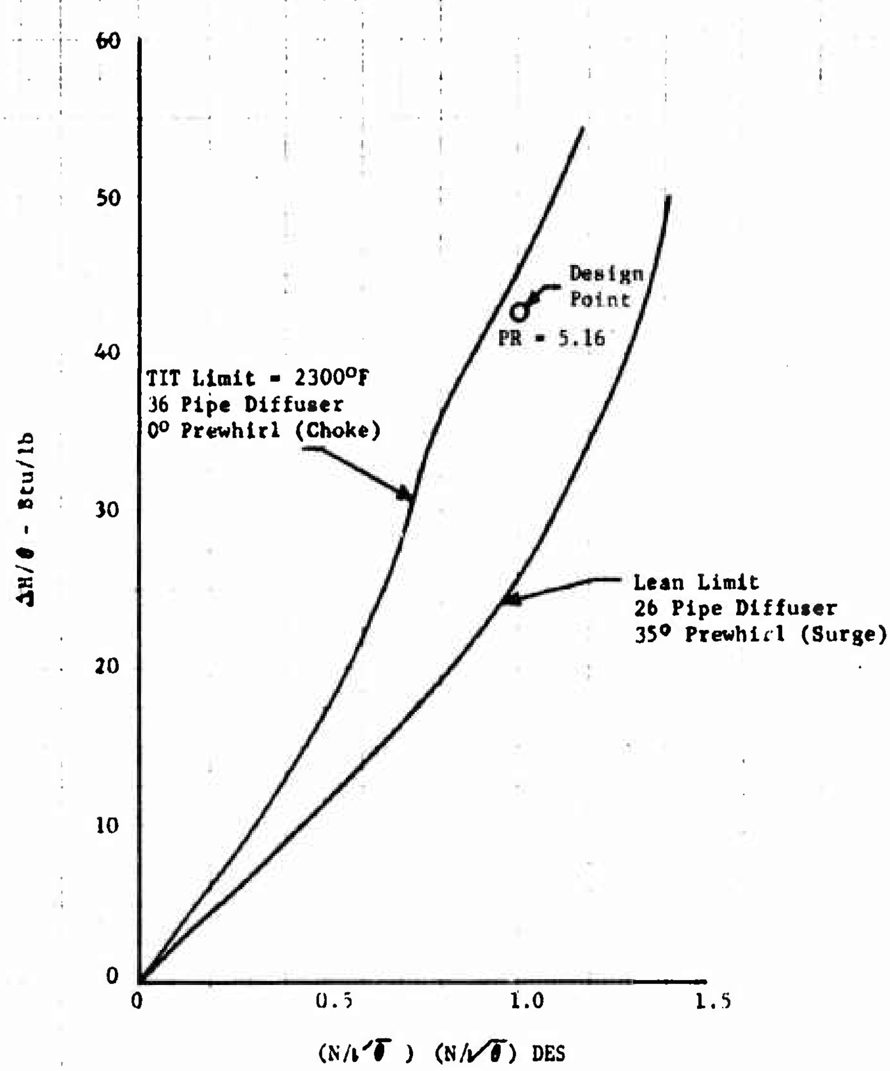

Figure 37. Total Predicted Hot Rig Operating Range.

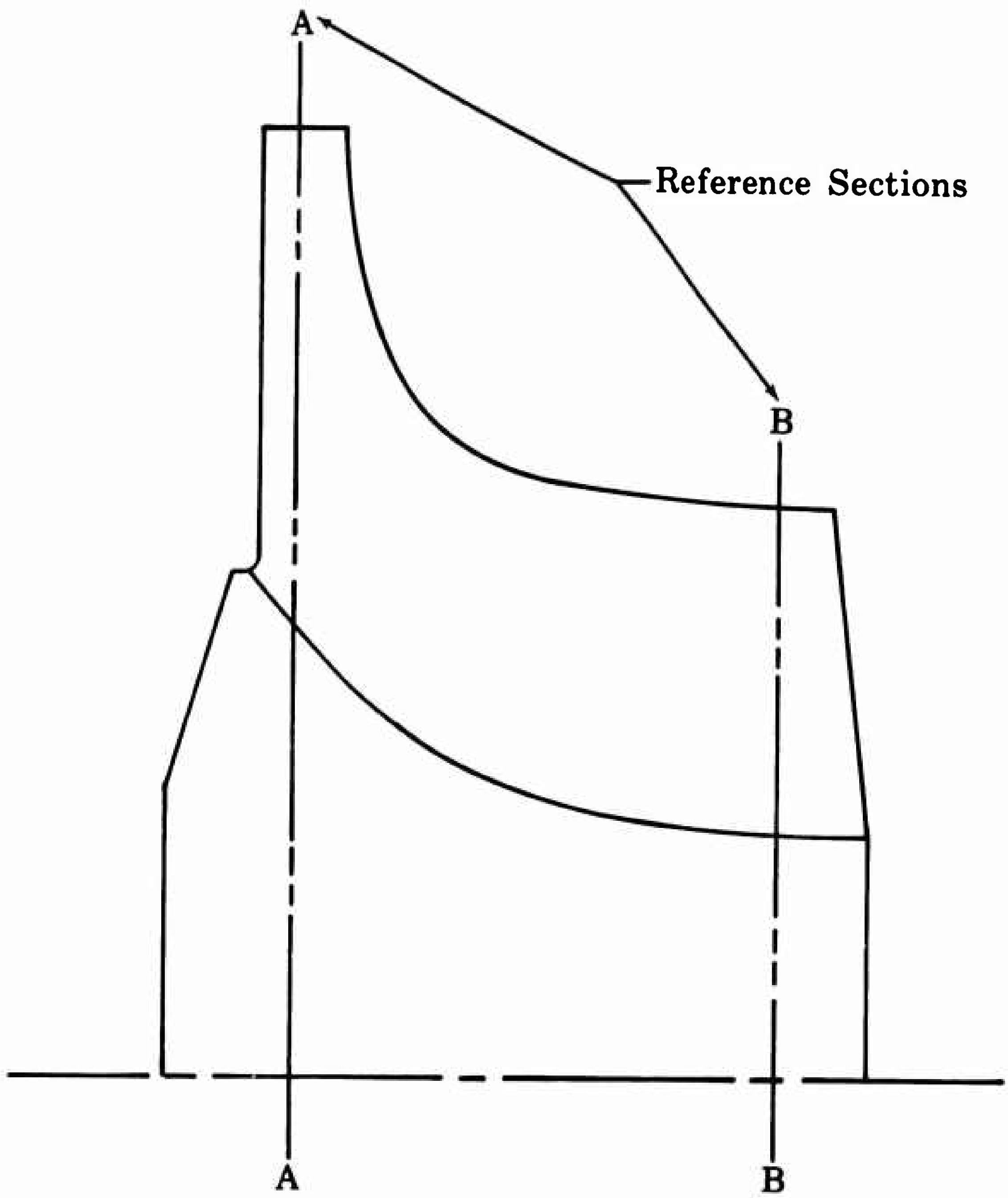

Figure 38. Typical 90-Degree IFR Turbine Rotor.

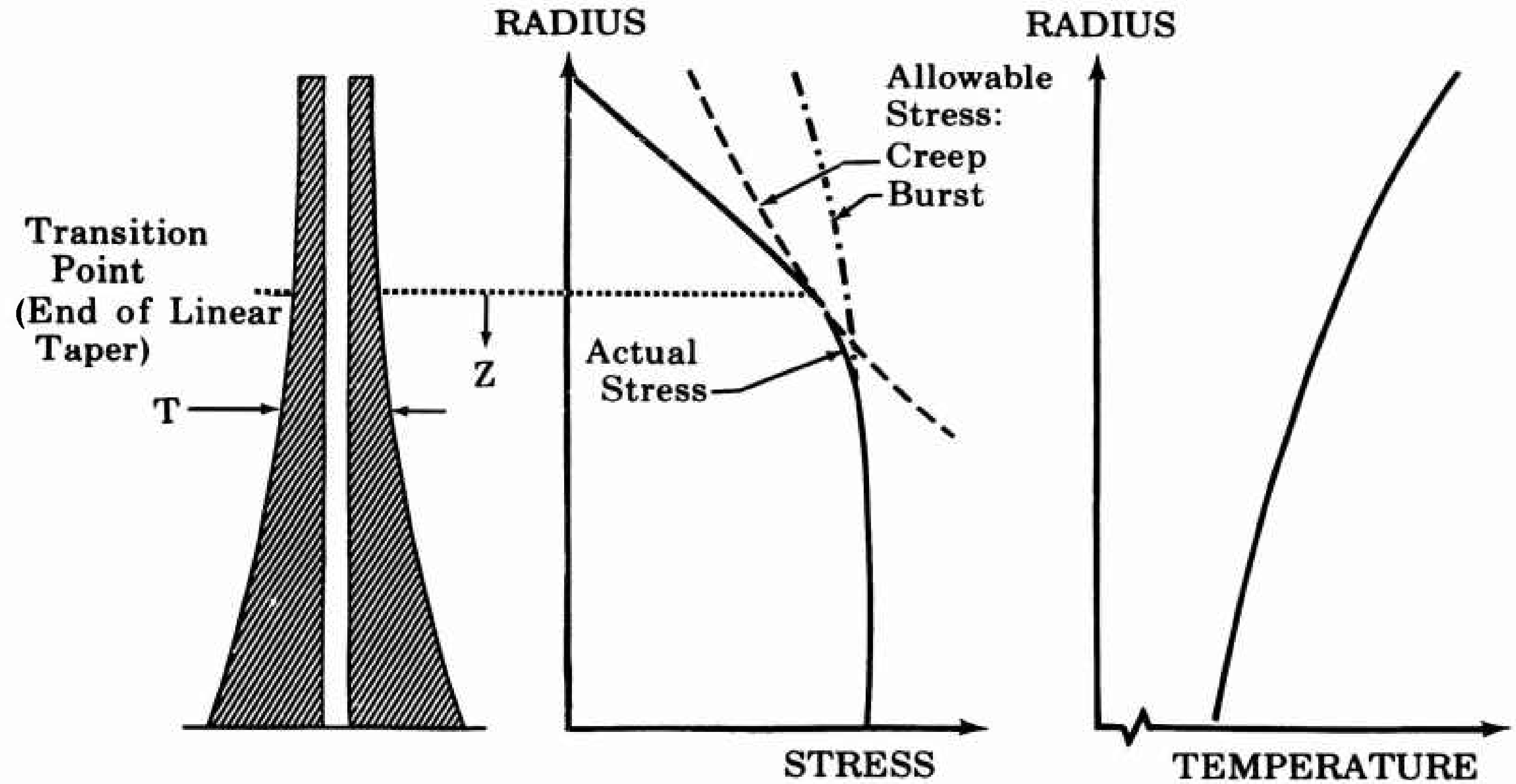

Figure 39. Thickness Distribution in a Reference Section.

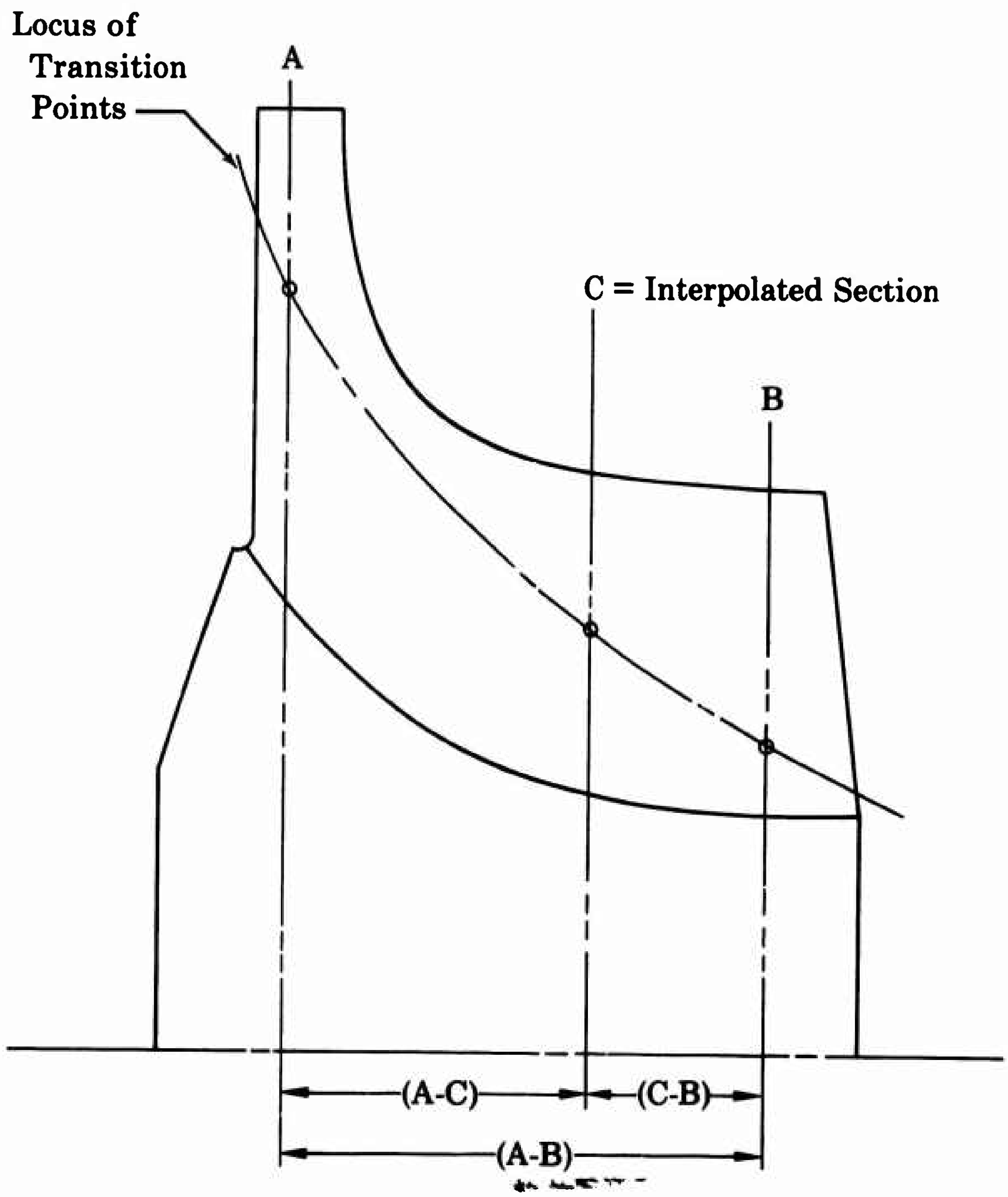

Figure 40. Typical Interpolated Section.

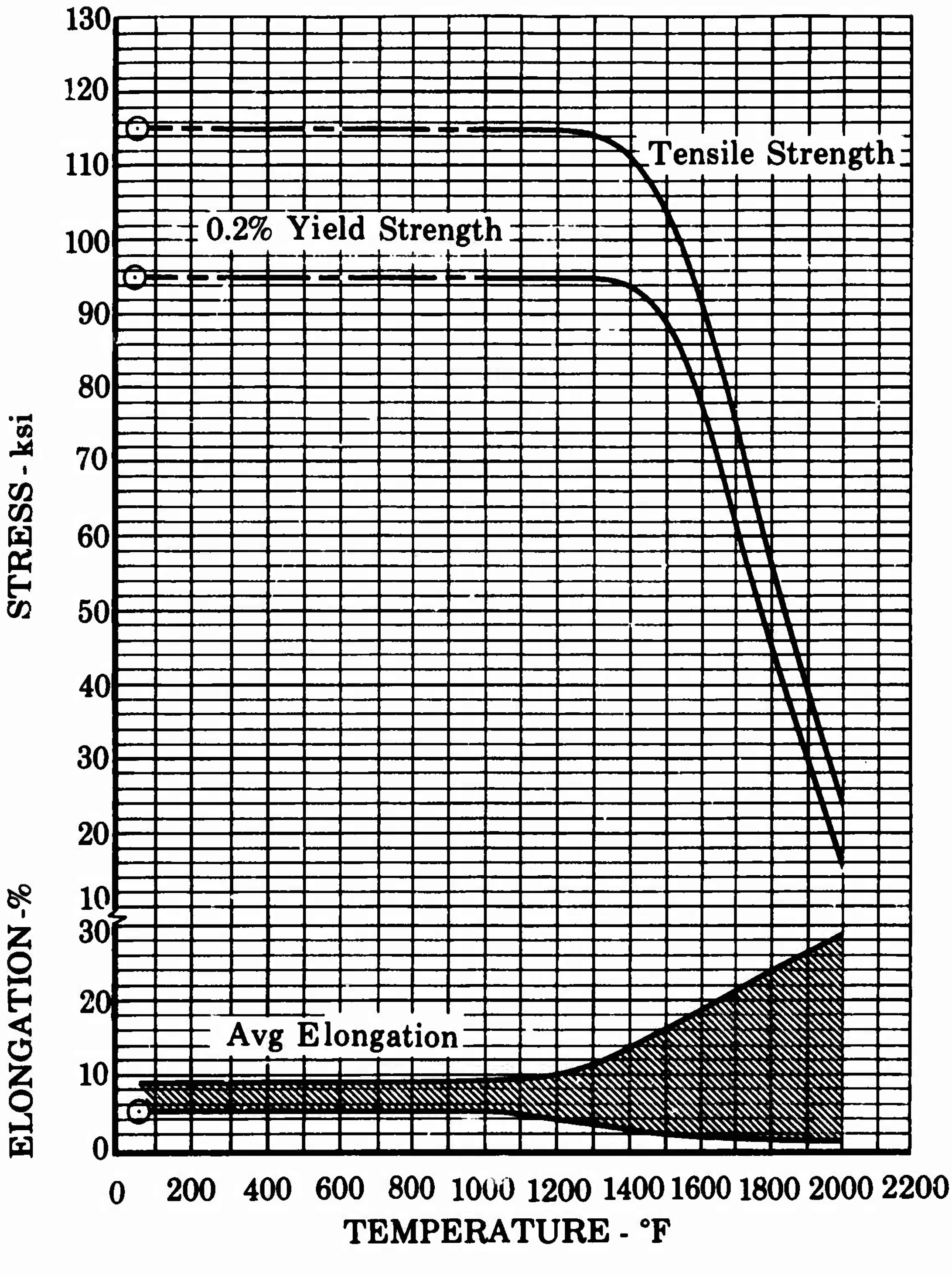

Figure 41. Tensile Properties of IN 100 (PWA 658).

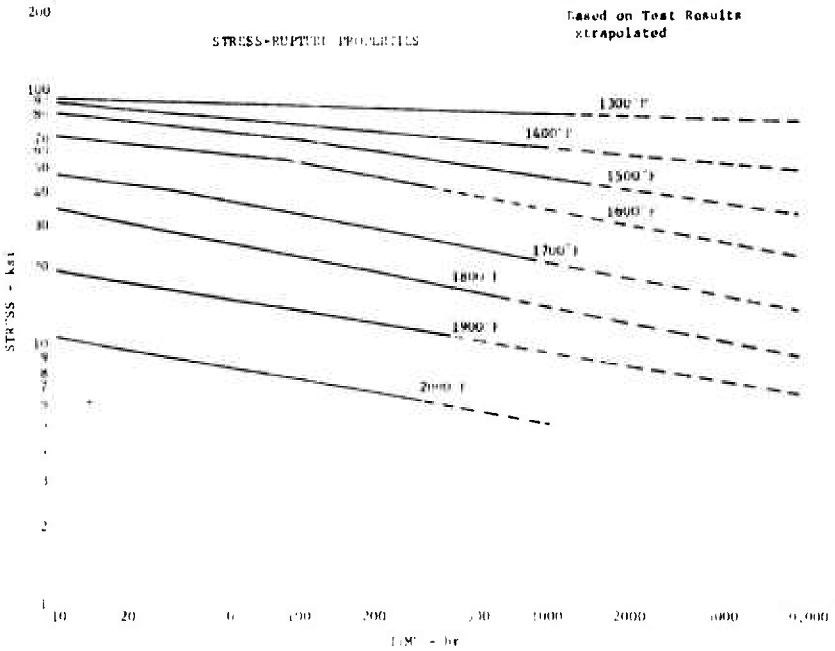

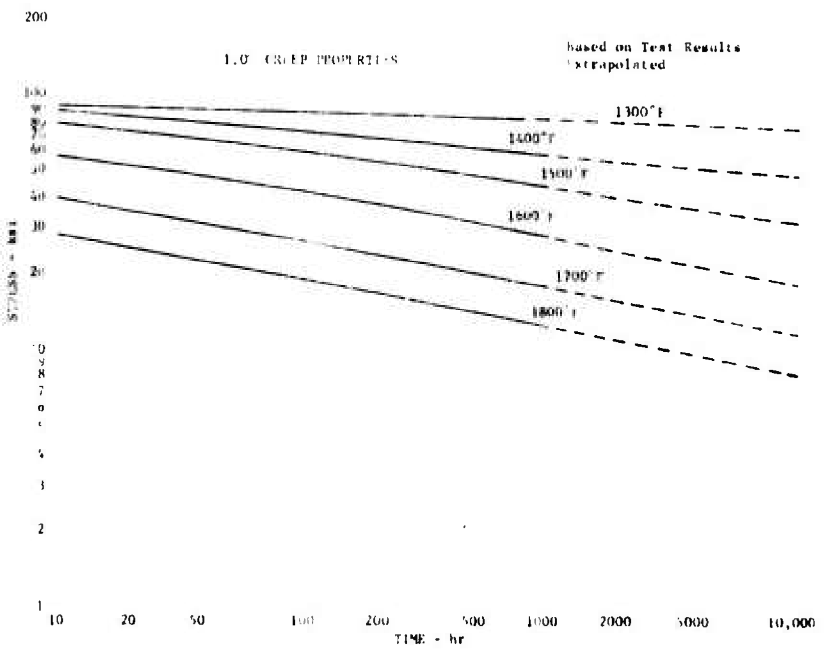

Figure 42. Stress-Rupture and 1% Creep Properties of IN 100 (PWA 658).

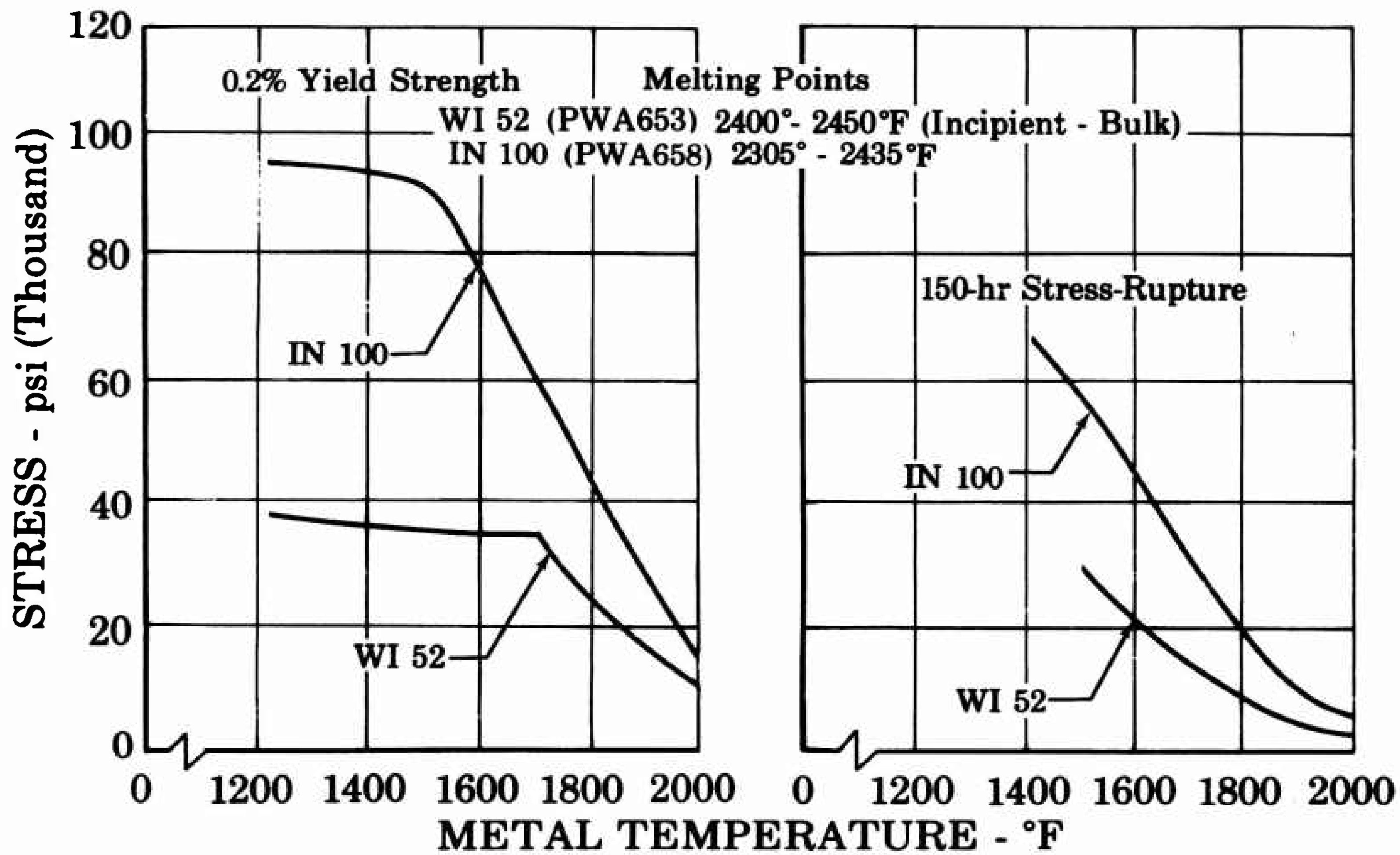

Figure 43. Comparison of WI 52 (PWA 653) and IN 100 (PWA 658) Properties.

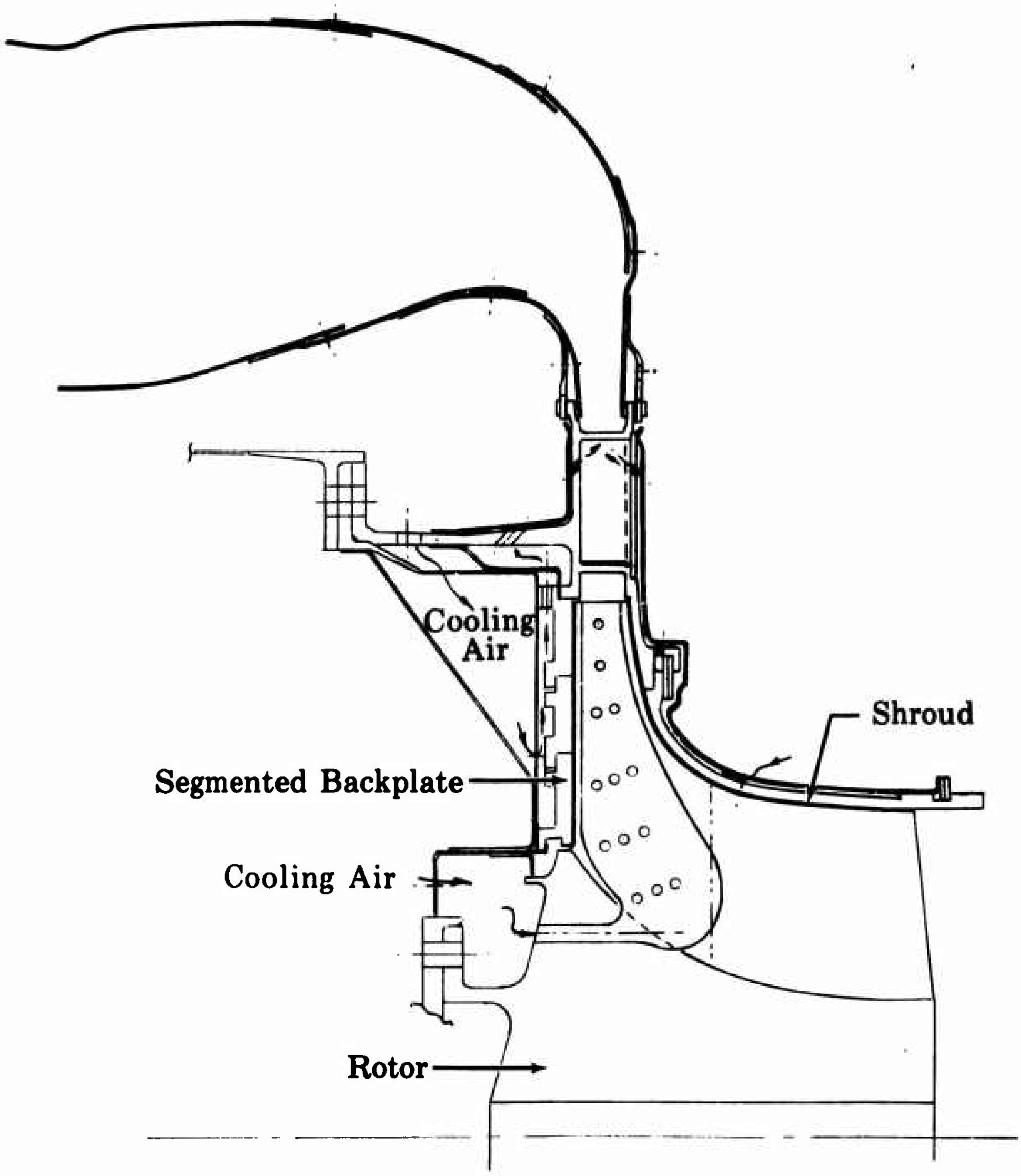

Figure 44. First-Iteration Mechanical Design.

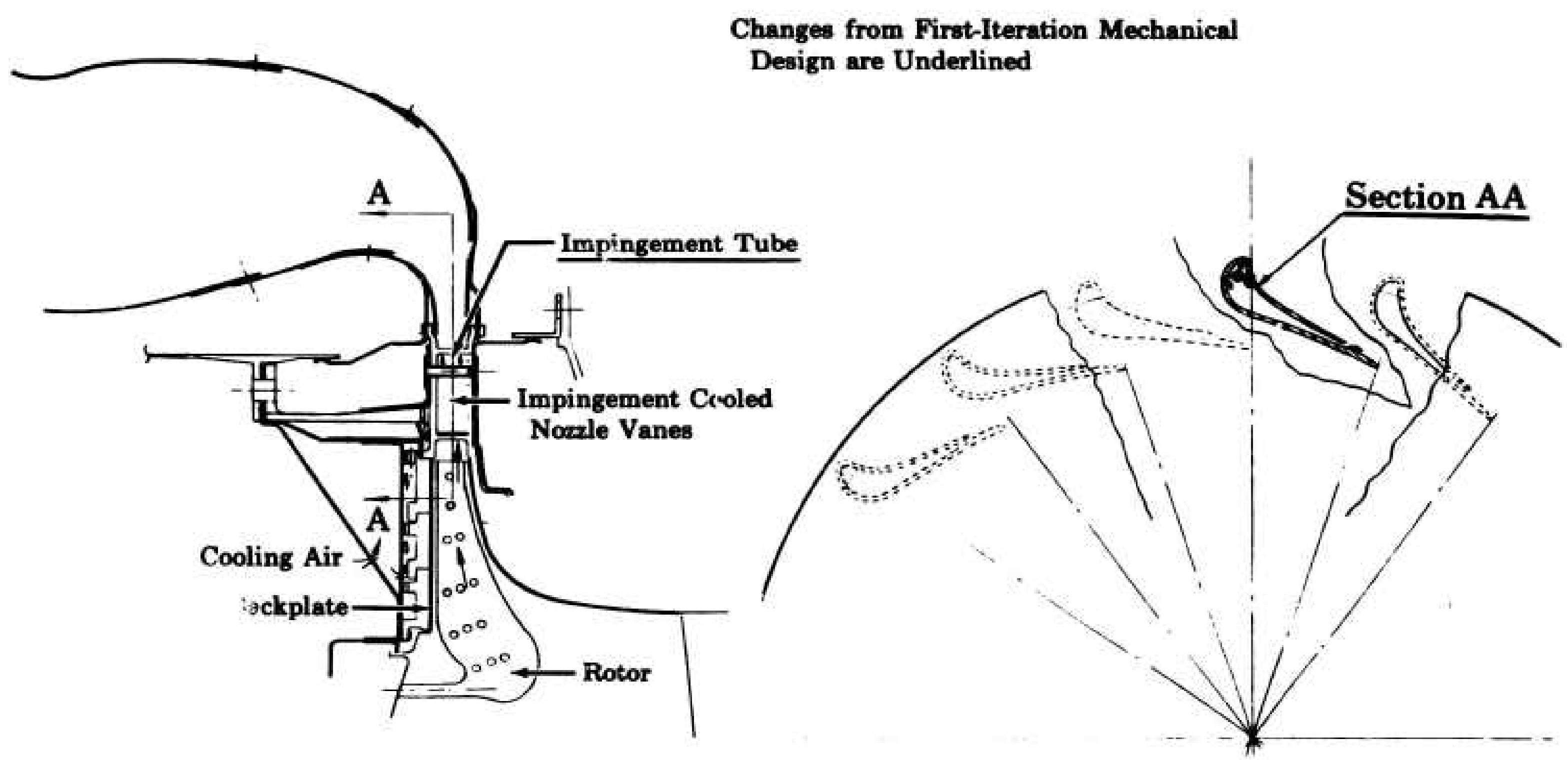

Figure 45. Second-Iteration Mechanical Design.

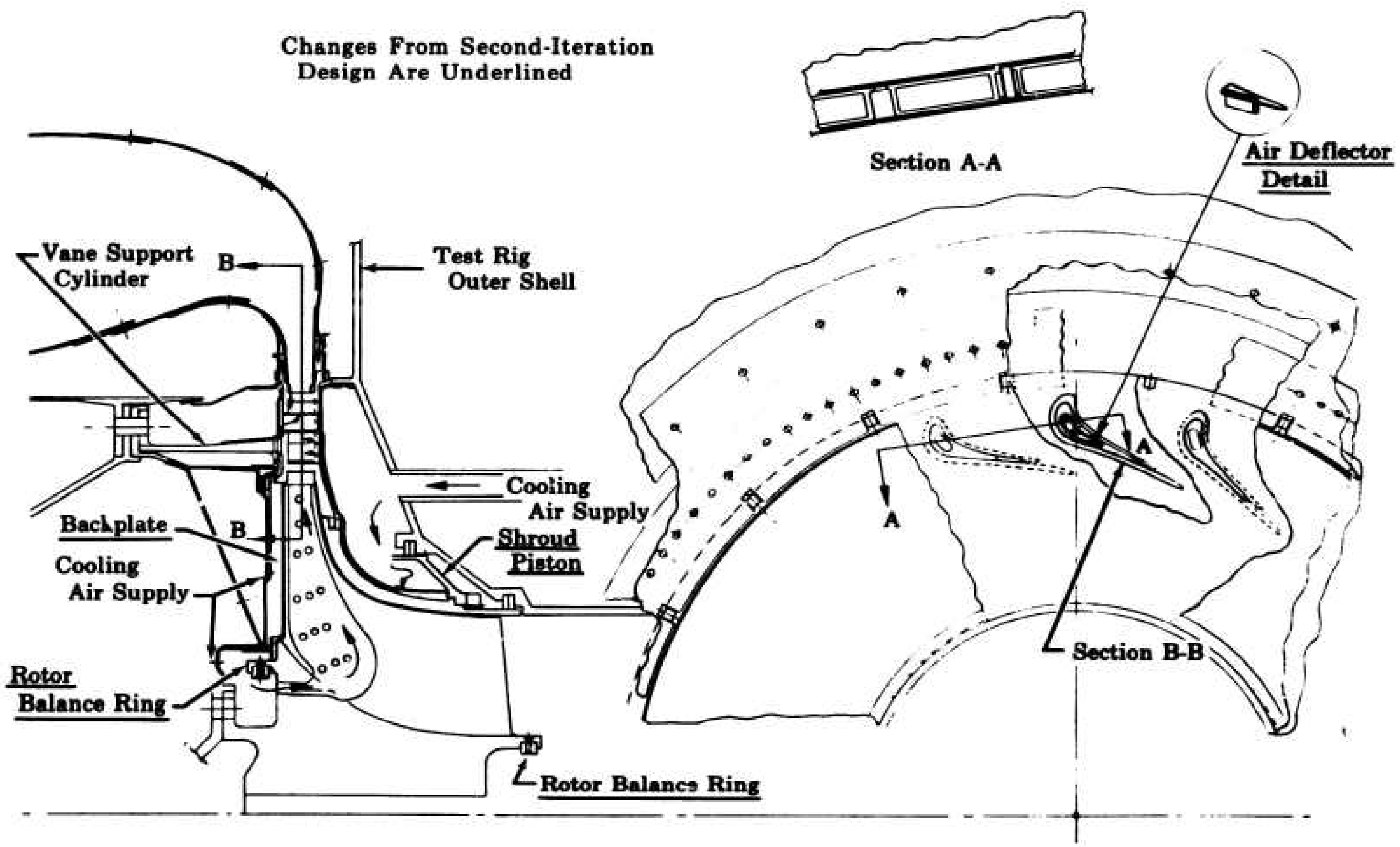

Figure 46. Third-Iteration Mechanical Design.

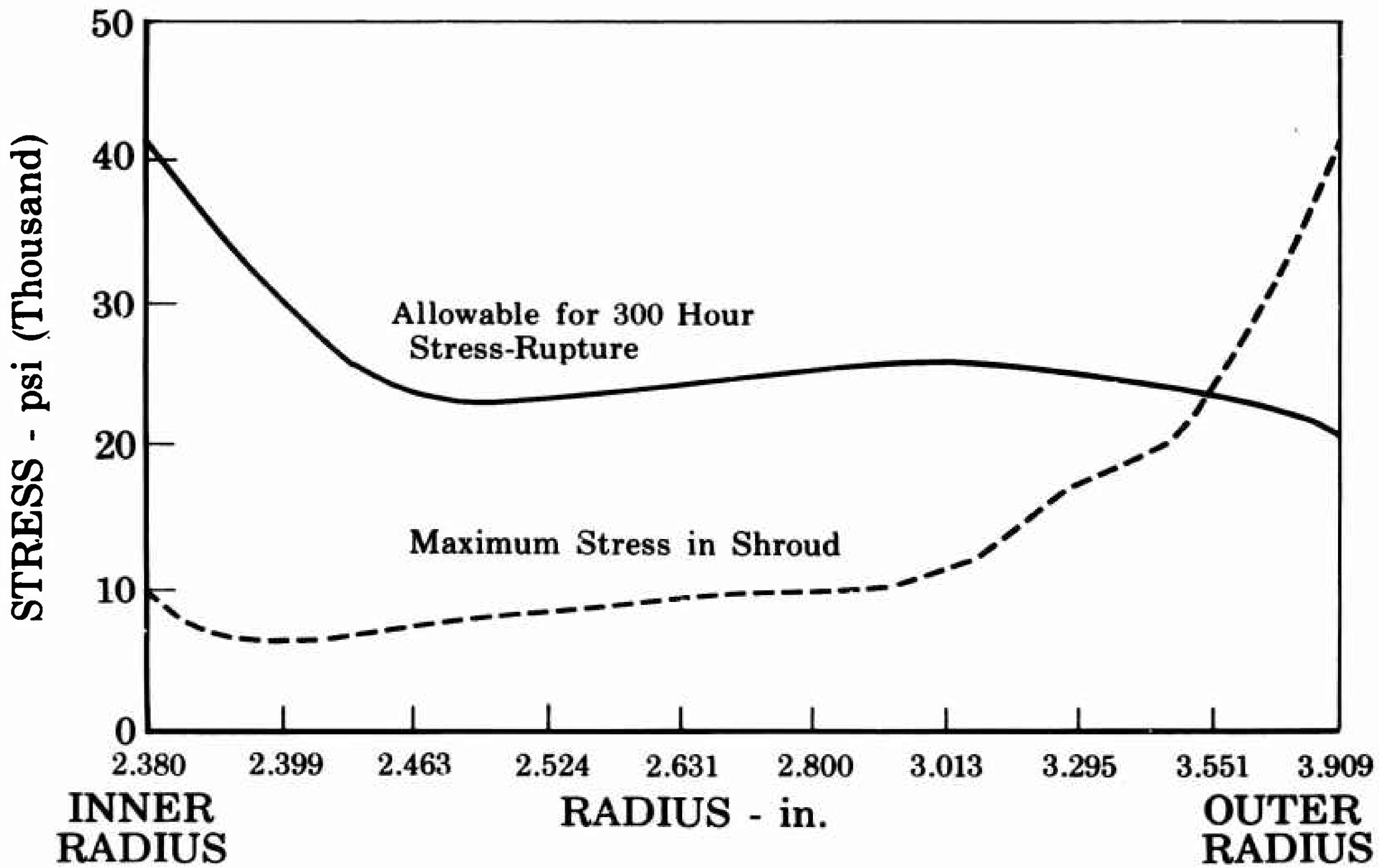

Figure 47. Shroud Stress Distribution at Design Point for Second-Iteration Mechanical Design.

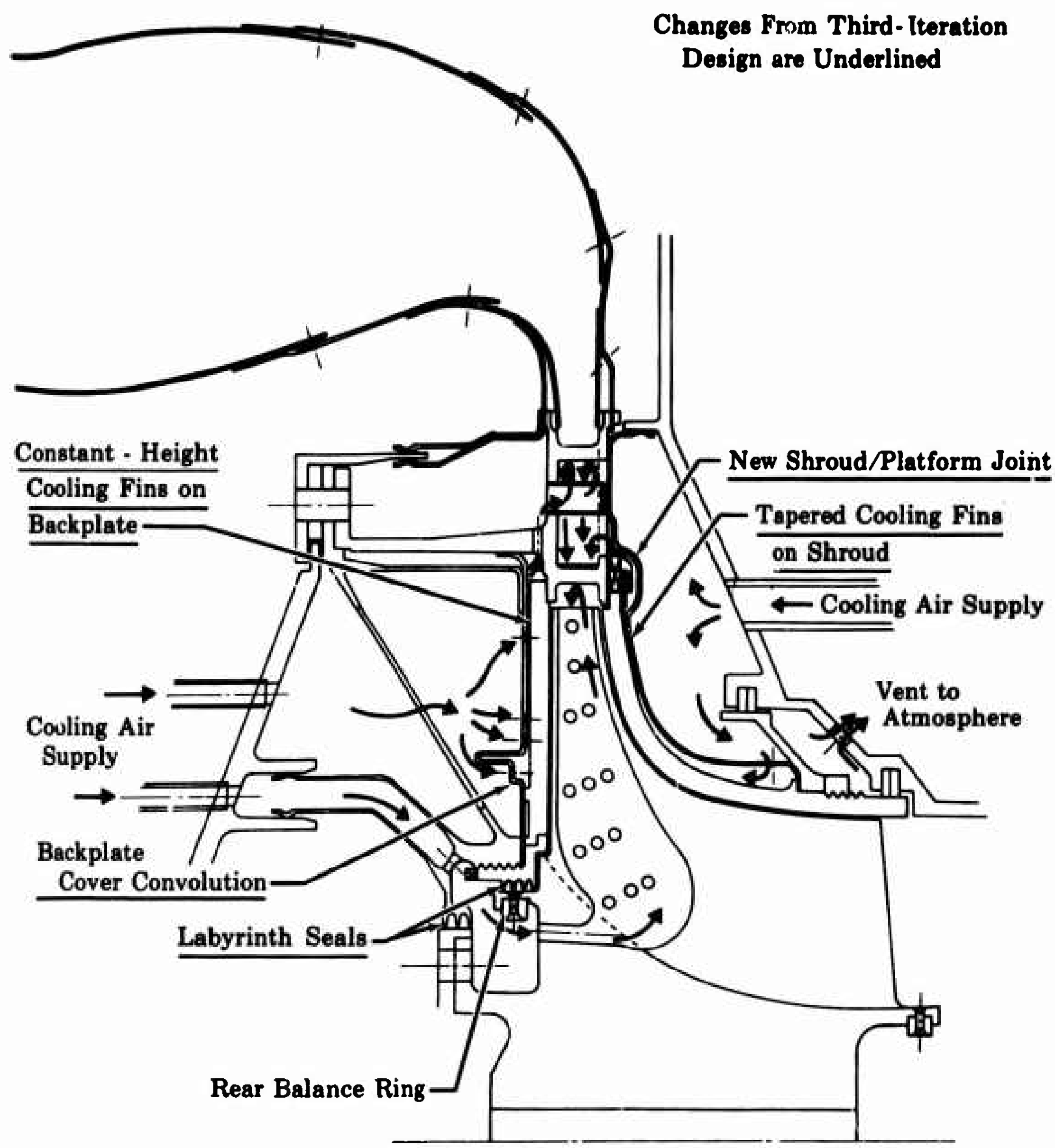

Figure 48. Fourth-Iteration Mechanical Design.

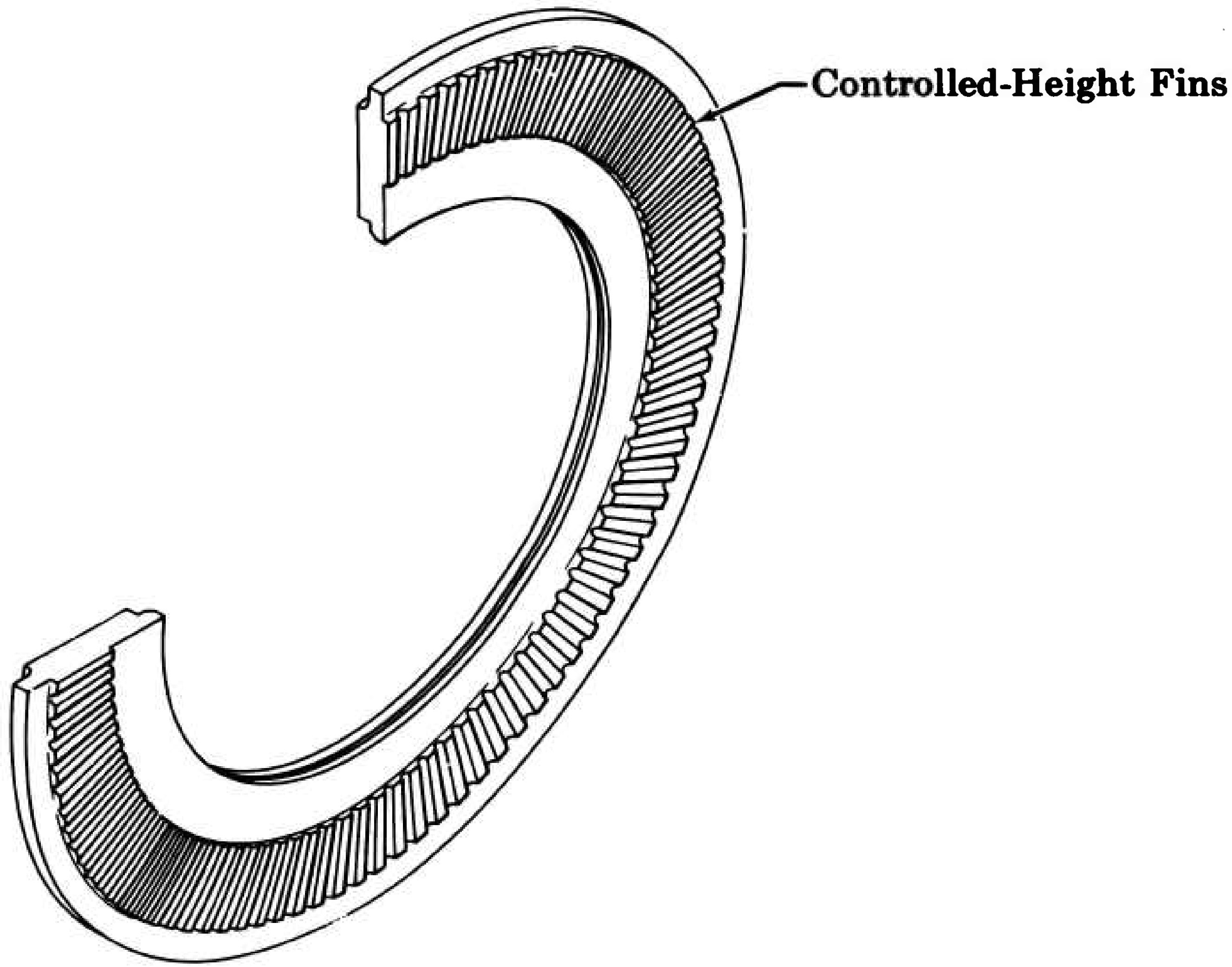

Figure 49. Radial Turbine Backplate.

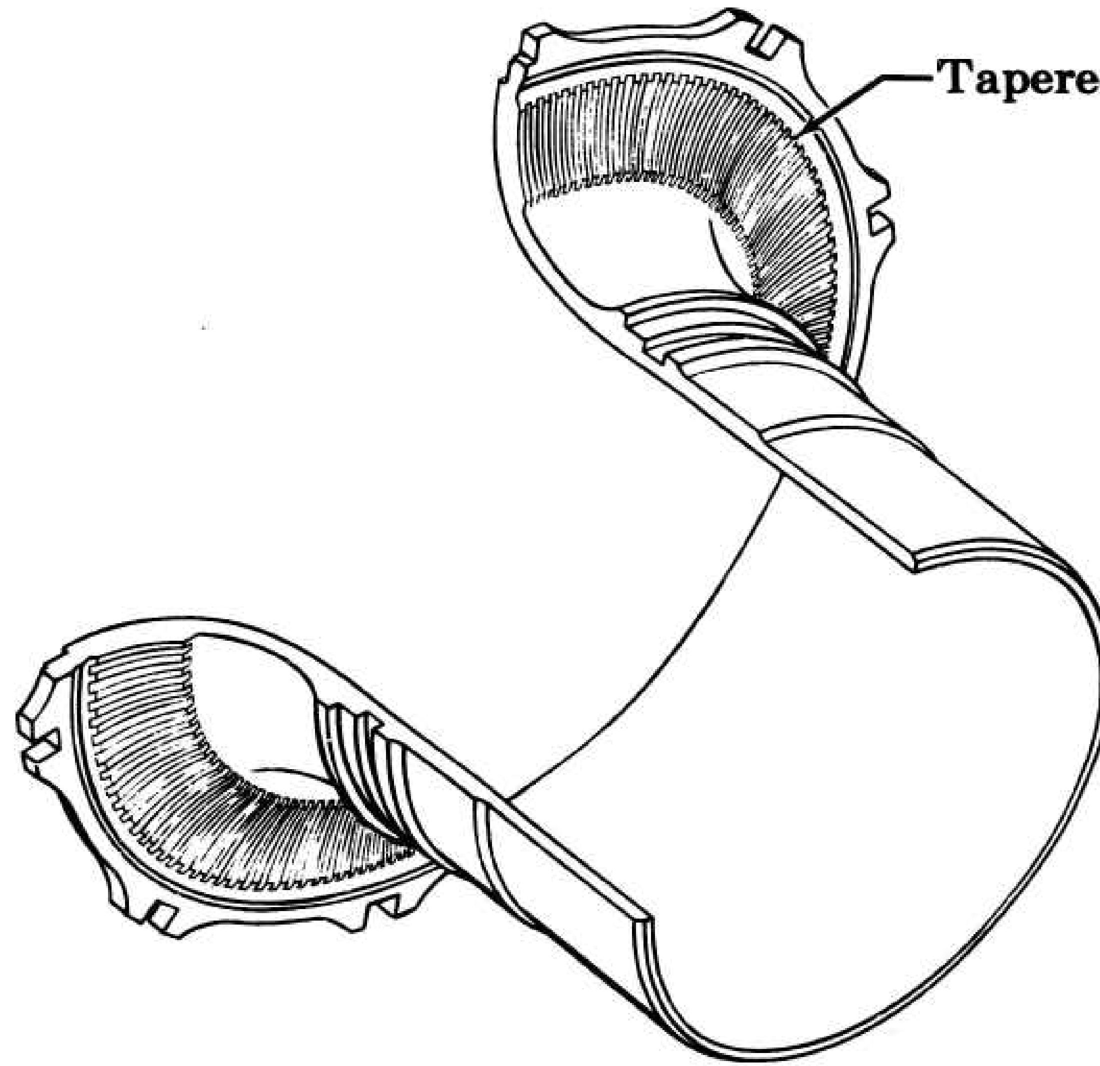

Figure 50. Radial Turbine Shroud.

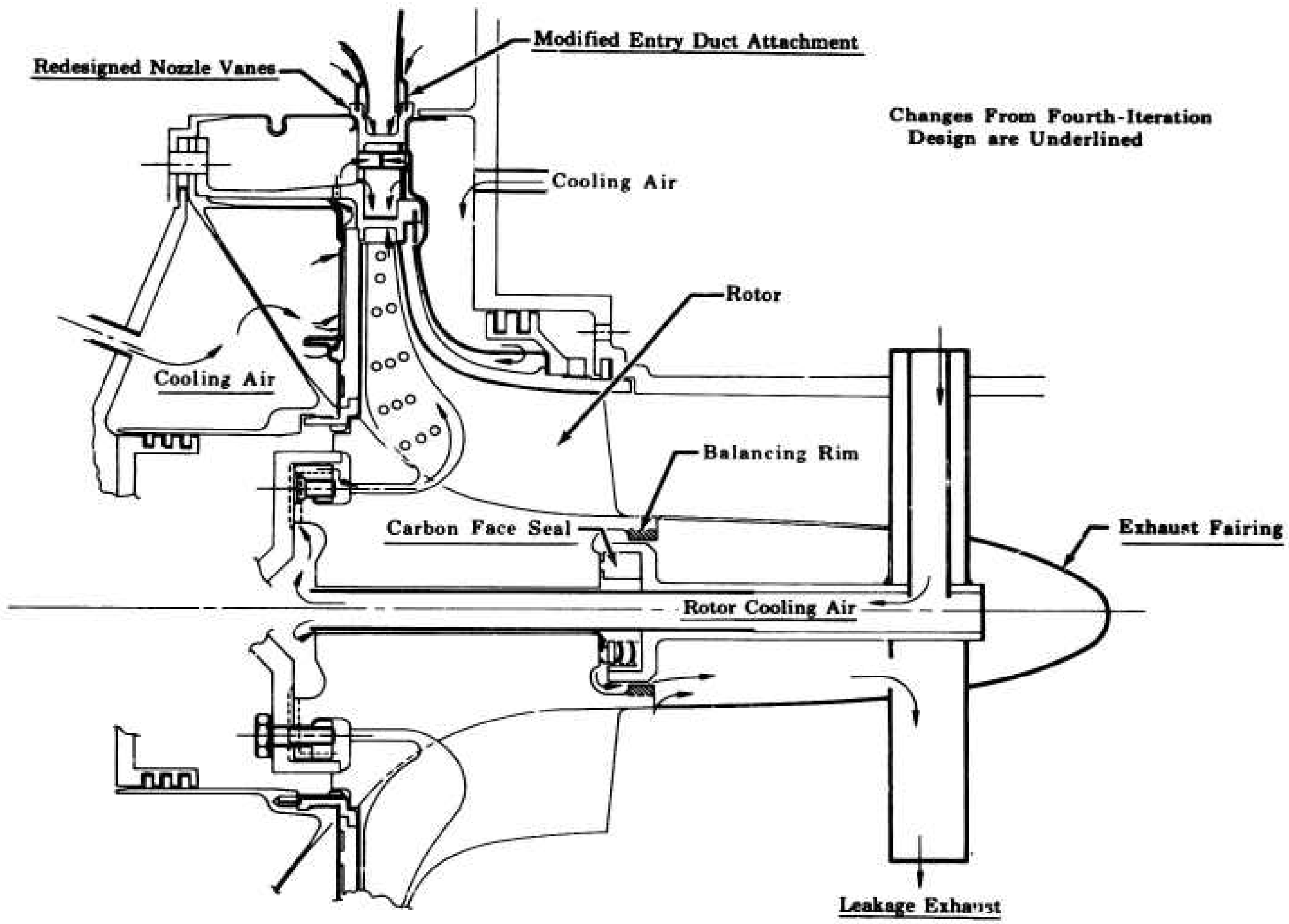

Figure 51. Fifth-Iteration Mechanical Design.

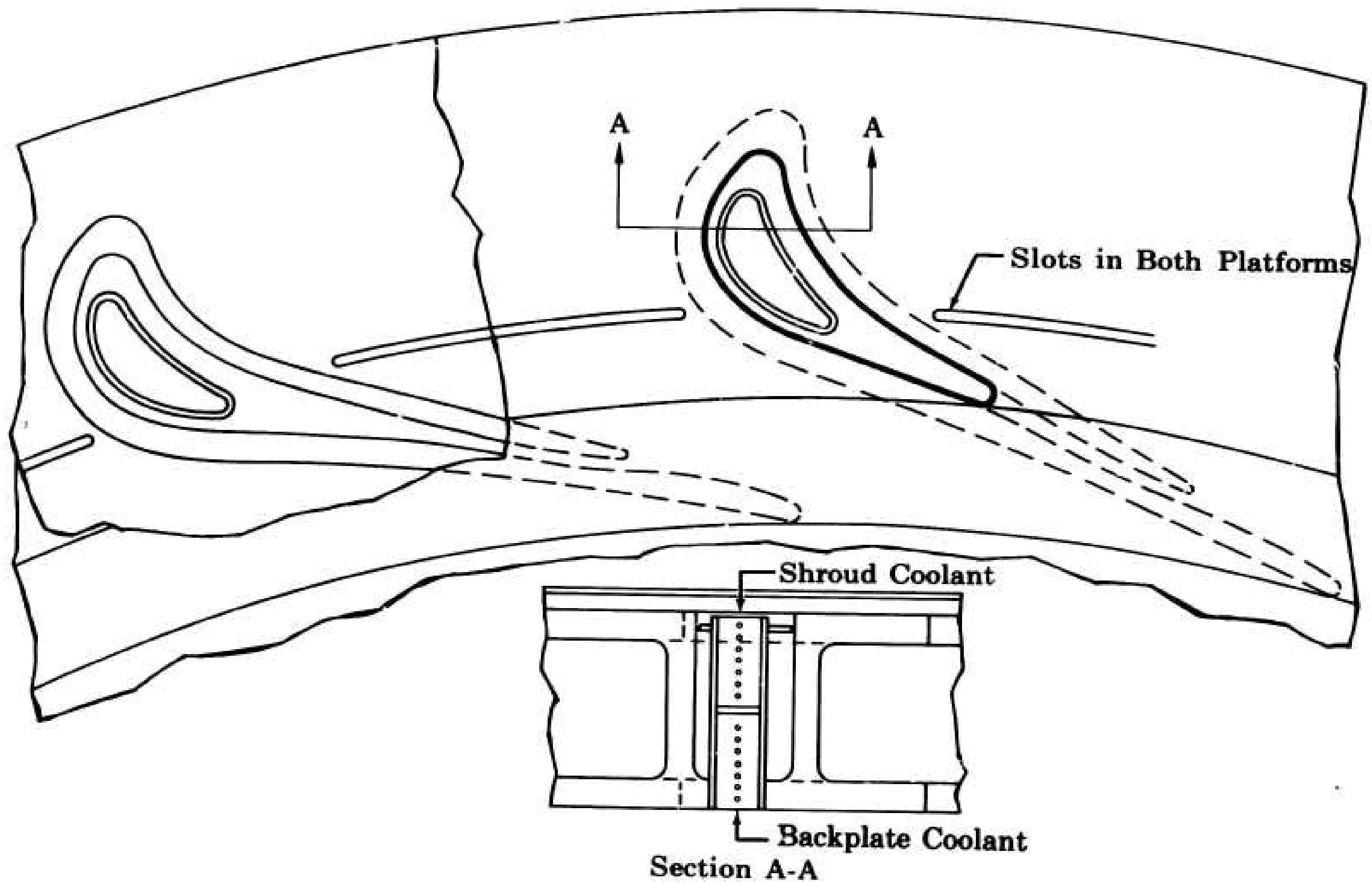

Figure 52. Fifth-Iteration Mechanical Design - Vane Detail.

Changes from Fifth-Iteration Design are Underlined

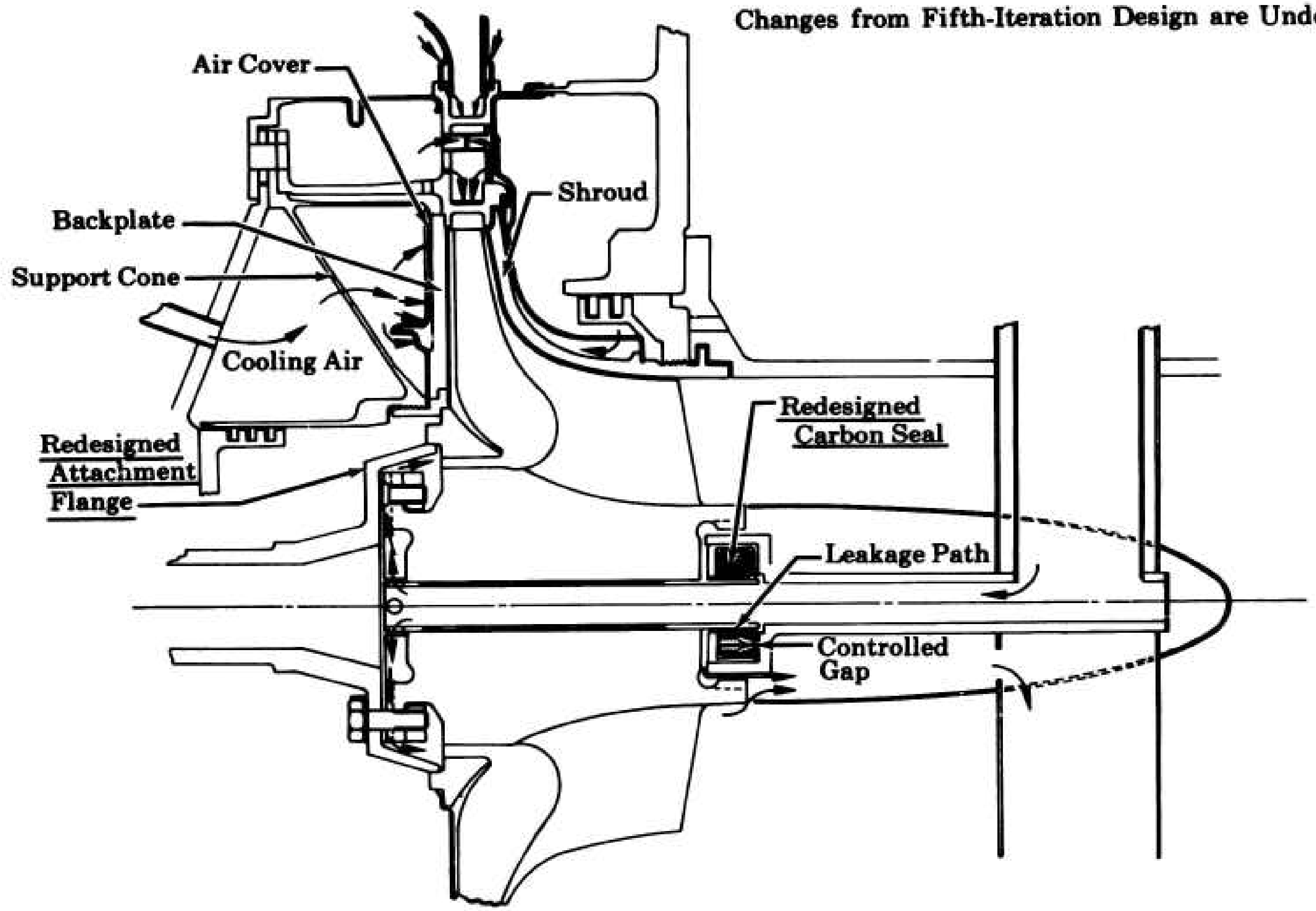

Figure 53. Sixth-Iteration Mechanical Design.

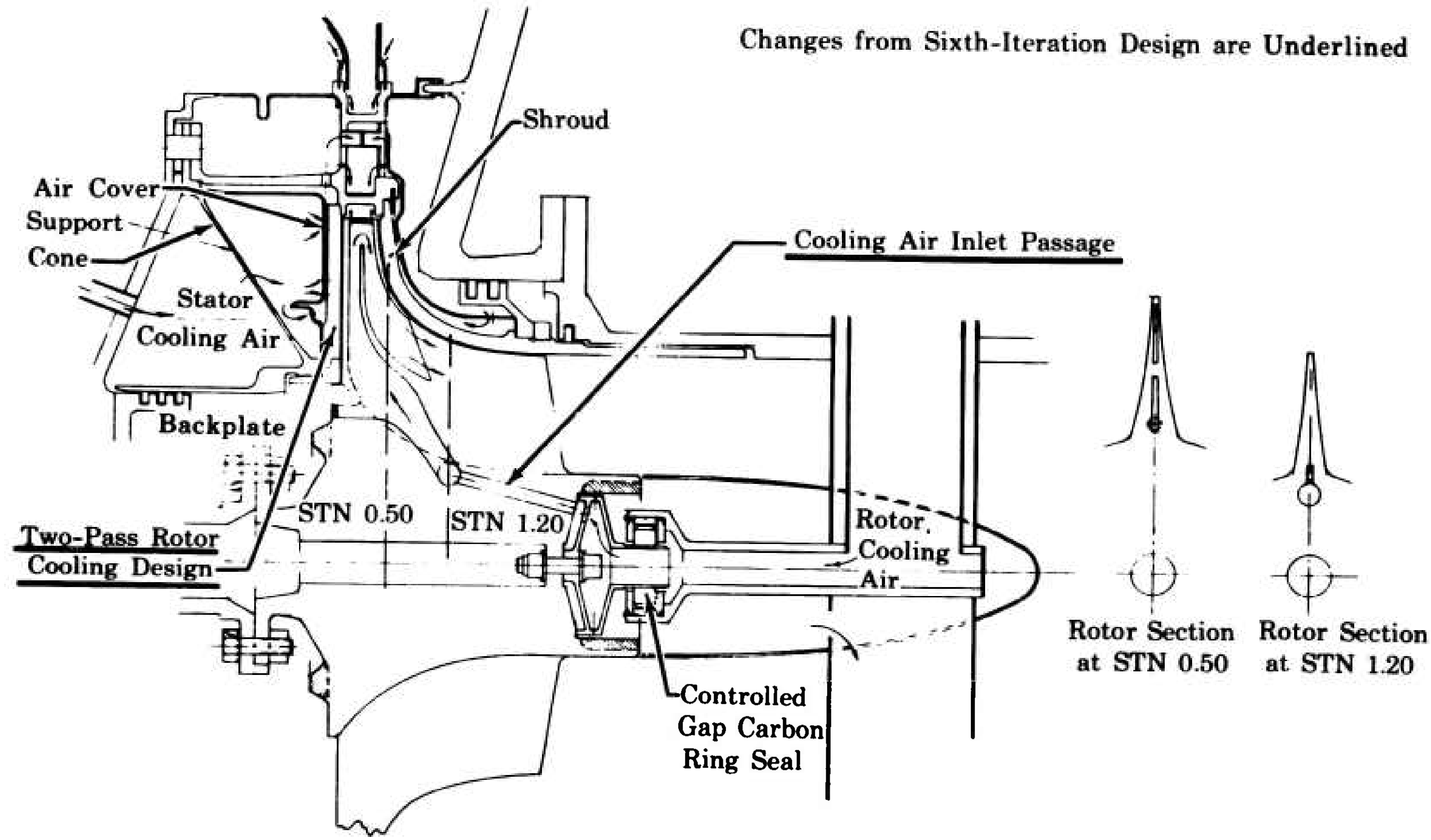

Figure 54. Seventh-Iteration Mechanical Design.

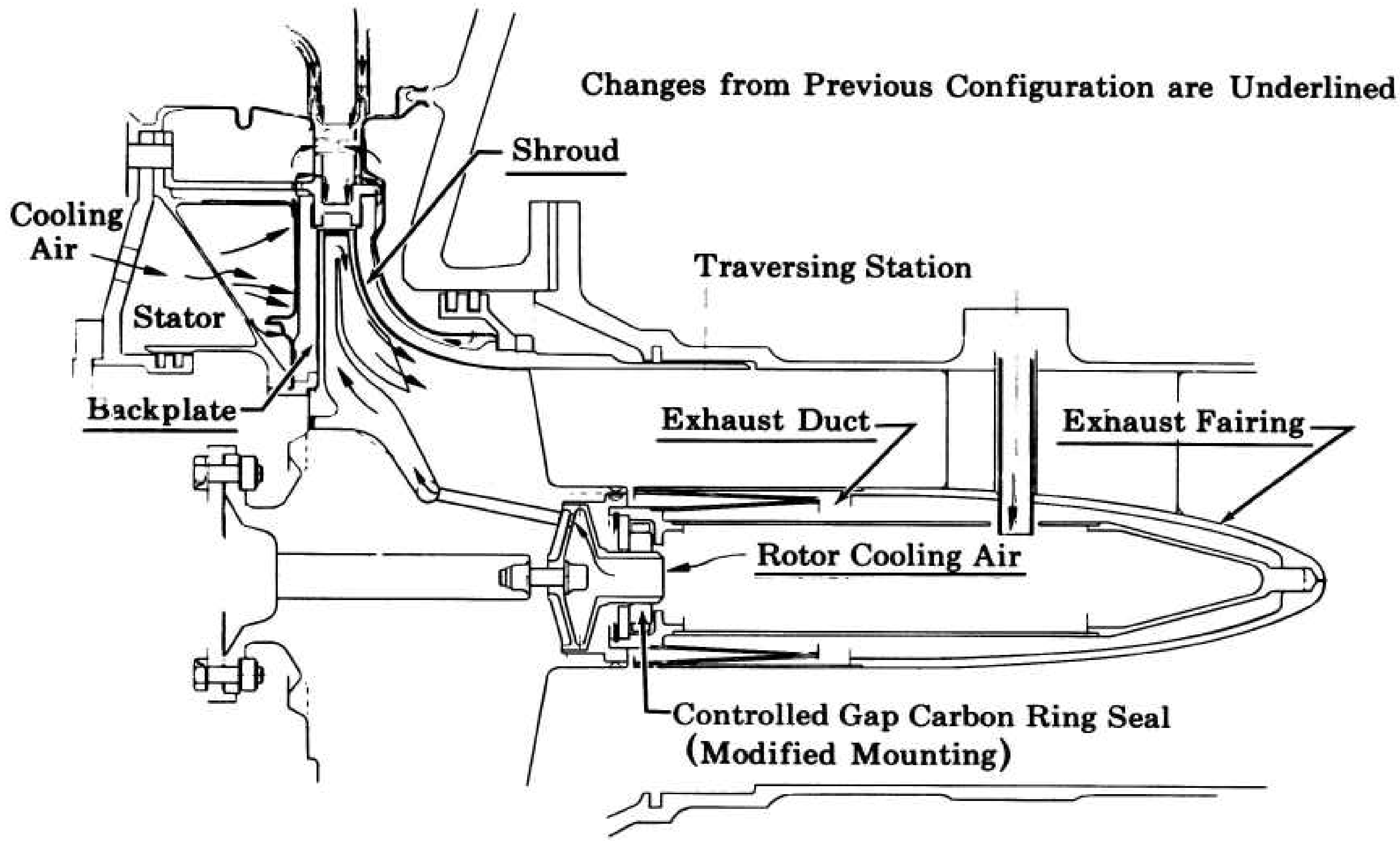

Figure 55. Eighth-Iteration Mechanical Design (Phase I-Final).

CALCULATED STRESSES IN NOZZLE VANE FOR 2300°F TIT.

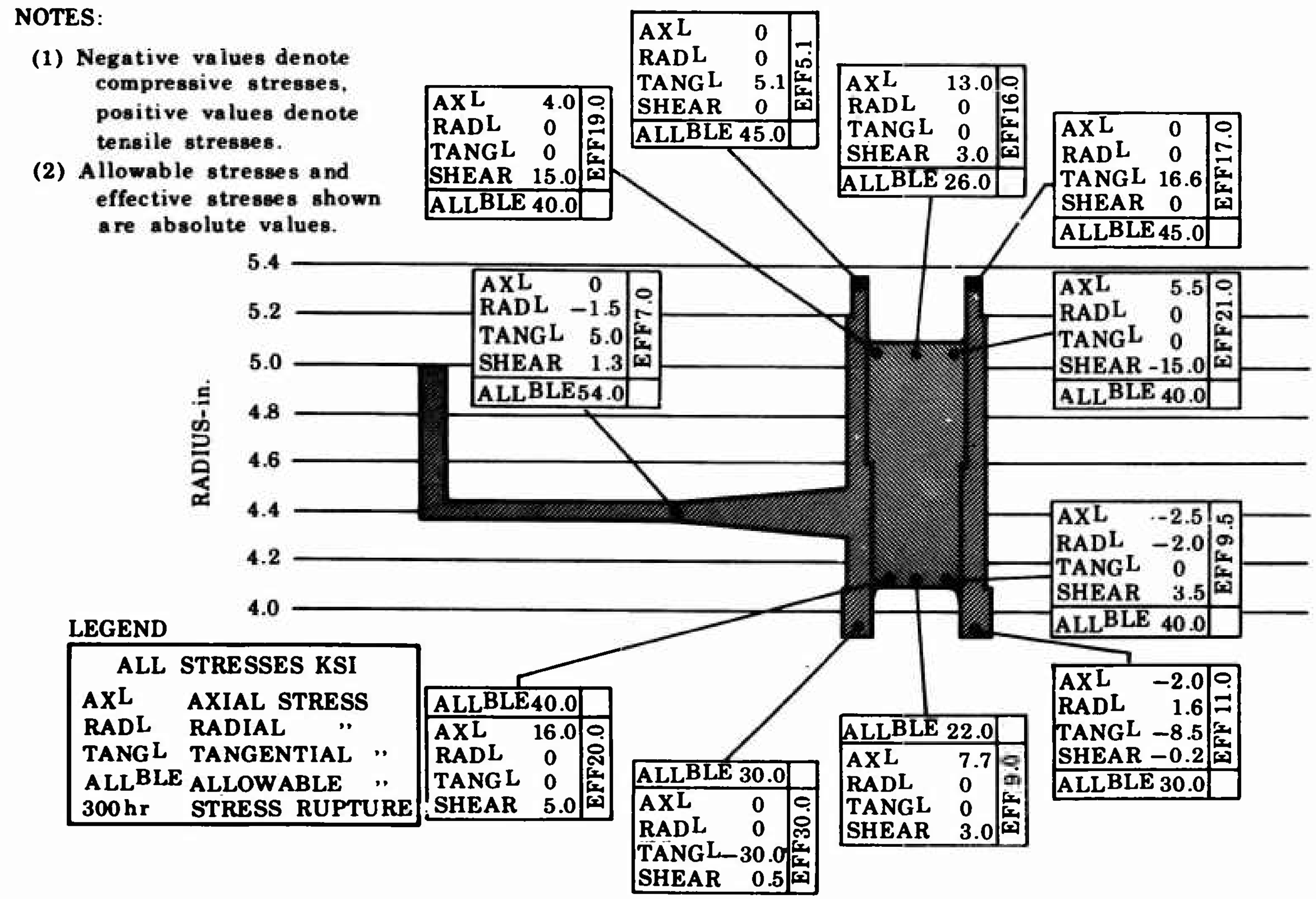

Figure 56. Calculated Stresses in Nozzle Vane.

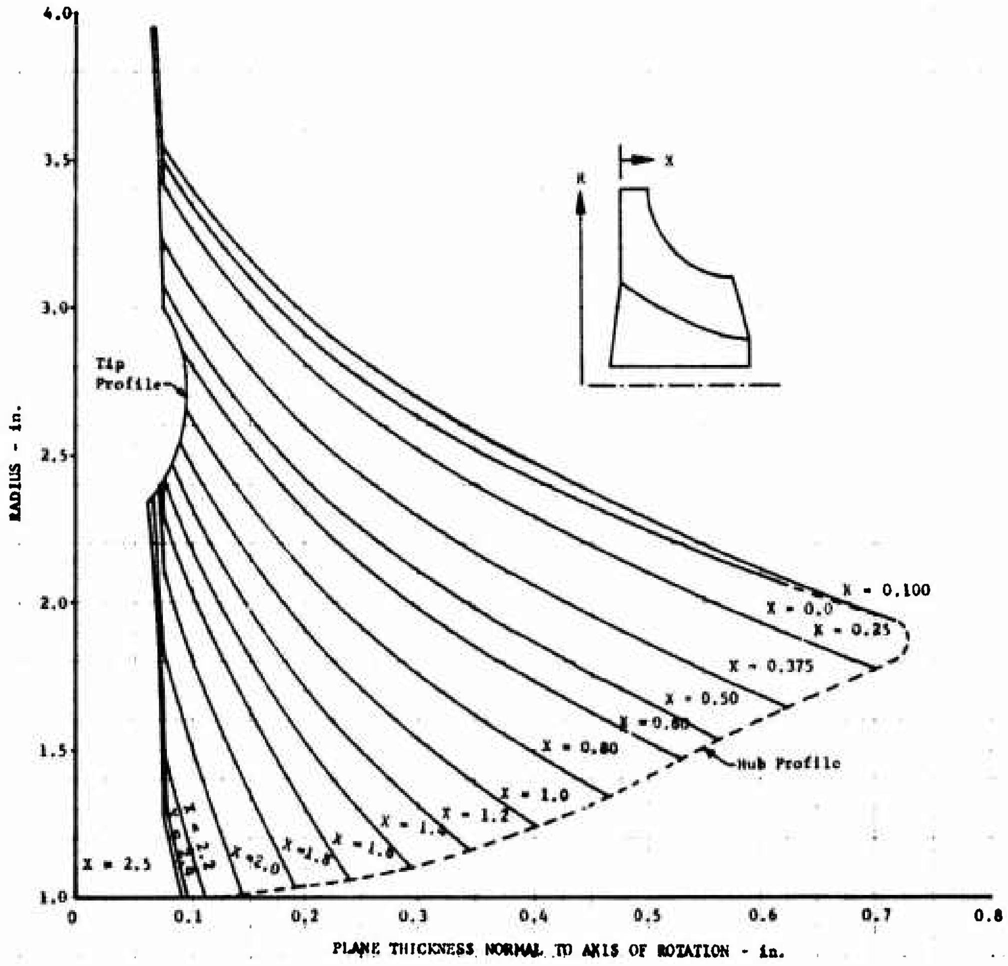

Figure 57. Blade Thickness Distribution for Double-Pass Rotor.

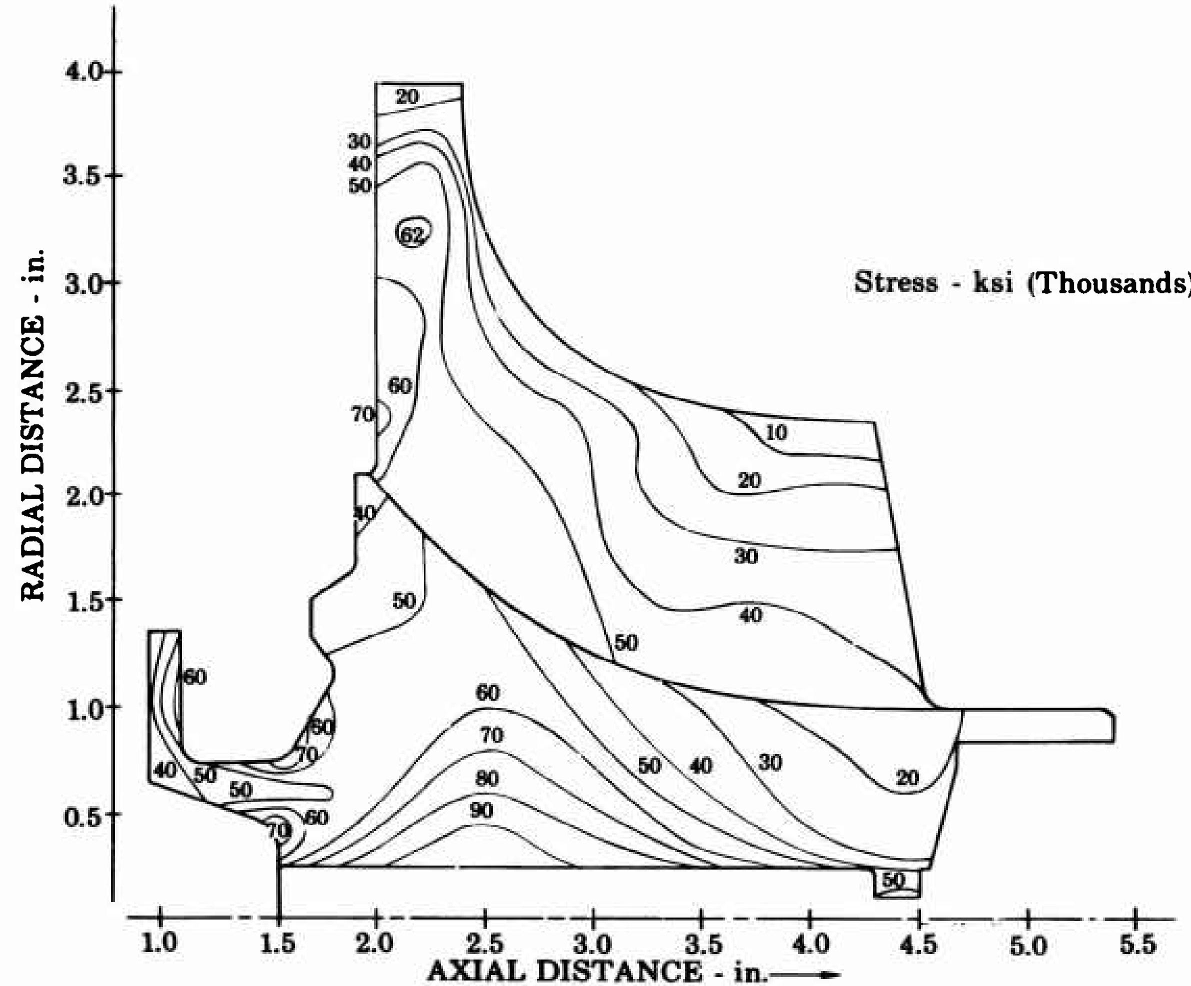

Figure 58. Radial Turbine Effective Isostress at 67,000 rpm.

LINES OF CONSTANT $\sigma e/\sigma ALL.$ AT 87,100 RPM (130% OVERSPEED) AFTER PLASTIC REDISTRIBUTION

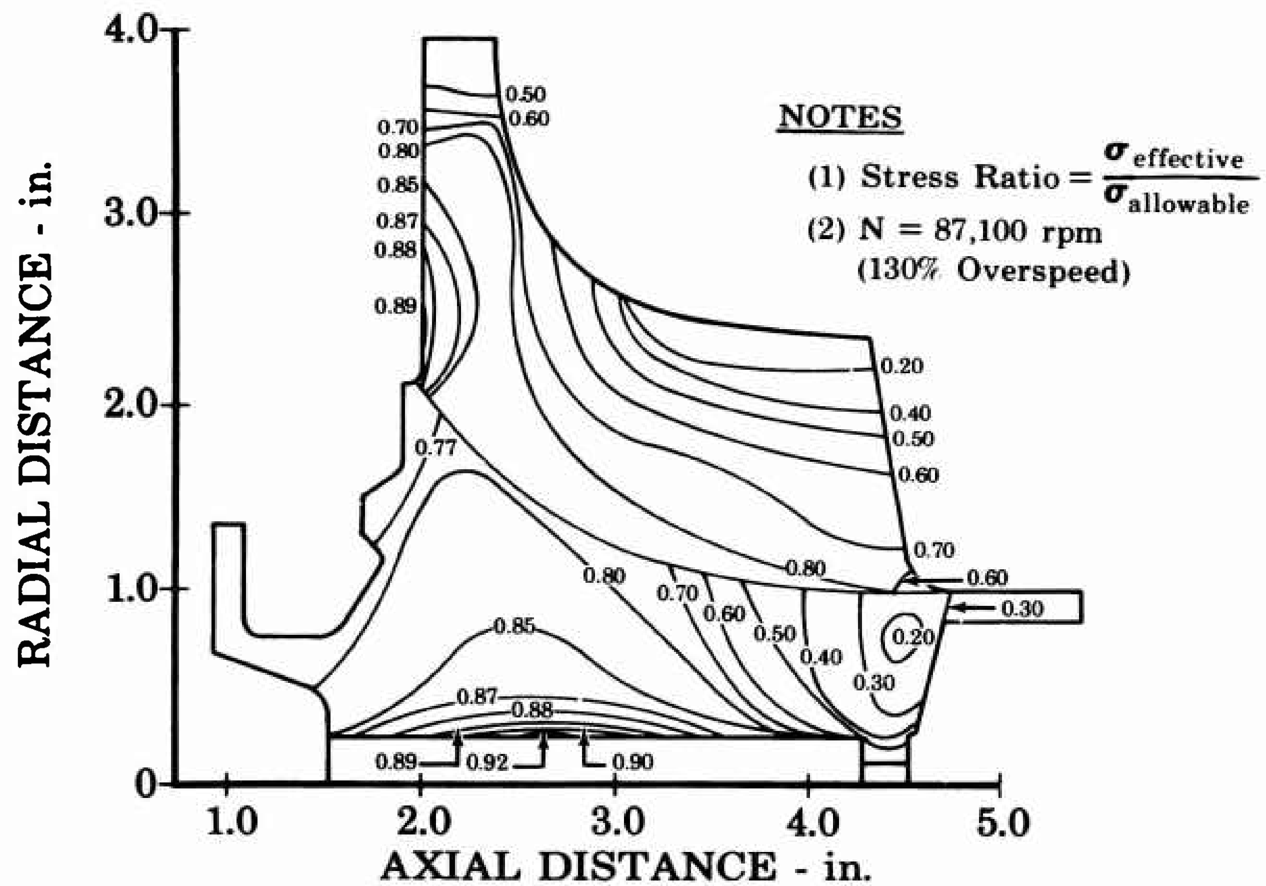

Figure 59. Stress Ratio Distribution After Plastic Redistribution.

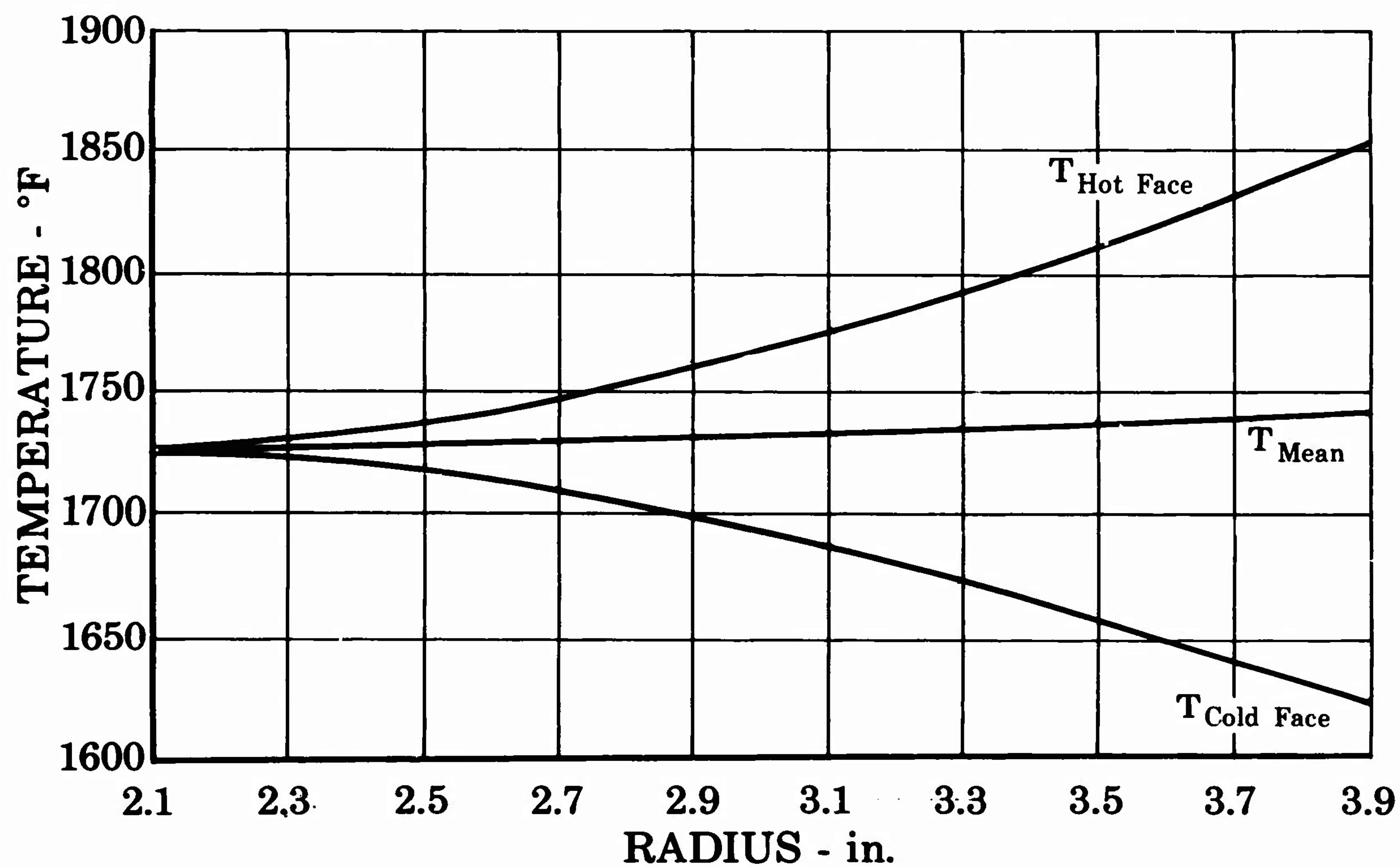

Figure 60. Backplate Hot and Cold Surface and Mean Temperature Distribution.

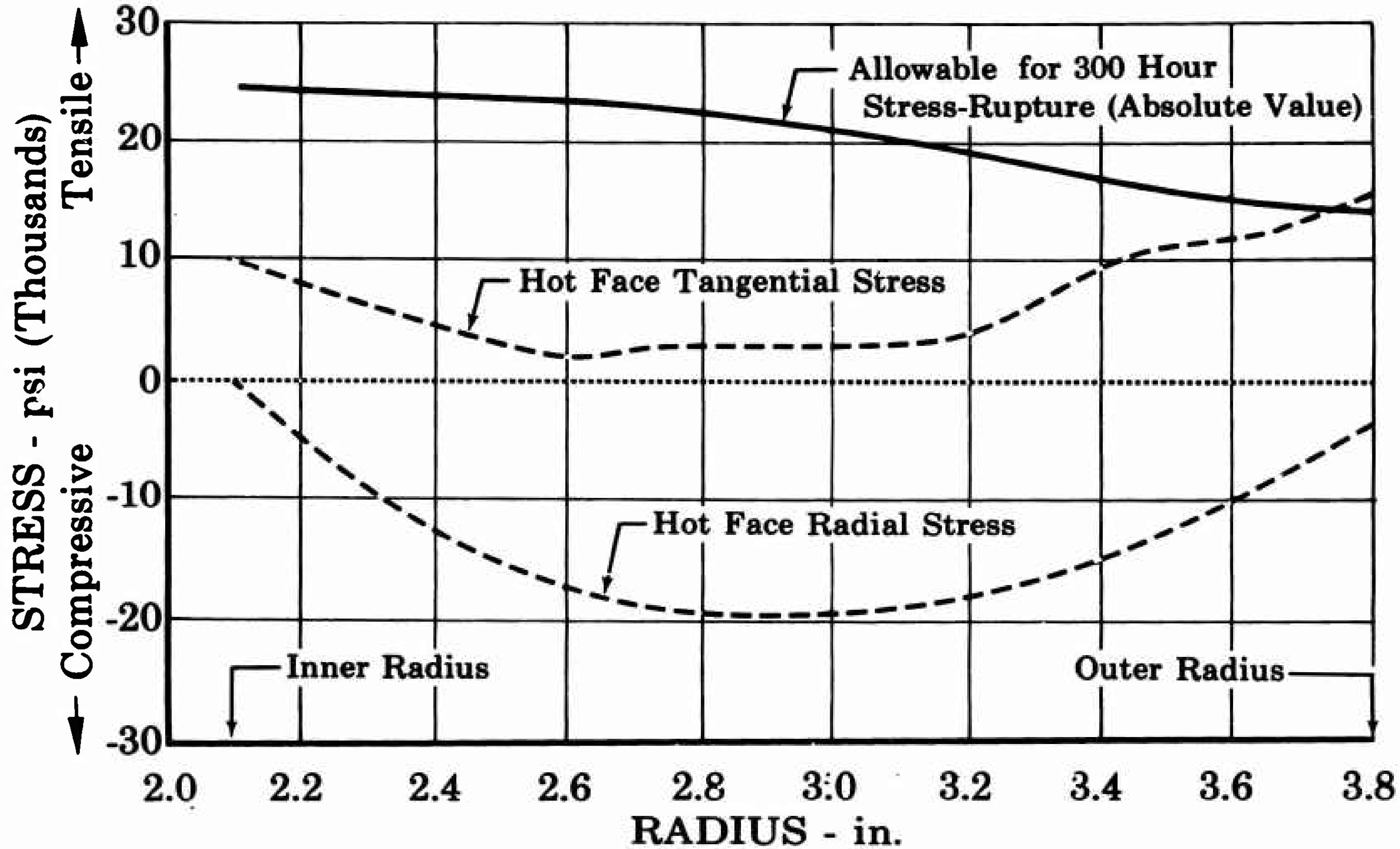

Figure 61. Backplate Stress Distribution.

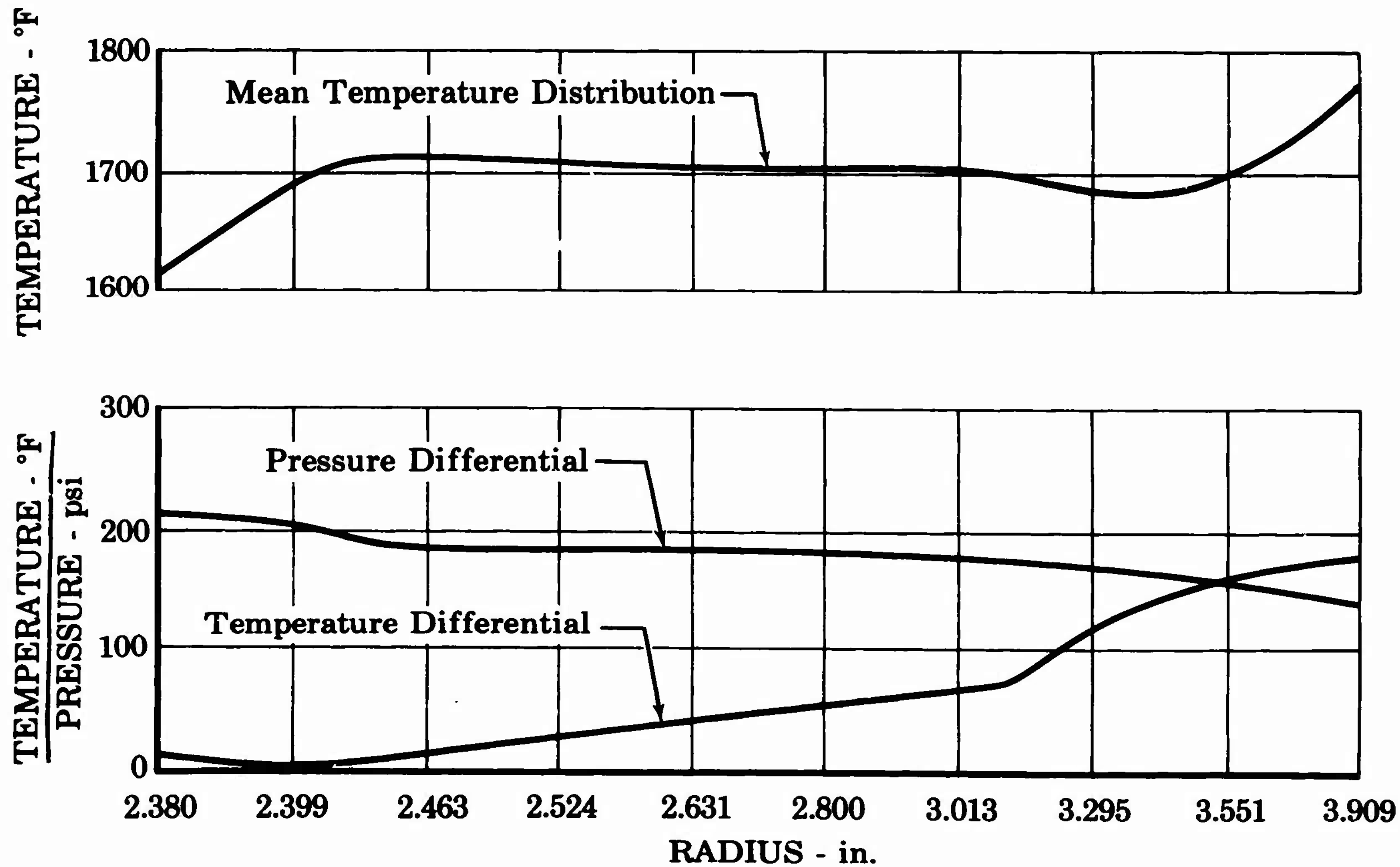

Figure 62. Shroud Temperature and Pressure Conditions at Design Point.

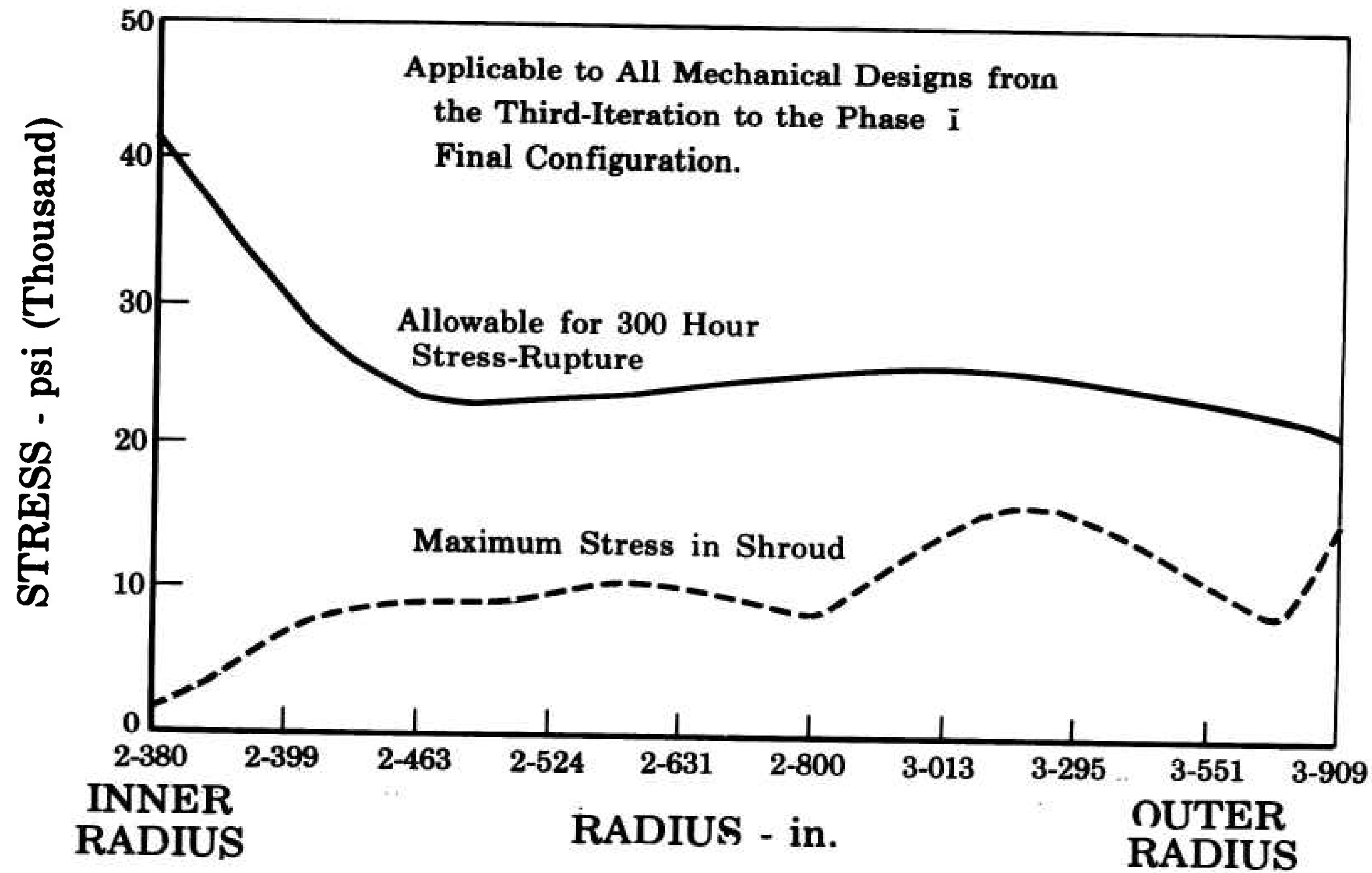

Figure 63. Shroud Stress Distribution at Design Point.

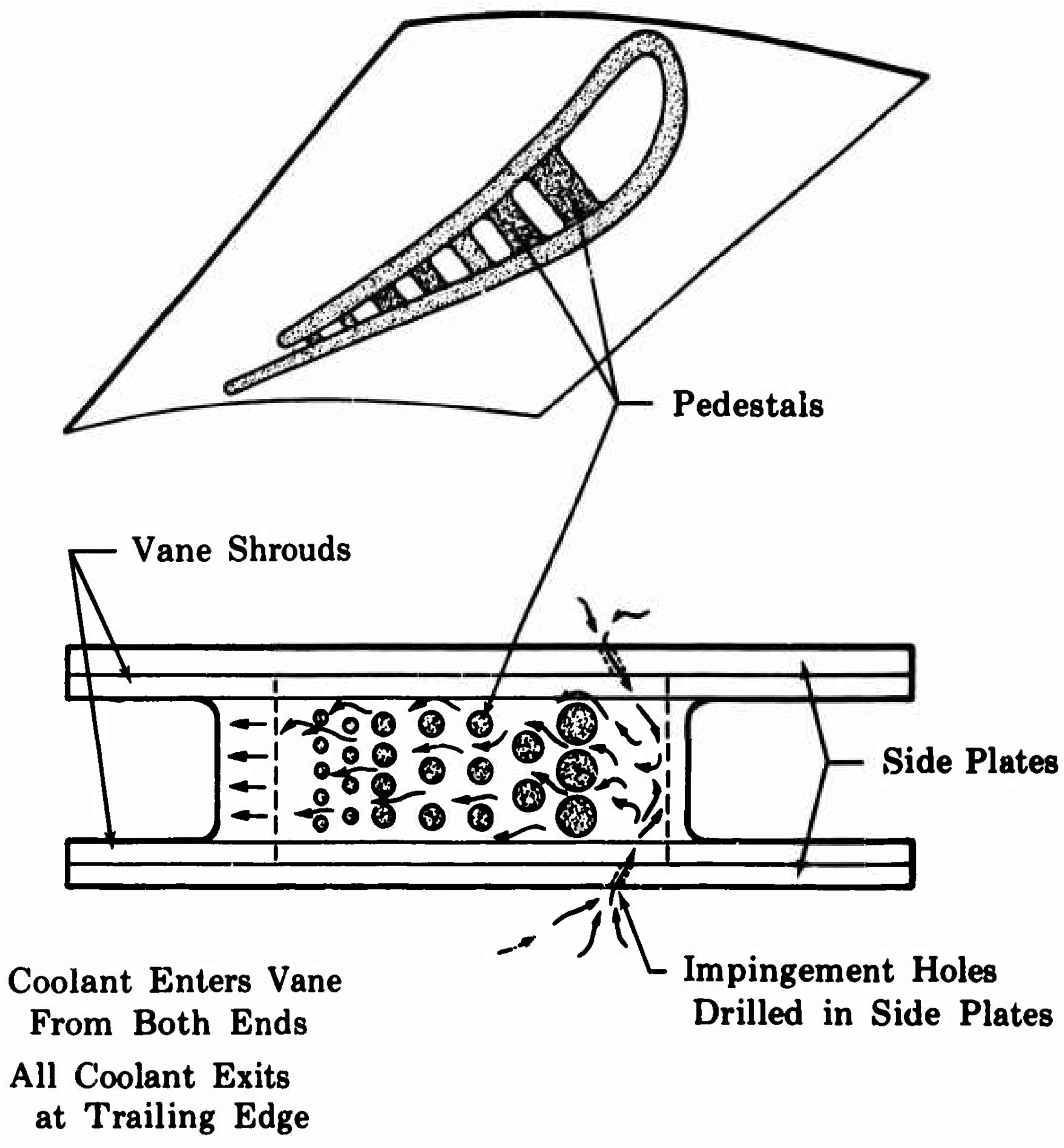

Figure 64. Original Nozzle Guide Vane Cooling Scheme.

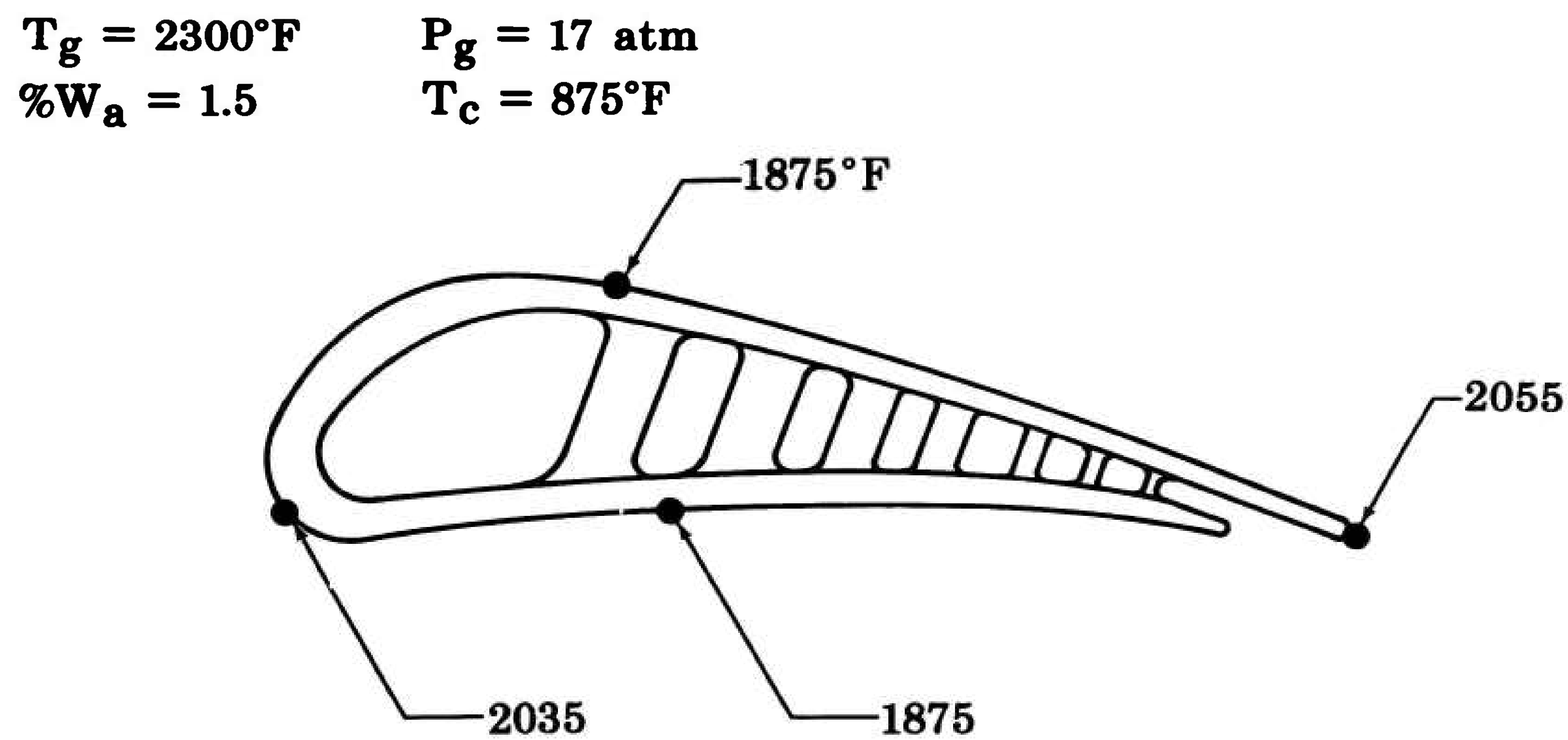

Figure 65. Original Nozzle Guide Vane Temperature Distribution.

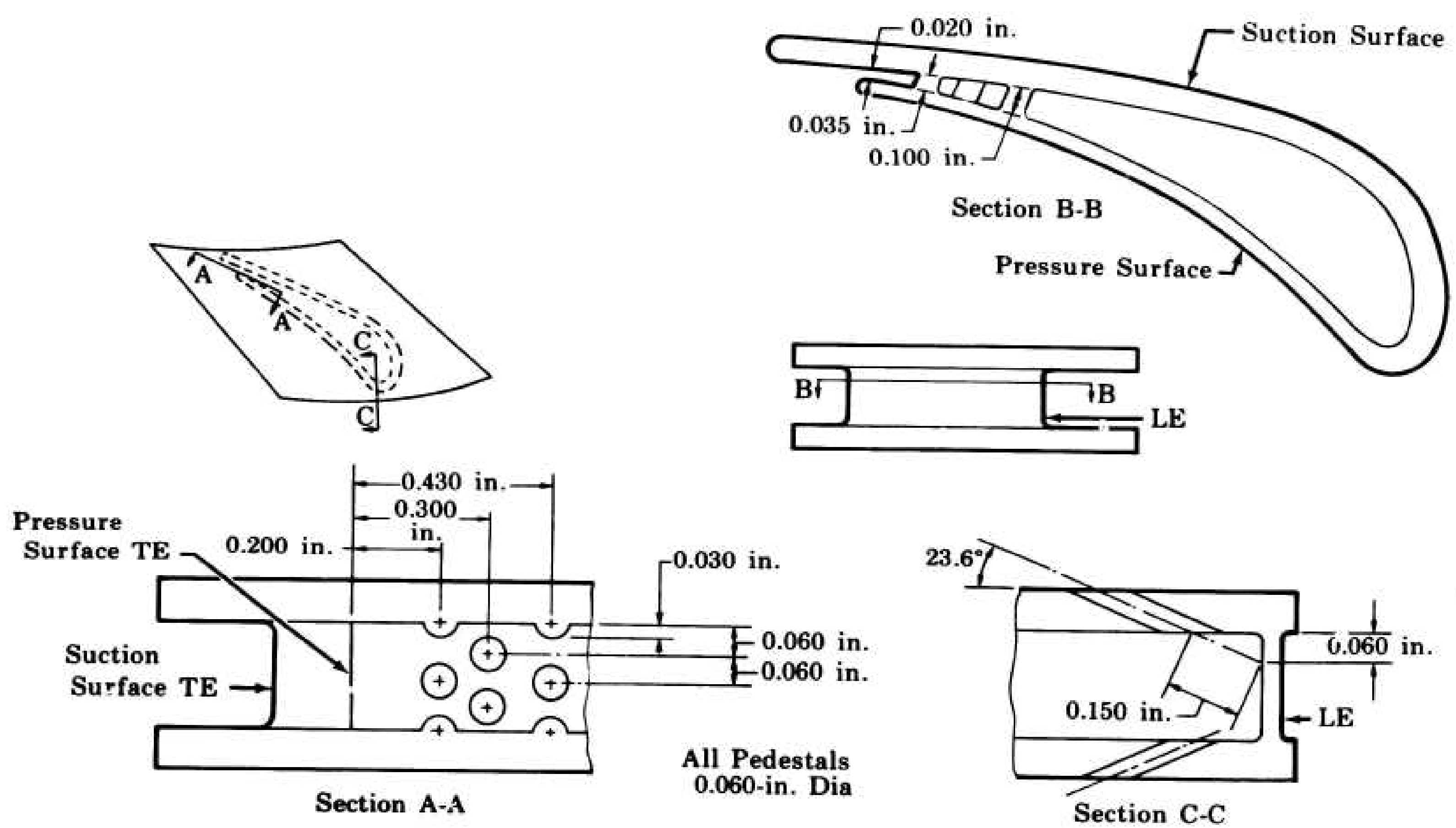

Figure 66. First-Iteration Nozzle Heat Transfer Design.

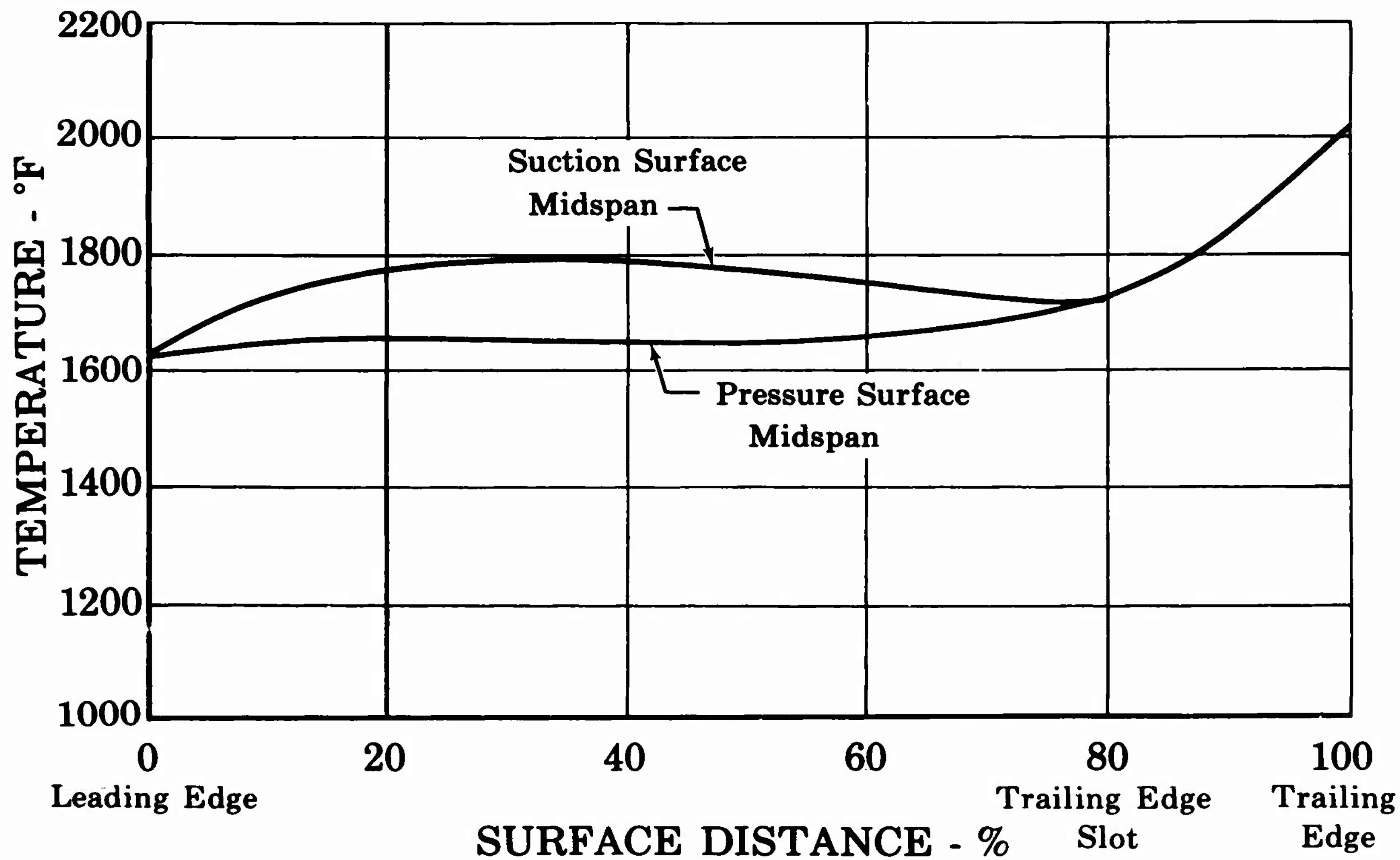

Figure 67. Estimated Temperature Distribution of First-Iteration Nozzle Heat Transfer Design.

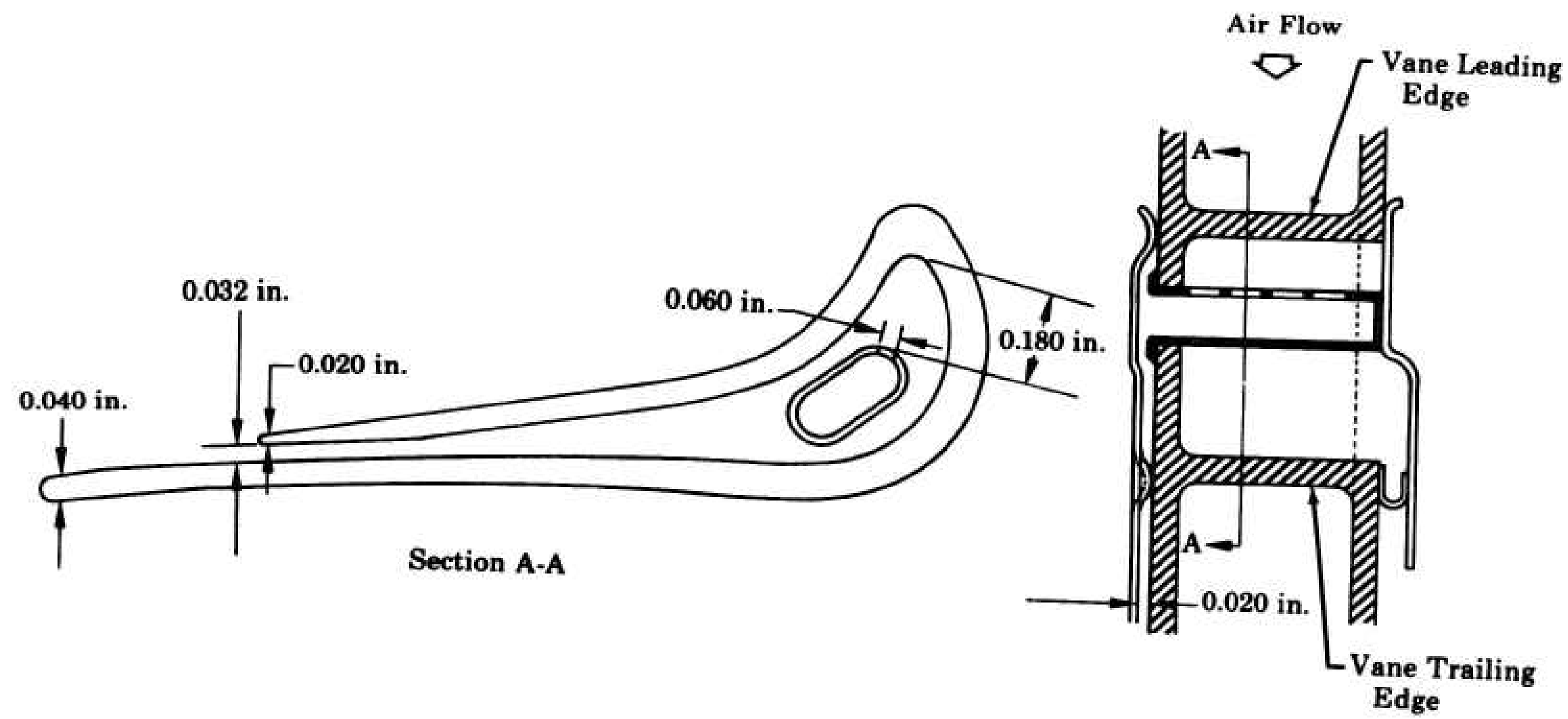

Figure 68. Second-Iteration Nozzle Heat Transfer Design.

HIGH TEMPERATURE RADIAL TURBINE VANE

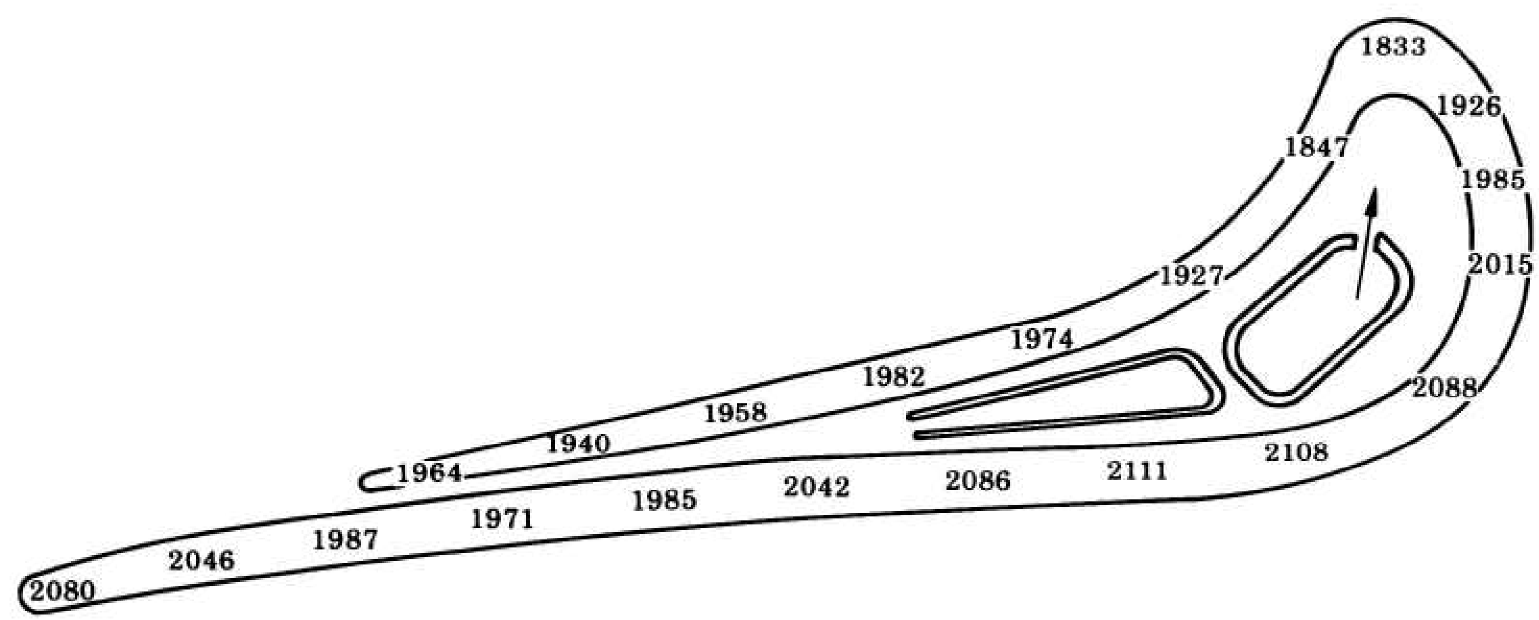

Figure 69. Third-Iteration Nozzle Heat Transfer Design (Calculated Metal Temperatures in °F).

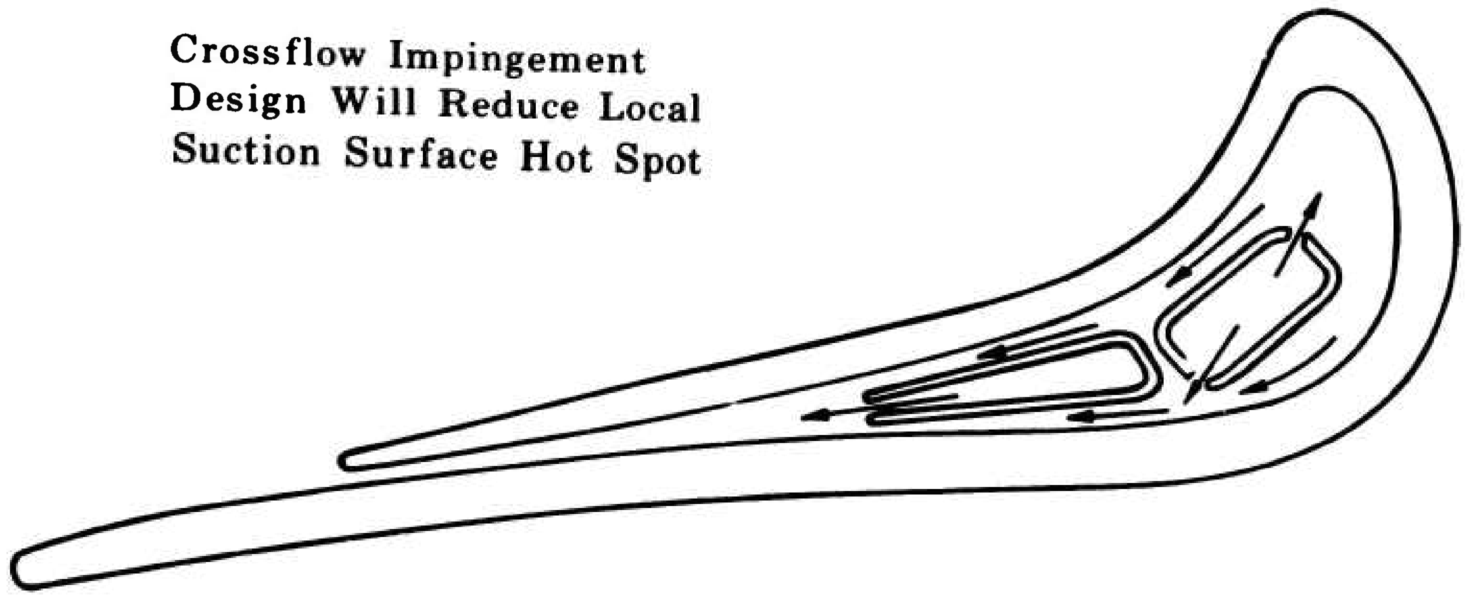

Figure 70. Fourth-Iteration Nozzle Heat Transient Design.

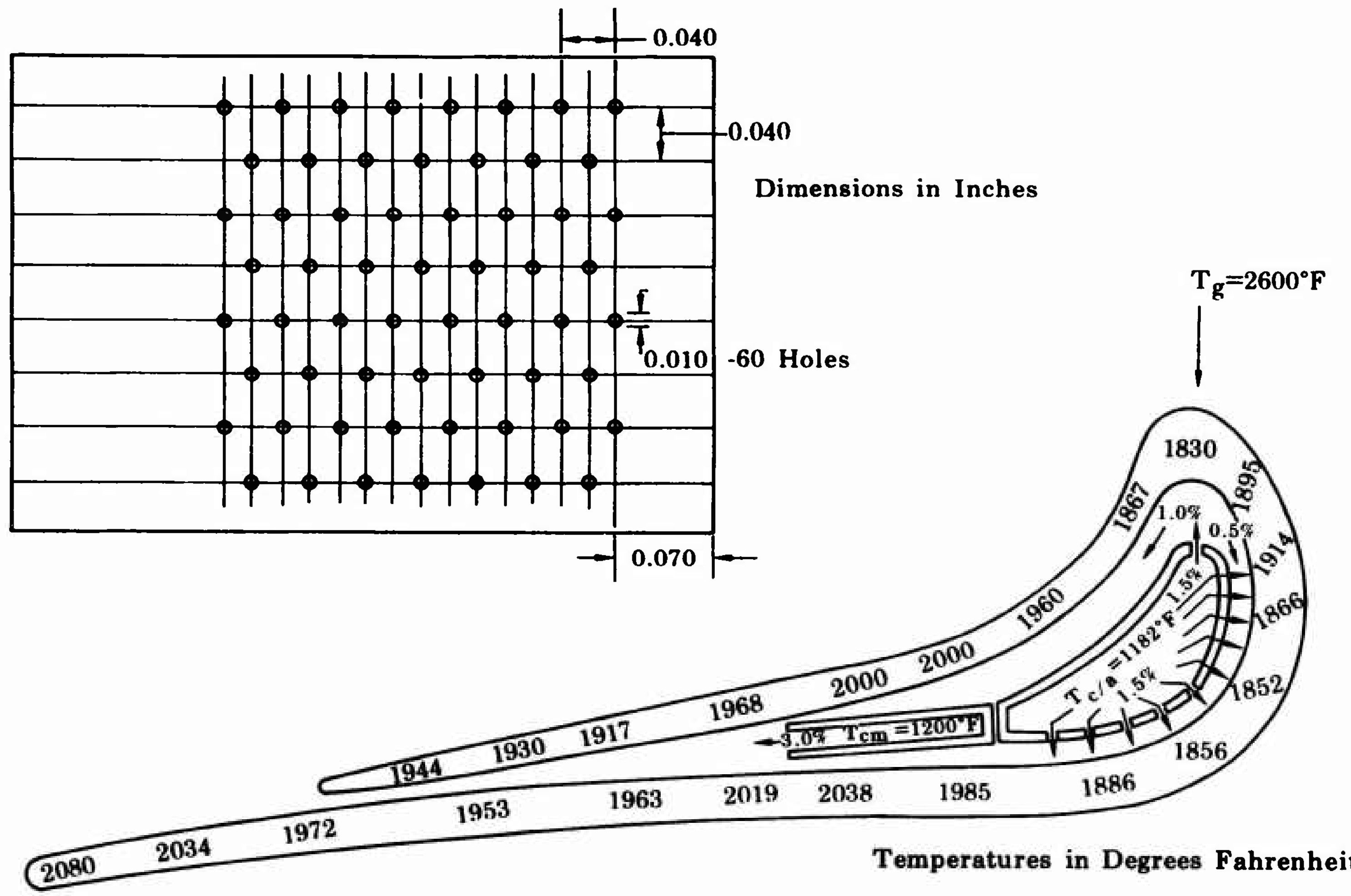

Figure 71. Fifth-Iteration Nozzle Heat Transfer Design.

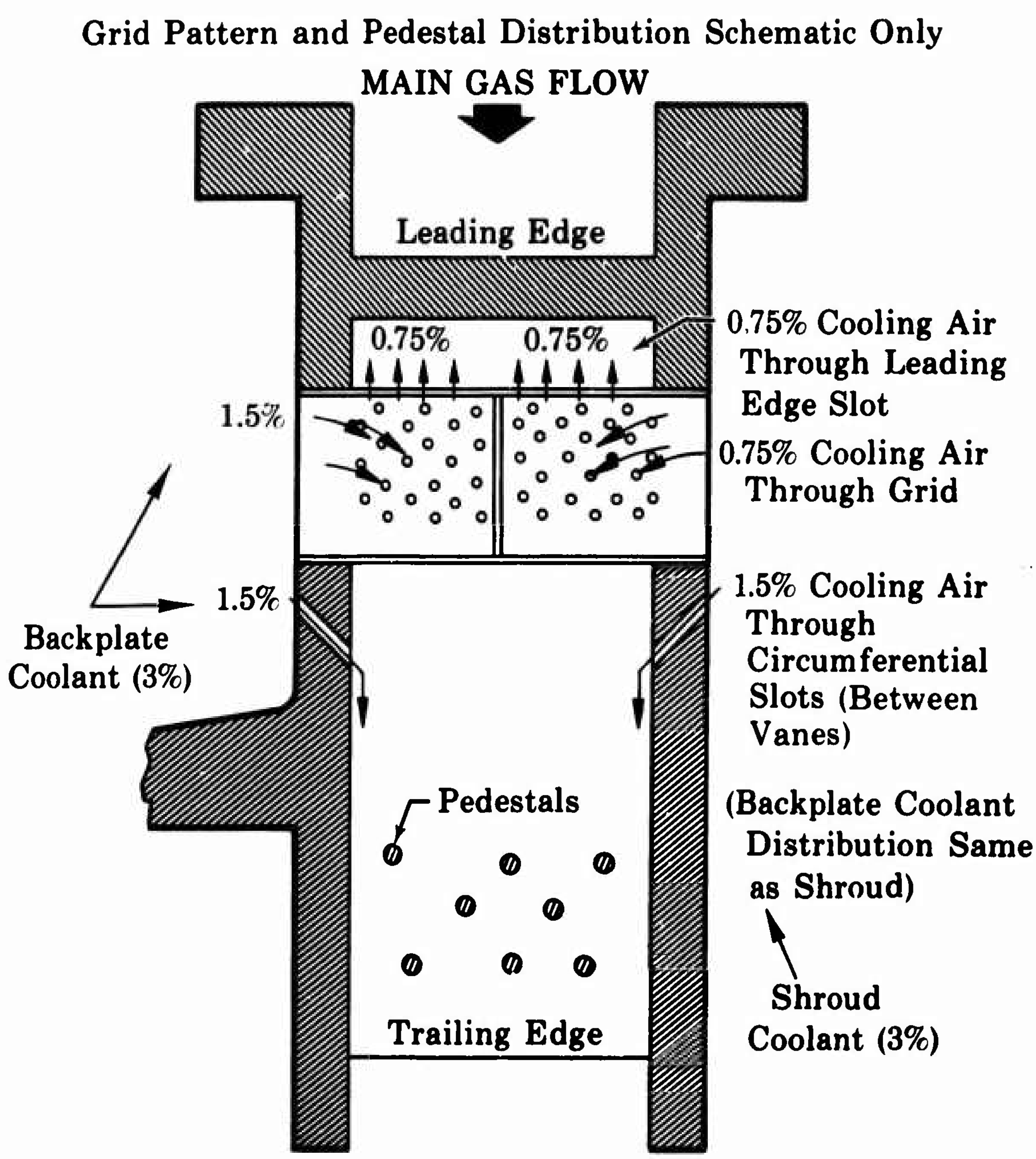

Figure 72. Sixth-Iteration Nozzle Heat Transfer Design.

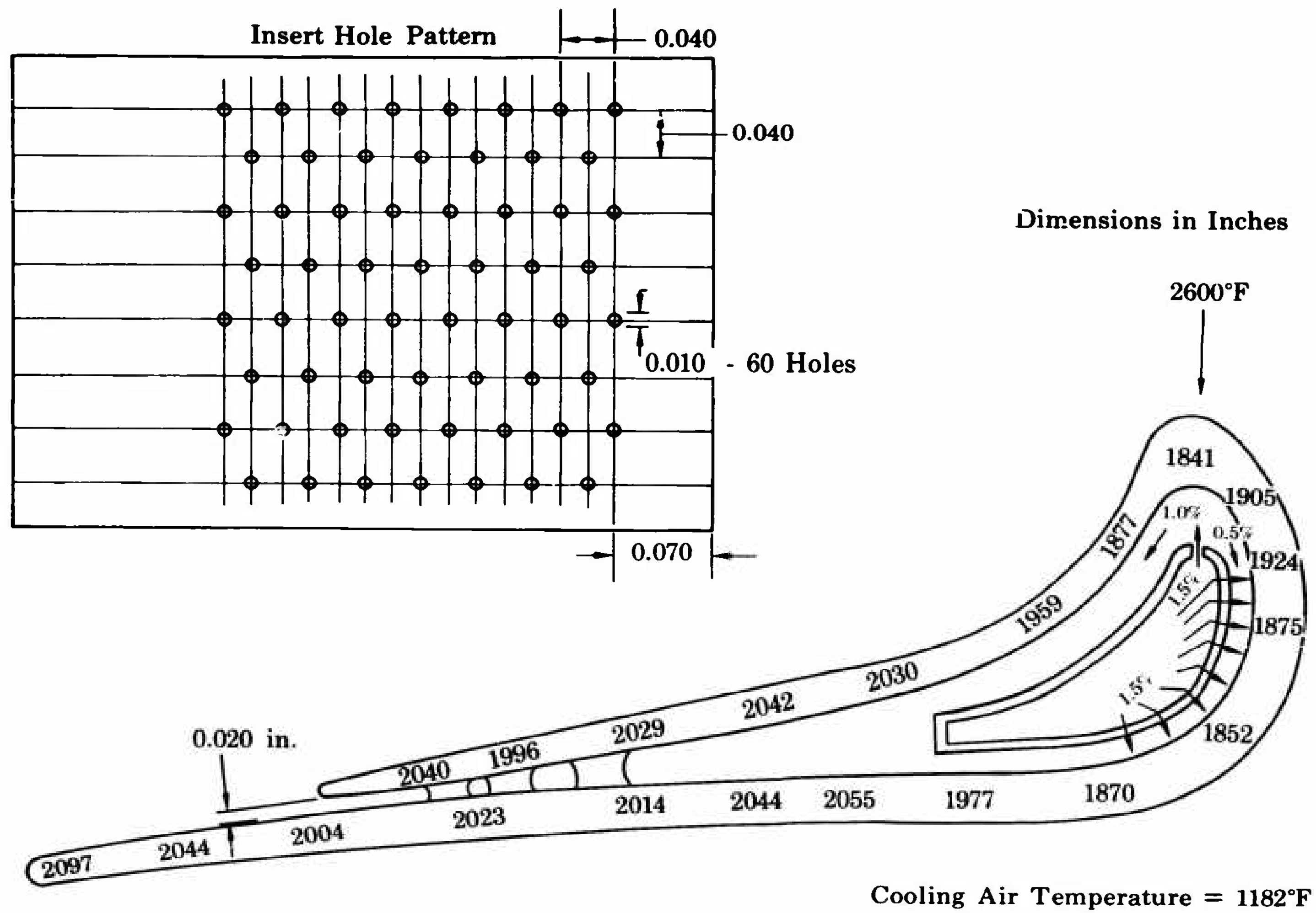

Figure 73. Metal Temperature for Sixth-Iteration Nozzle Heat Transfer Design.

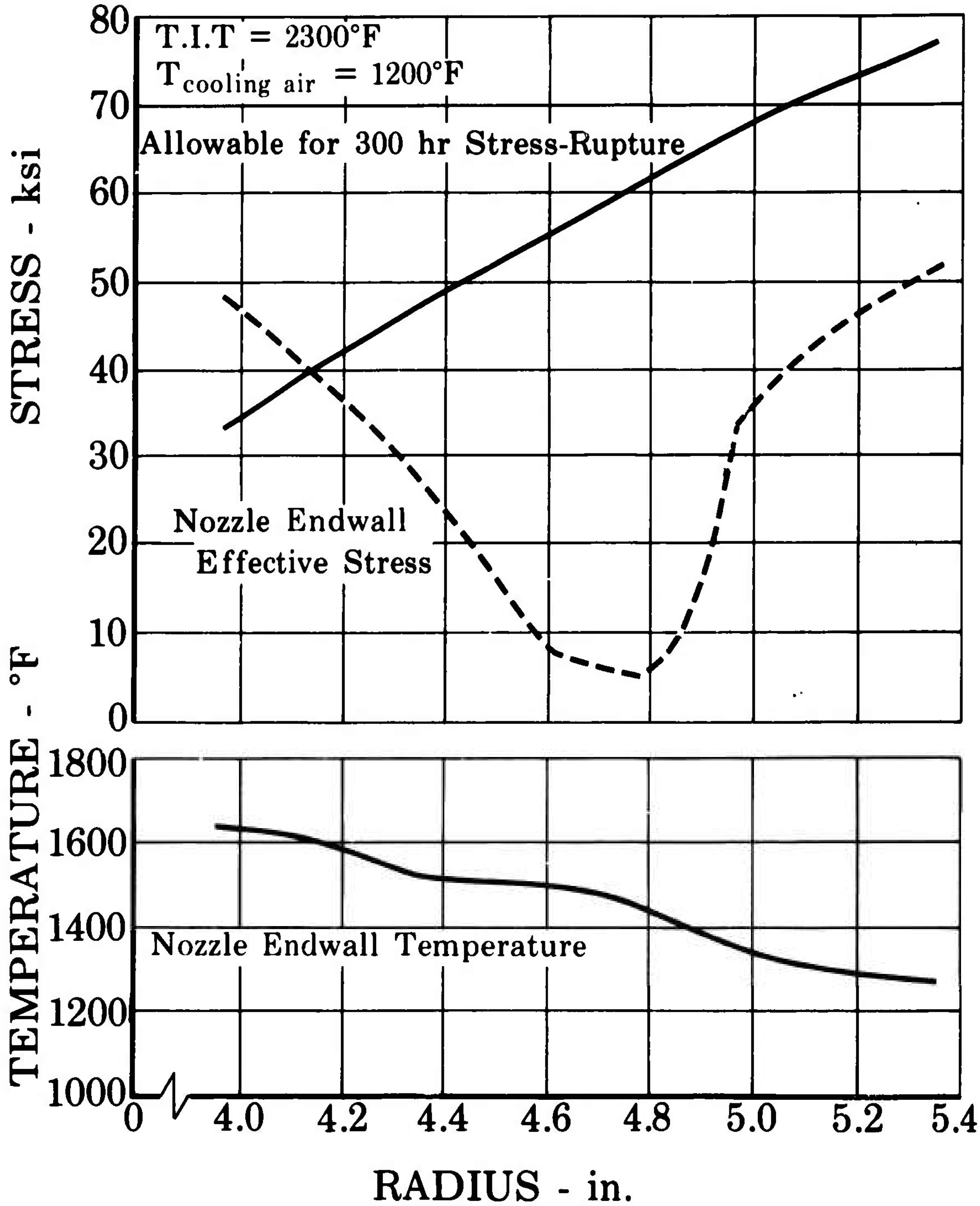

Figure 74. Sixth-Iteration Nozzle Endwall Temperature and Stress Distribution.

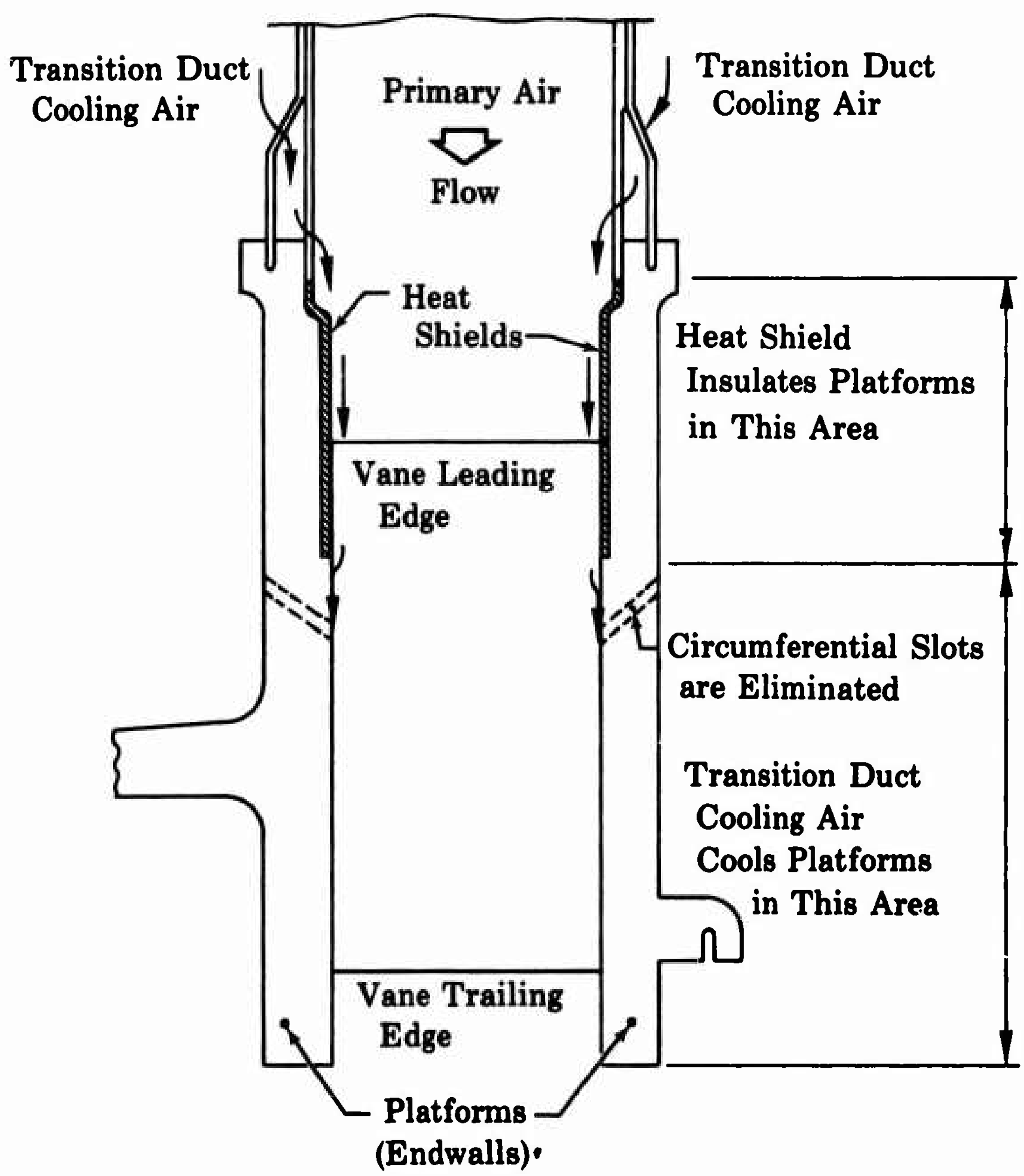

Figure 75. Seventh-Iteration Nozzle Cooling Design Schematic (Phase I - Final Configuration).

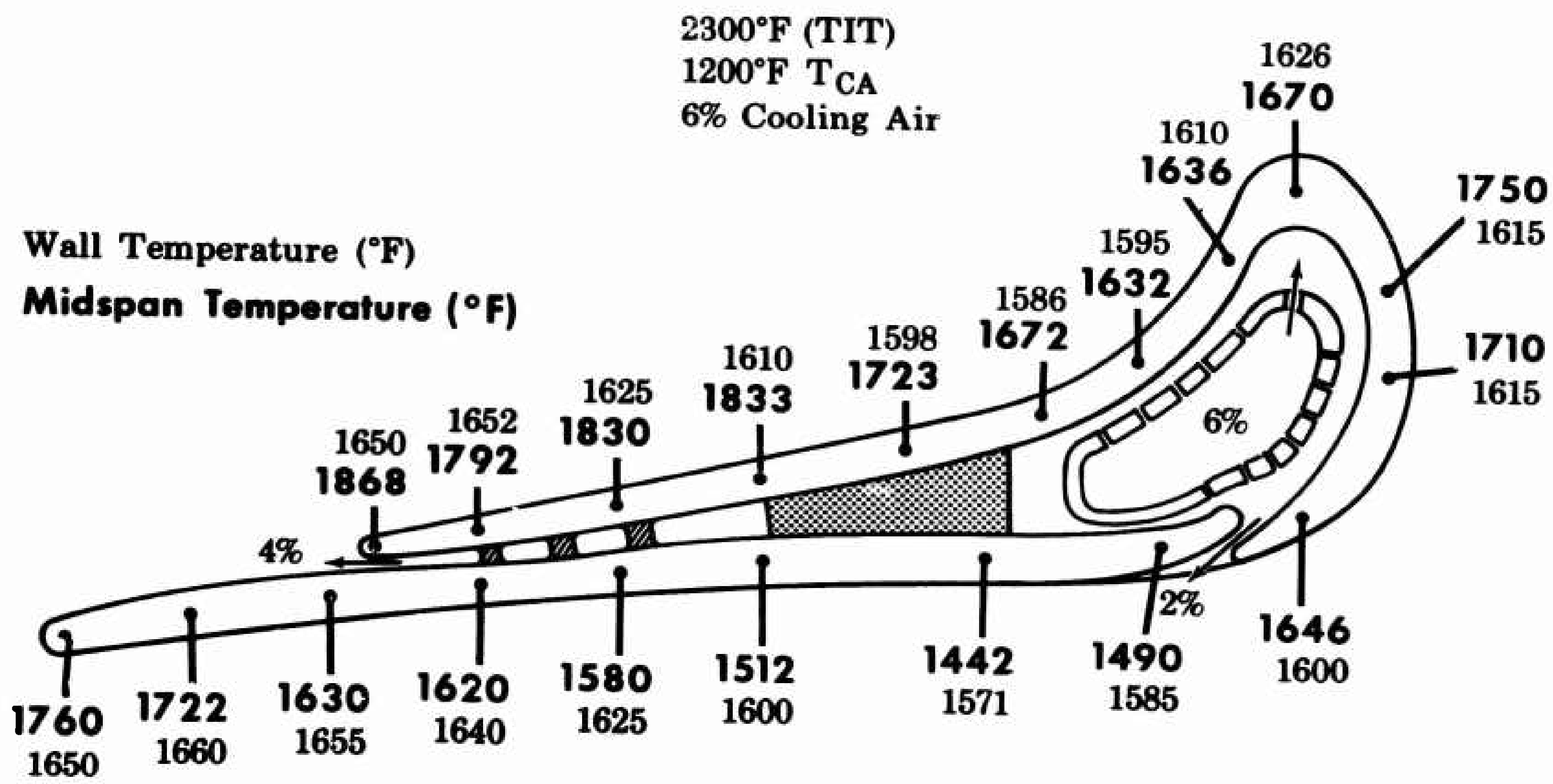

Figure 76. Seventh-Iteration Nozzle Cooling Design Vane Temperature (Phase I - Final Configuration).

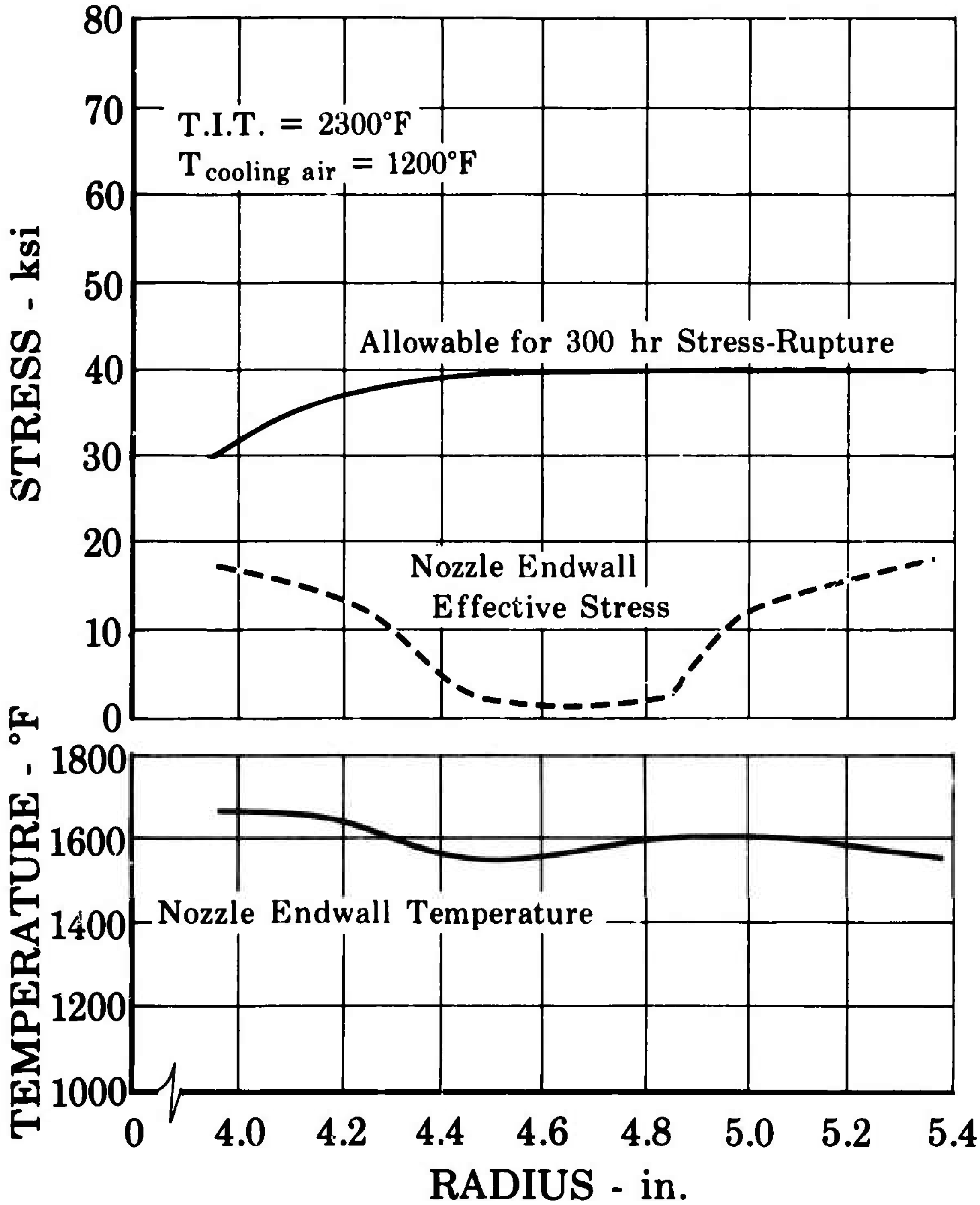

Figure 77. Seventh-Iteration Nozzle Temperature and Stress Distribution (Phase I - Final Configuration).

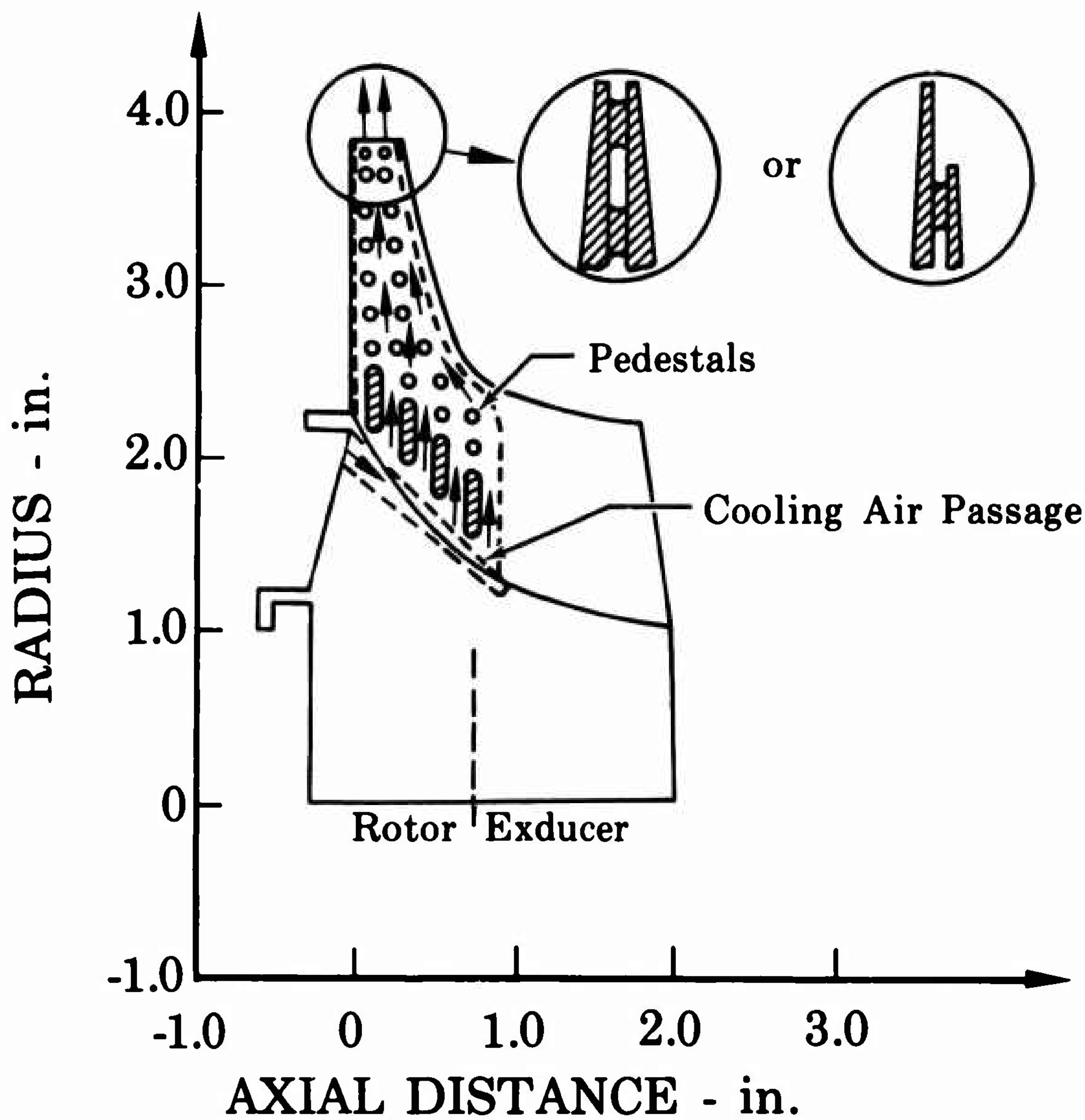

Figure 78. Original Rotor Cooling Design.

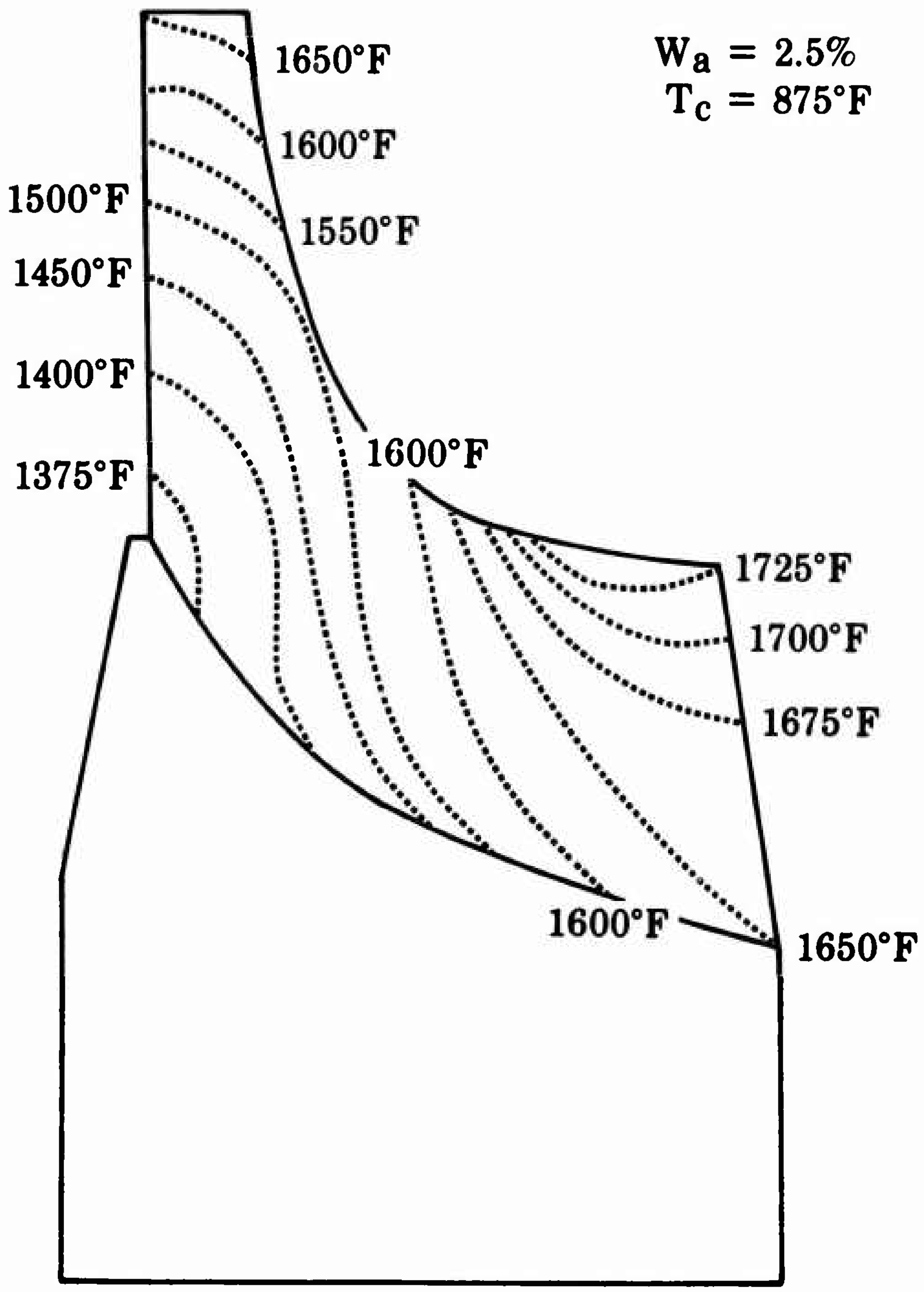

Figure 79. Original Rotor Temperature Distribution.

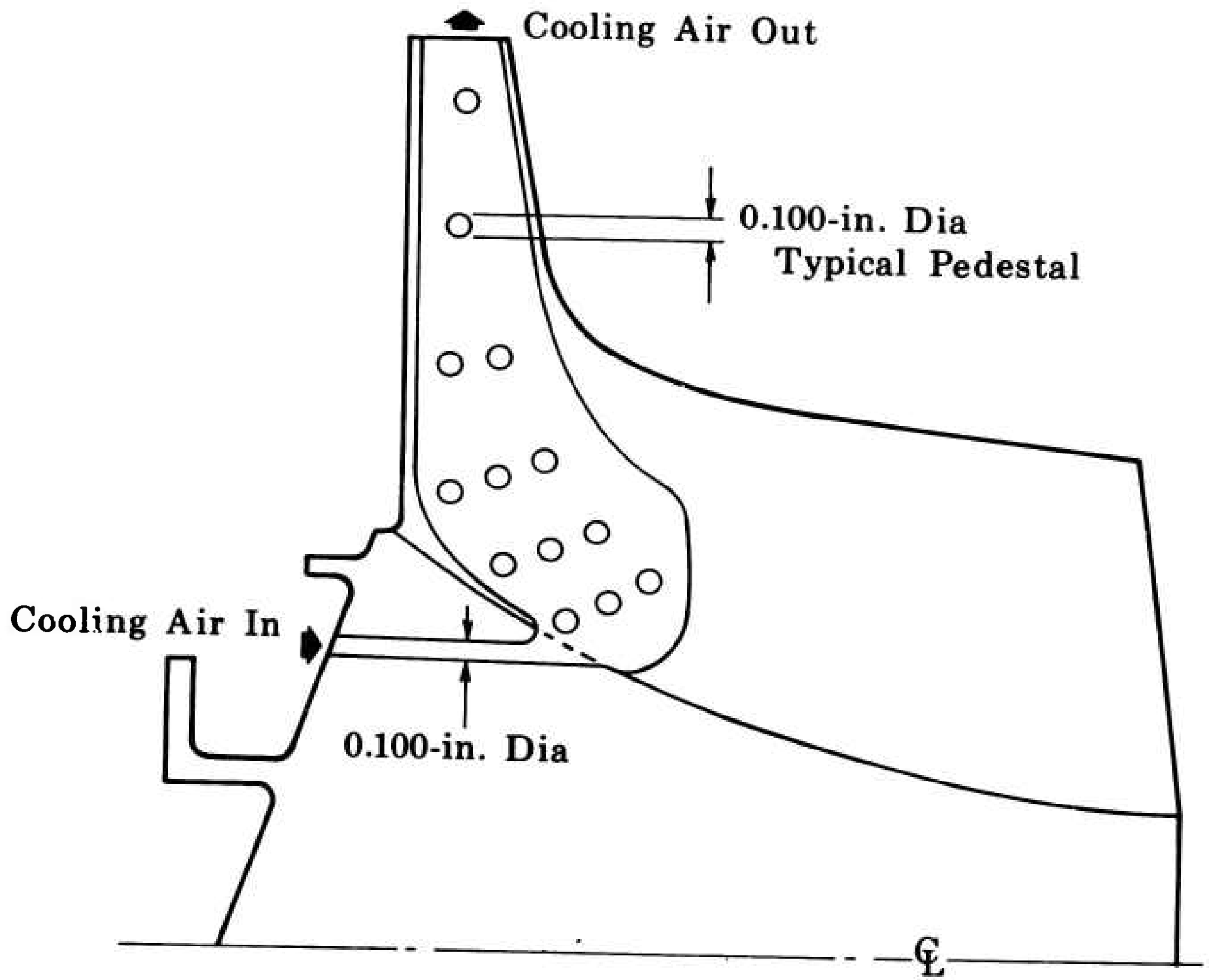

Figure 80. First-Iteration Rotor Heat Transfer Design.

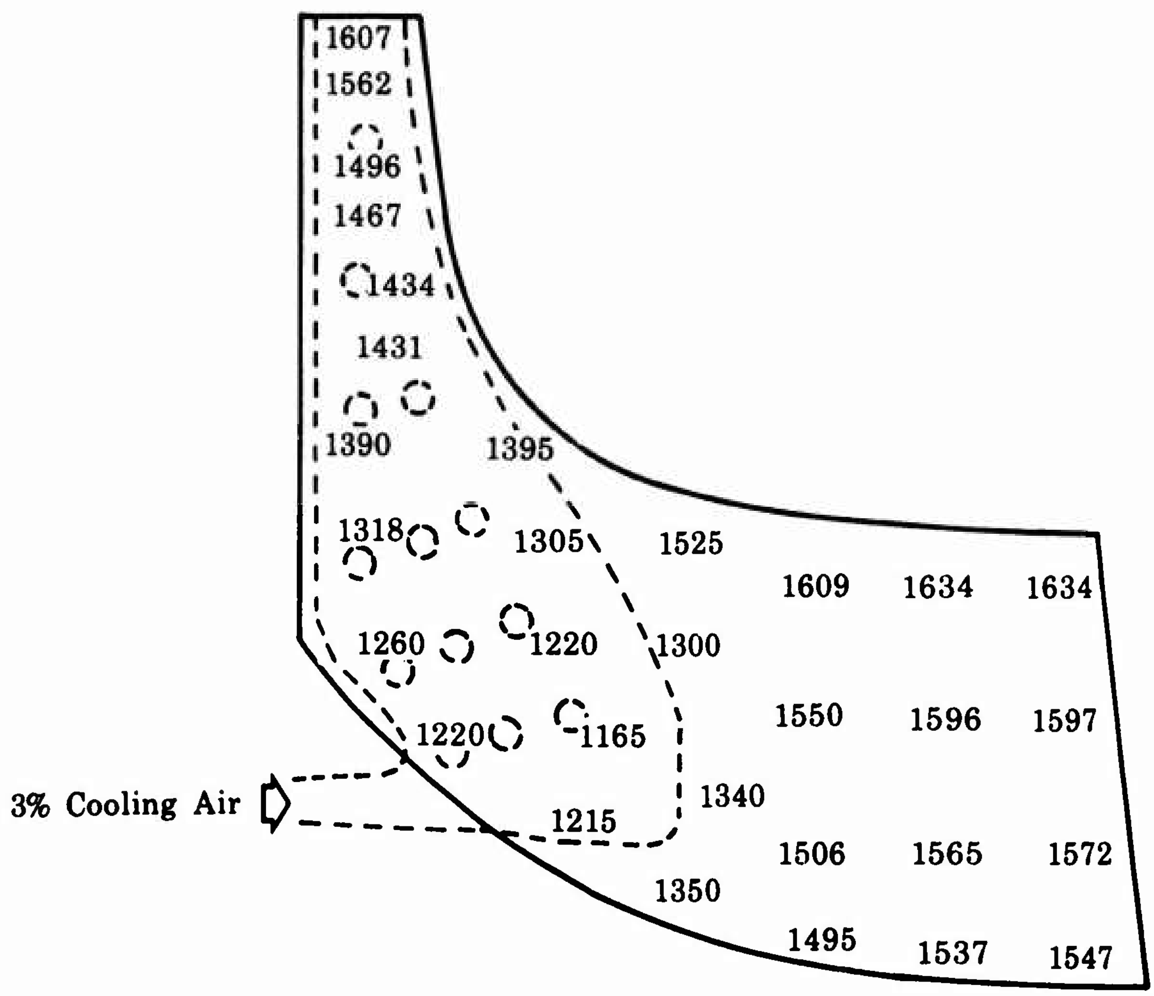

Figure 81. First-Iteration Pressure Surface Temperature Distribution.

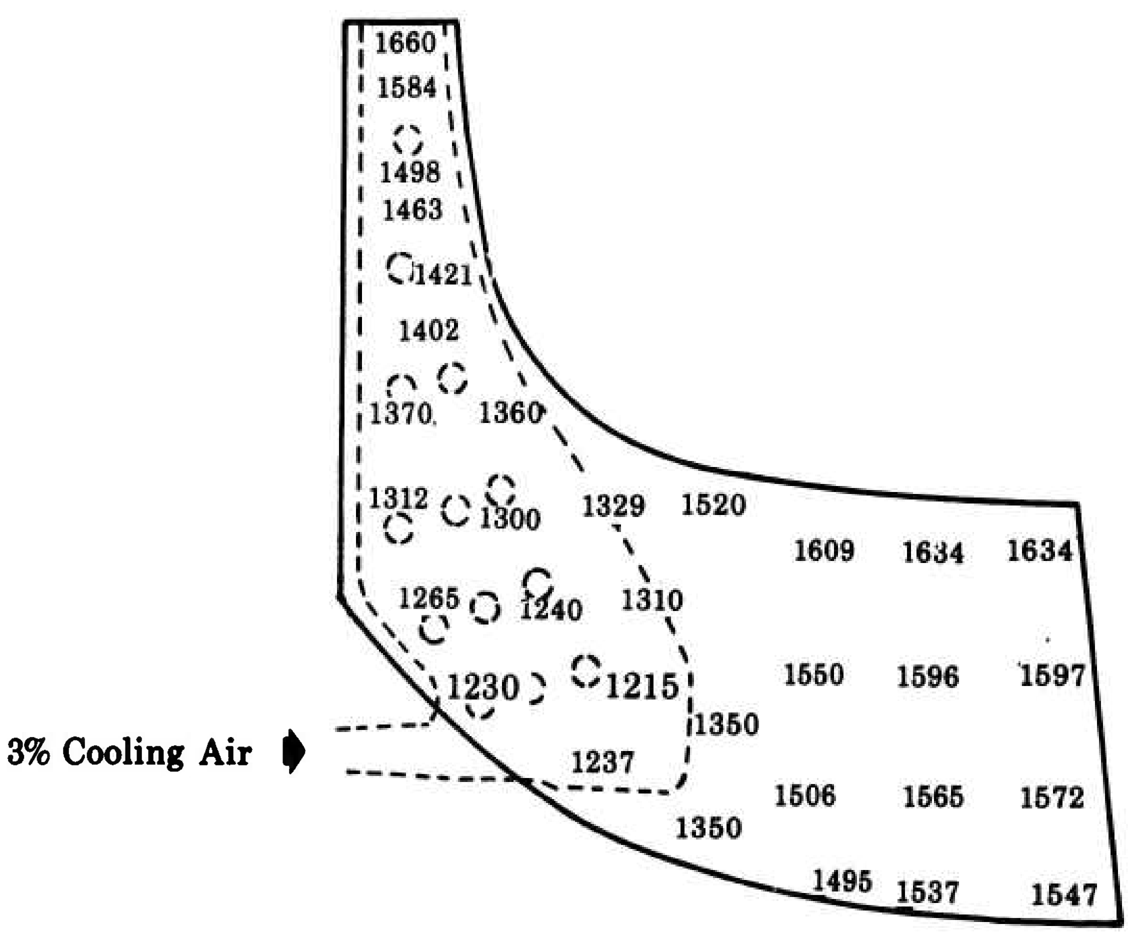

Figure 82. First-Iteration Suction Surface Temperature Distribution.

SECOND ITERATION SINGLE-PASS ROTOR HAS BACKWALL COOLING AND INCREASED COOLING AIRFLOW

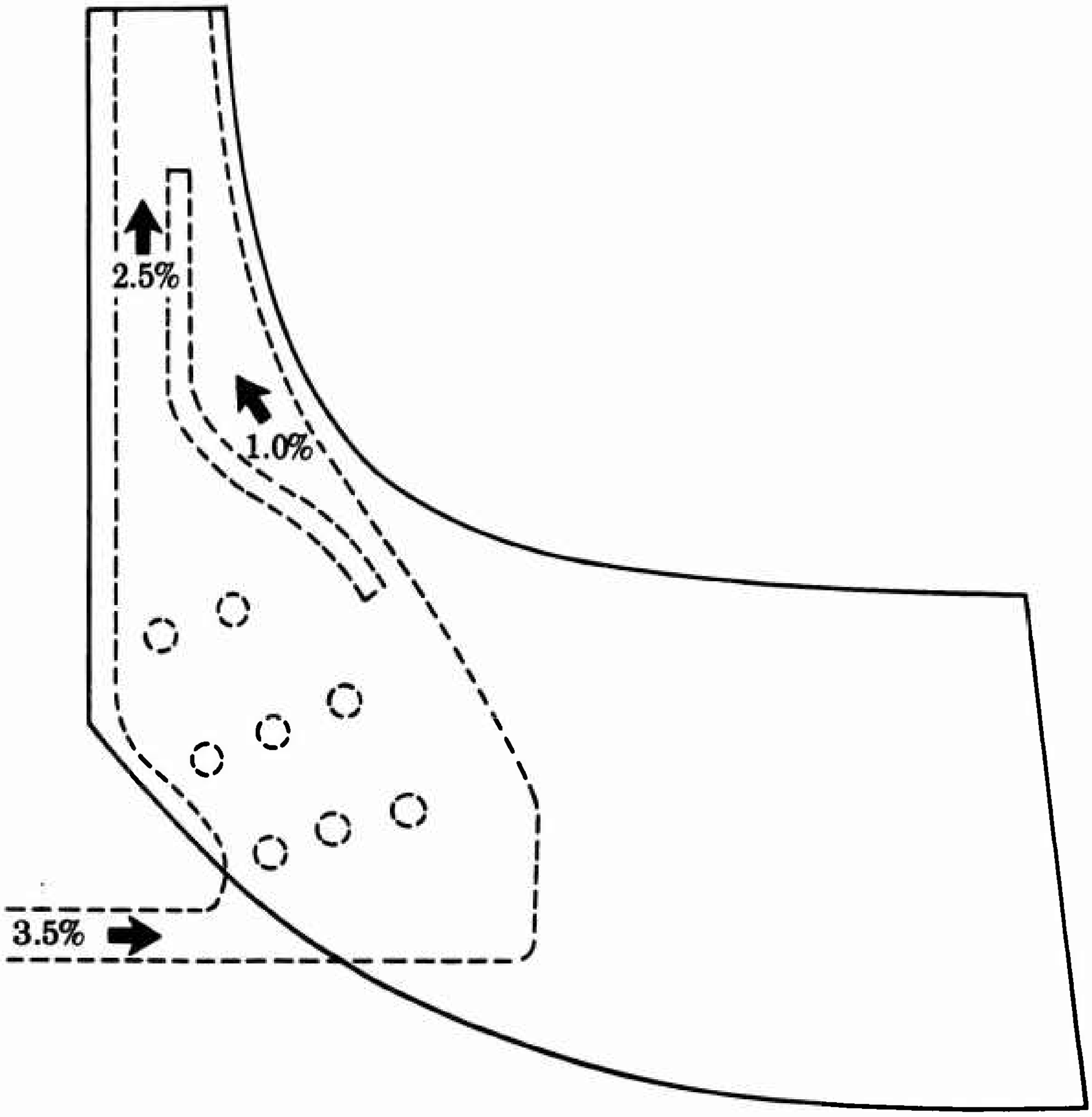

Cooling Air, T_{in} = 850°F

Figure 83. Second-Iteration Single-Pass Rotor.

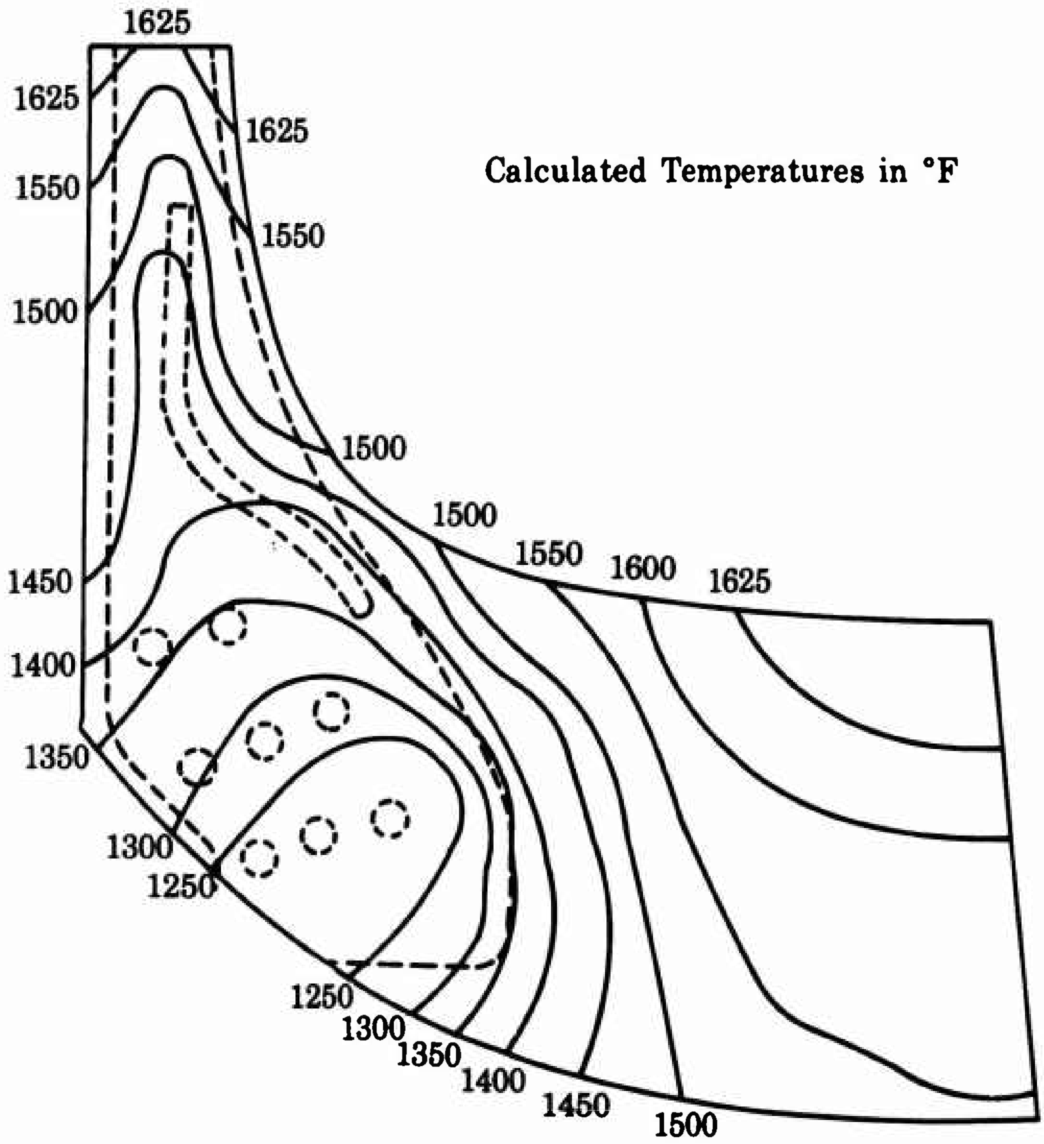

Figure 84. Temperature Distribution of Second-Iteration, Single-Pass Rotor (Pressure Side).

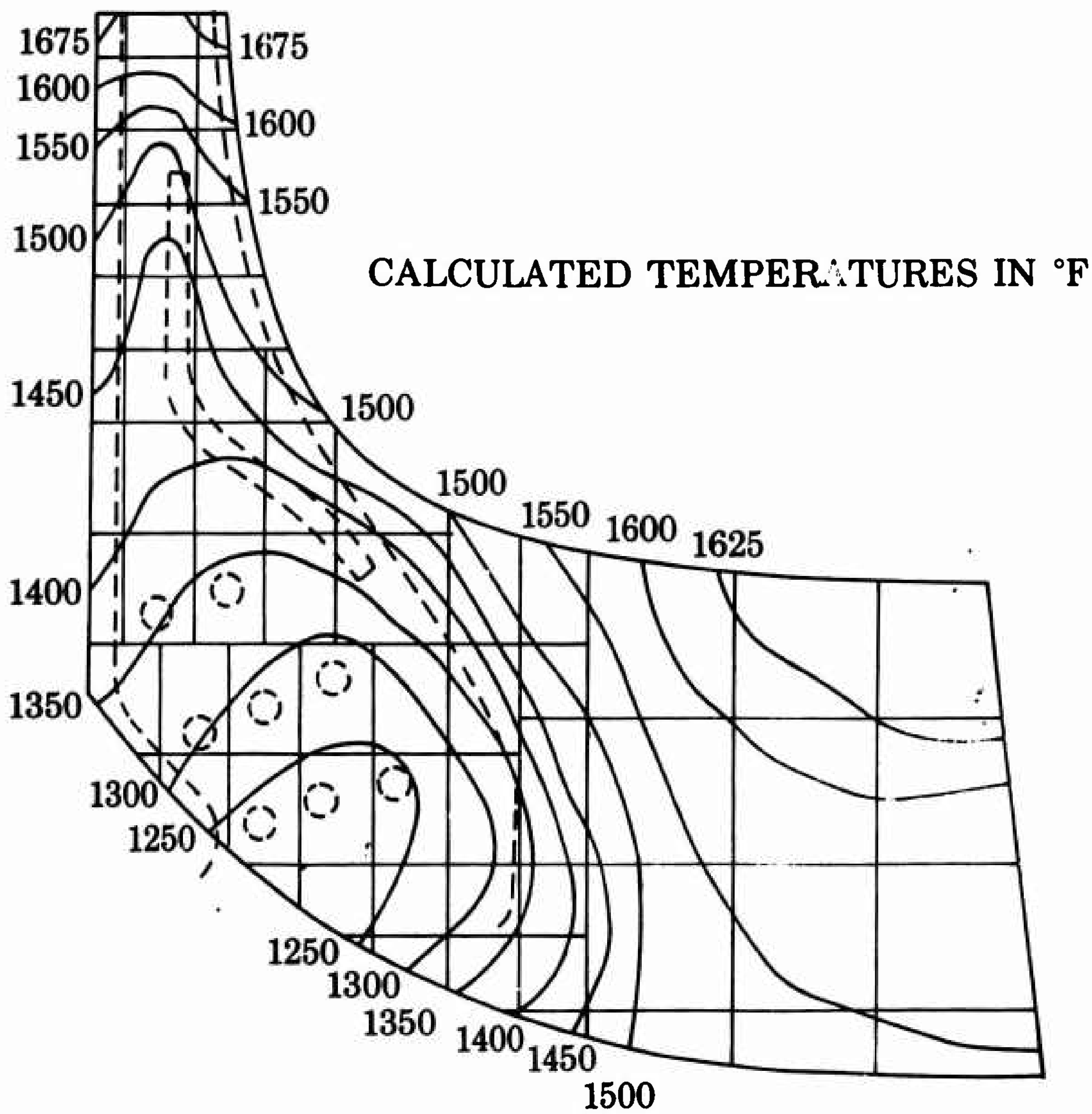

Figure 85. Temperature Distribution of Second-Iteration, Single-Pass Rotor (Suction Side).

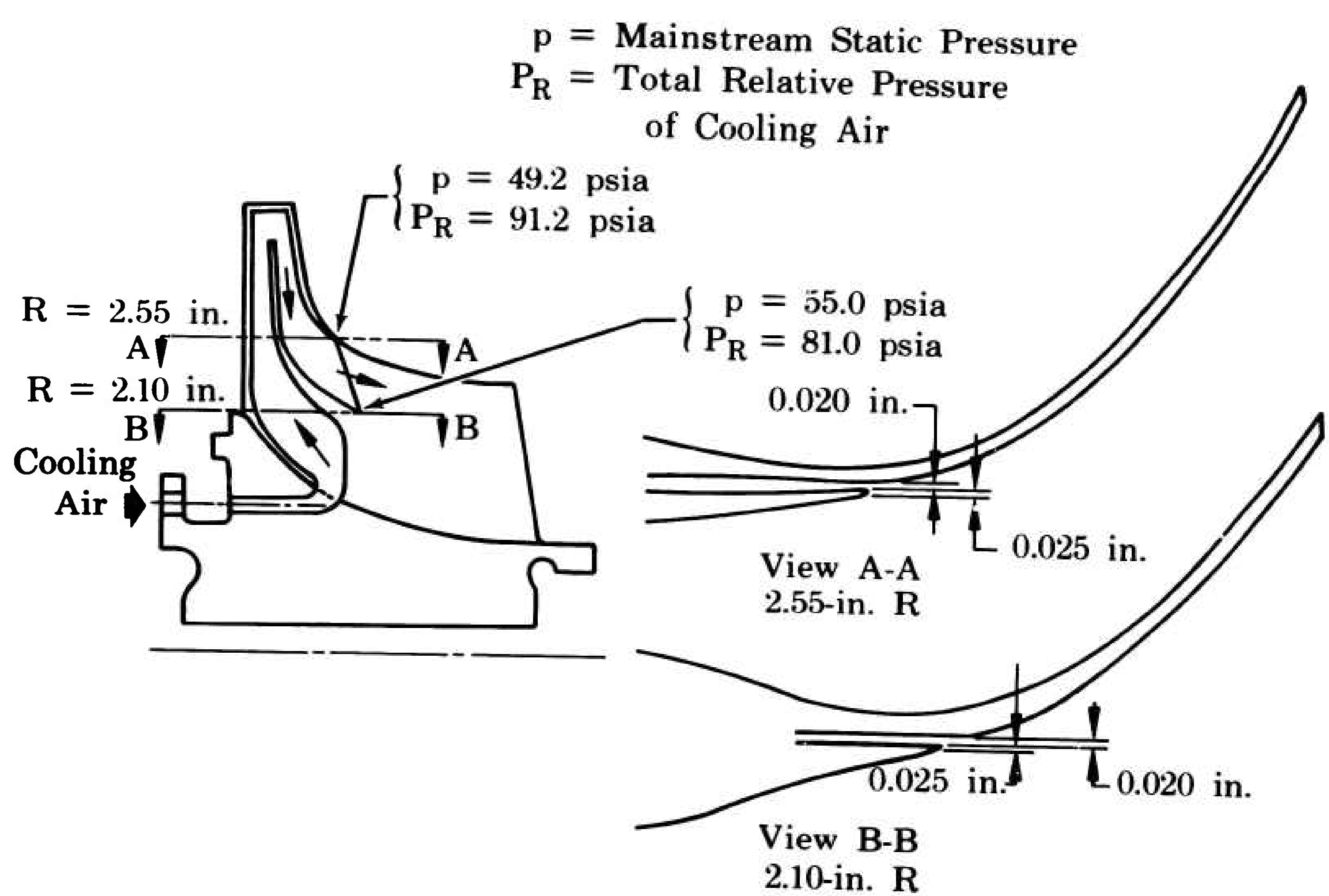

Figure 86. First-Iteration Double-Pass Rotor.

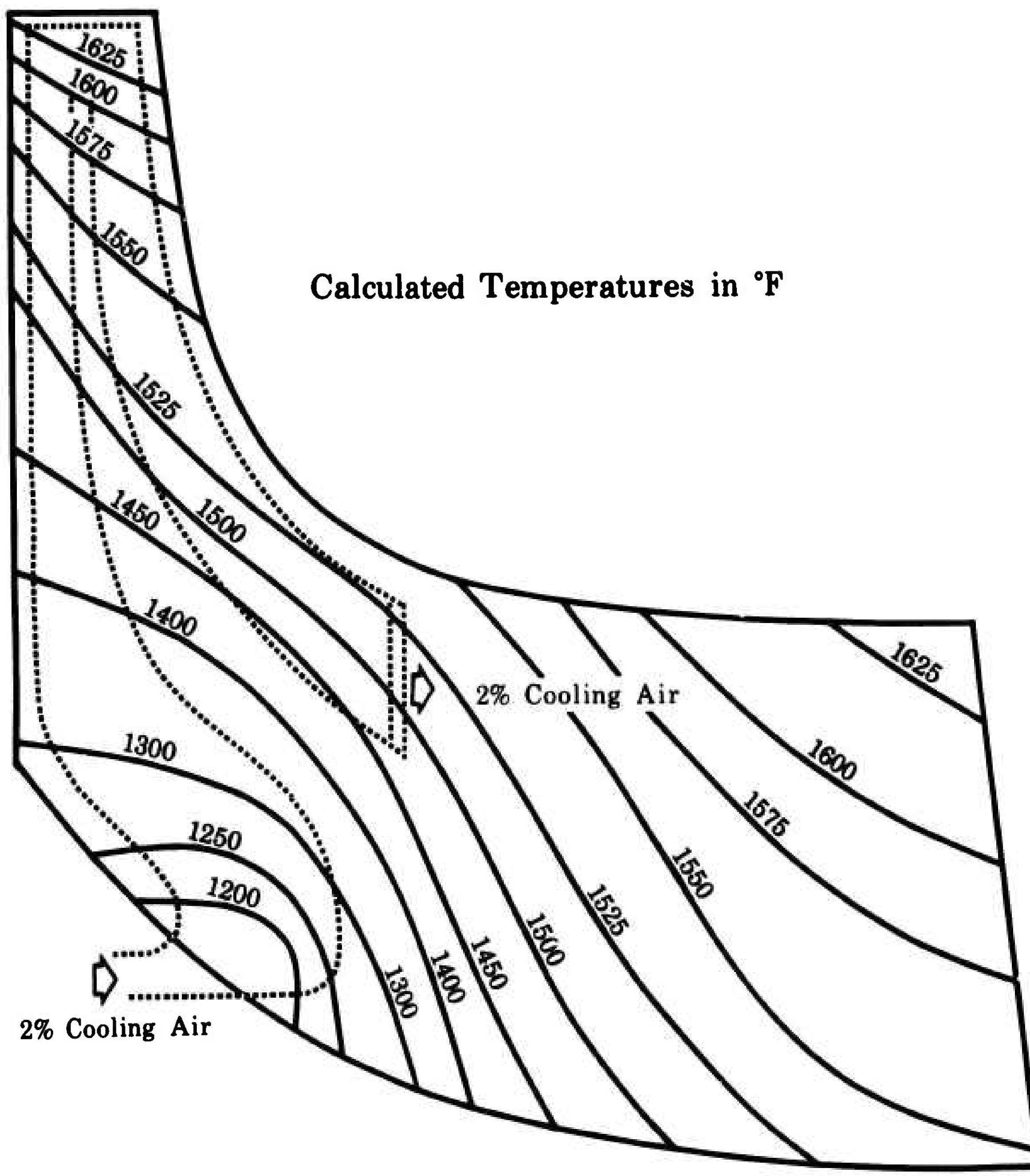

Figure 87. Mean Temperature Distribution for First-Iteration Double-Pass Rotor.

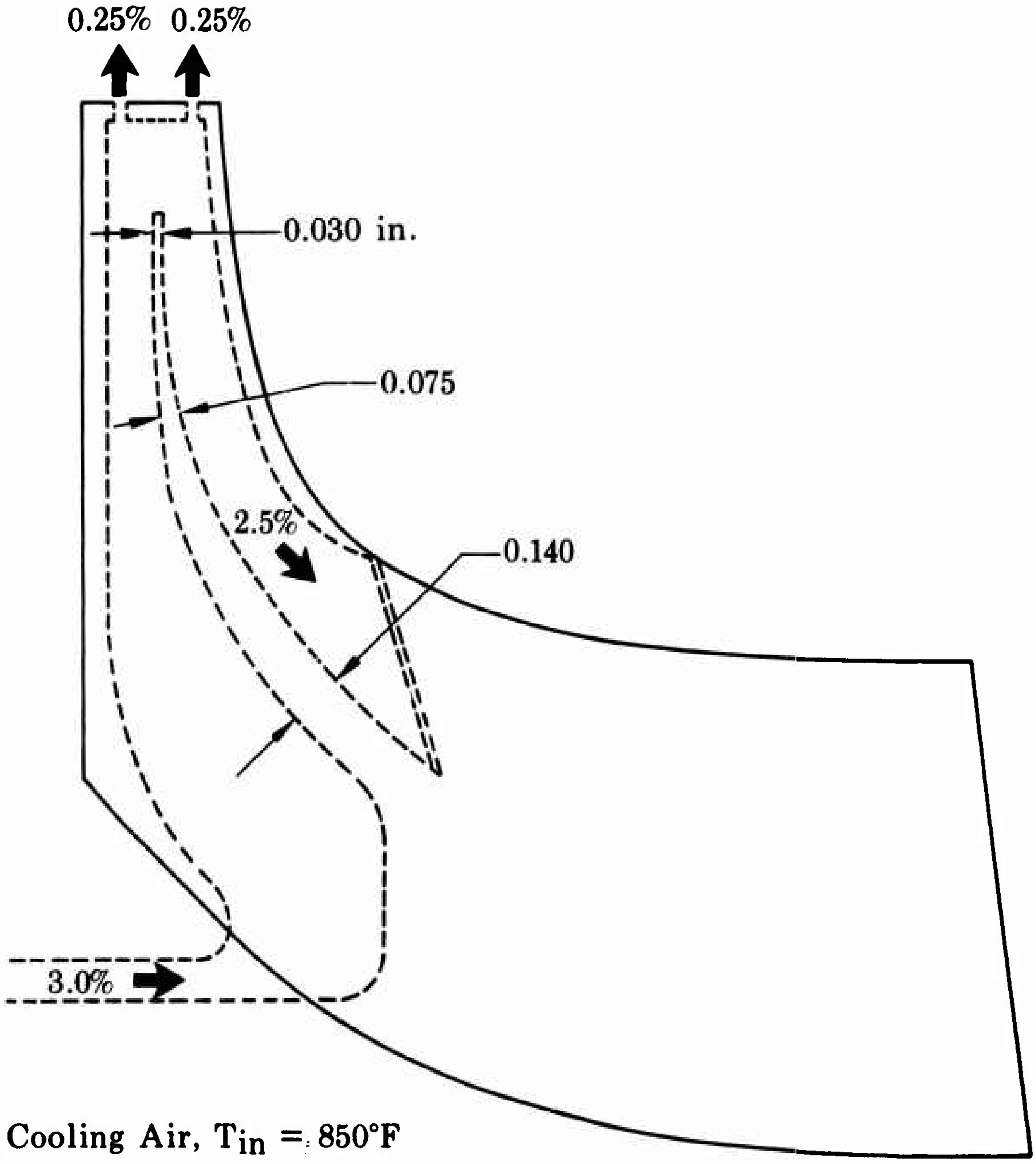

Figure 88. Second-Iteration, Two-Pass Rotor (Tip Ejection, Backwall Cooling and Increased Cooling Airflow).

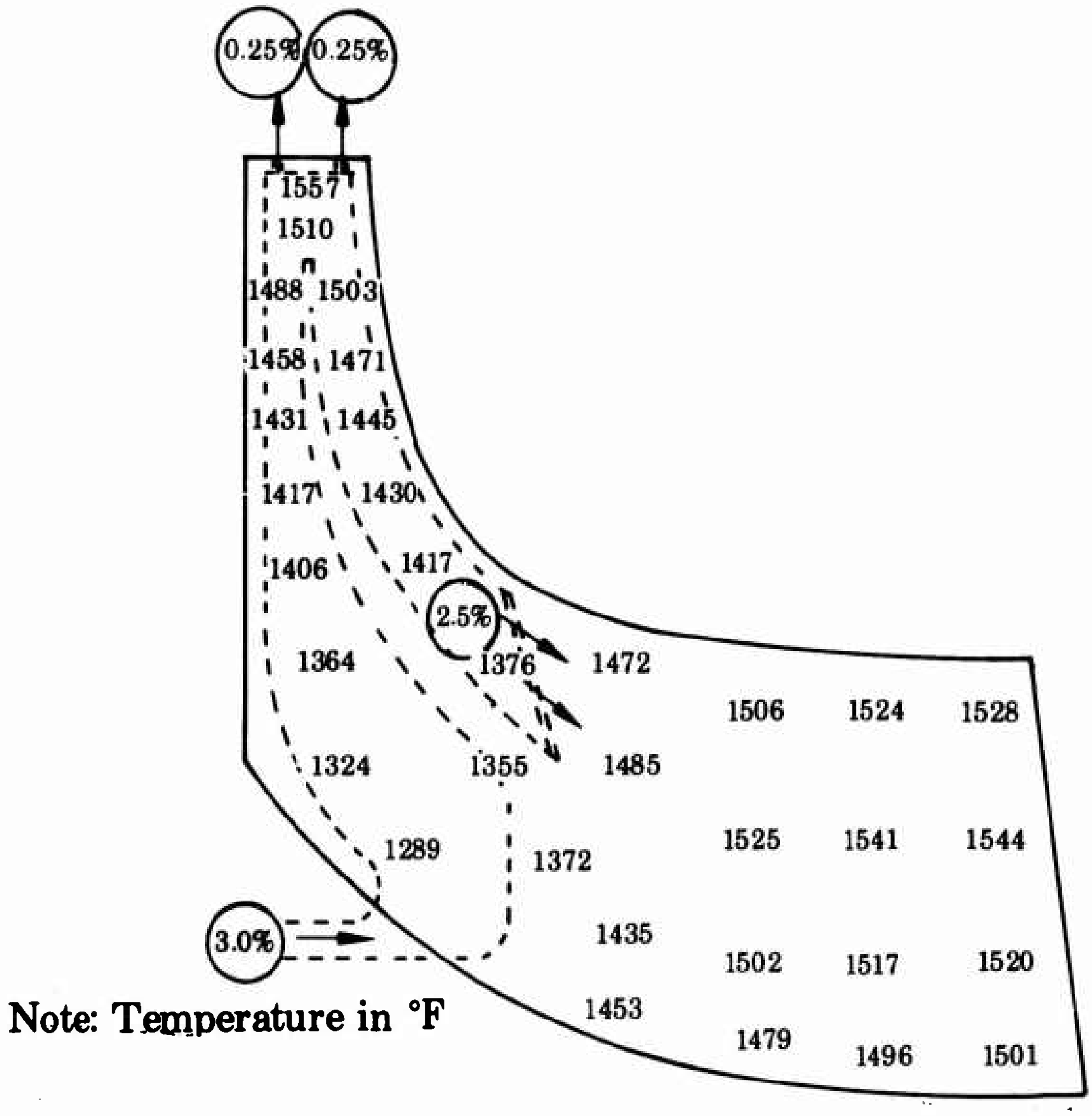

Figure 89. Pressure Surface Temperature of a Double-Pass Rotor with 3% Cooling Airflow.

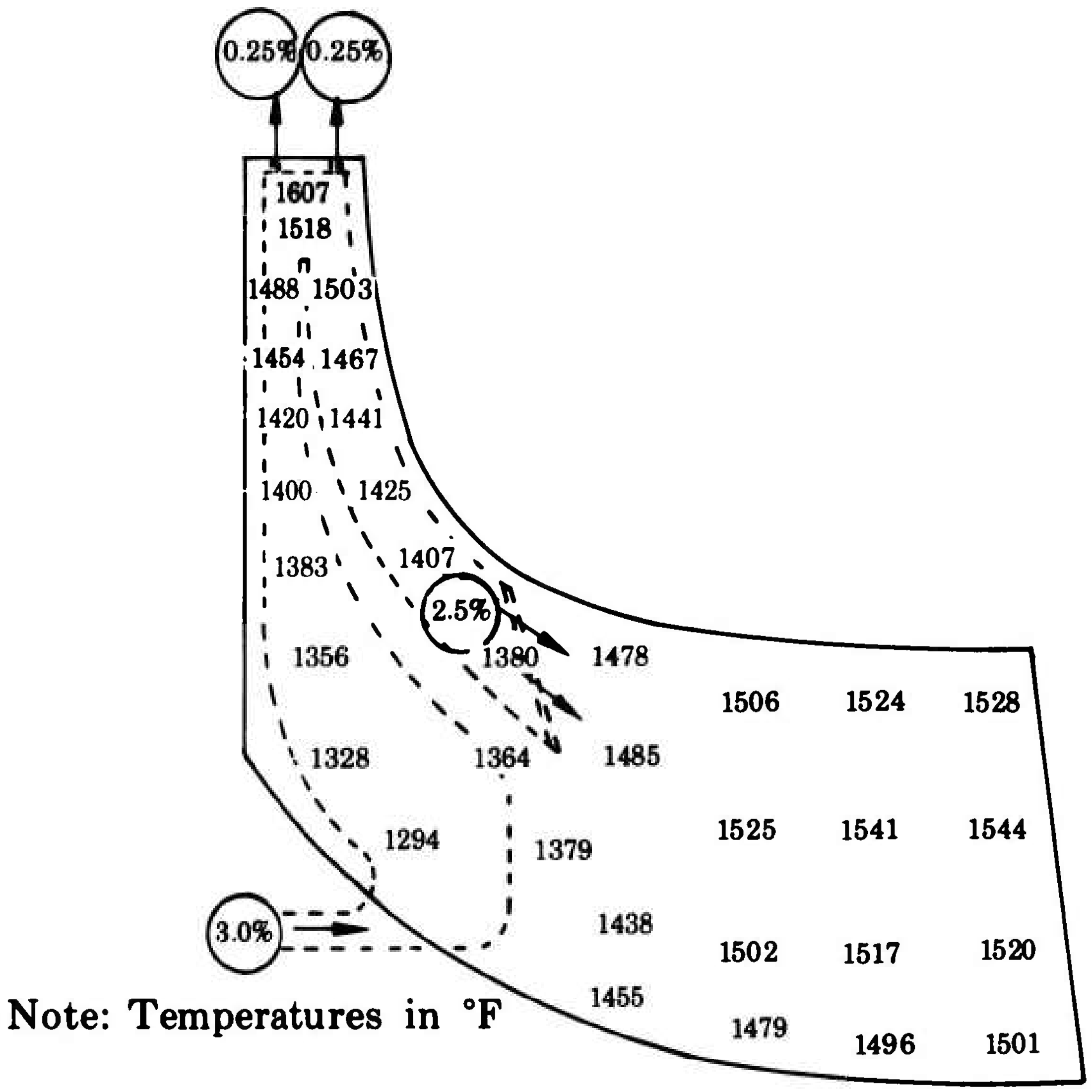

Figure 90. Suction Surface Temperature Distribution of the Second-Iteration Double-Pass Rotor.

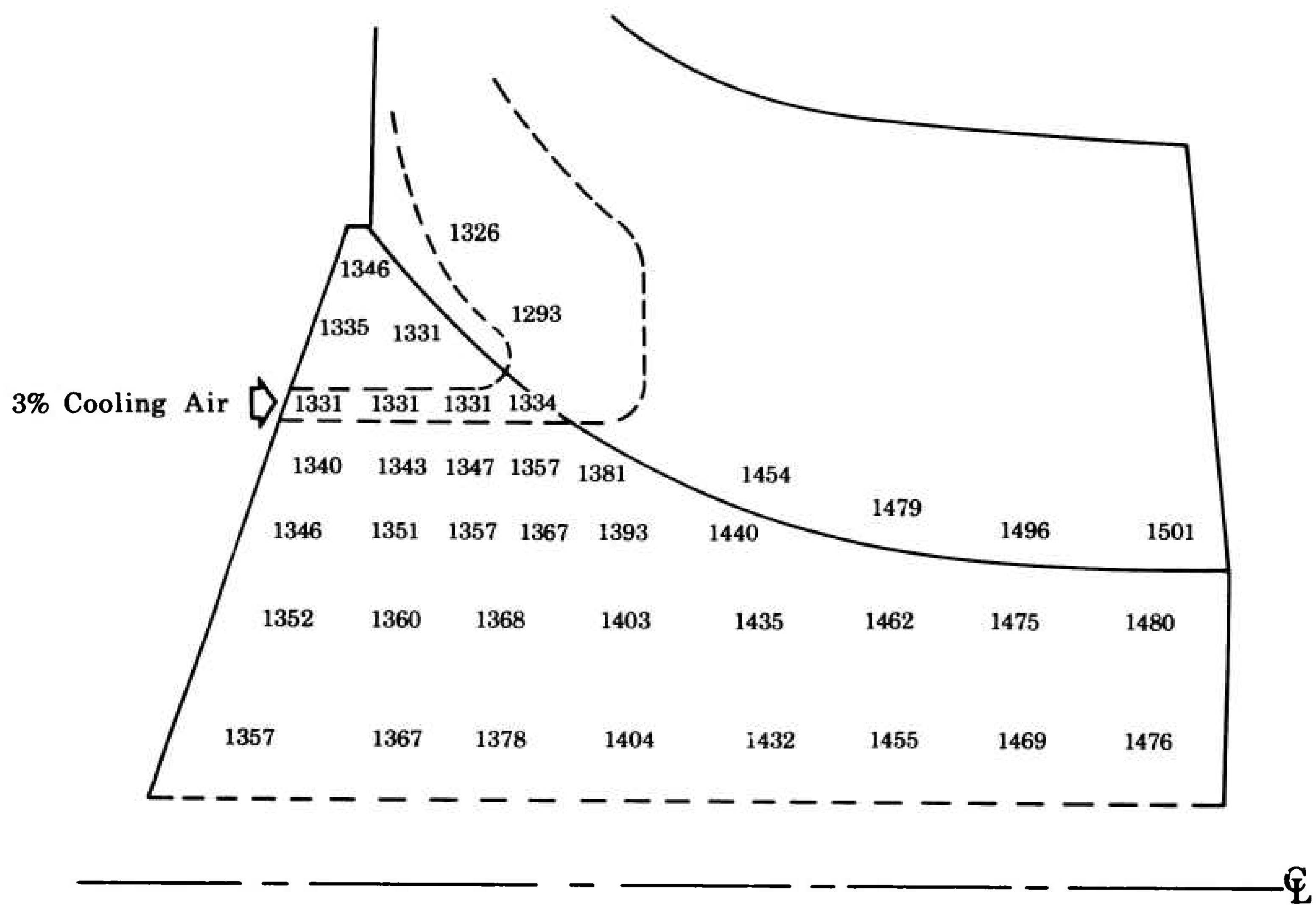

Figure 91. Second-Iteration Double-Pass Rotor Hub Temperature Distribution.

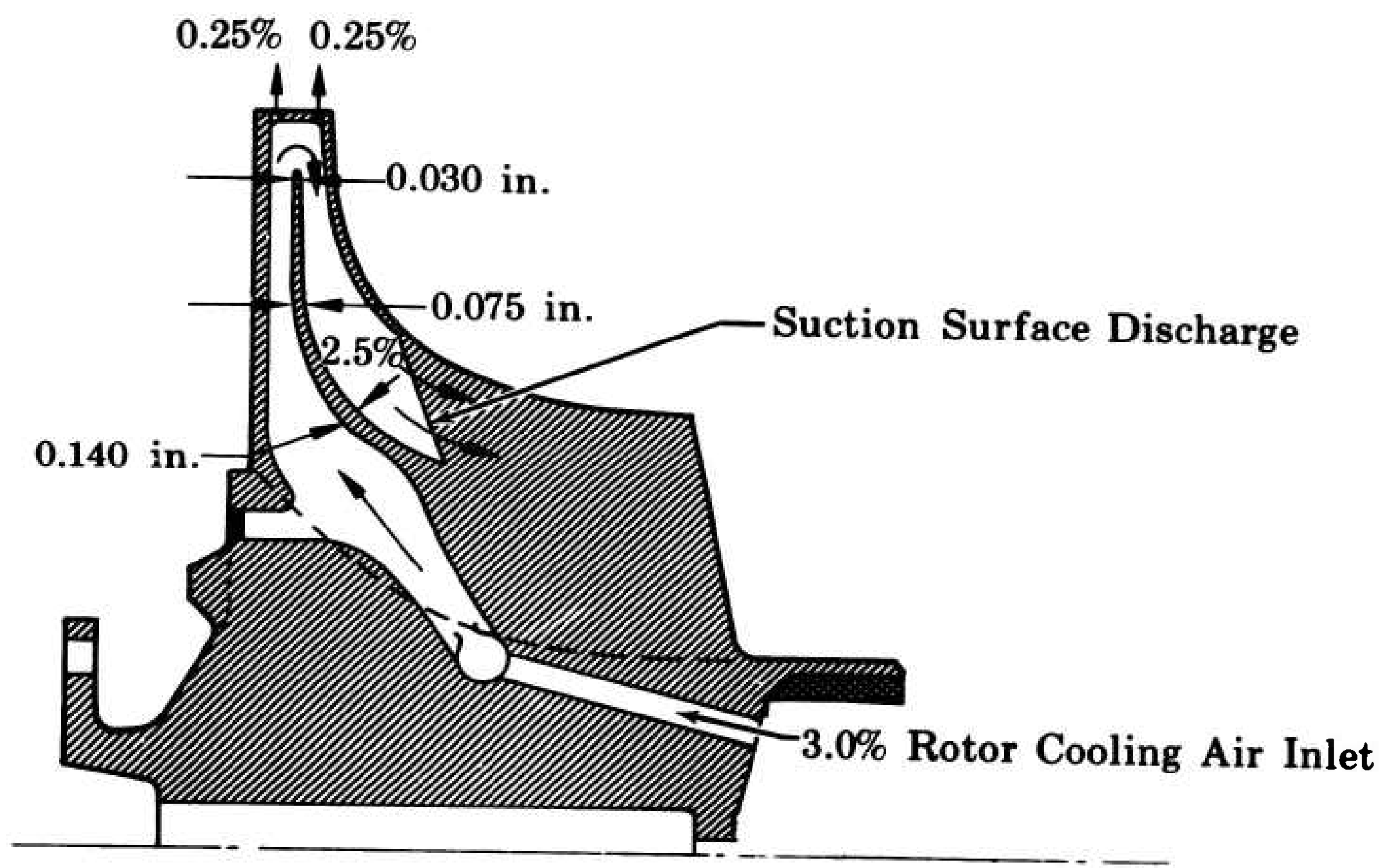

Figure 92. Third-Iteration Double-Pass Rotor (Phase I - Final).

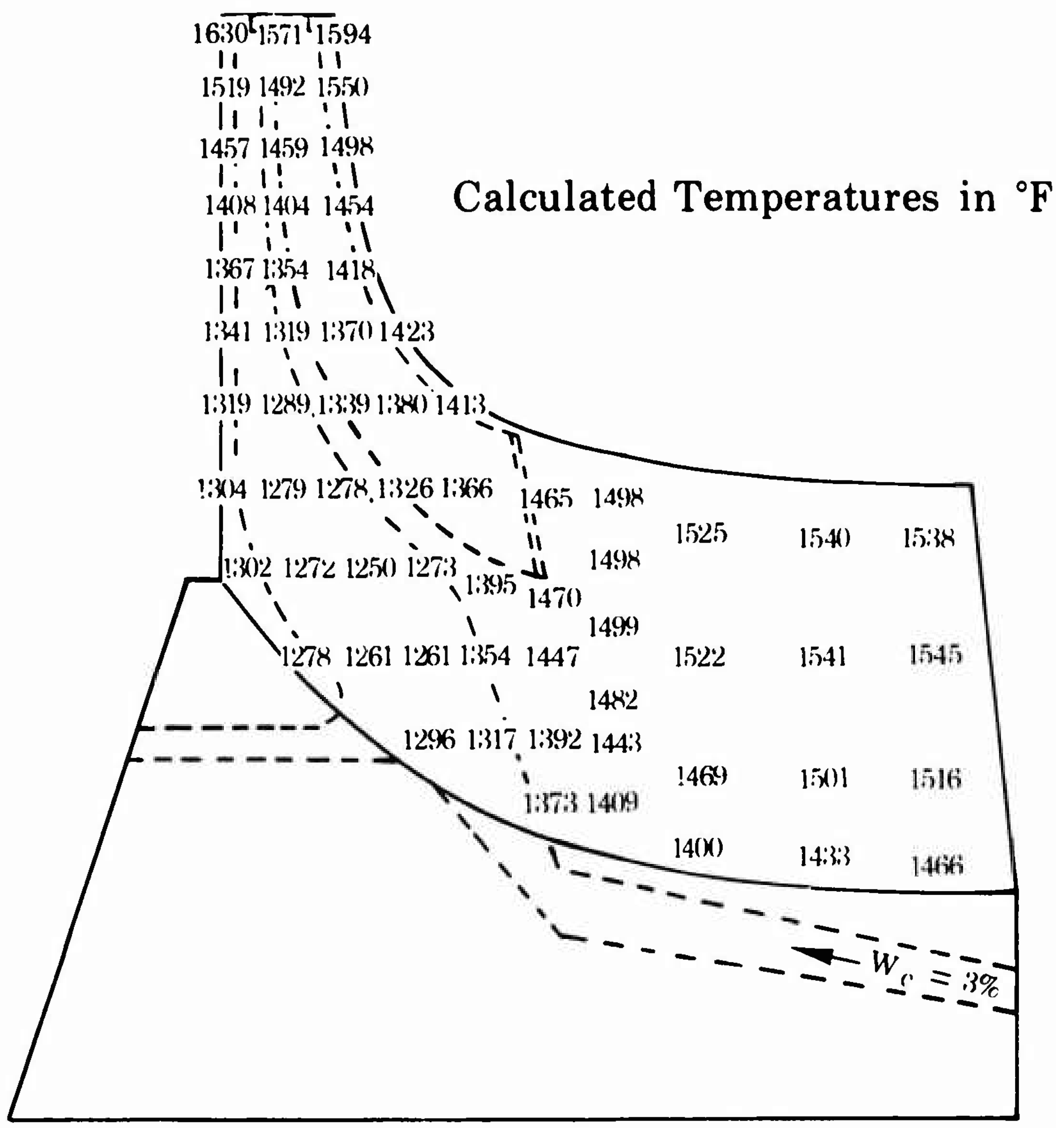

Figure 93. Third-Iteration, Double-Pass Rotor Pressure Surface Temperature Distribution.

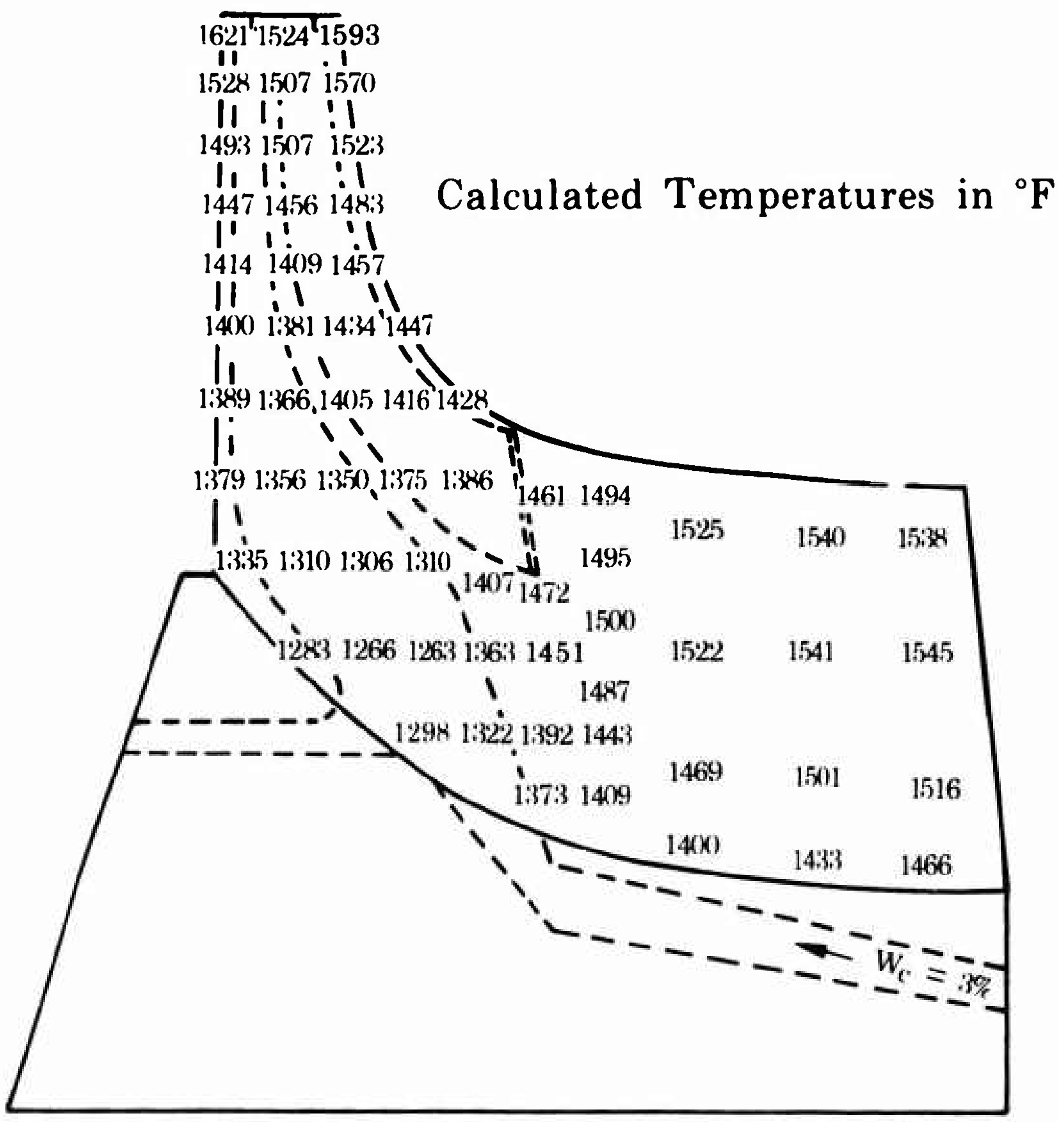

Figure 94. Third-Iteration Double Pass Rotor Suction Surface Temperature Distribution.

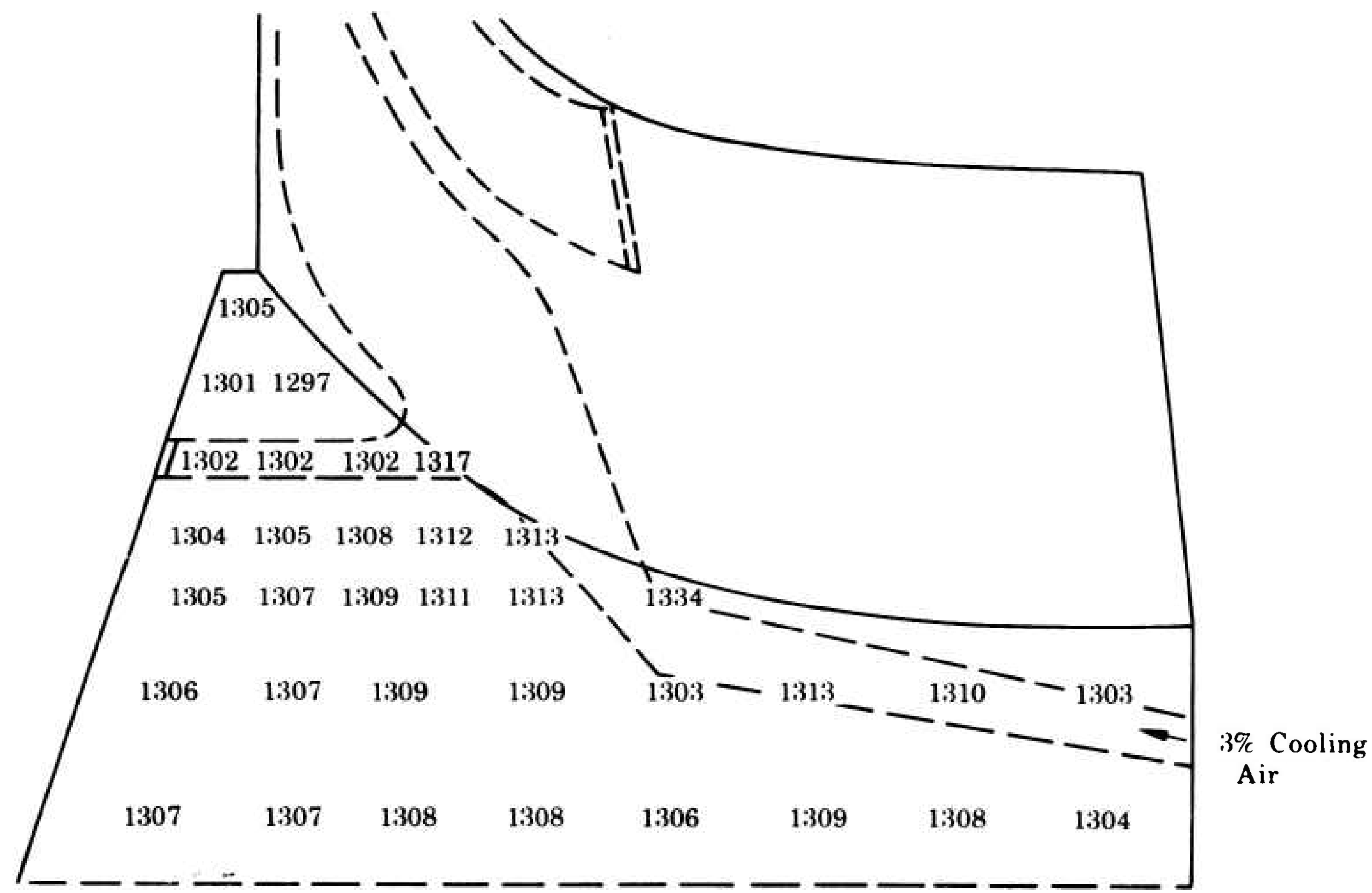

Figure 95. Third-Iteration Double Pass Rotor Hub Temperature Distribution at Design Point.

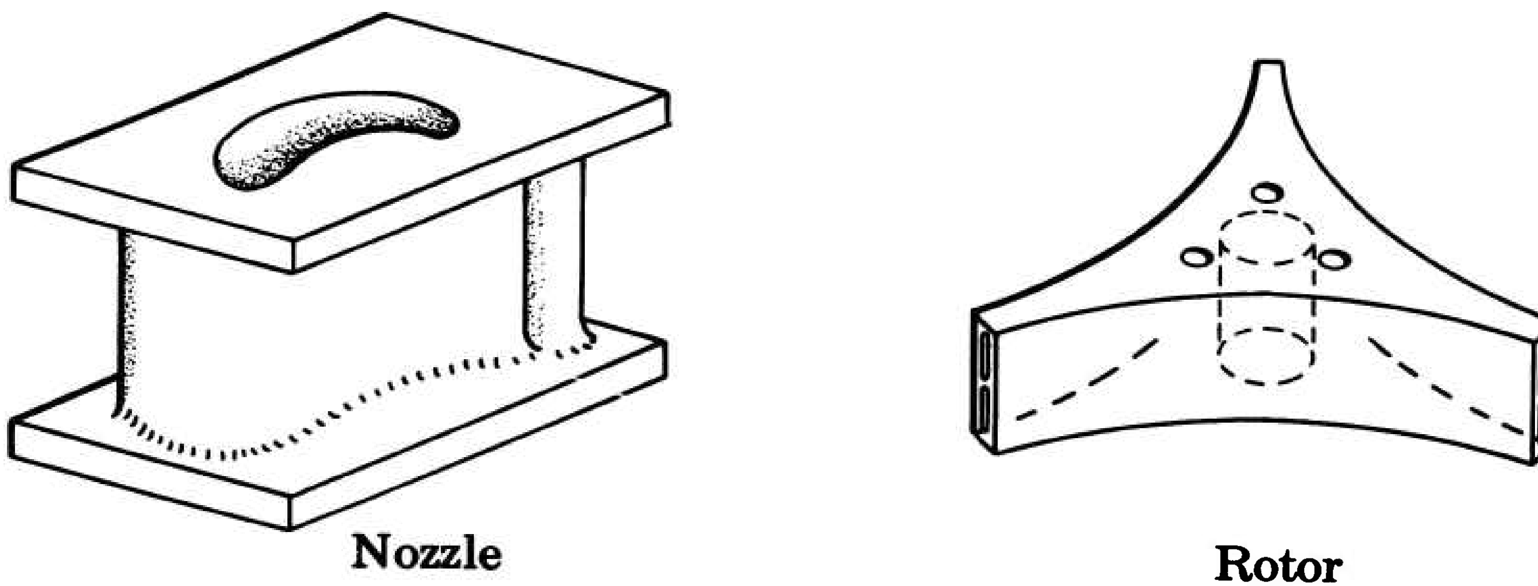

Figure 96. Original Fabrication Study Specimens.

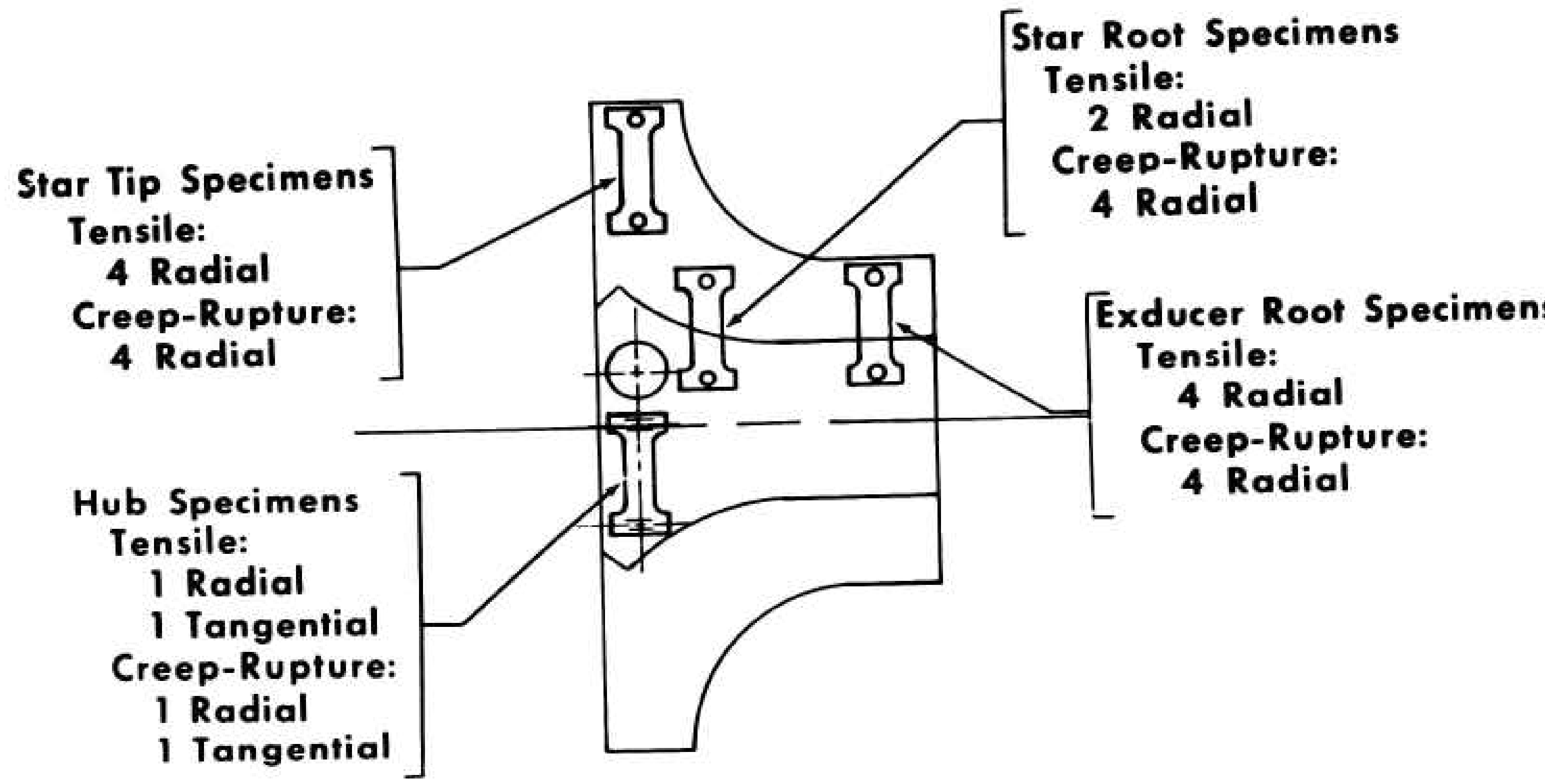

Figure 97. Metallurgical Test Program.

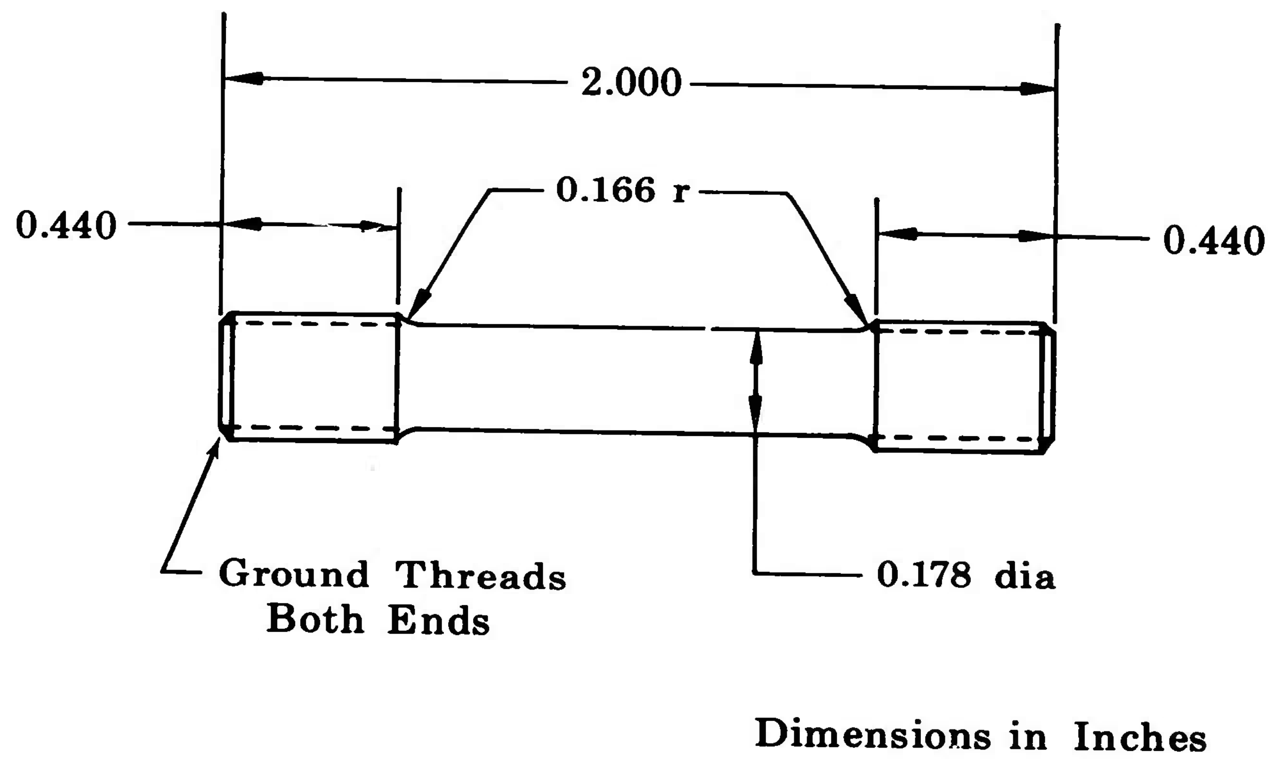

Figure 98. Cylindrical Metallurgical Specimen.

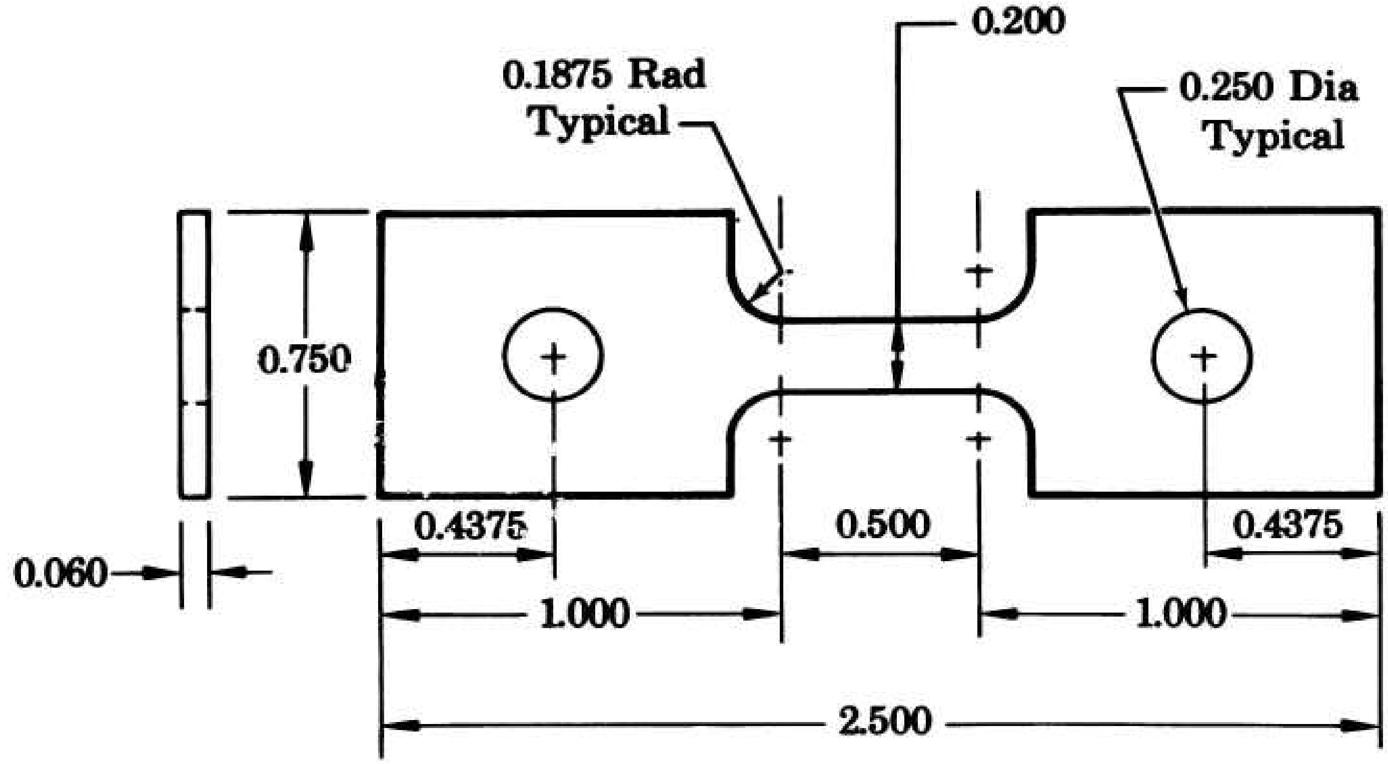

Dimensions in Inches

Figure 99. Original Flat Metallurgical Specimen.

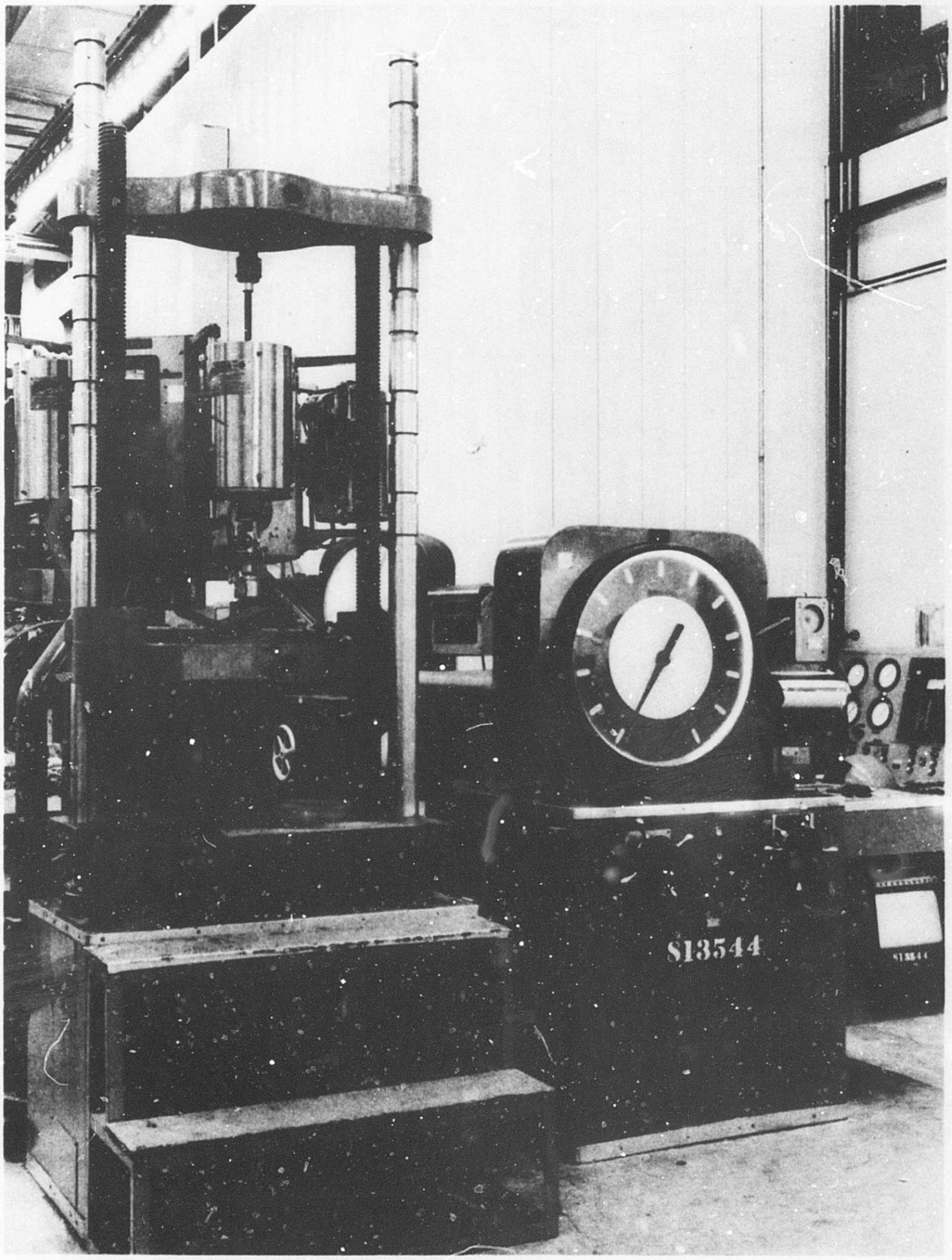

Figure 100. Young Universal Testing Machine.

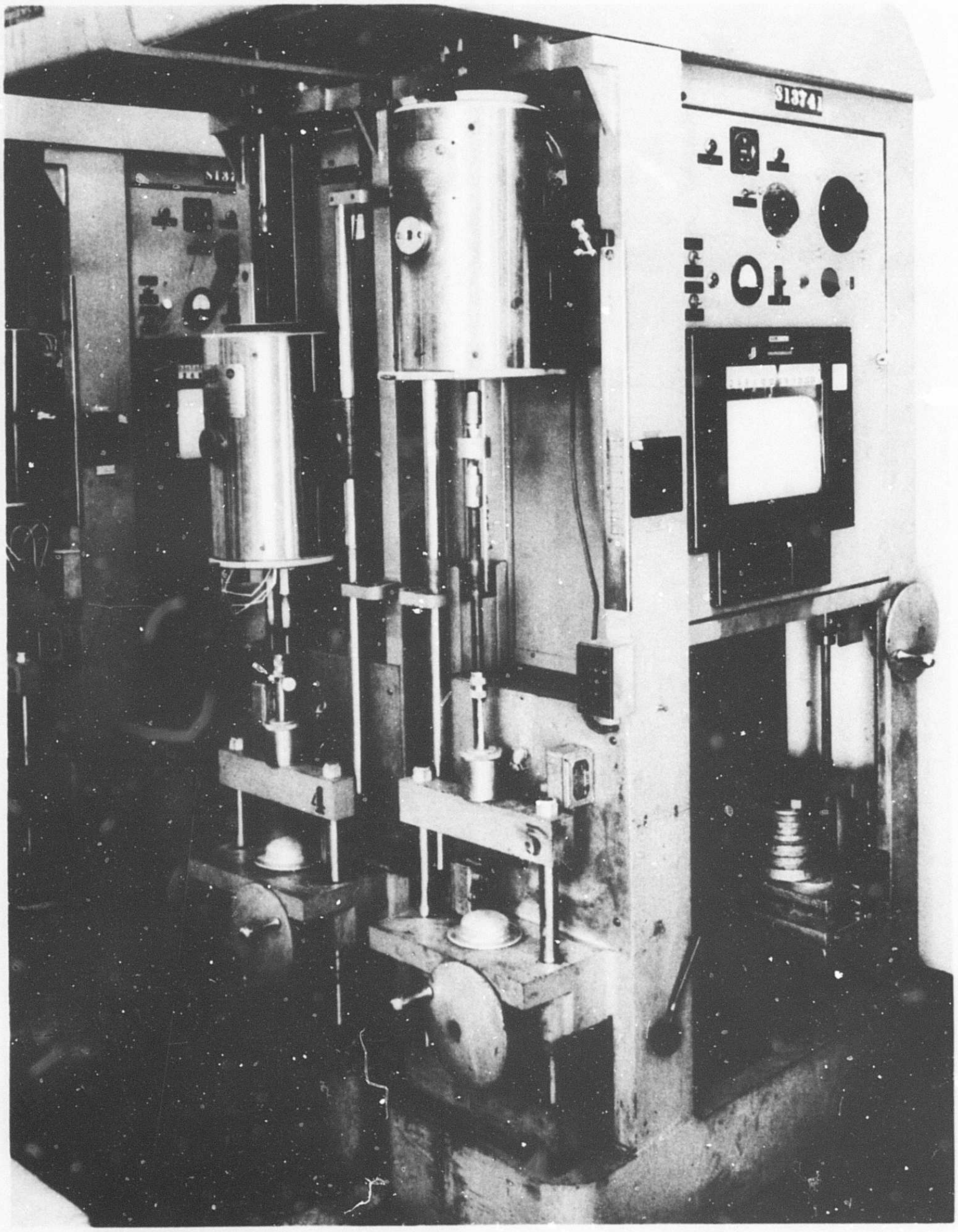

Figure 101. Satec Testing Machine.

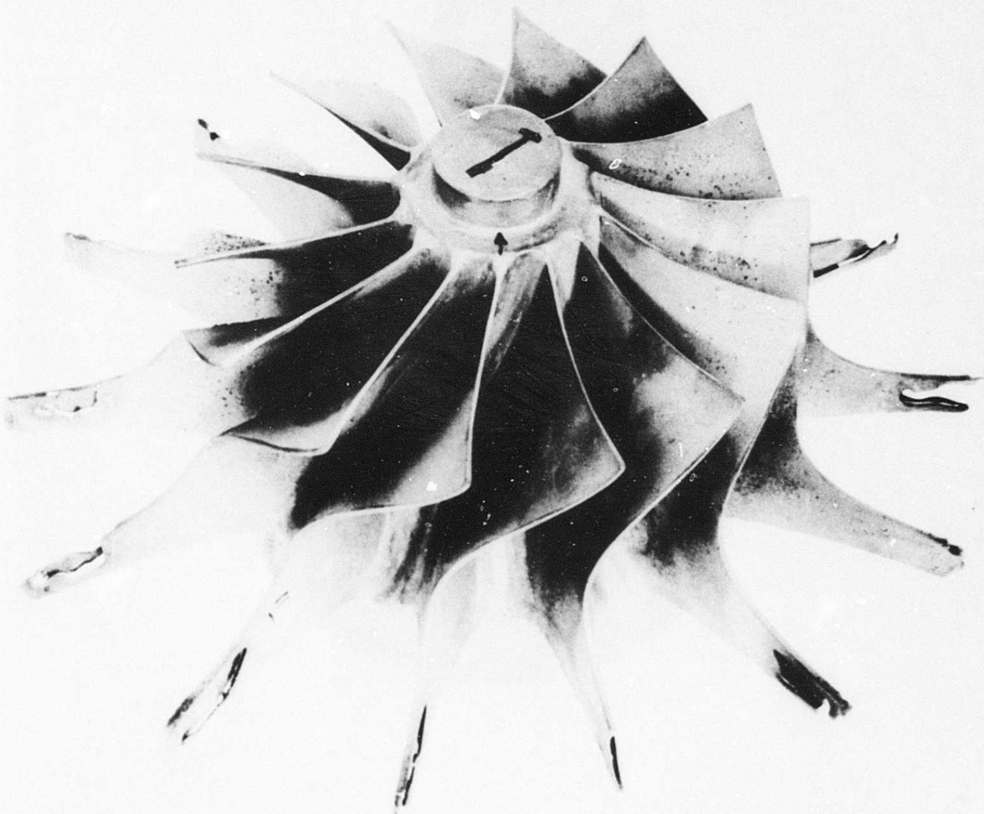

Figure 102. Overall View of Part No. A-1
as Received from Vendor.

Figure 103. Casting Deficiencies Shown in Vendor Part No. A-1 (View 1).

Figure 104. Casting Deficiencies Shown in Vendor Part No. A-1 (View 2).

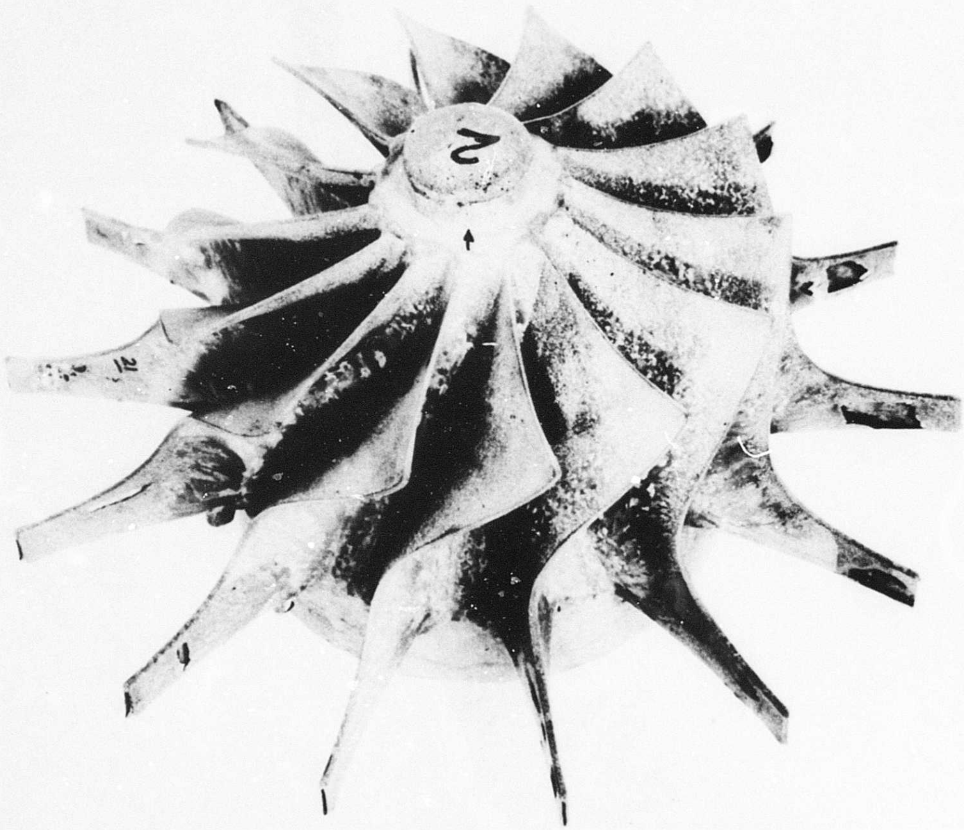

Figure 105. Overall View of Part No. A-2
as Received from Vendor.

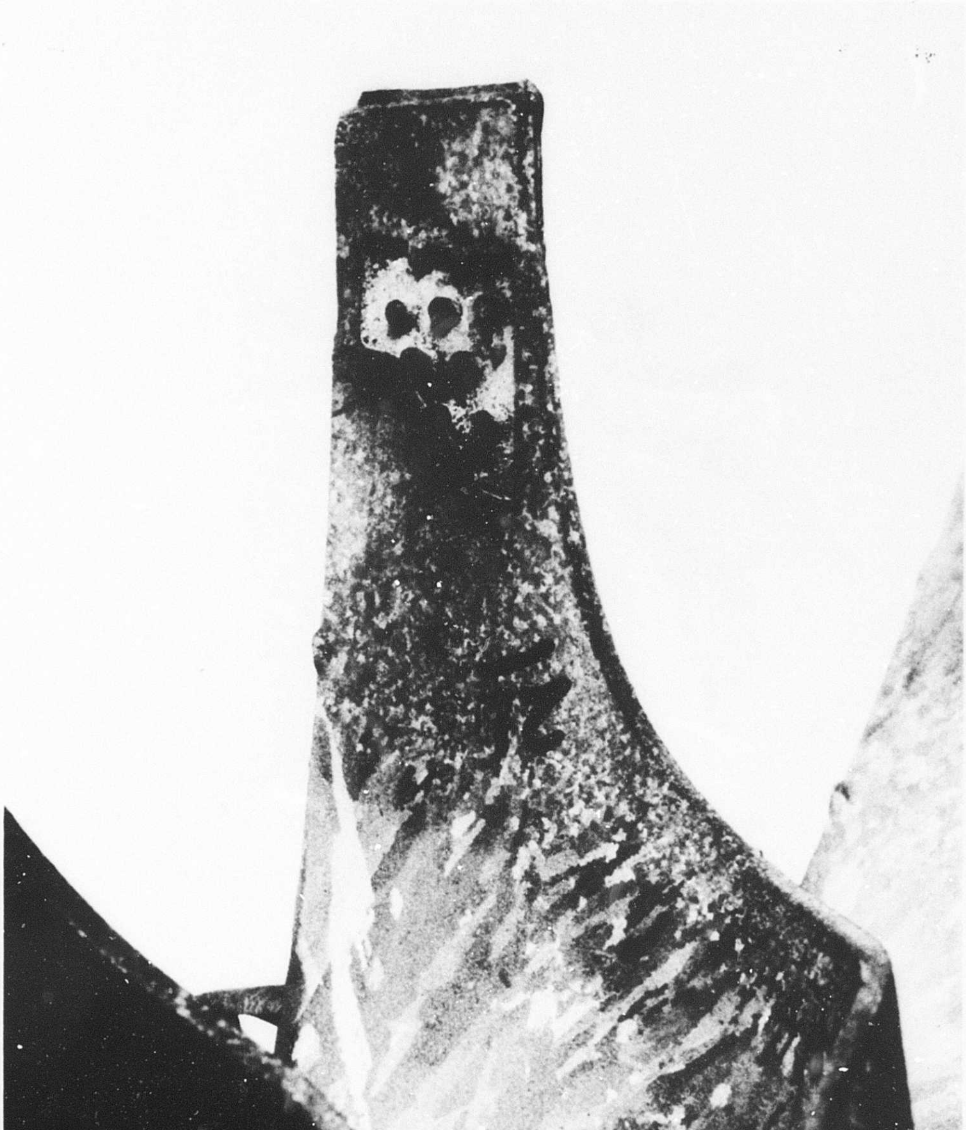

Figure 106. Part No. A-2 as Received from Vendor Showing Core Breakthrough.

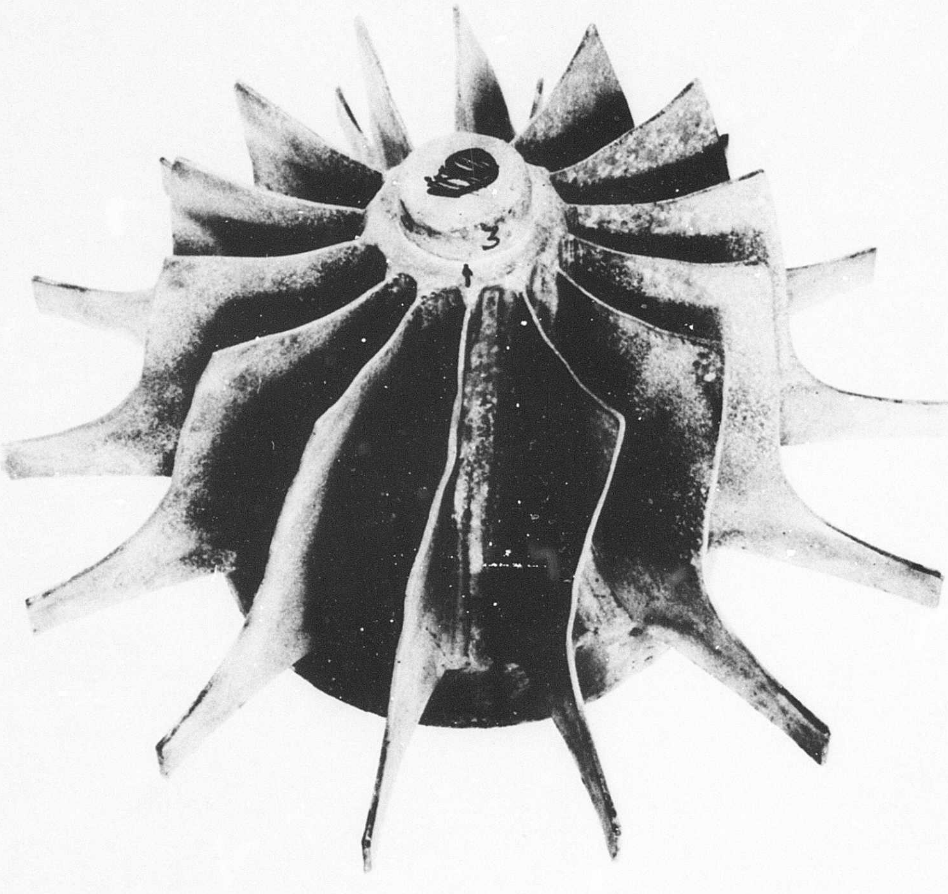

Figure 107. Overall View of Part No. A-3 as Received from Vendor.

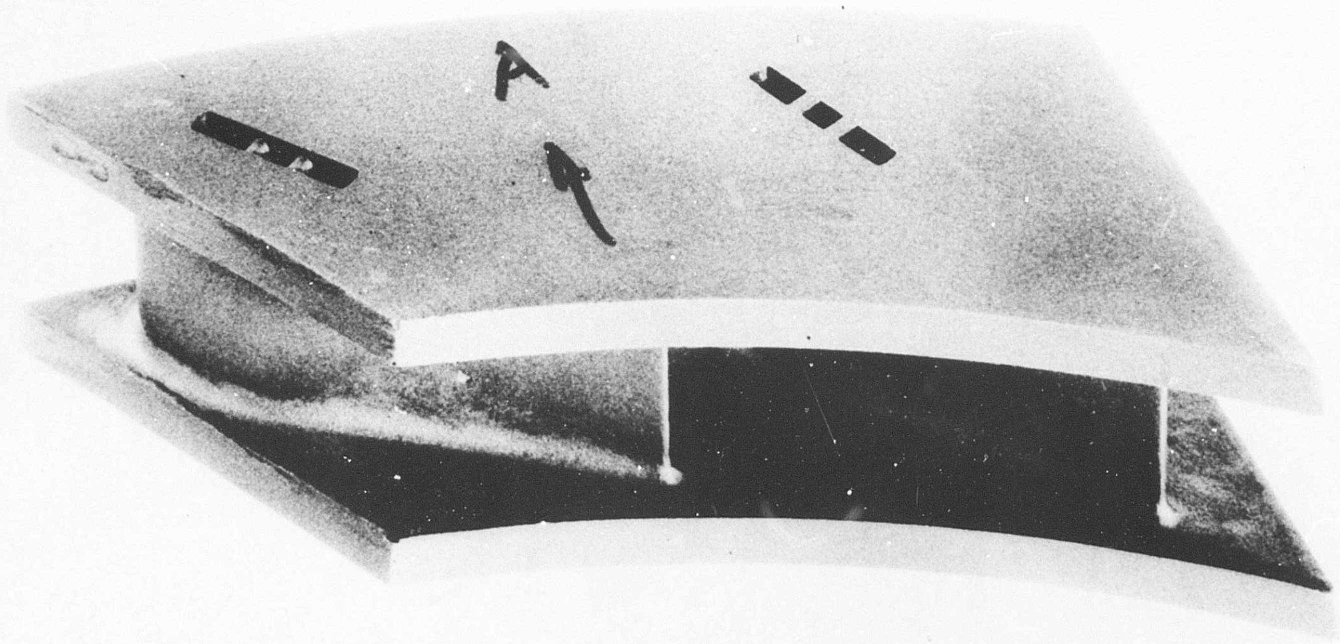

Figure 108. Nozzle Vane Segment, Part No. A-4.

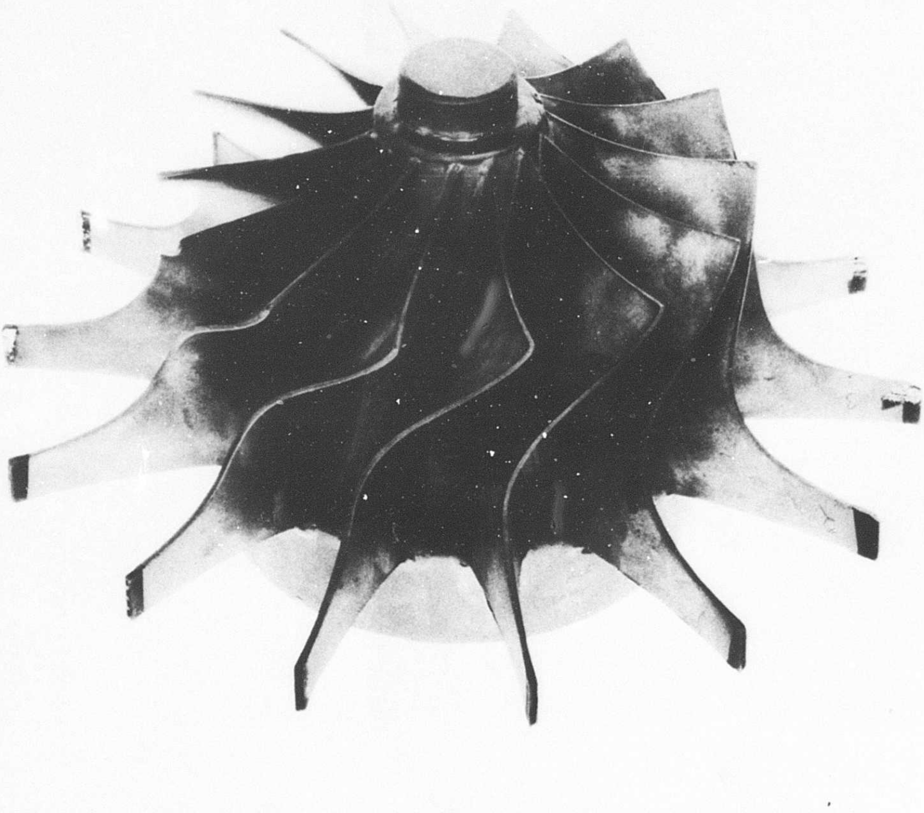

Figure 109. Overall View of Vendor Part No. C-1.

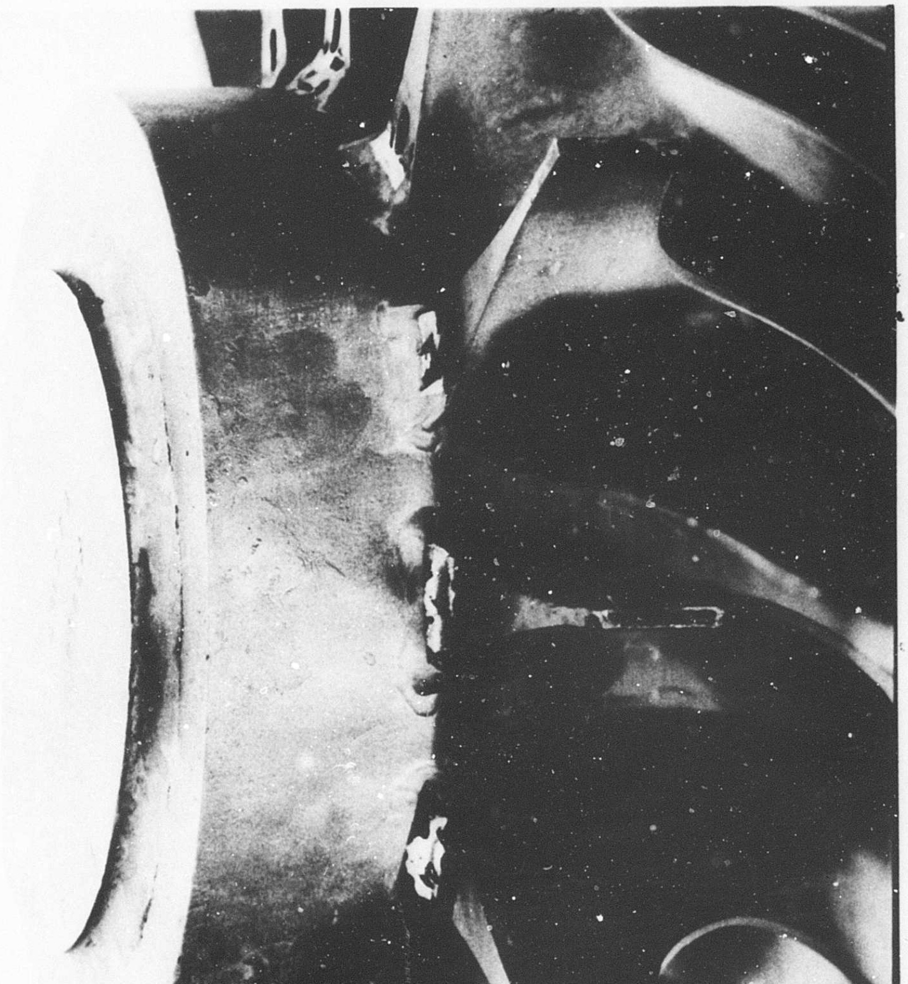

Figure 110. Typical Leading Edge, Part No. C-1.

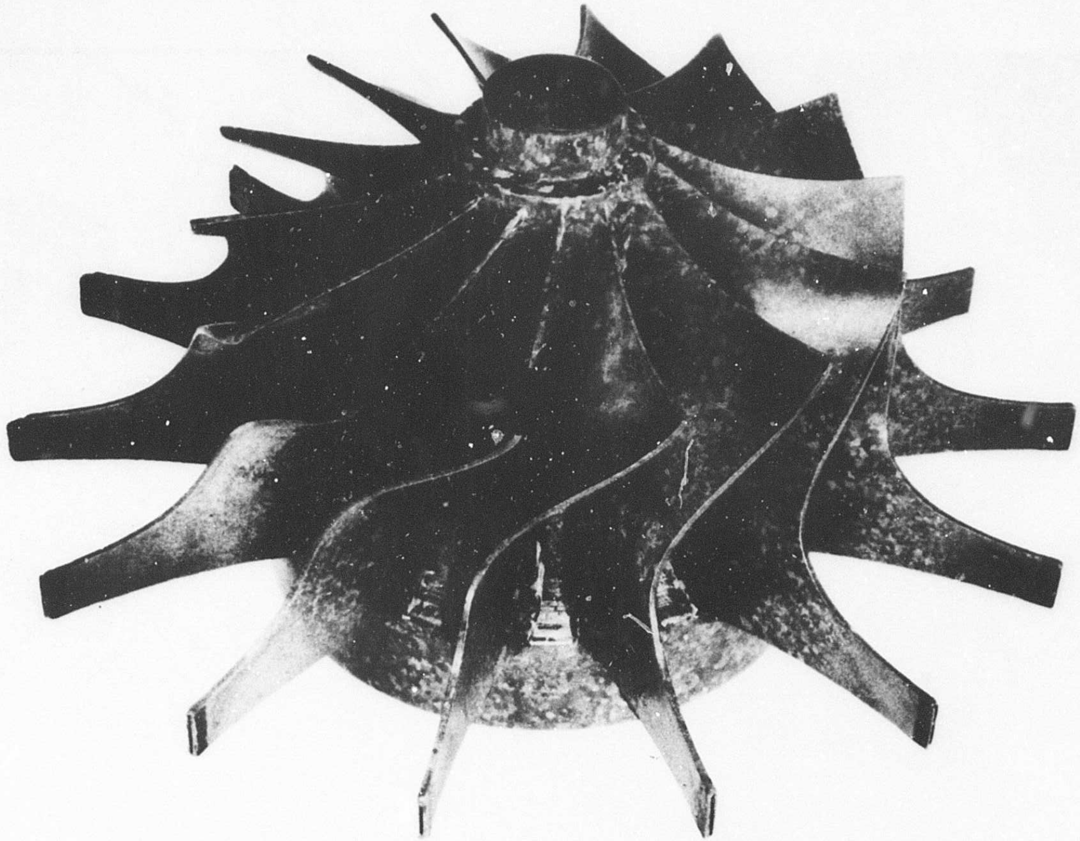

Figure 111. Overall View of Part No. C-2 After Etching.

Figure 112. Closeup View of Part No. C-2.

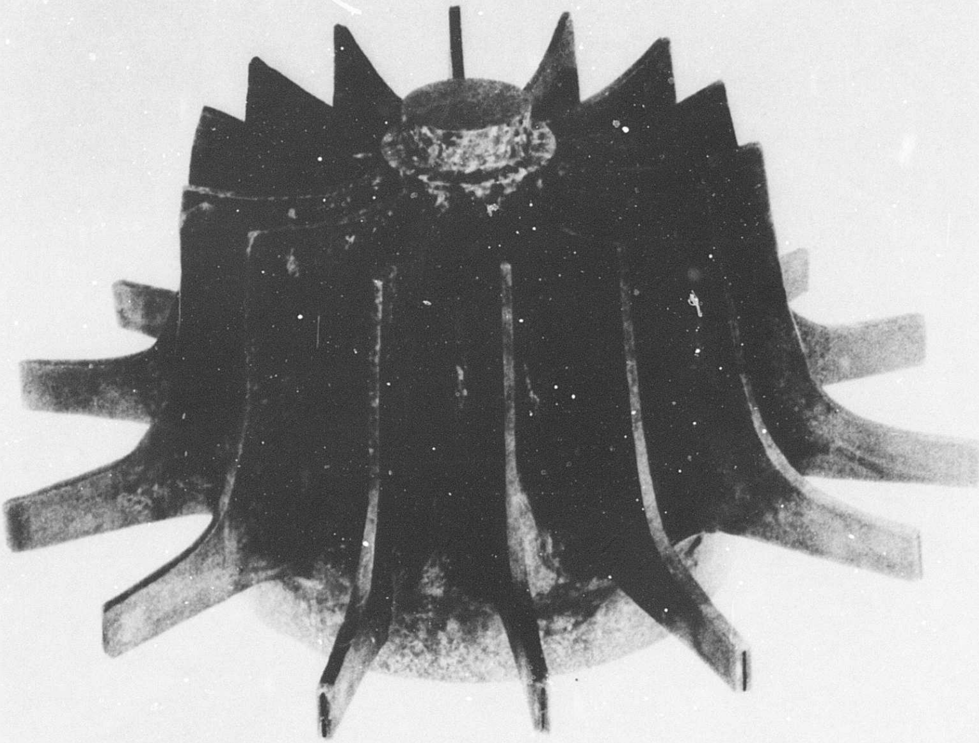

Figure 113. Overall View of Part No. C-3 After Etching.

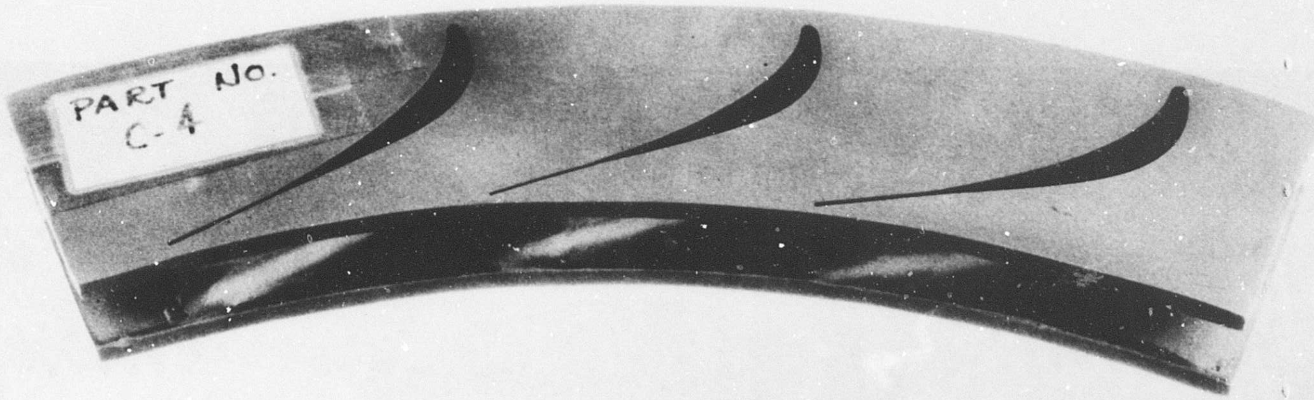

Figure 114. Nozzle Segment, Part No. C-4.

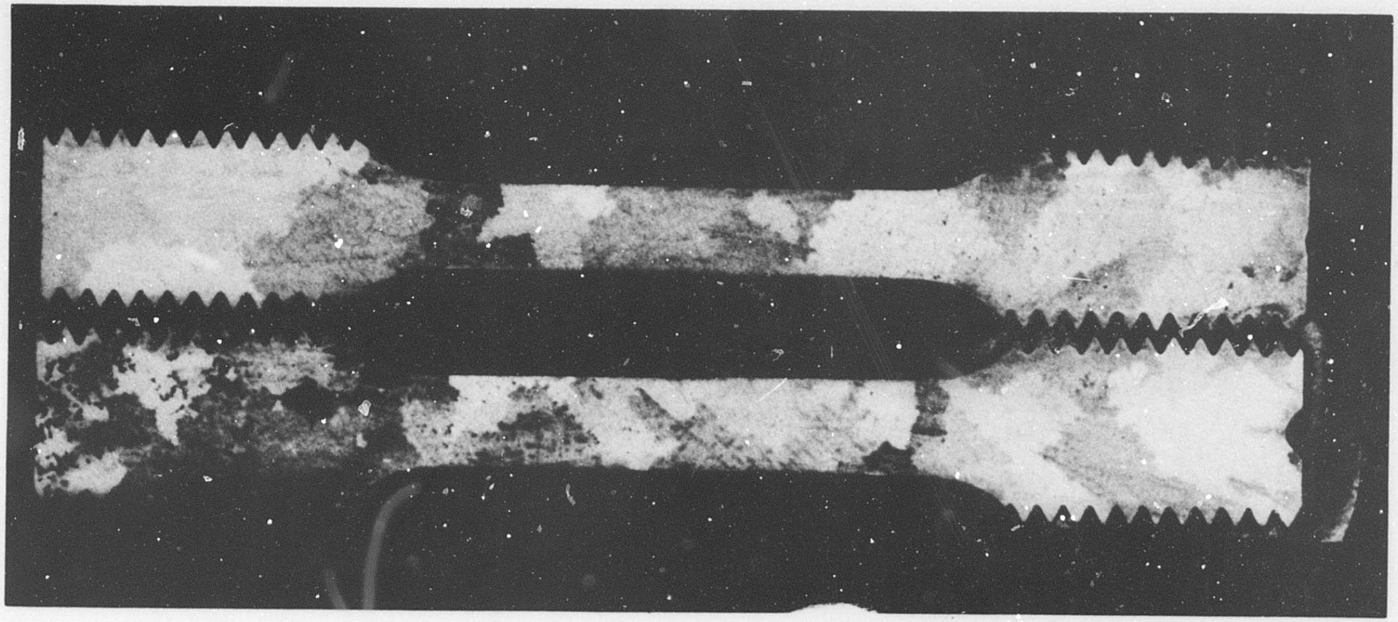

Figure 115. Vendor A Round Specimen.

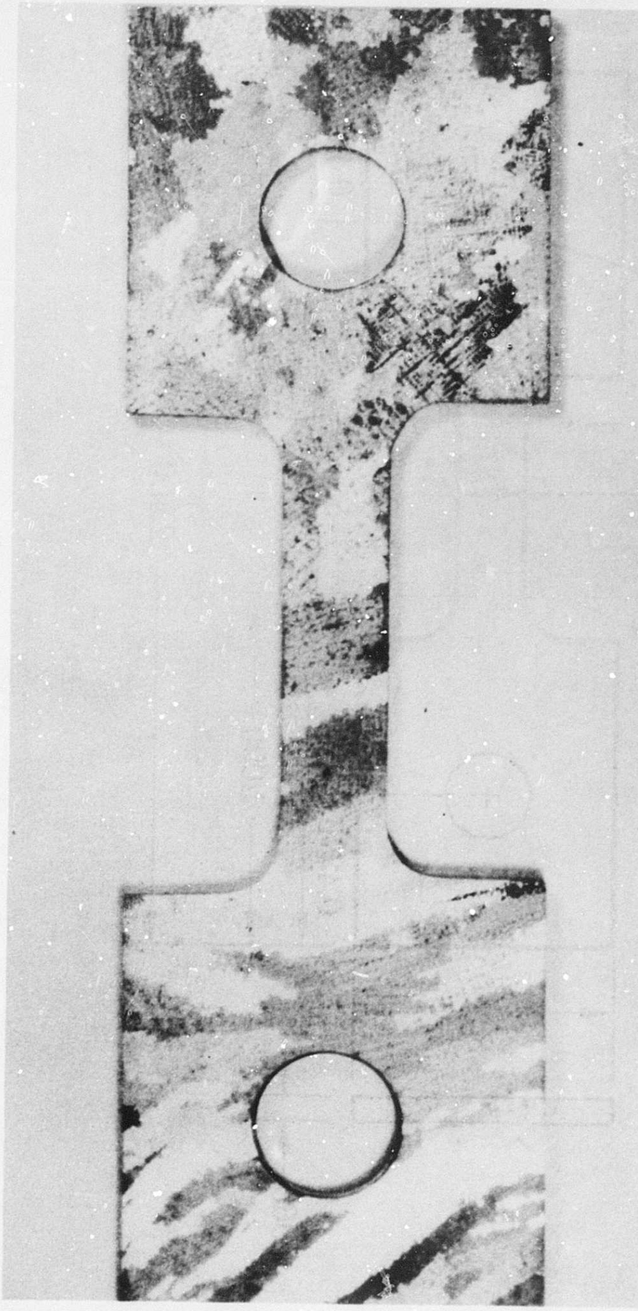

Figure 116. Vendor A Flat Specimen.

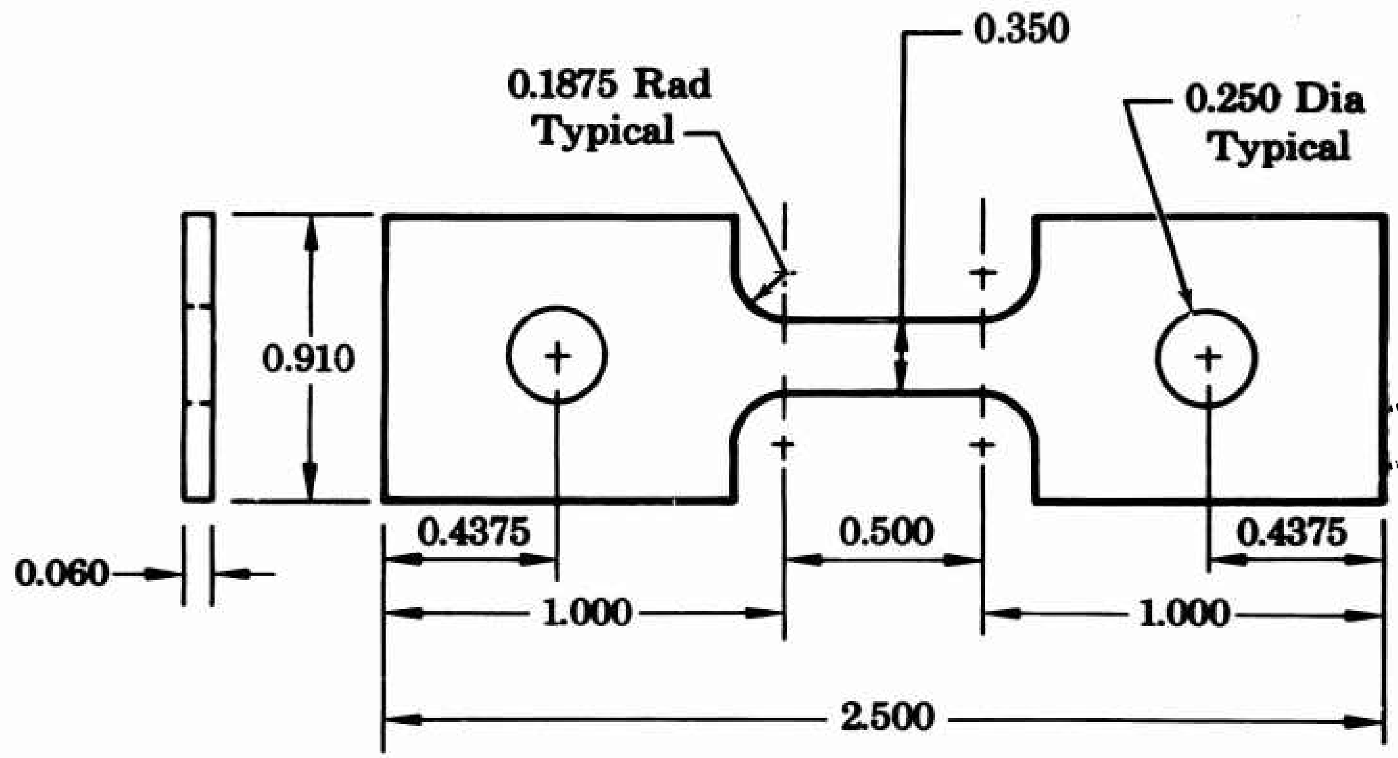

Dimensions in Inches

Figure 117. Modified Flat Metallurgical Specimen.

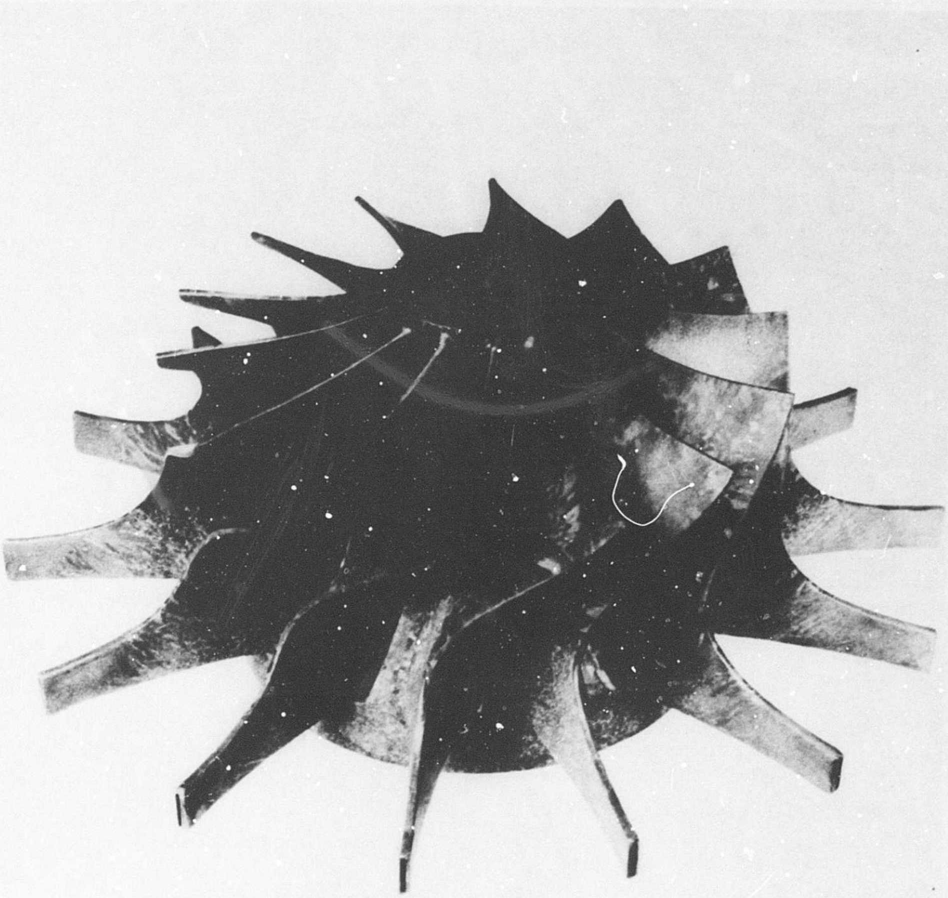

Figure 118. Overall View of Part No. B-1 After Etching.

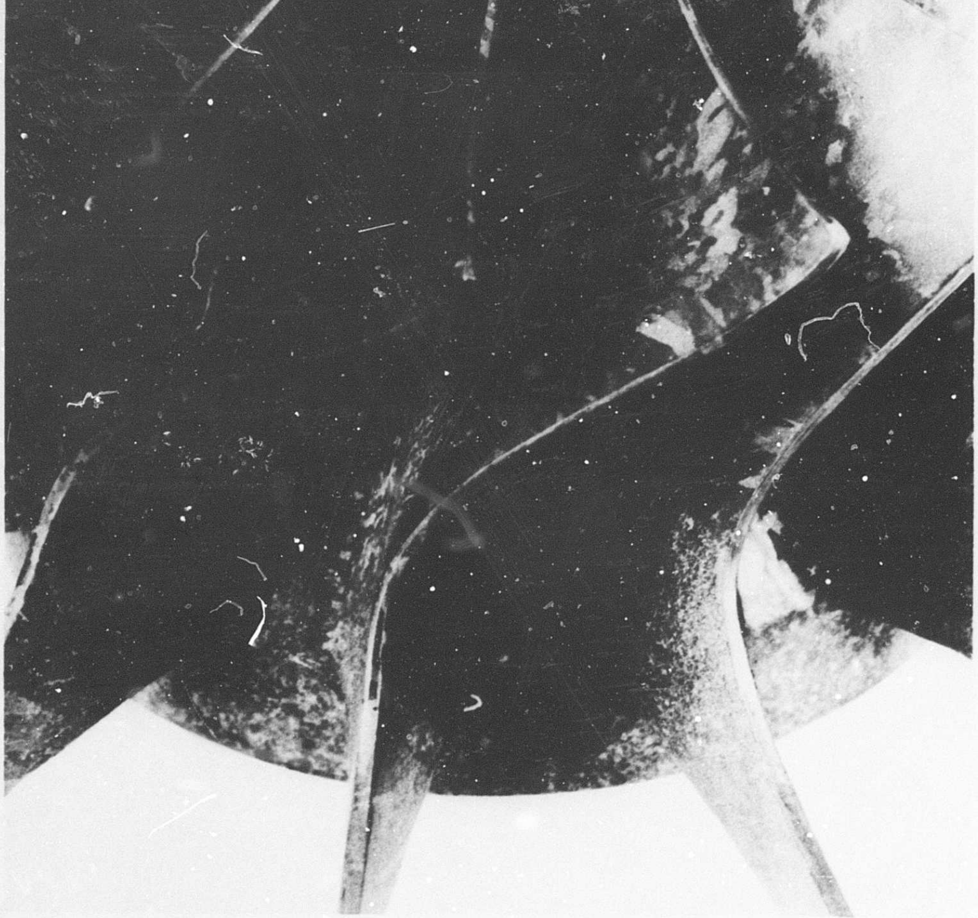

Figure 119. Closeup View of Part No. B-1
After Etching (View 1).

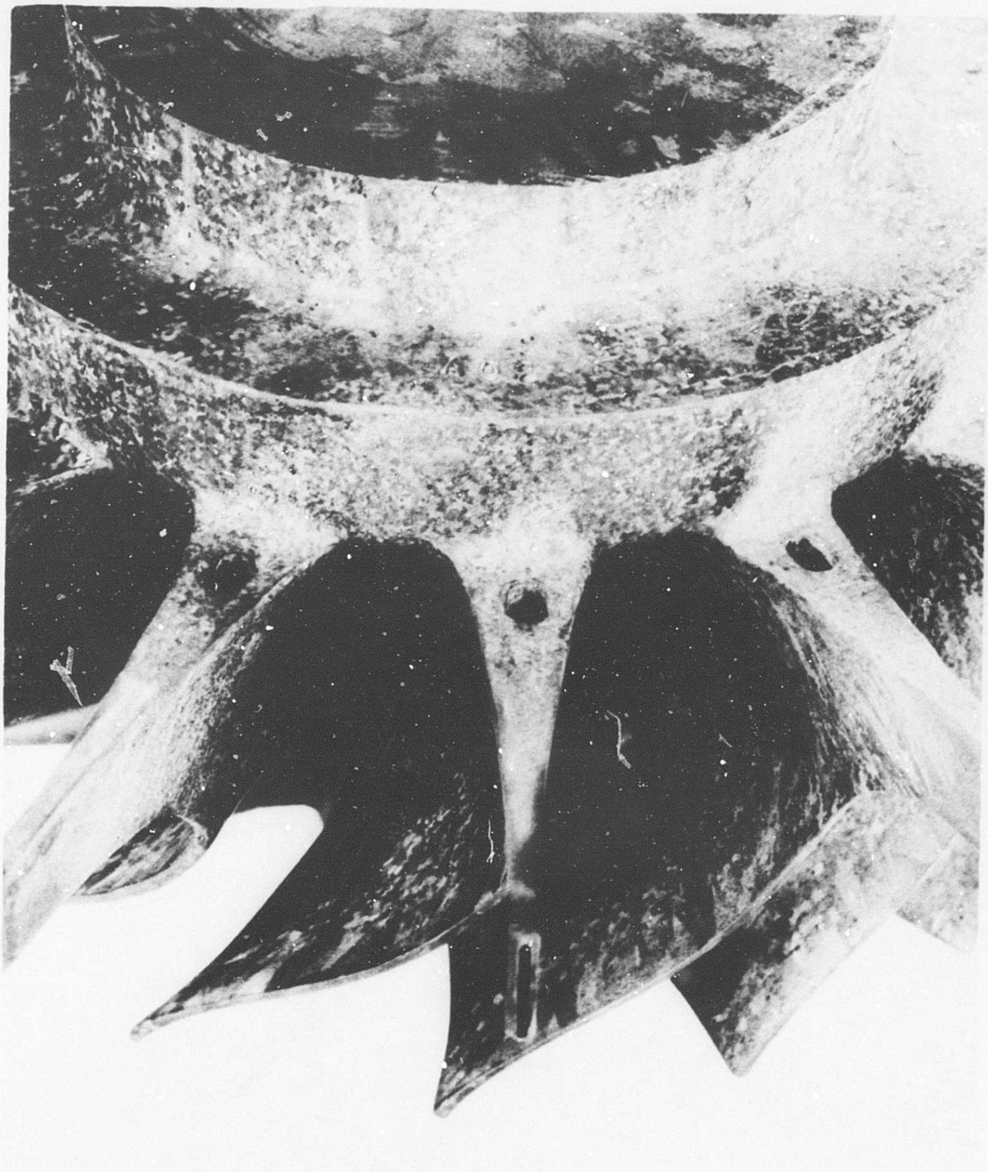

Figure 120. Closeup View of Part No. B-1
After Etching (View 2).

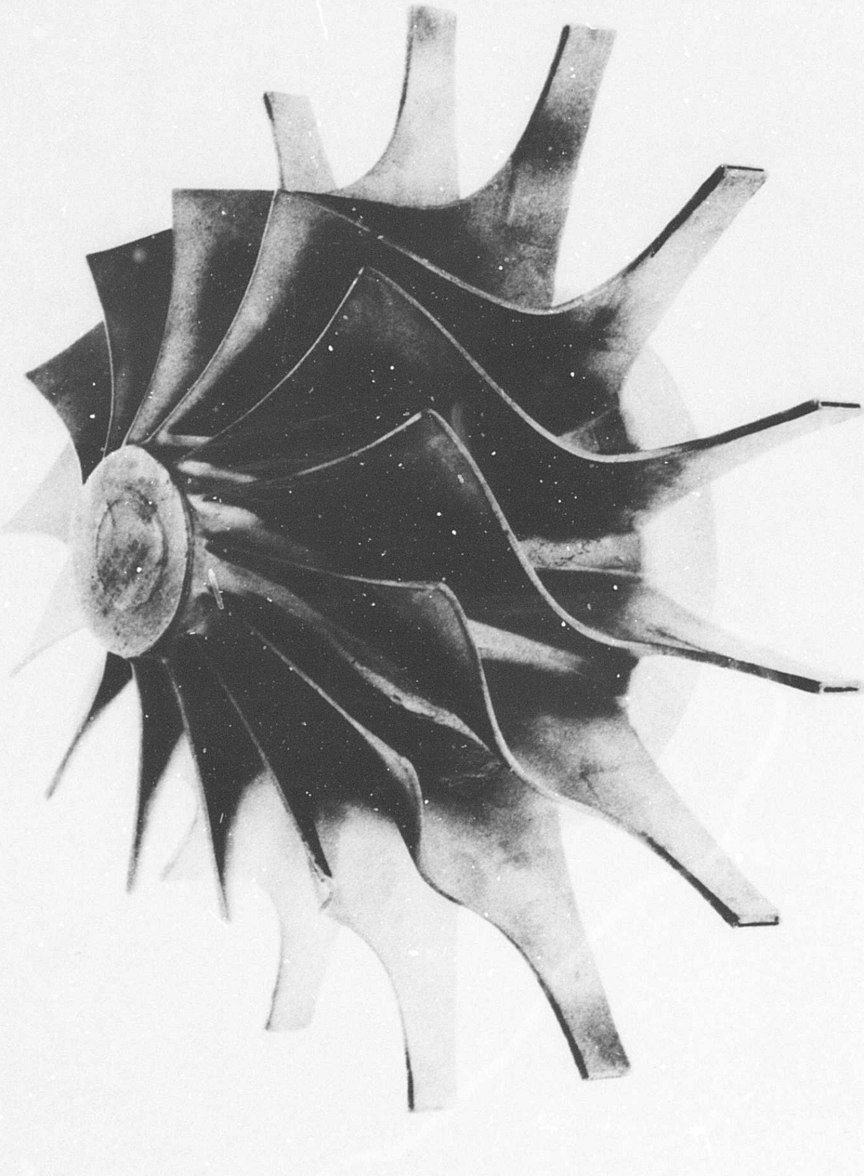

Figure 121. Overall View of Part No. B-2
Before Etching.

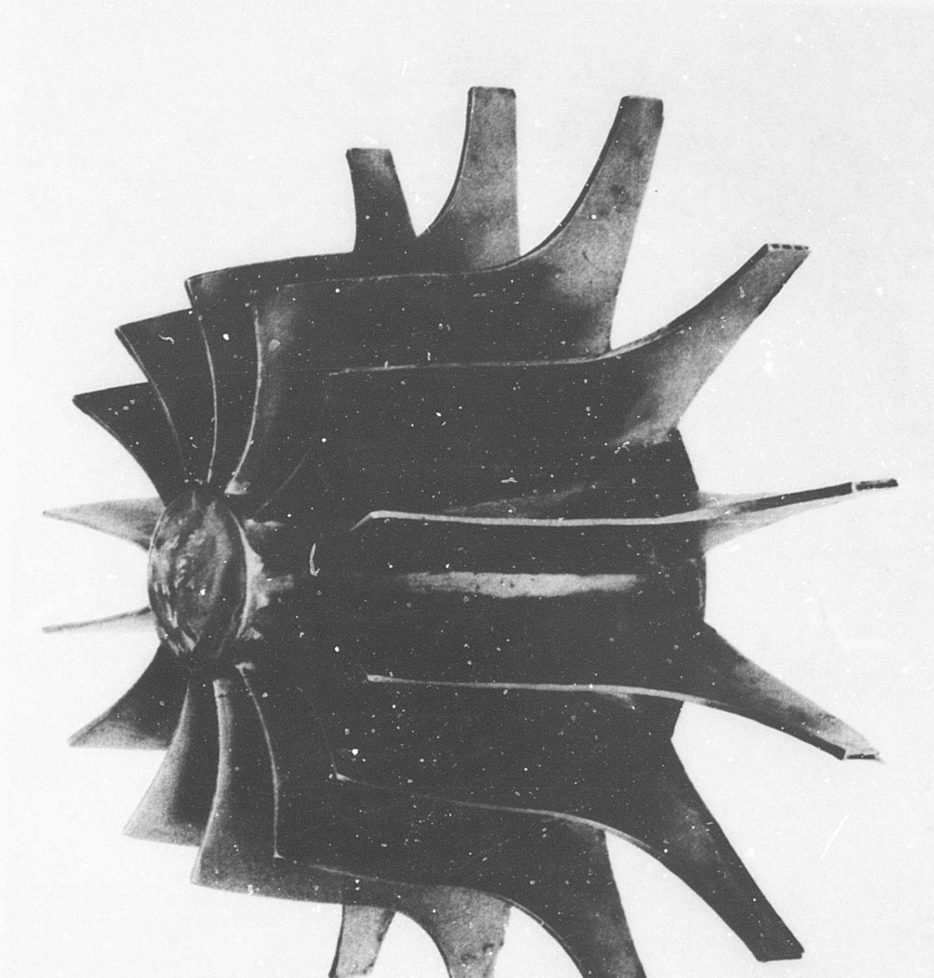

Figure 122. Overall View of Part No. D-3
Before Etching.

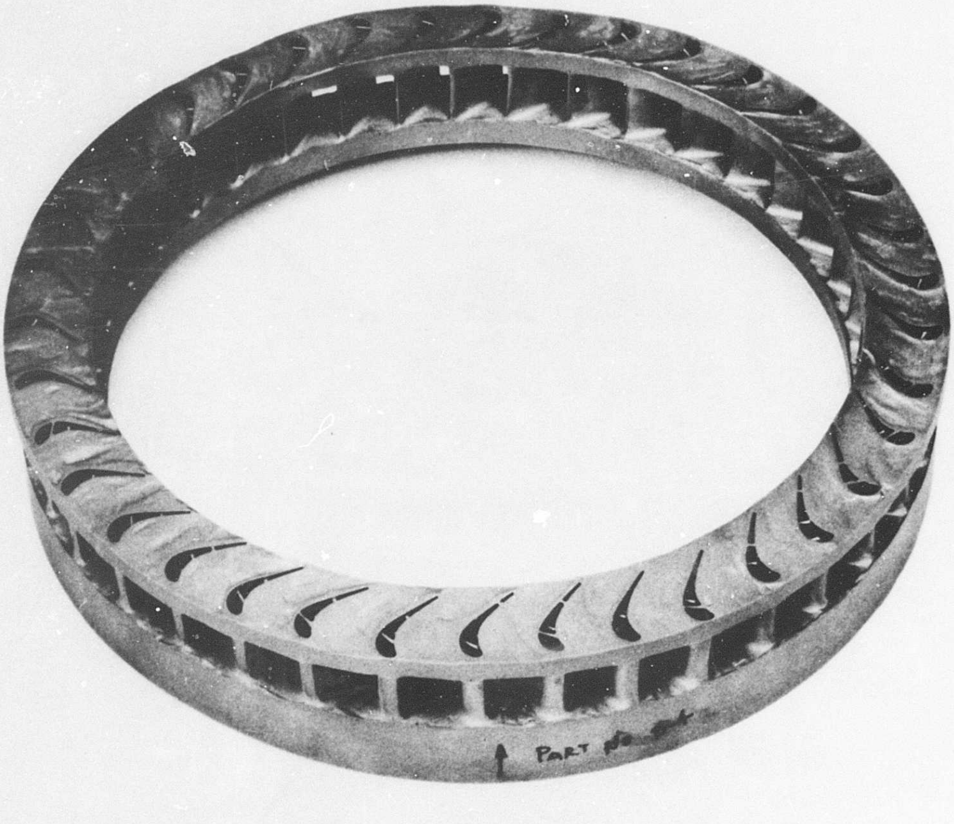

Figure 123. Overall View of Part No. B-4
Before Etching.

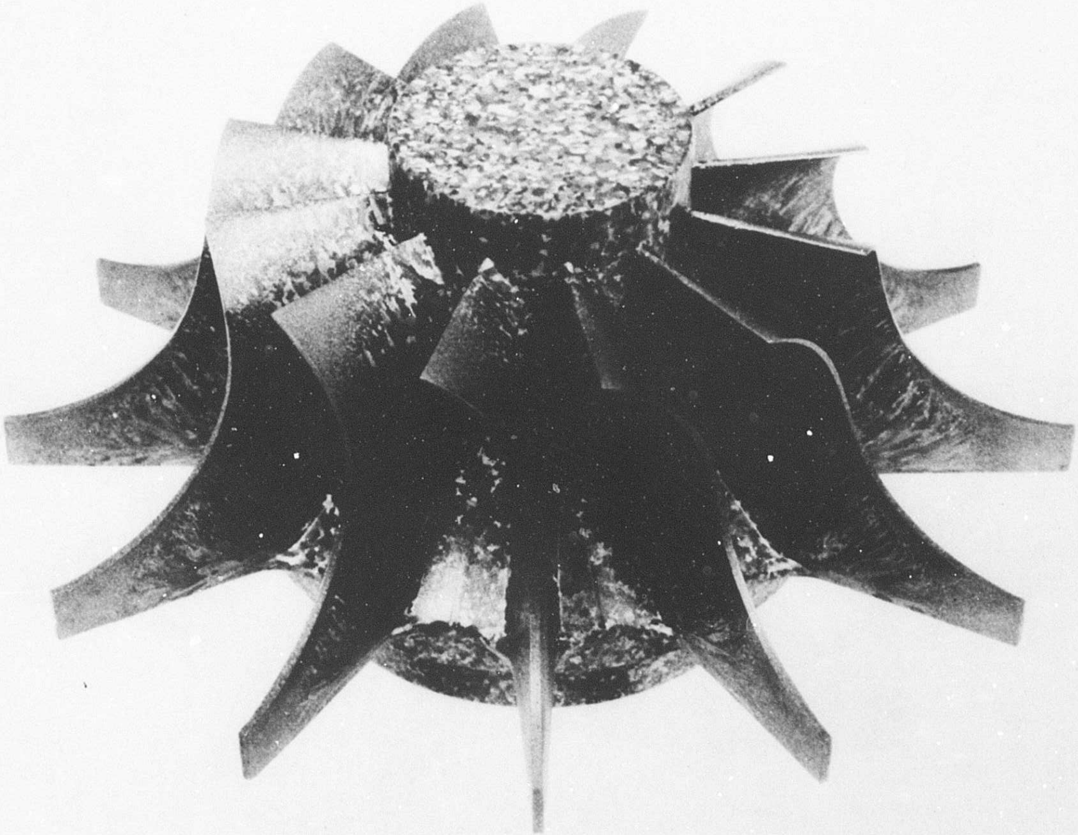

Figure 124. Overall View of Part No. B-5 After Etching.

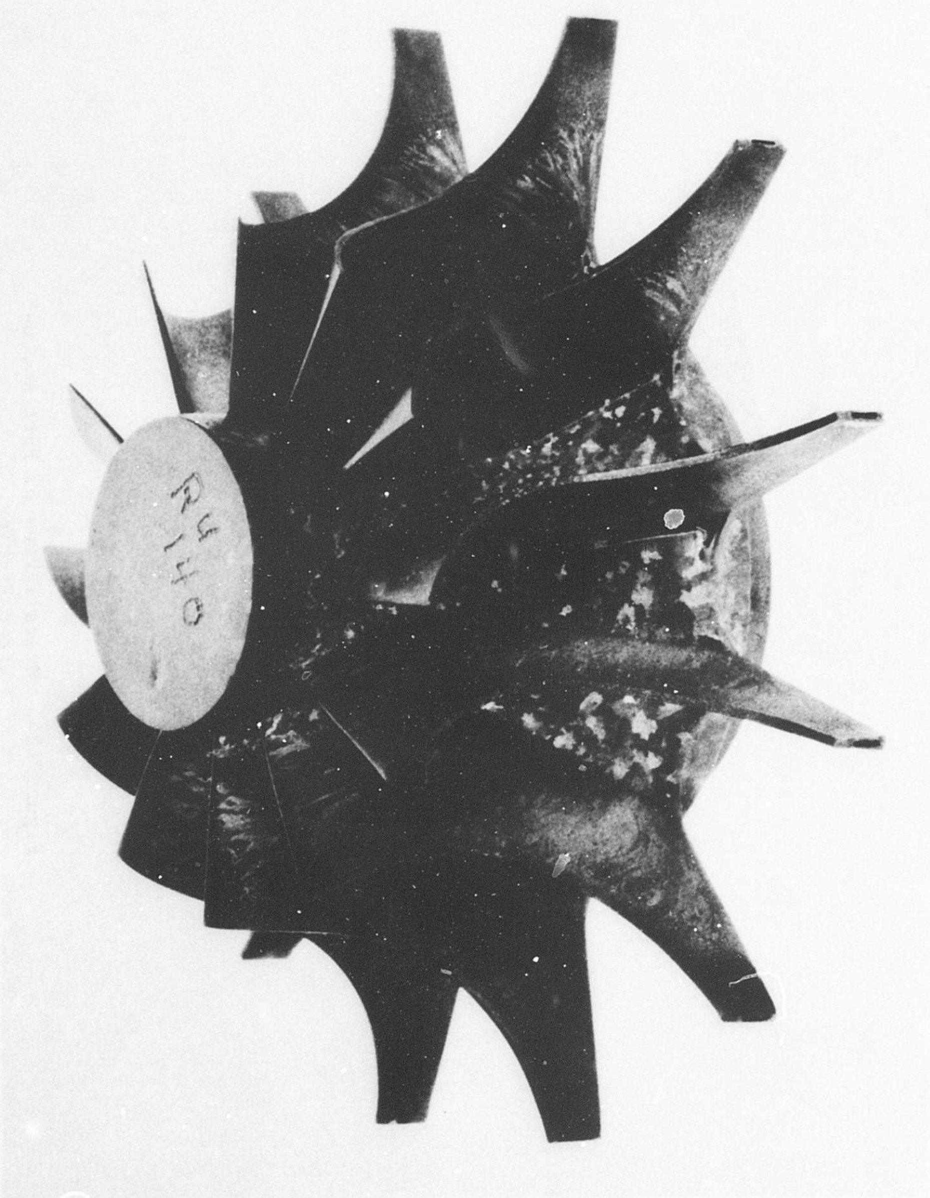

Figure 125. Overall View of Part No. B-6
After Etching.

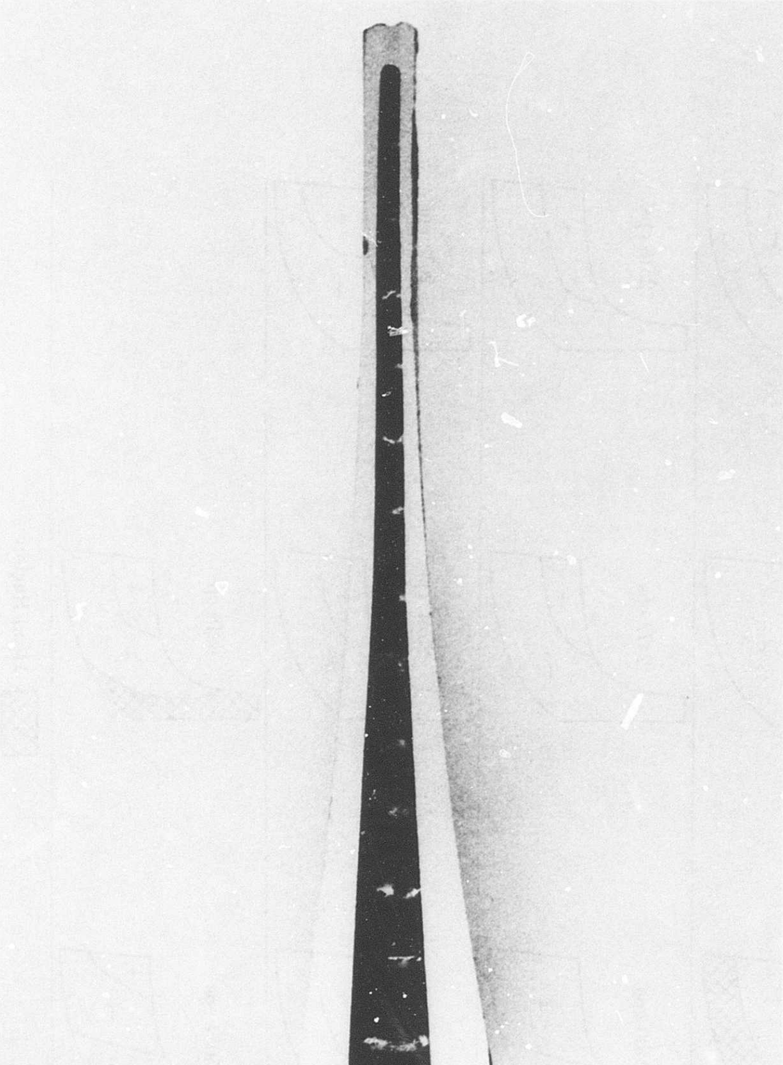

Figure 126. Cross Section of Rotor
Tip Brazed Closed.

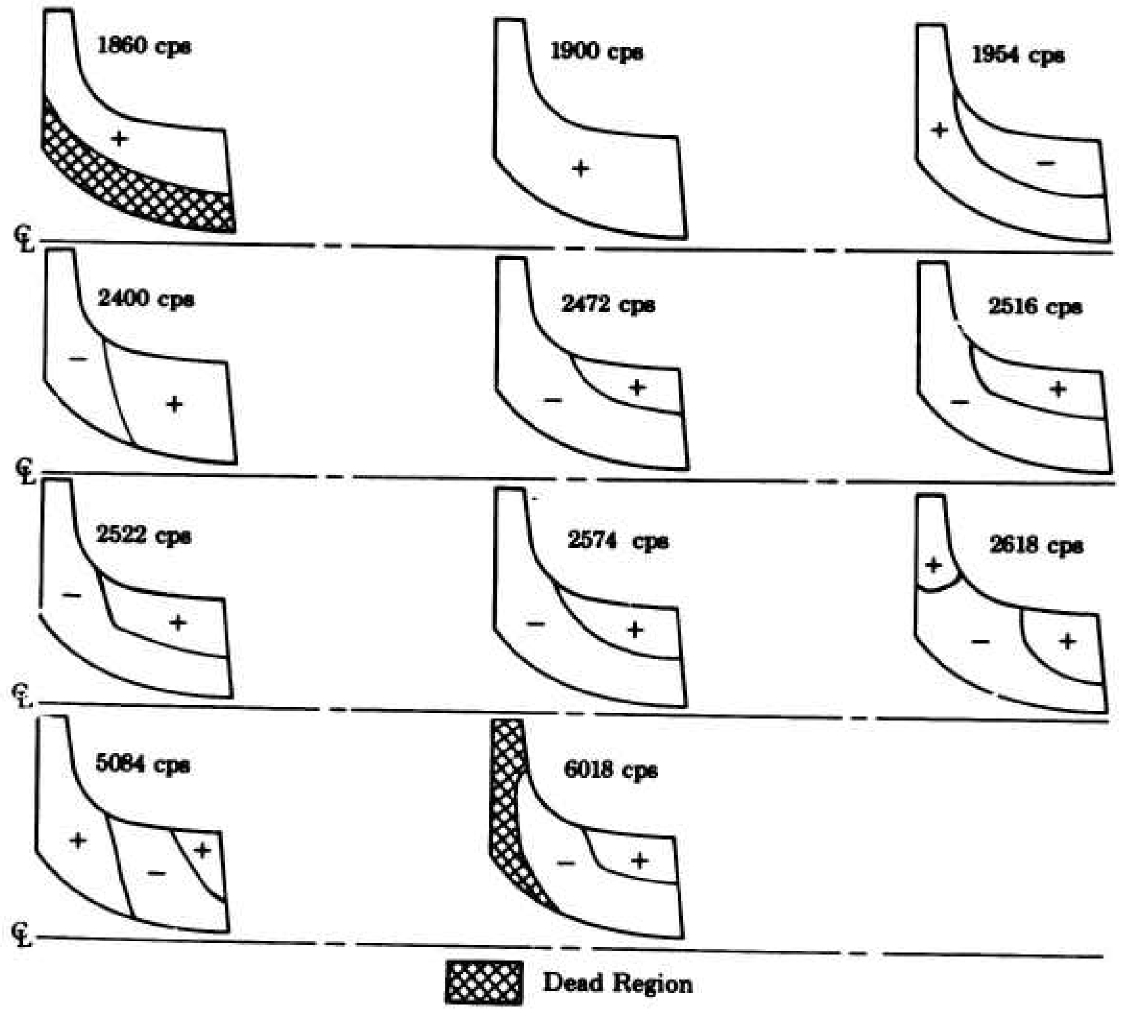

Figure 127. Nodal Patterns of 11-Inch Diameter Rotor, Blade No. 5 (Highest Natural Frequency).

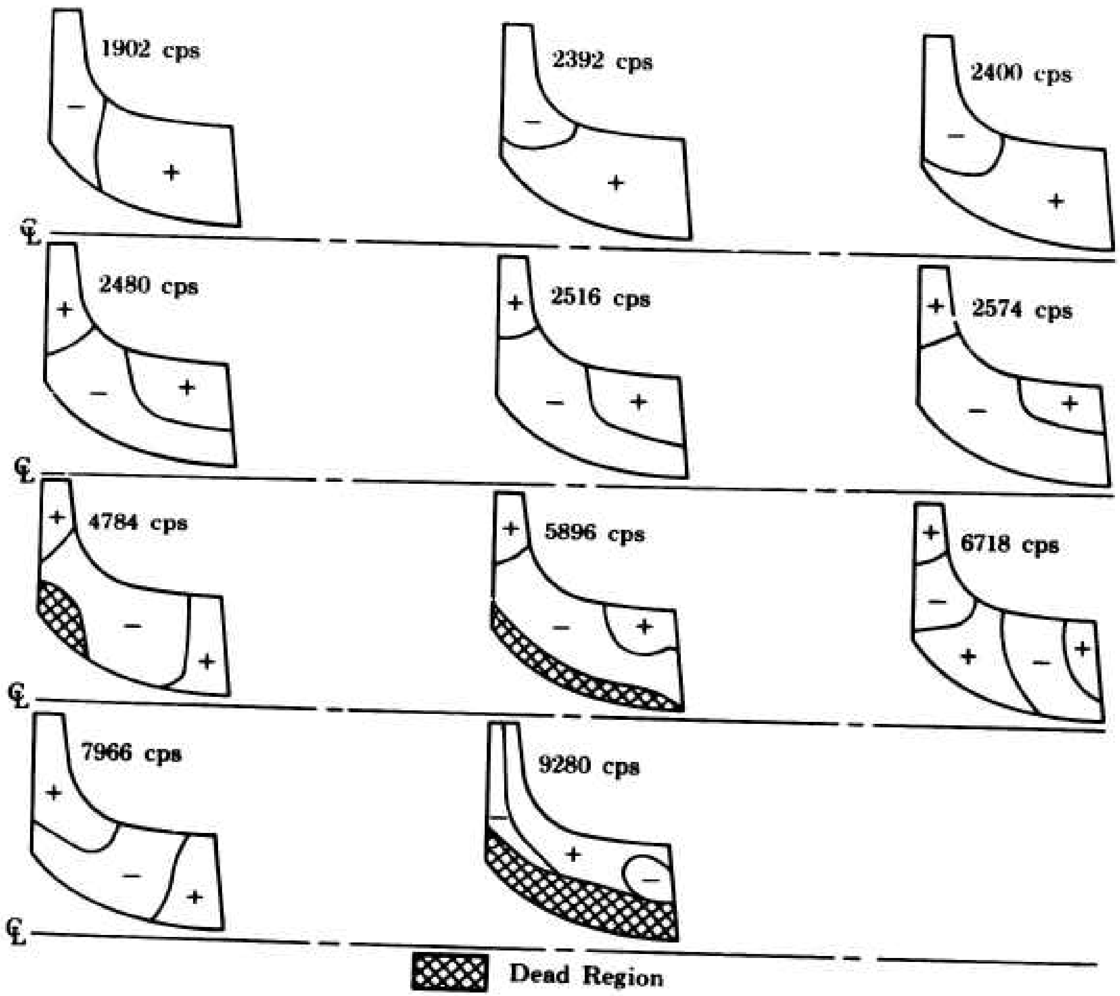

Figure 128. Nodal Patterns of 11-Inch Diameter Rotor, Blade No. 7 (Lowest Natural Frequency).

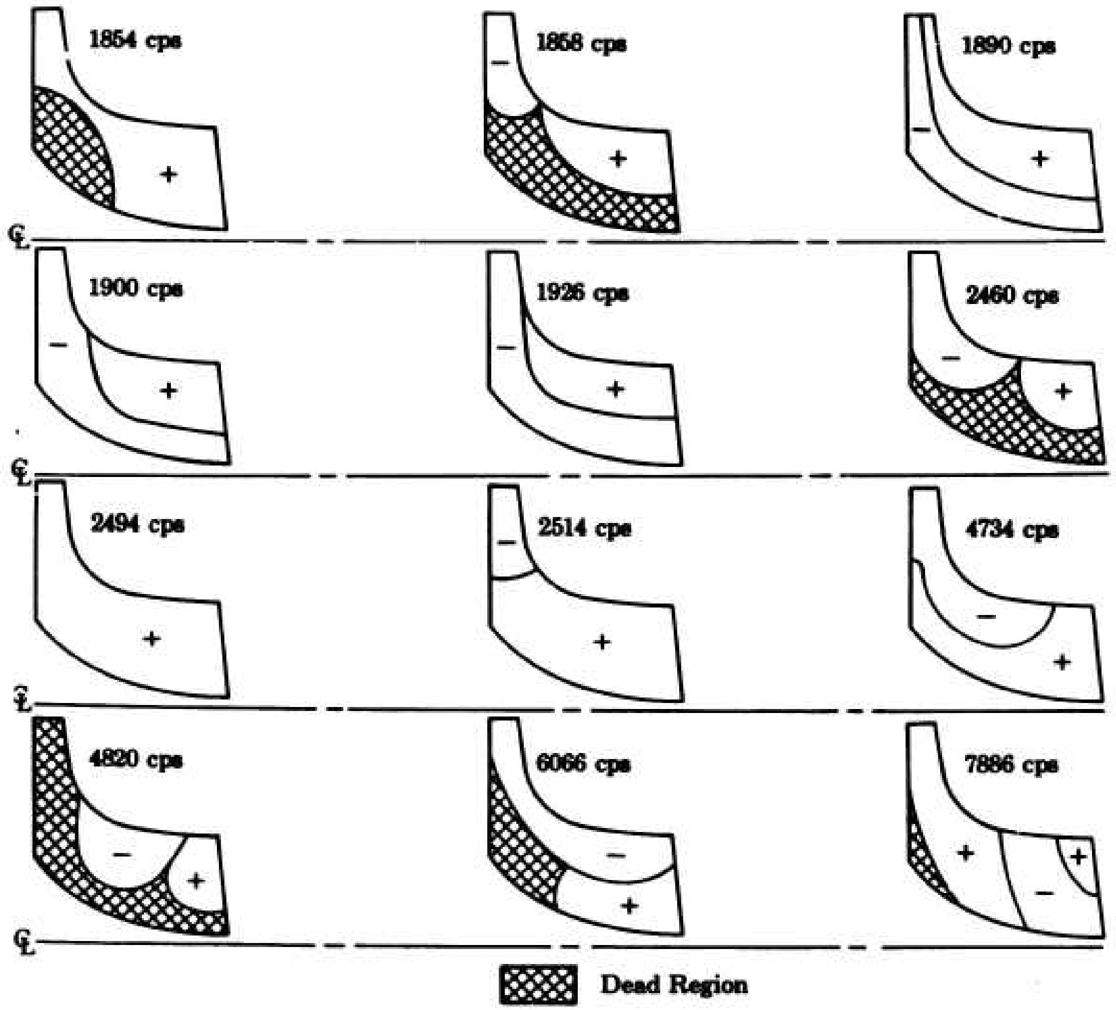

Figure 129. Nodal Patterns of 11-Inch Diameter Rotor, Blade No. 8 (Average Natural Frequency).

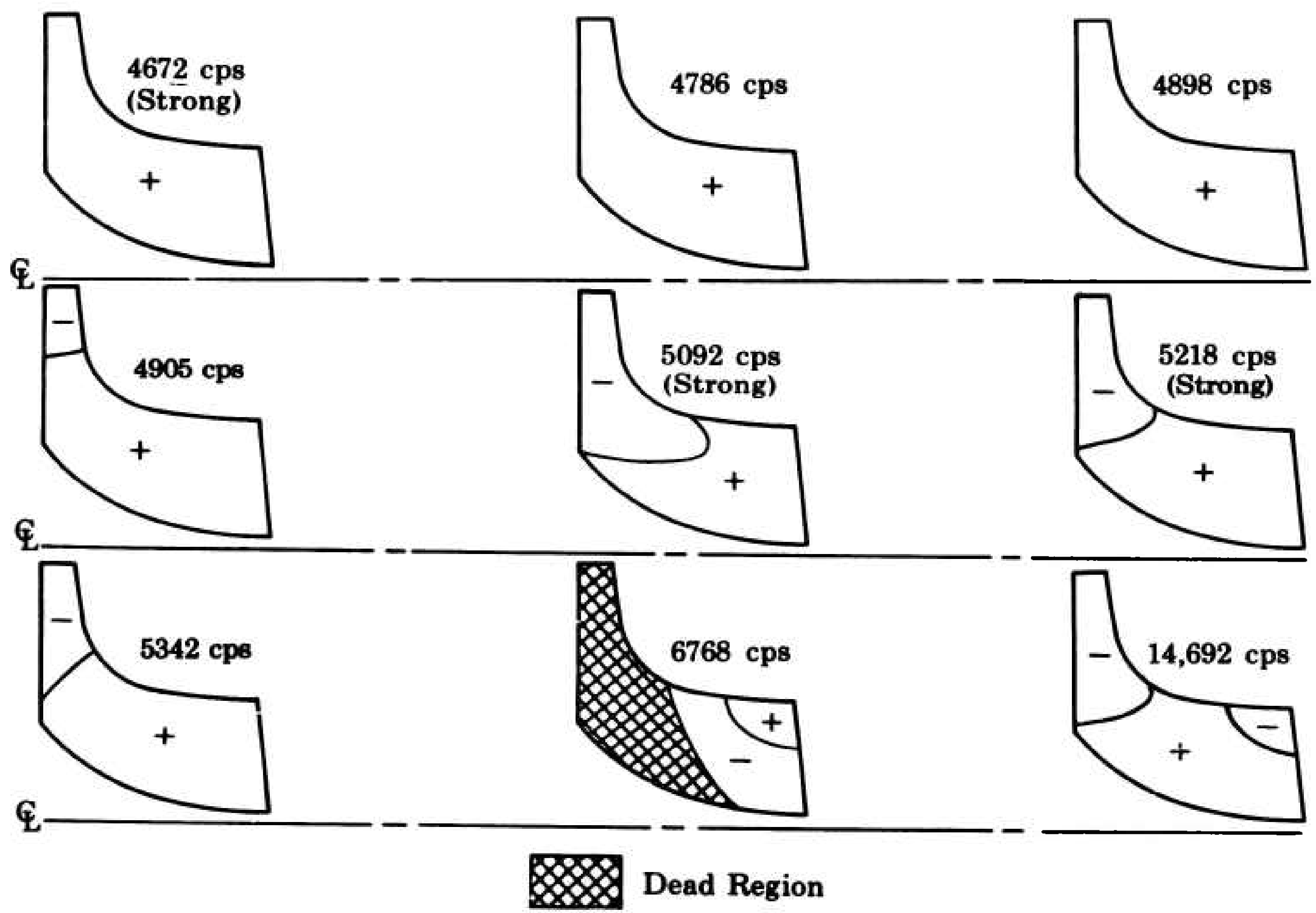

Figure 130. Nodal Patterns of 8-Inch Diameter Rotor (Blade No. 5).

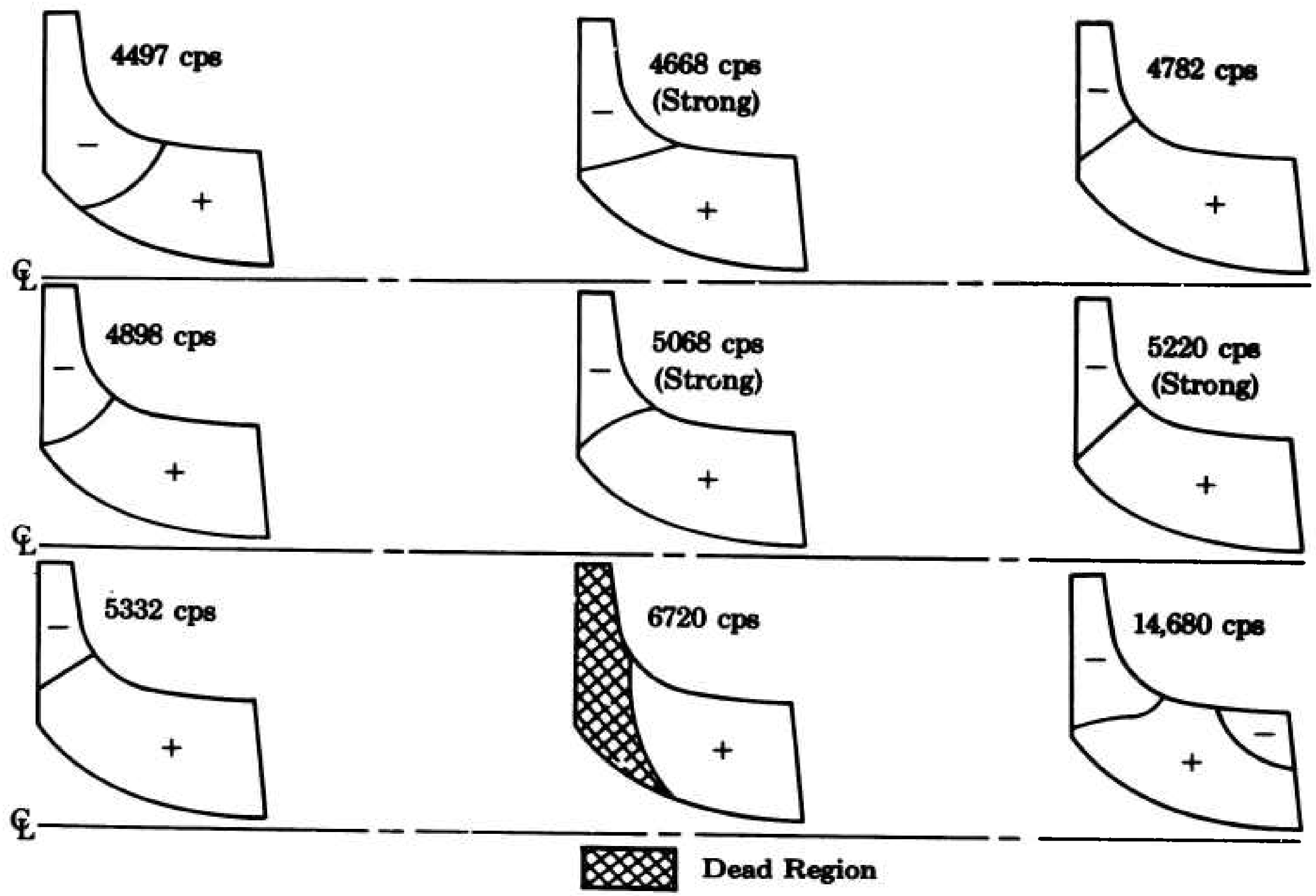

Figure 131. Nodal Patterns of 8-Inch Diameter Rotor (Blade No. 4).

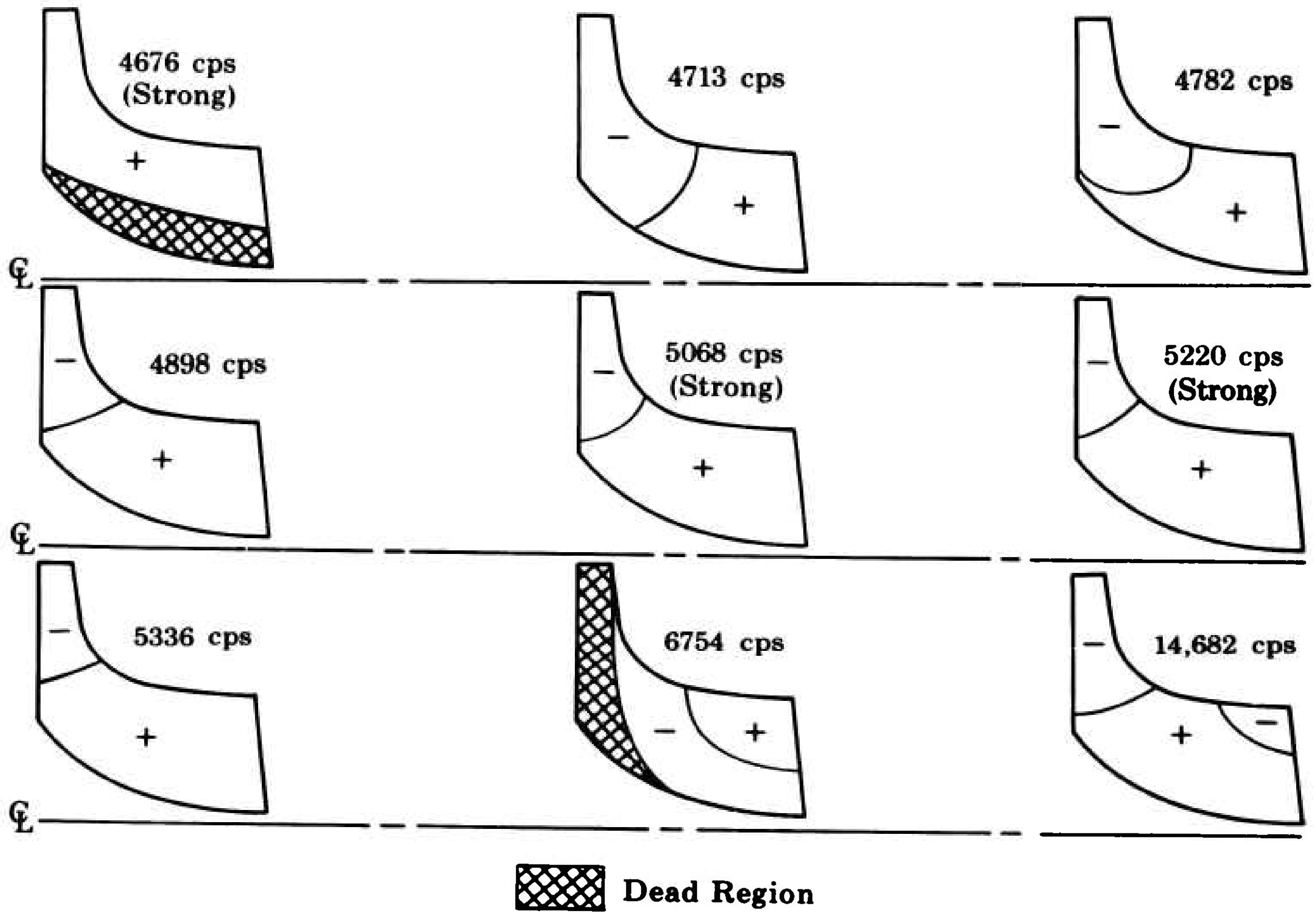

Figure 132. Nodal Patterns of 8-Inch Diameter Rotor (Blade No. 11).

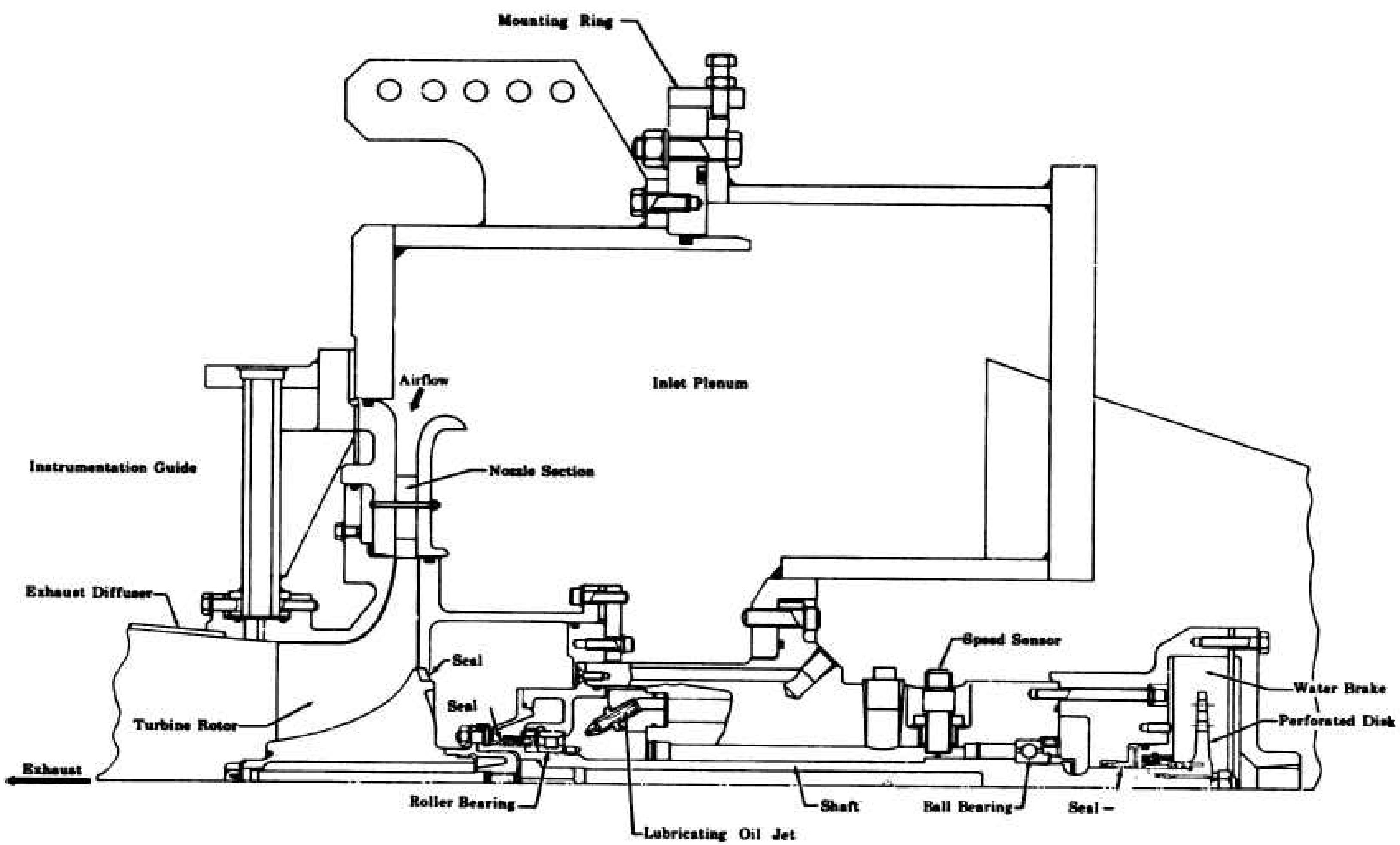

Figure 133. General Arrangement of Cold-Flow Turbine Rig.

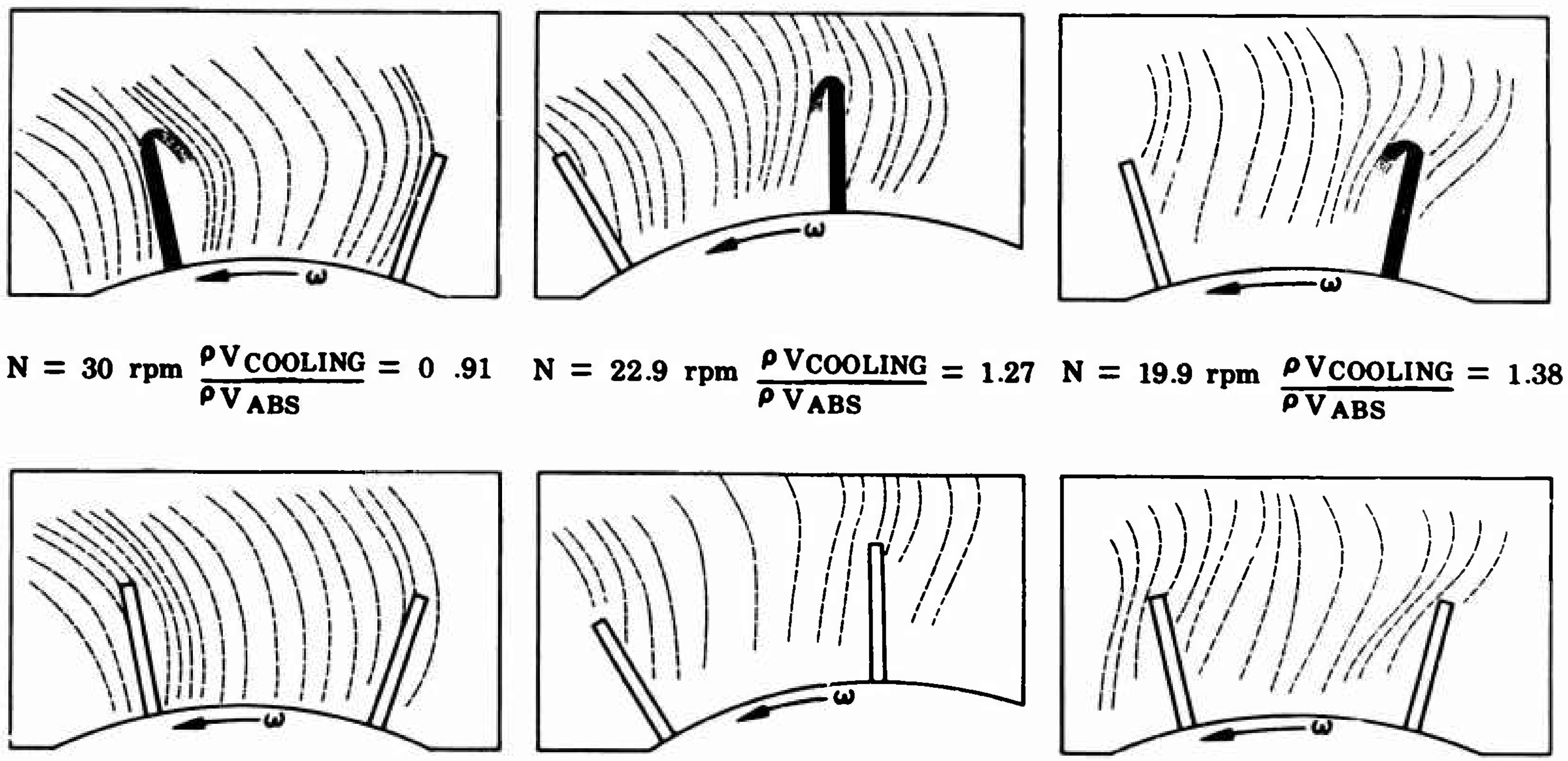

$N = 30$ rpm $\frac{\rho V_{COOLING}}{\rho V_{ABS}} = 0.91$ $N = 22.9$ rpm $\frac{\rho V_{COOLING}}{\rho V_{ABS}} = 1.27$ $N = 19.9$ rpm $\frac{\rho V_{COOLING}}{\rho V_{ABS}} = 1.38$

N = 30 rpm N = 22.1 rpm N = 18.9 rpm

Figure 134. Relative Flow Patterns With and Without Cooling Air Ejection at Rotor Tip.

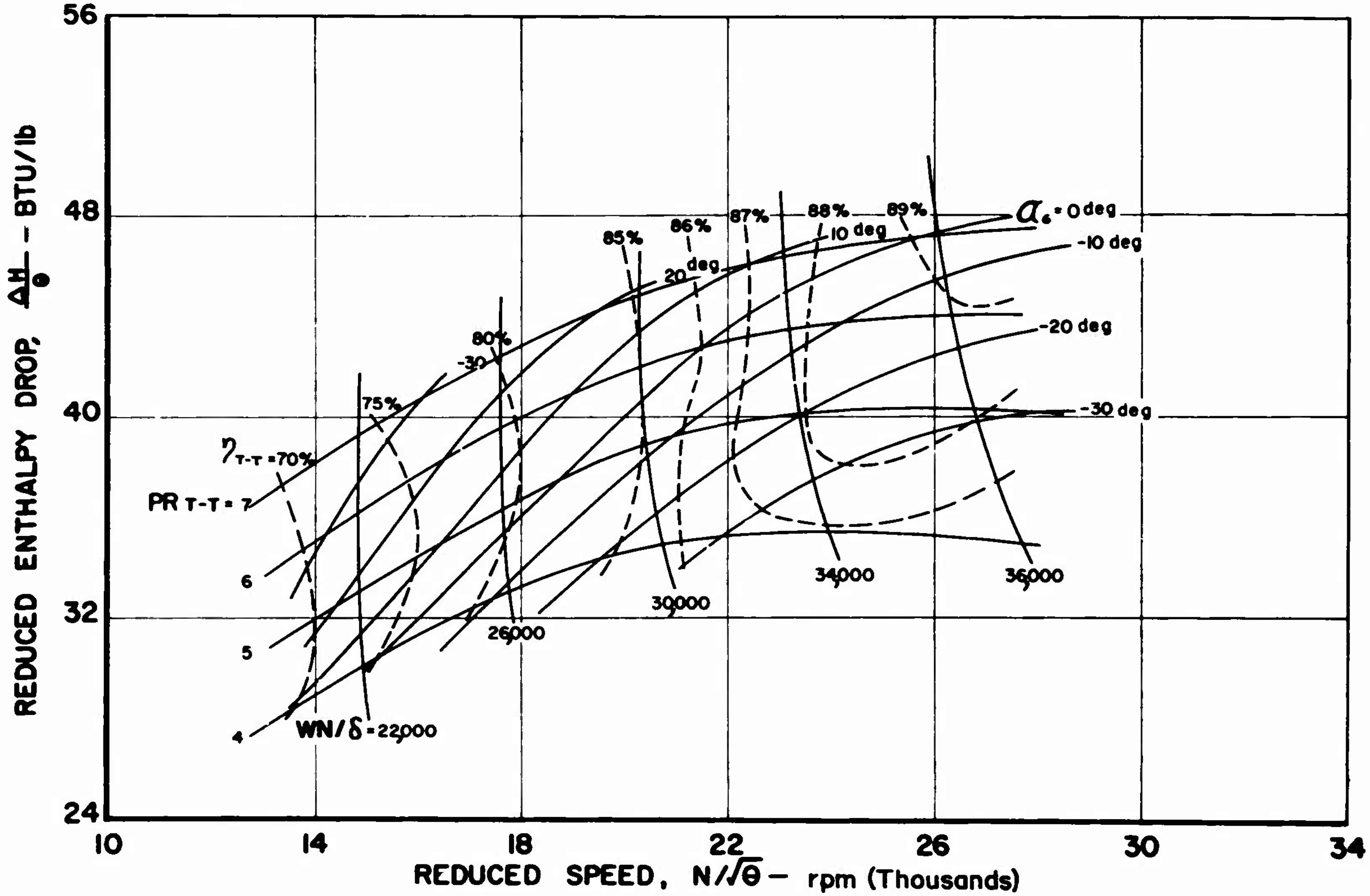

Figure 135. Universal Performance Map,
Cold-Flow Tests (Build No. 2).

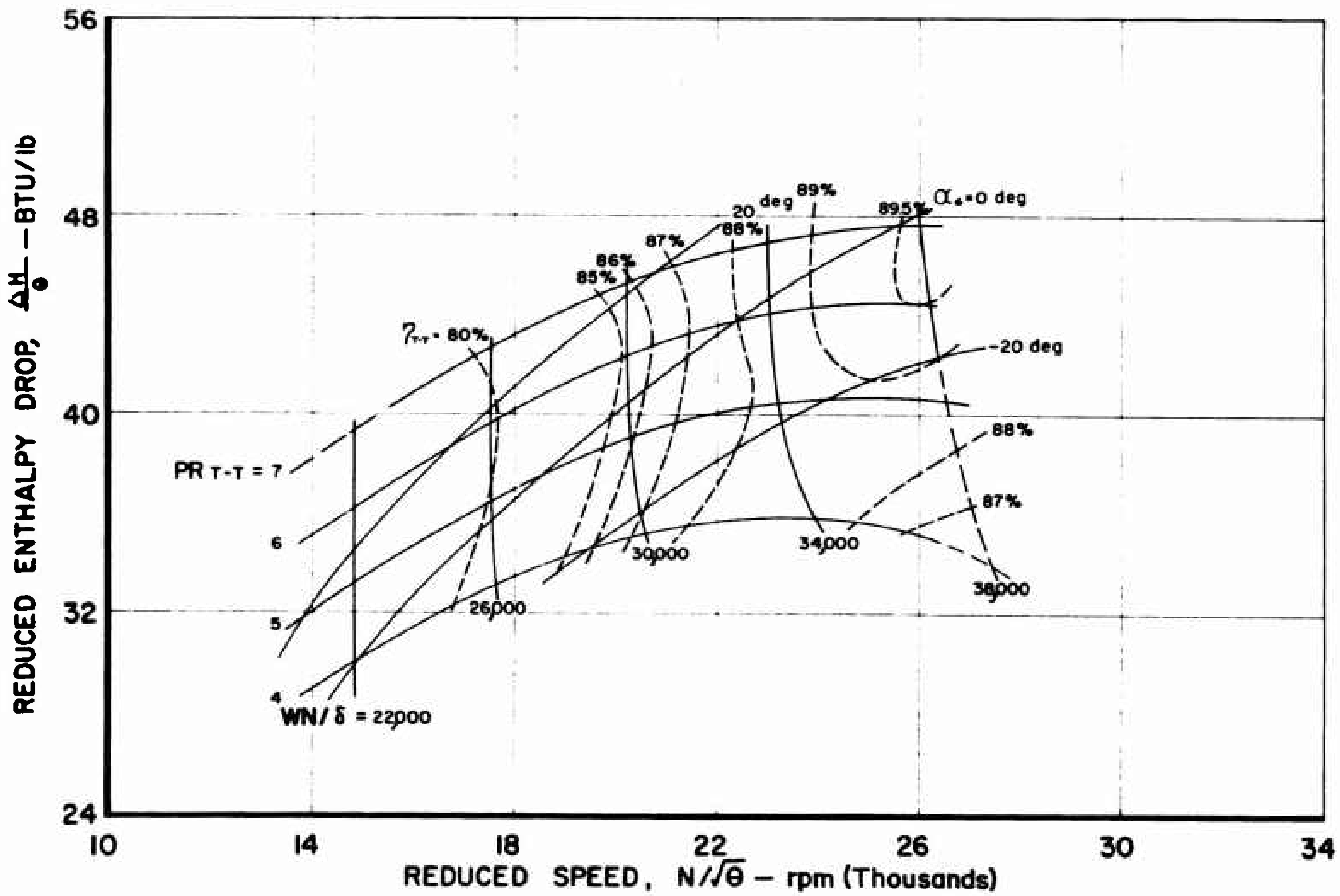

Figure 136. Universal Performance Map, Cold-Flow Tests (Build No. 3).

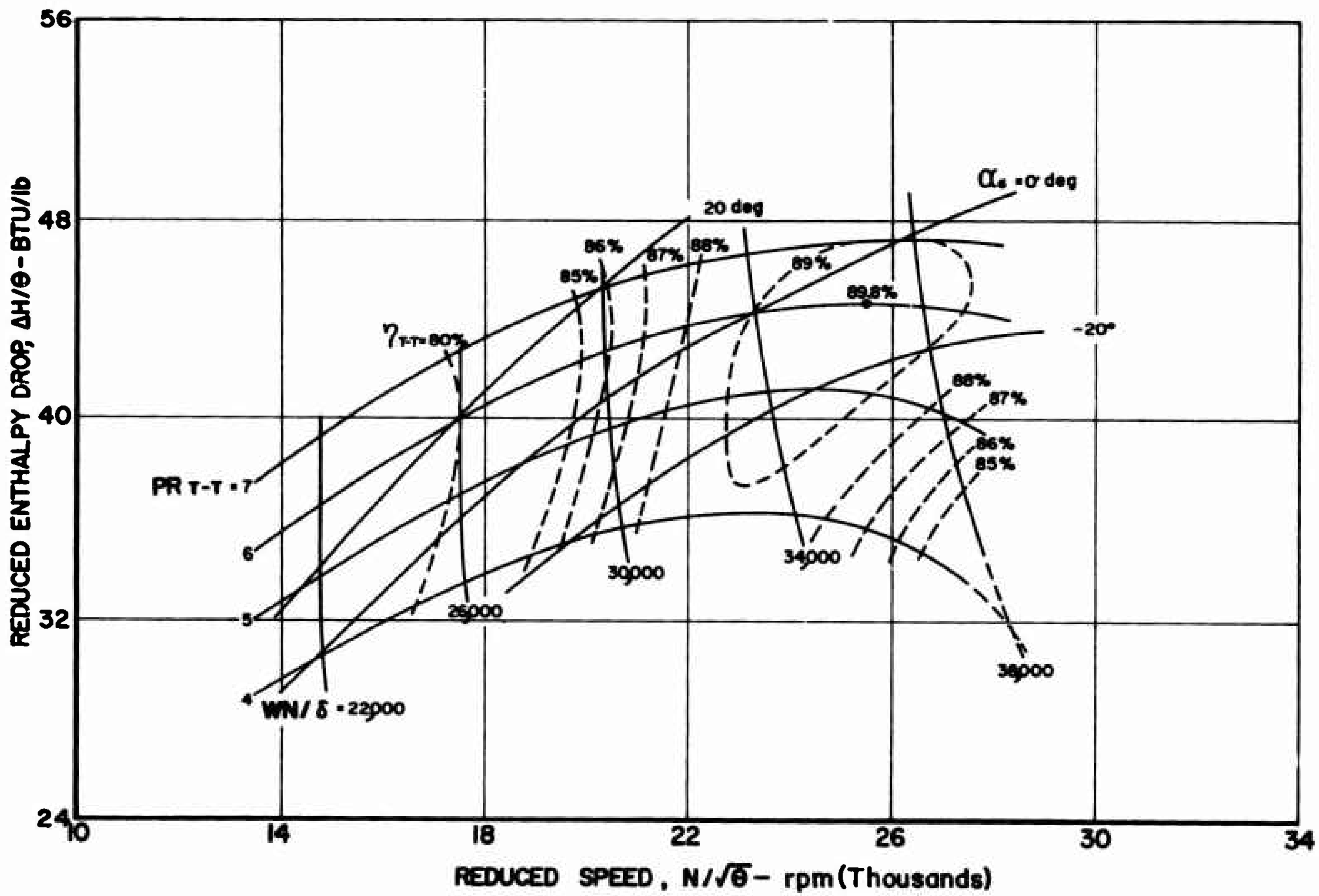

Figure 137. Universal Performance Map, Cold-Flow Tests (Build No. 1).

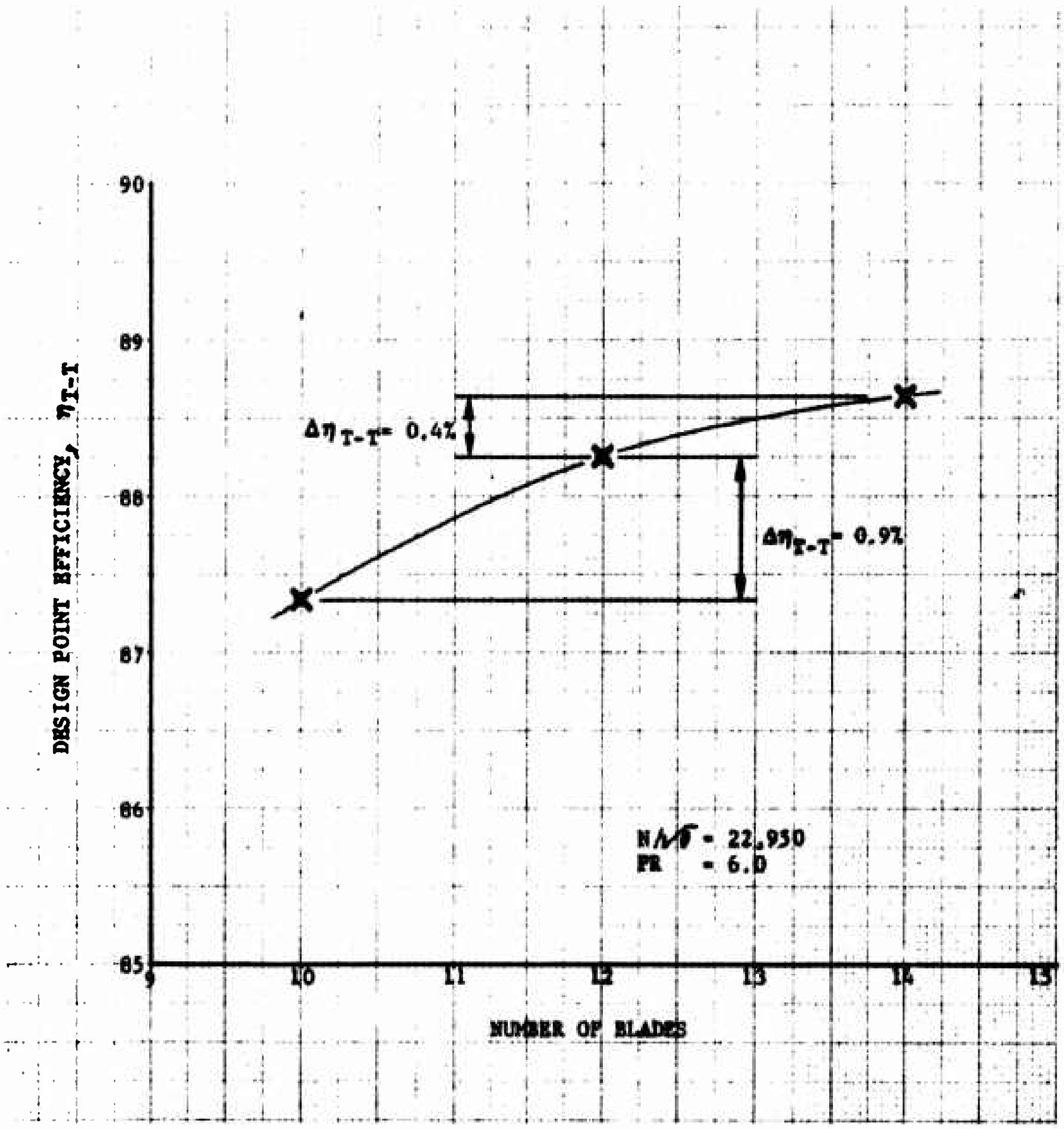

Figure 138. Measured Variation of Turbine Design Point Efficiency With Number of Rotor Blades.

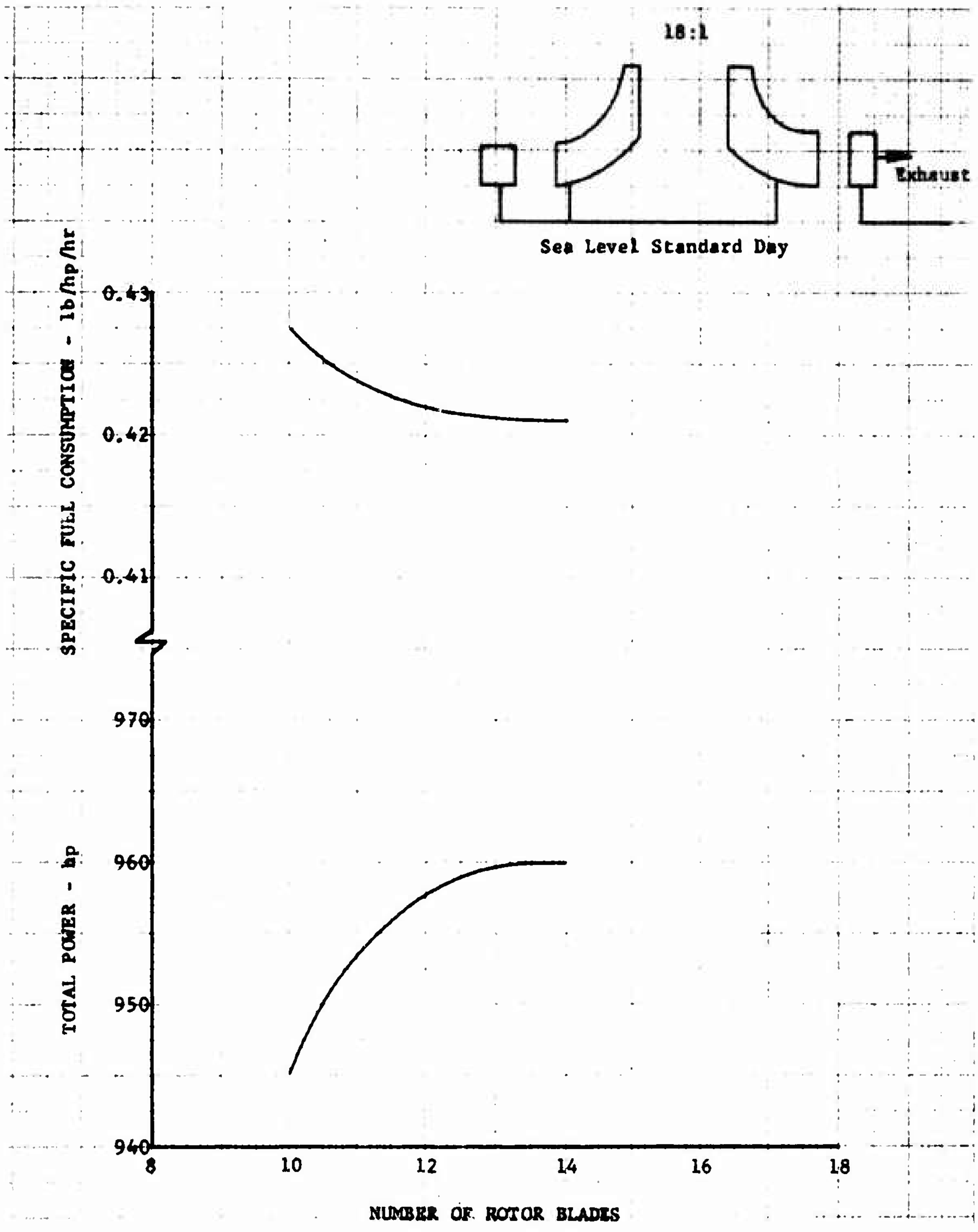

Figure 139. Cycle Analysis Indicates 14 Blades Optimum.

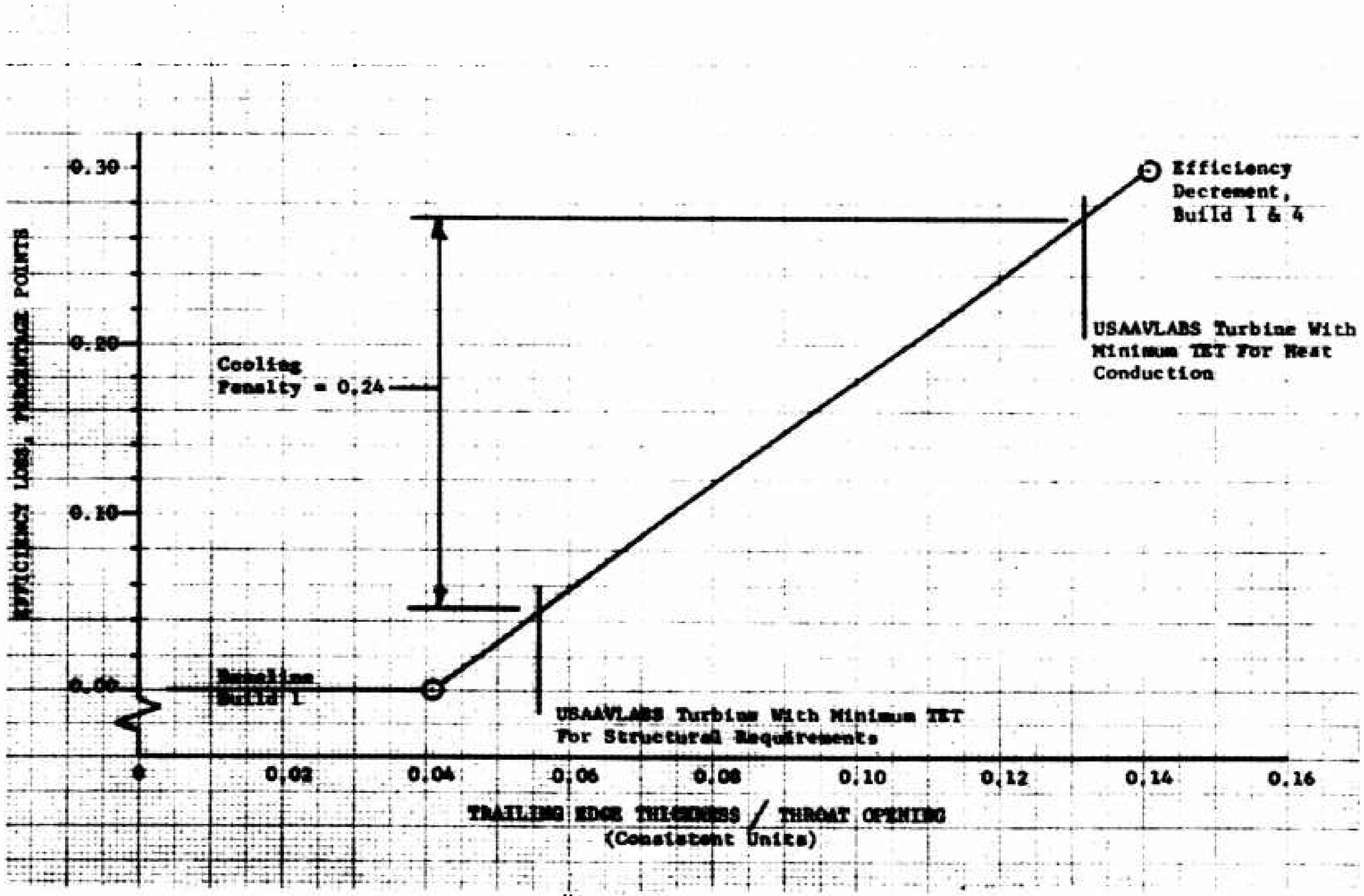

Figure 140. Effect of Increasing Vane TET/Throat Opening Ratio.

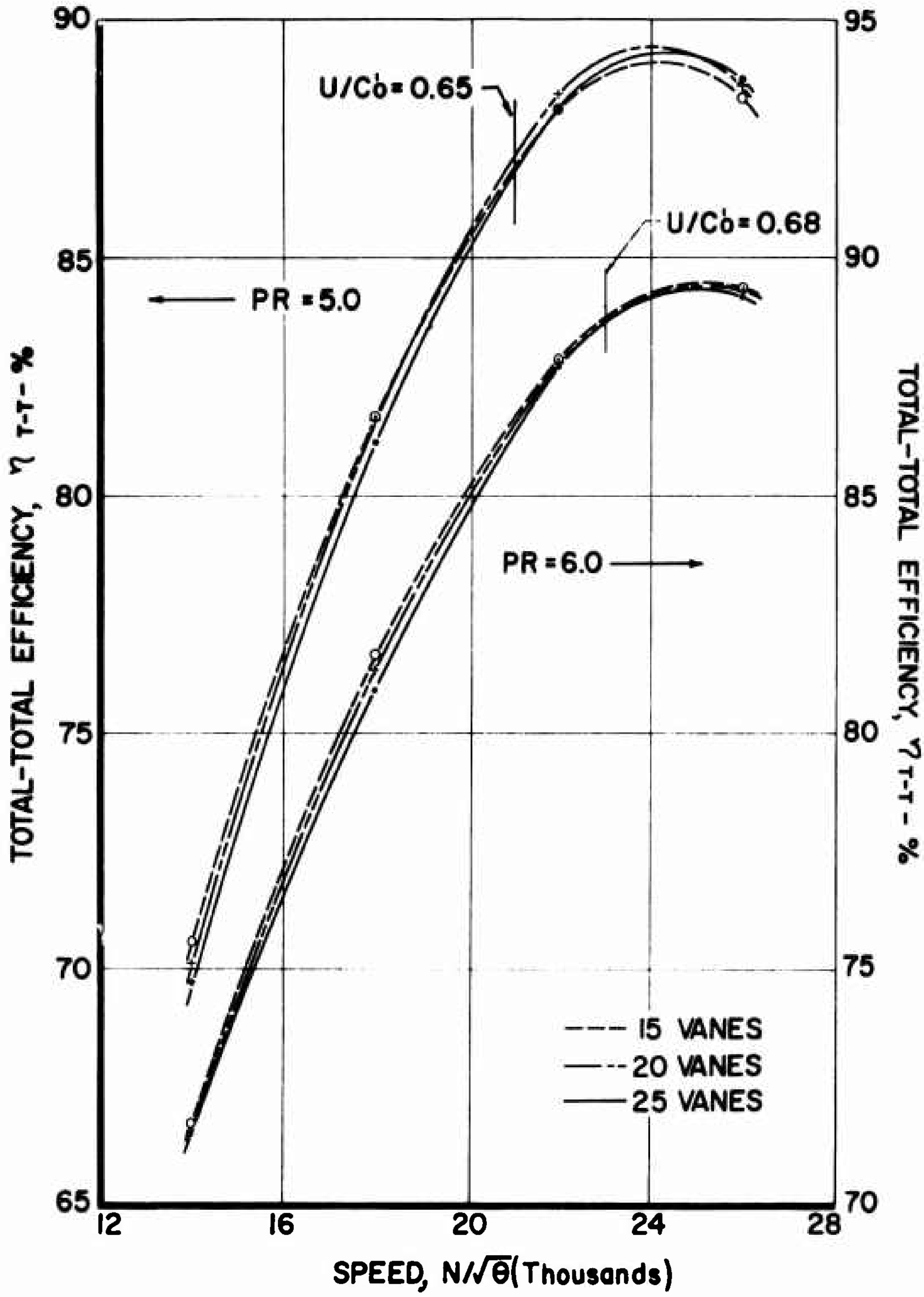

Figure 141. Effect of Nozzle Vane Number on Efficiency.

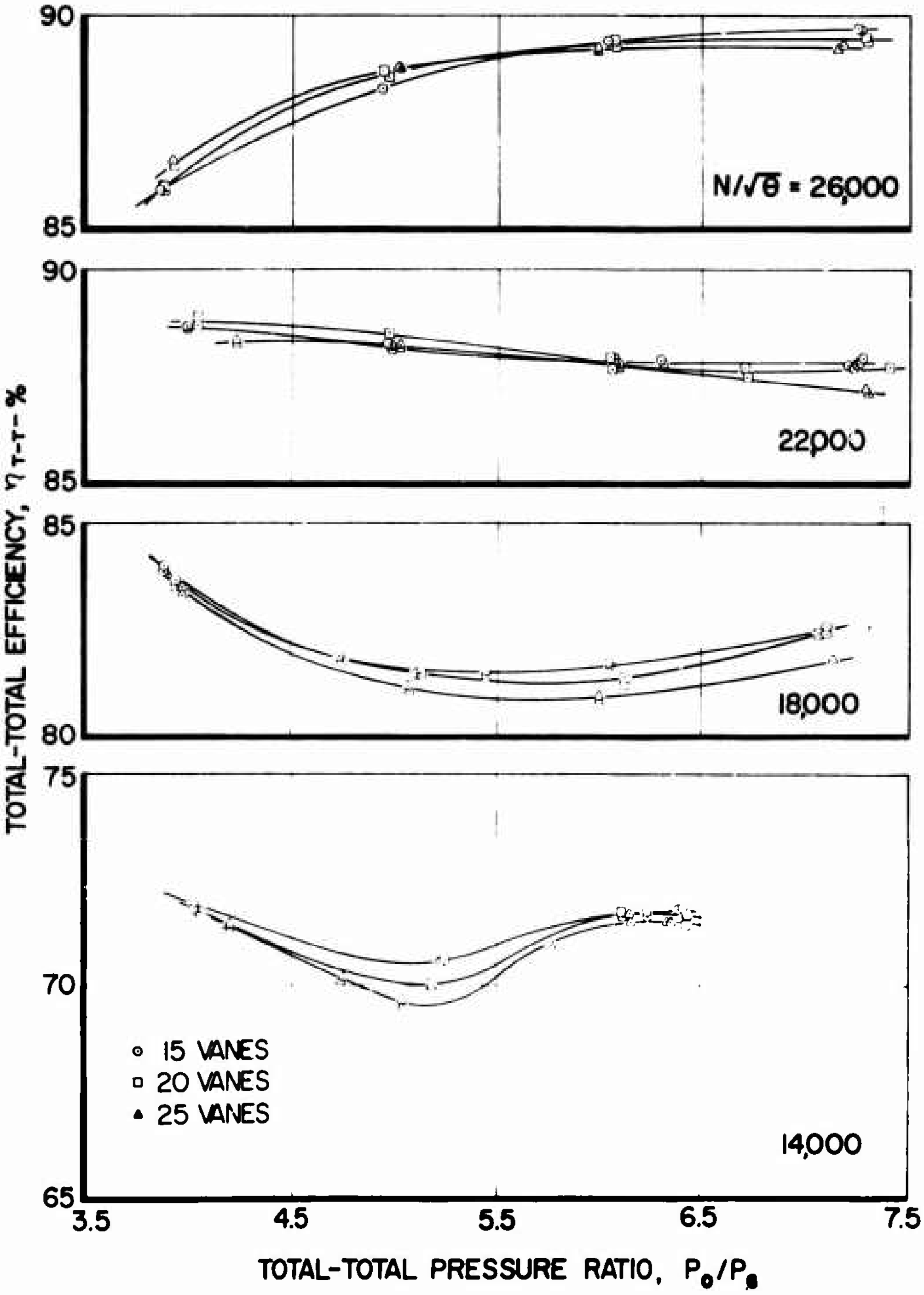

Figure 142. Comparison of Off-Design Performance.

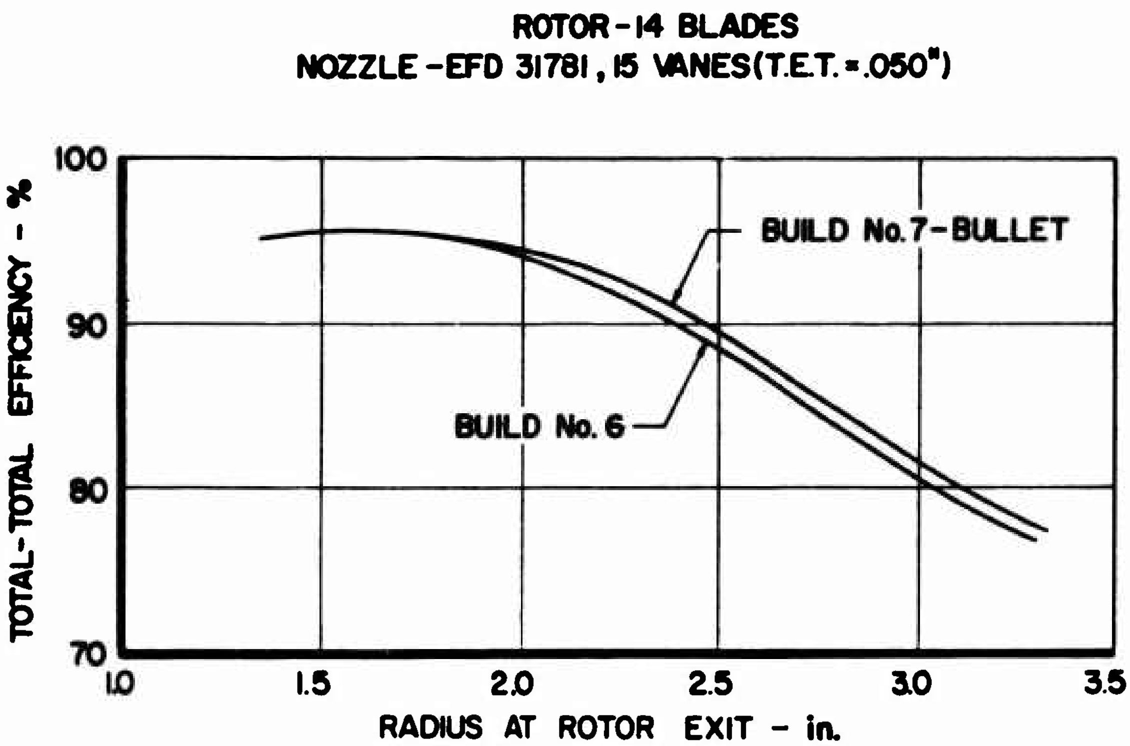

Figure 143. Cold-Flow Test, Build No. 7 (Total - Total Efficiency vs Radius at Rotor Exit).

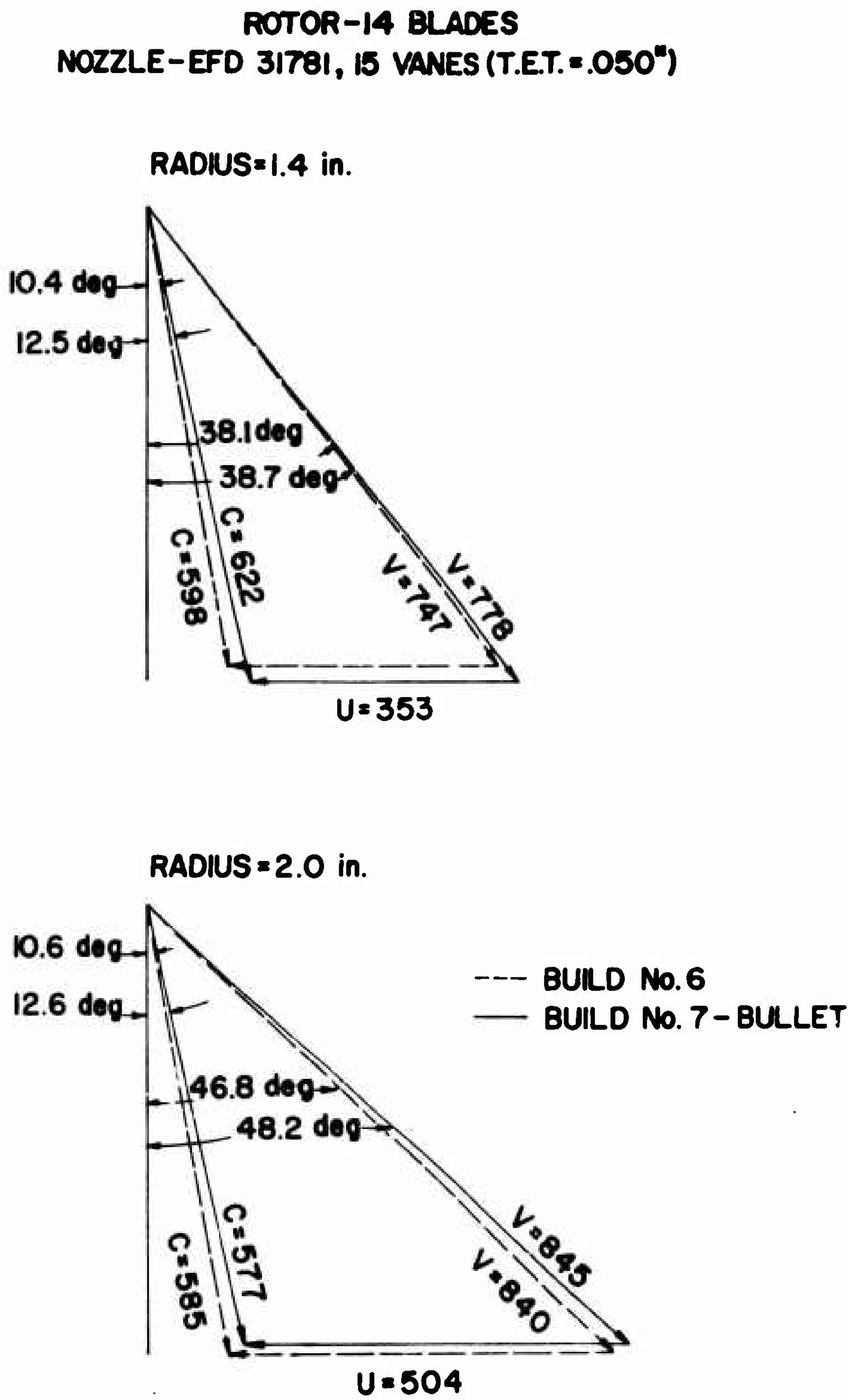

Figure 144. Cold-Flow Tests, Build No. 7 (14-Bladed Rotor, Radii 1.4 and 2.0 in.).

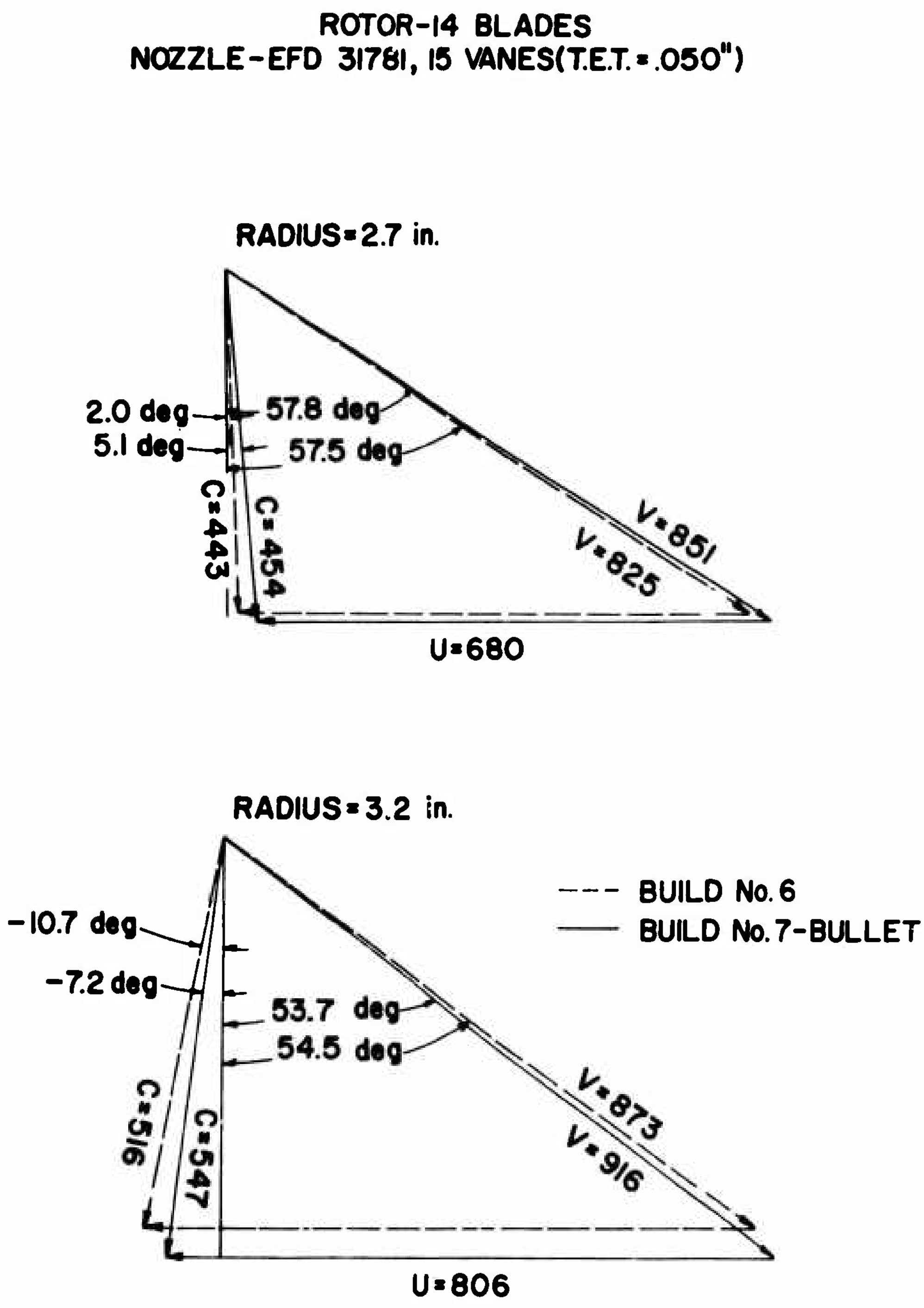

Figure 145. Cold-Flow Tests, Build No. 7 (14-Bladed Rotor, Radii 2.7 and 3.2 in.).

APPENDIX I
COLD-FLOW TEST
DATA (CURVES)

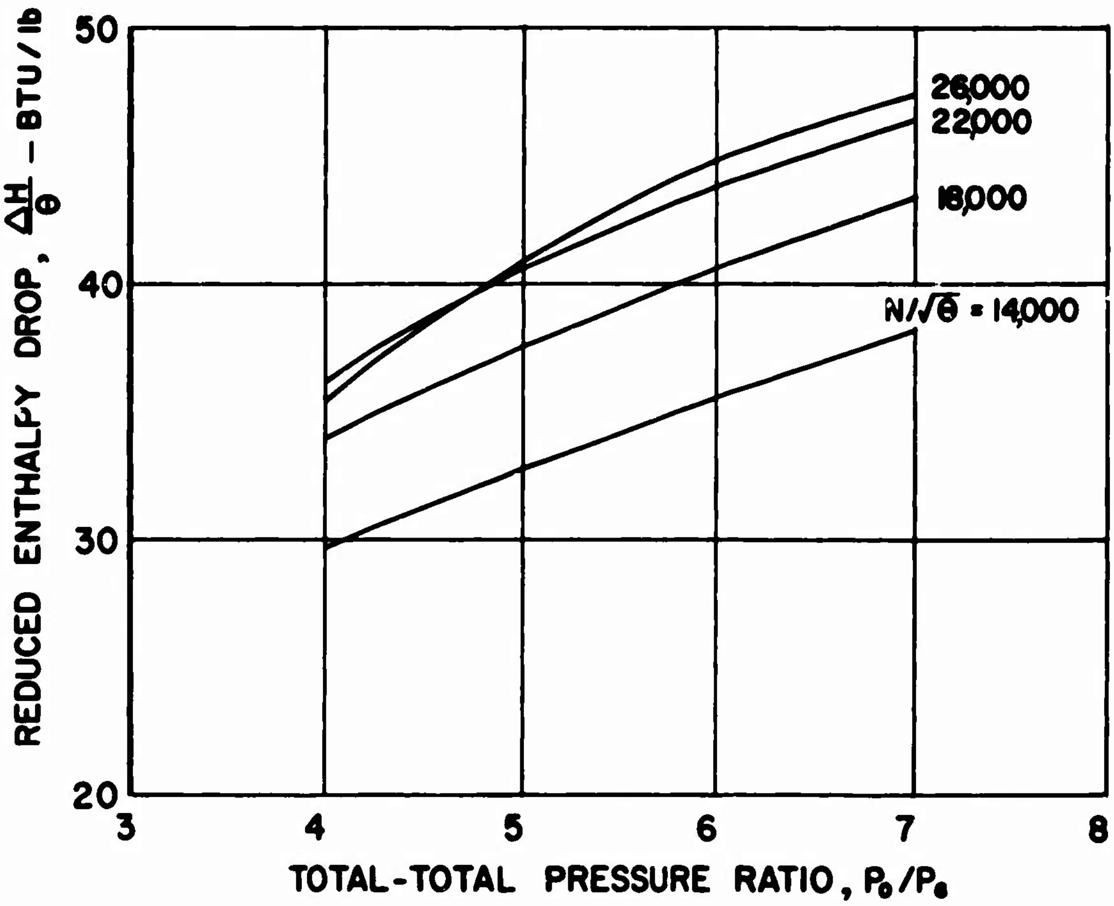

Figure 146. Build 1 - Reduced Enthalpy Drop vs Total-Total Pressure Ratio.

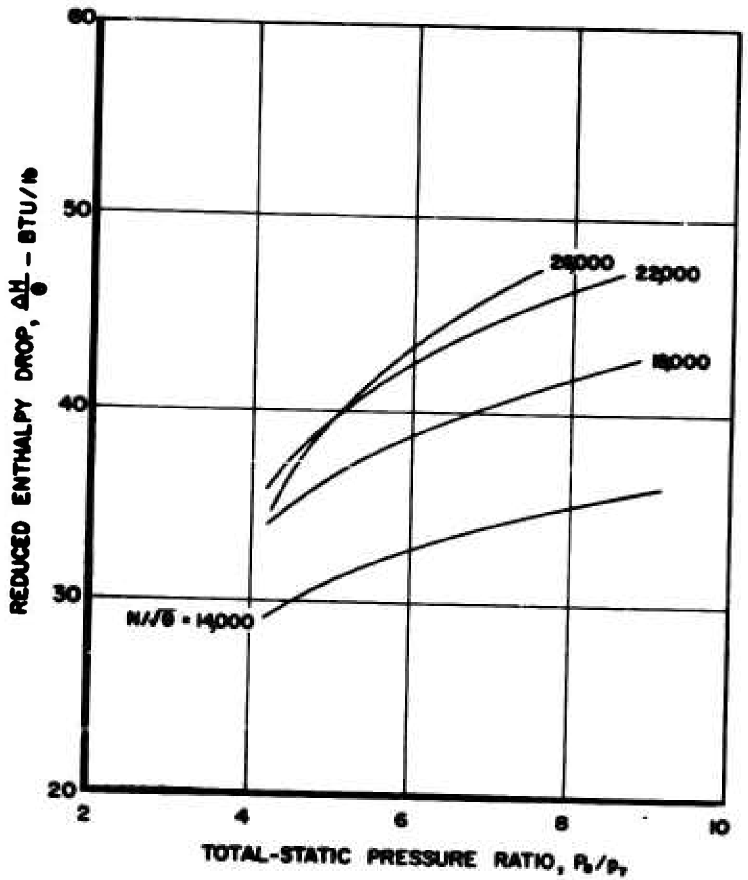

Figure 147. Build 1 - Reduced Enthalpy Drop vs Total-Static Pressure Ratio.

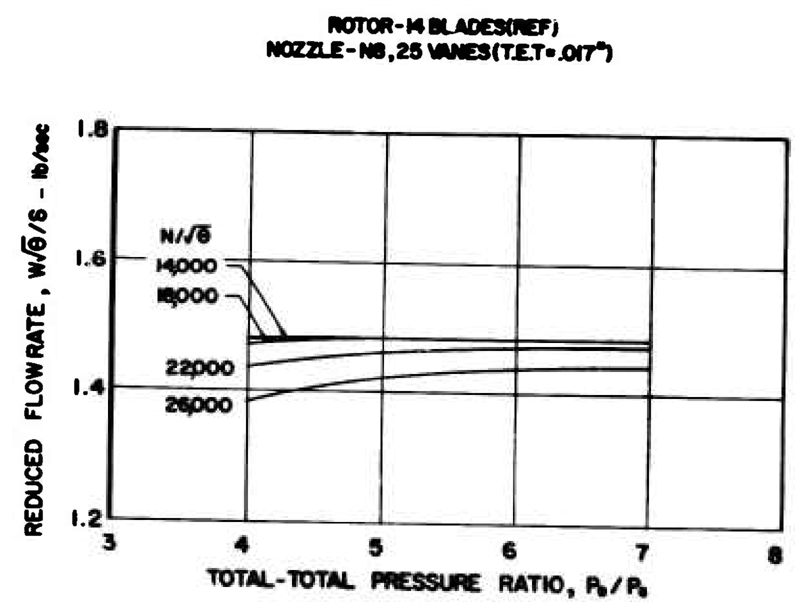

Figure 148. Build 1 - Reduced Flowrate vs Total-Total Pressure Ratio.

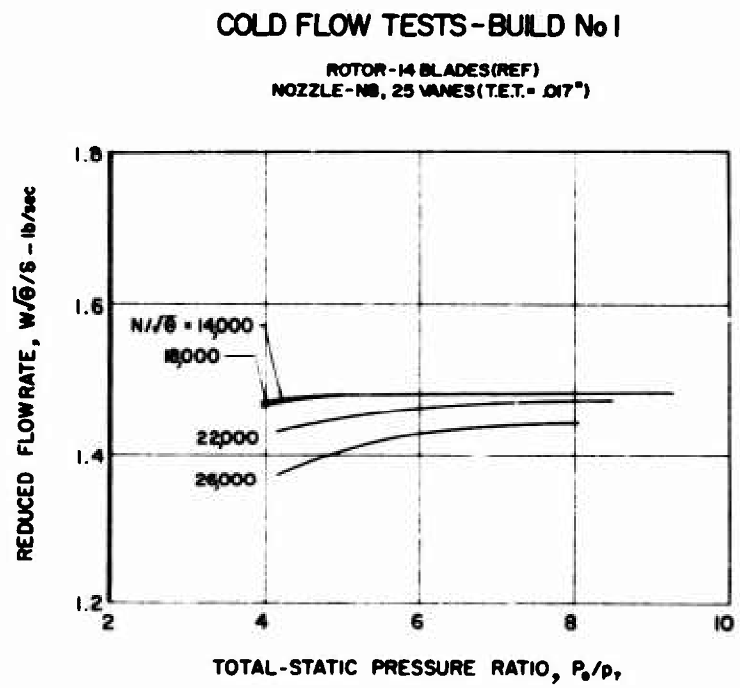

Figure 149. Build 1 - Reduced Flowrate vs Total-Static Pressure Ratio.

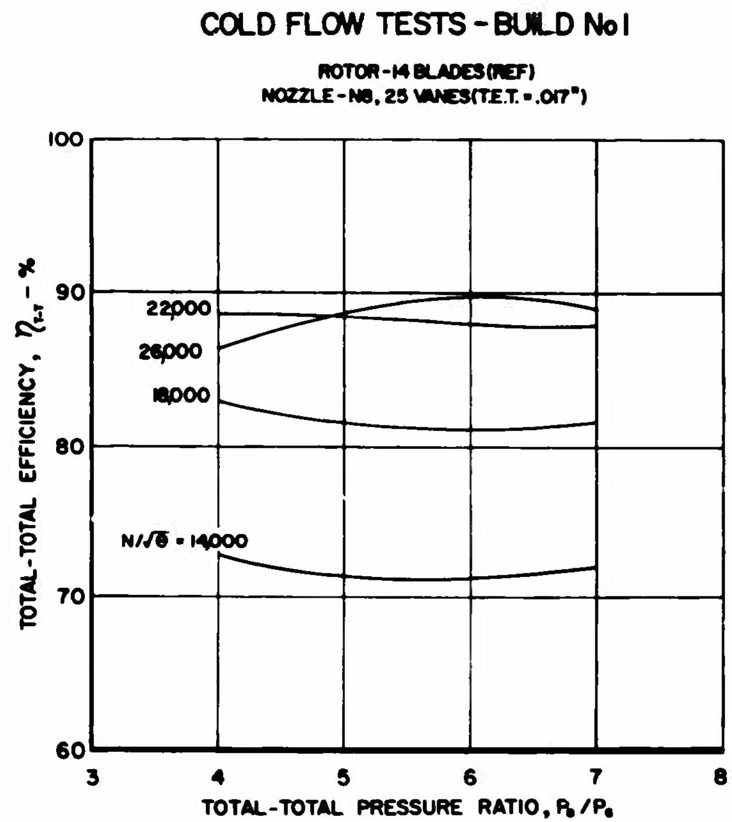

Figure 150 Build 1 - Total-Total Efficiency vs Total-Total Pressure Ratio.

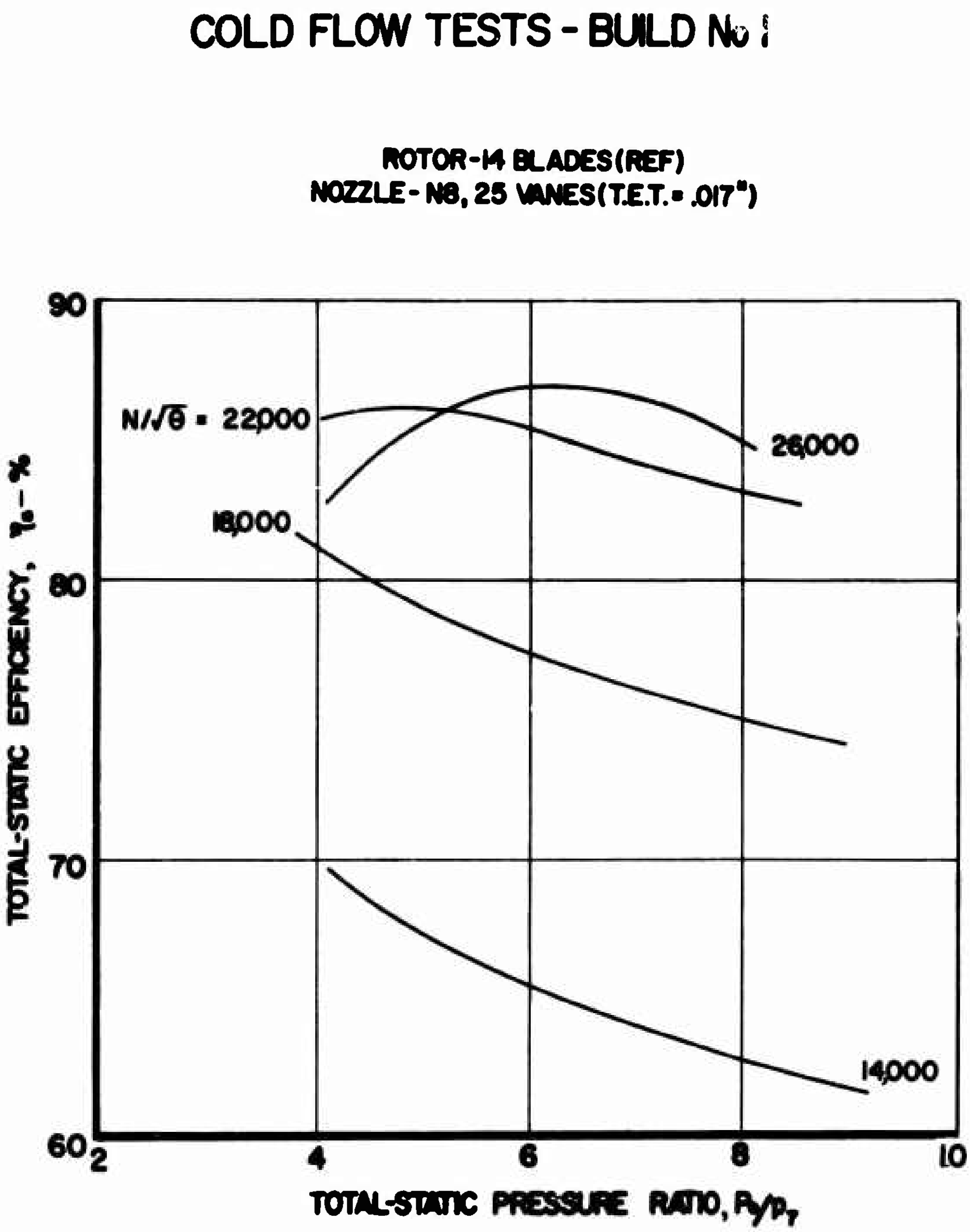

Figure 151. Build 1 - Total-Static Efficiency vs Total-Static Pressure Ratio.

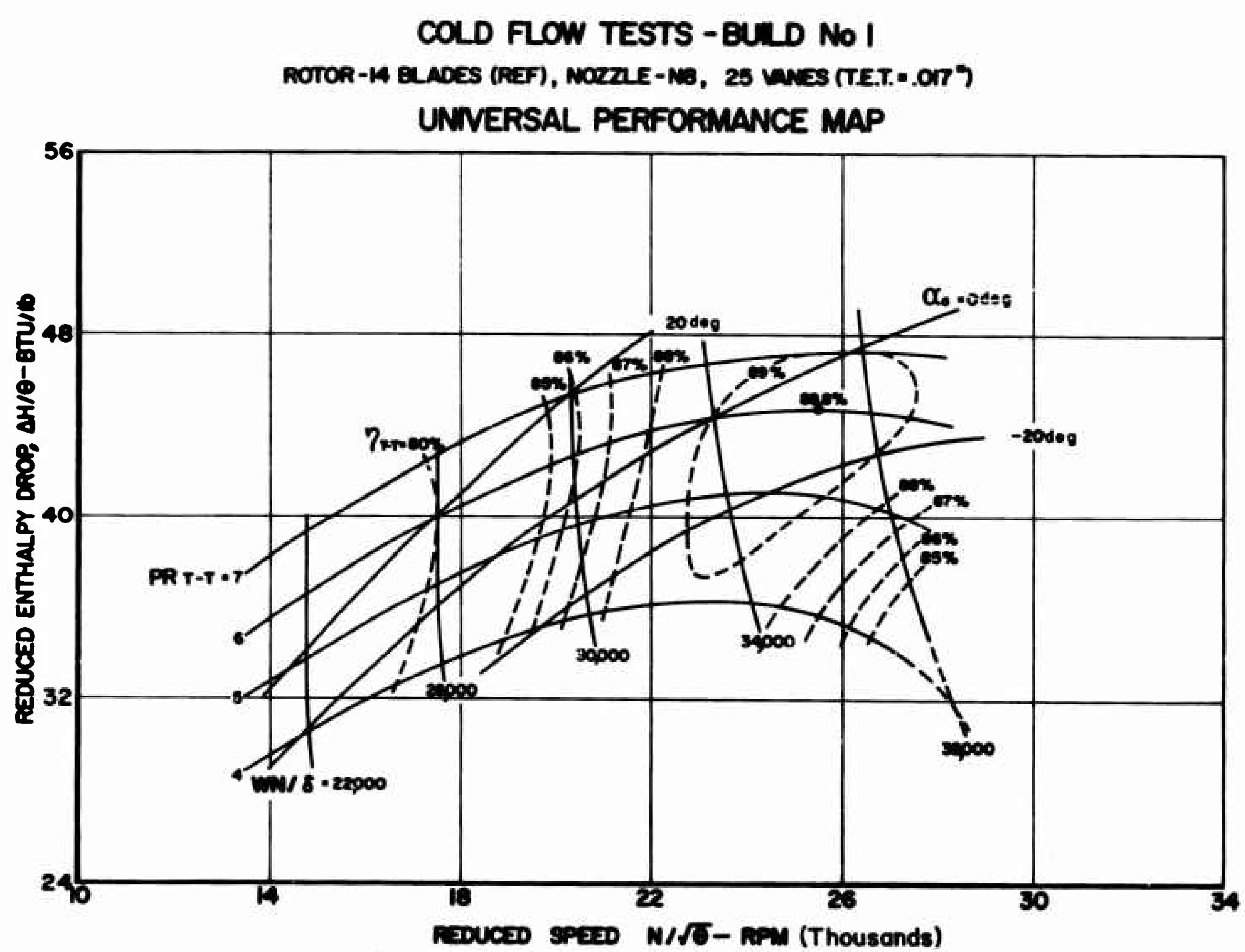

Figure 152. Build 1 - Reduced Enthalpy Drop vs Reduced Speed.

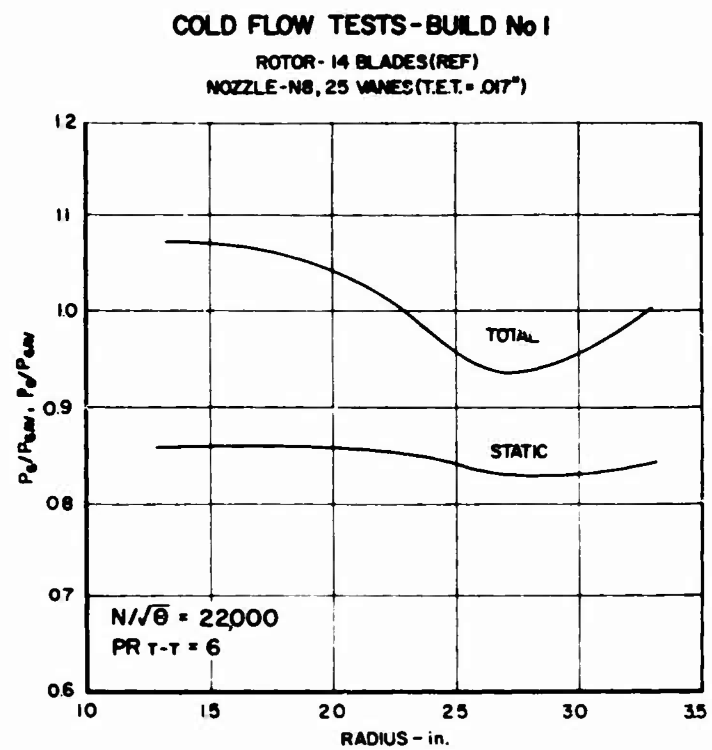

Figure 153. Build 1 - P_6/P_{6AV}, P_6/P_{6AV} vs Radius.

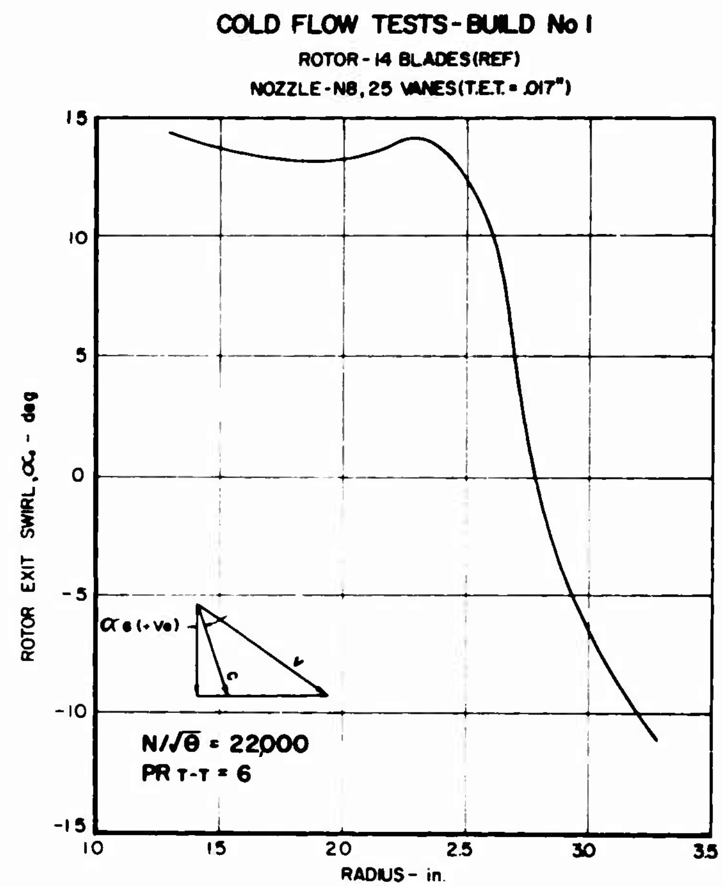

Figure 154. Build 1 - Rotor Exit Swirl vs Radius.

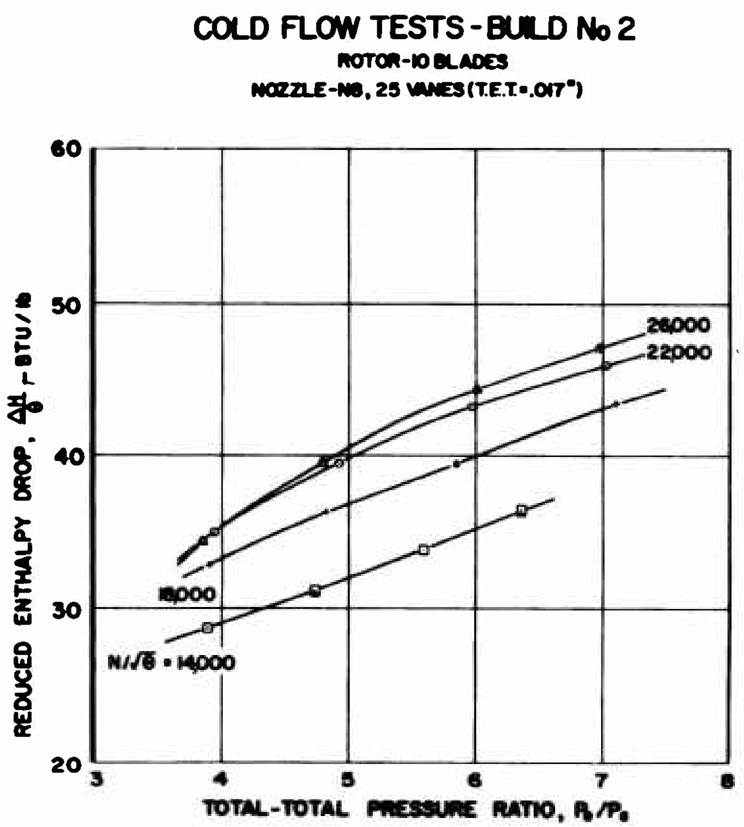

Figure 155. Build 2 - Reduced Enthalpy Drop vs Total-Total Pressure Ratio.

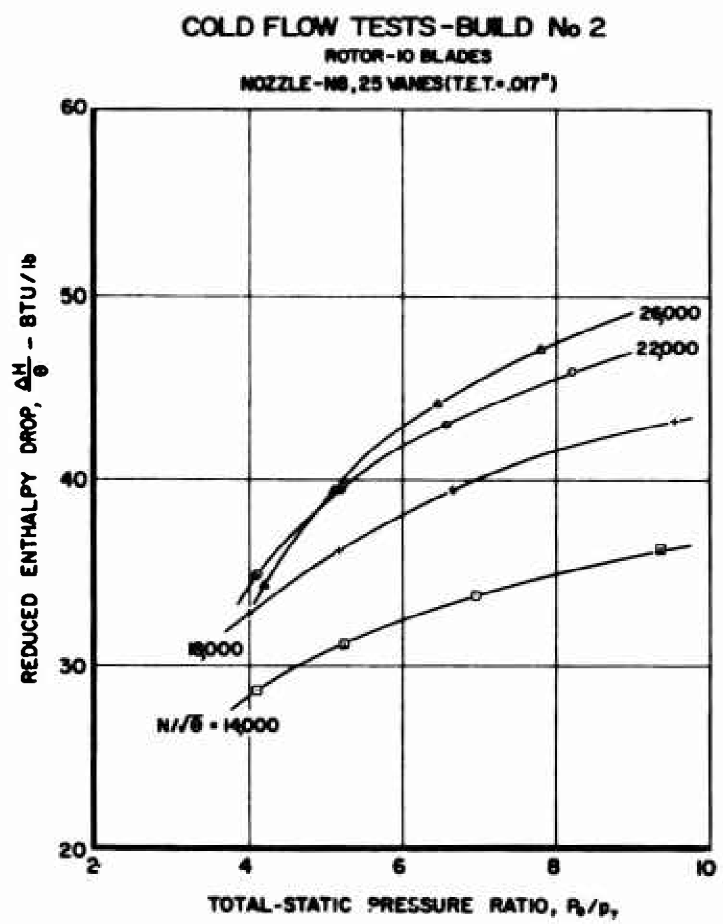

Figure 156. Build 2 - Reduced Enthalpy Drop vs Total-Static Pressure Ratio.

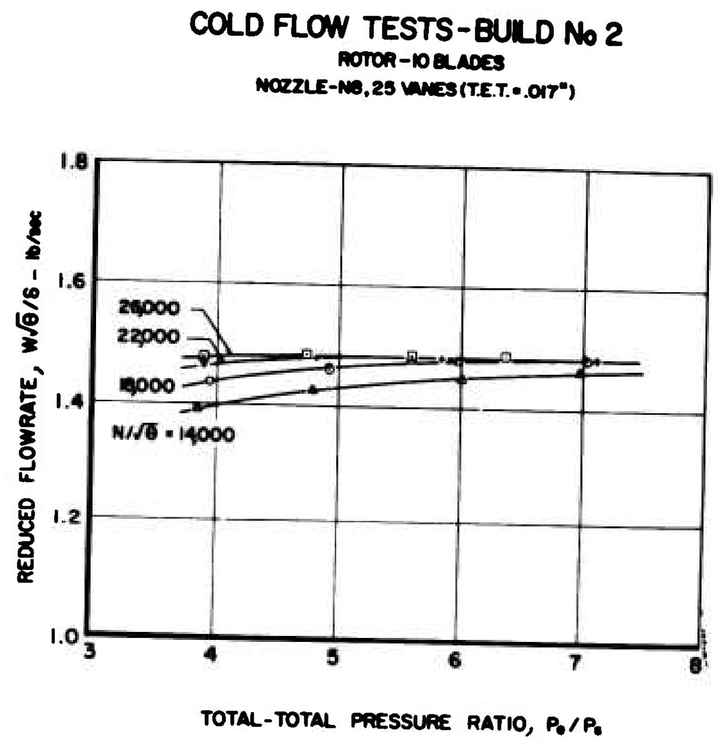

Figure 157. Build 2 - Reduced Flowrate vs Total-Total Pressure Ratio.

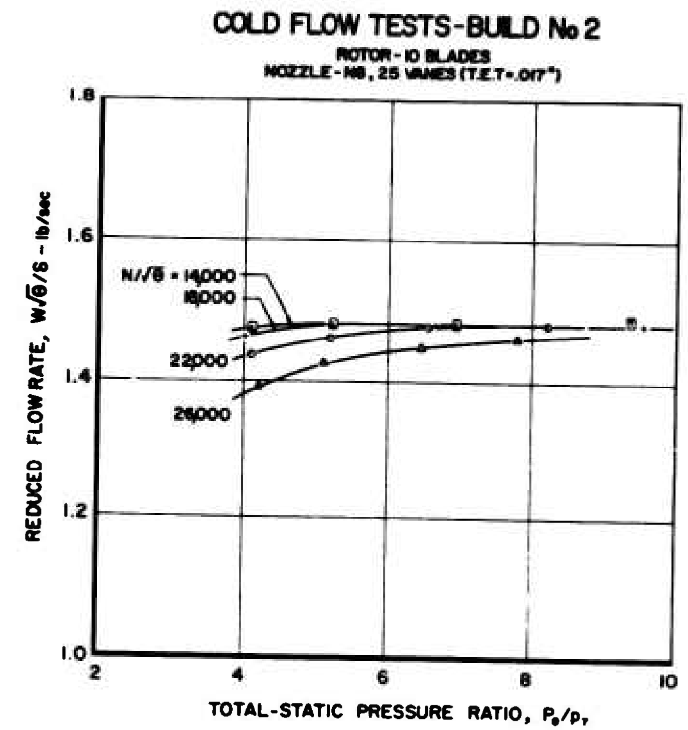

Figure 158. Build 2 - Reduced Flowrate vs Total-Static Pressure Ratio.

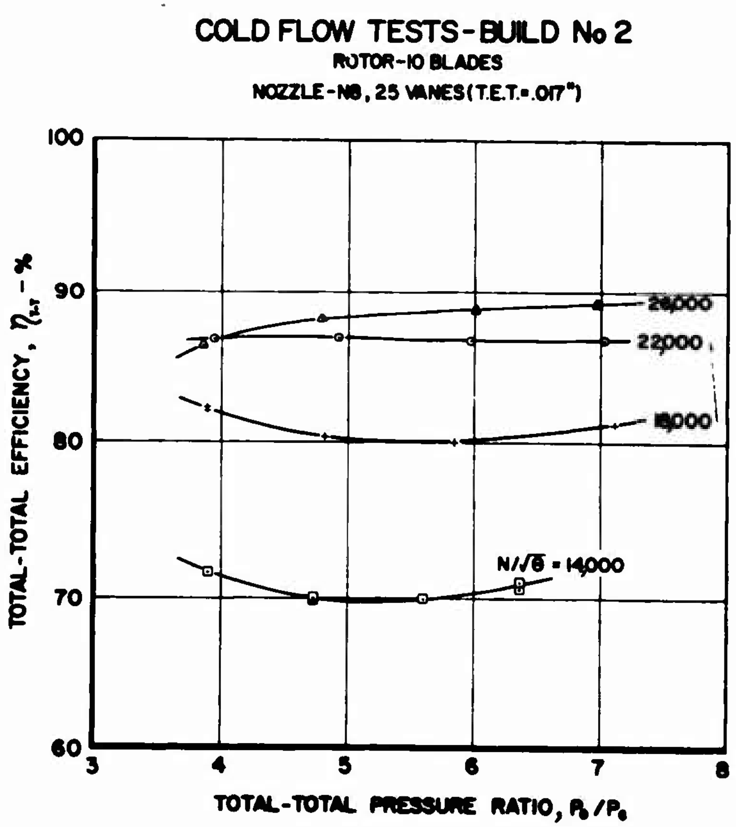

Figure 159. Build 2 - Total-Total Efficiency vs Total-Total Pressure Ratio.

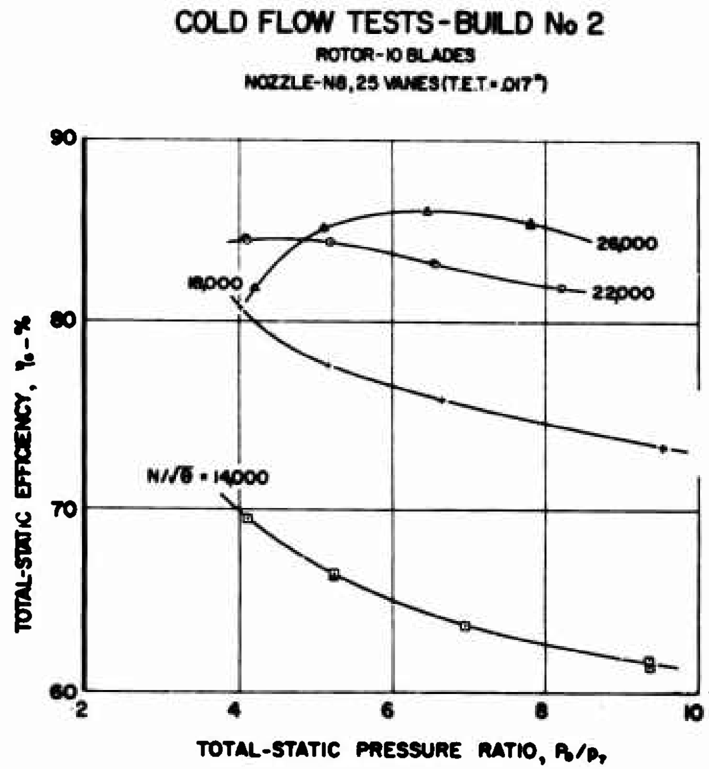

Figure 160. Build 2 - Total-Static Efficiency vs Total-Static Pressure Ratio.

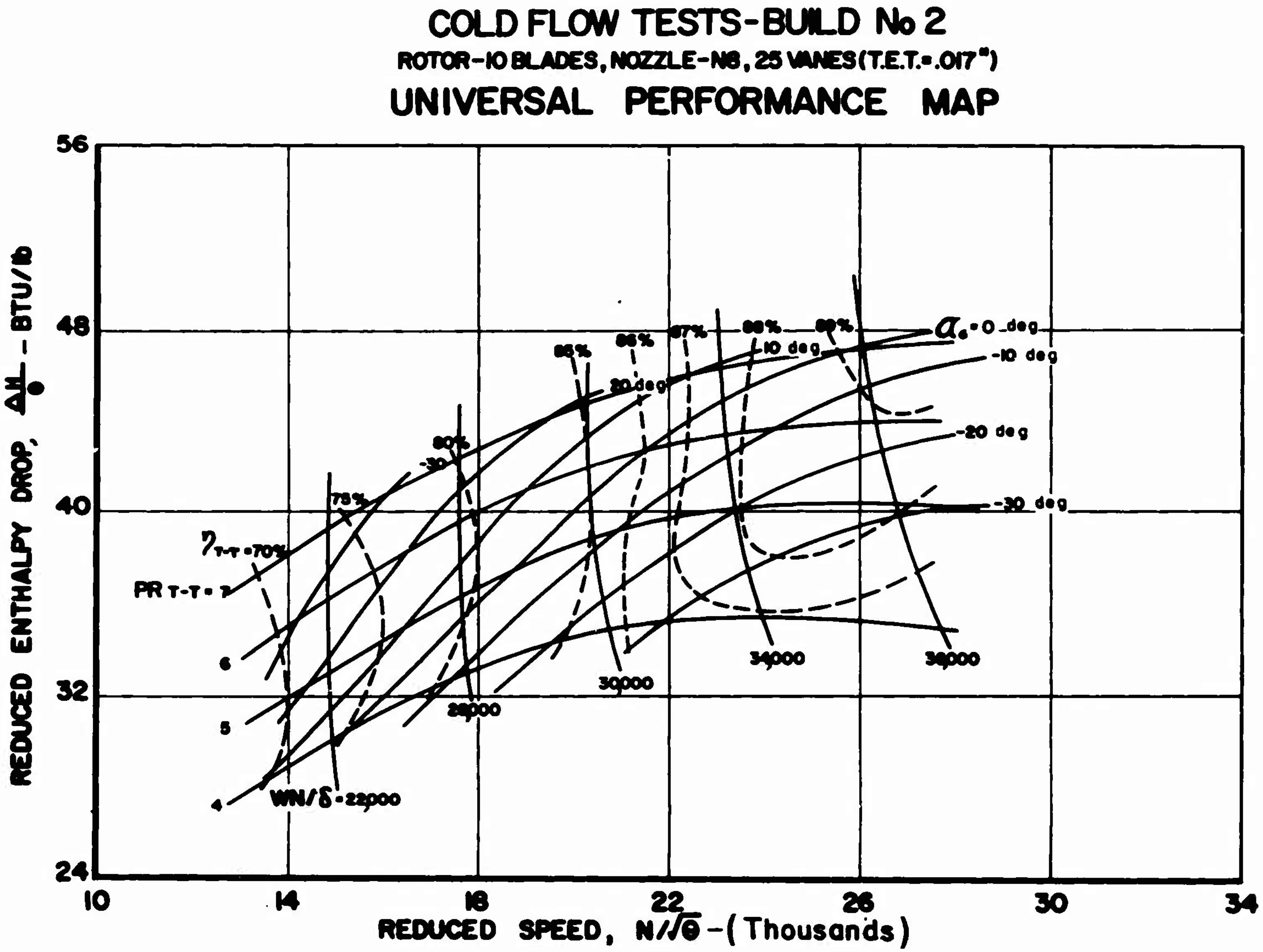

Figure 161. Build 2 - Reduced Enthalpy Drop vs Reduced Speed.

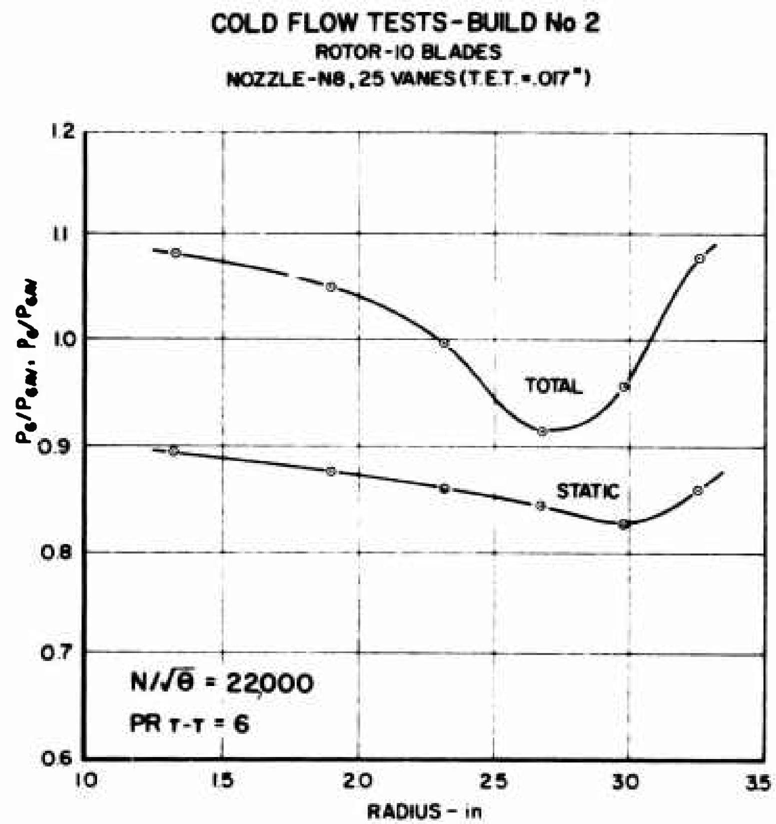

Figure 162. Build 2 - P_6/P_{6AV}, P_6/P_{6AV} vs Radius.

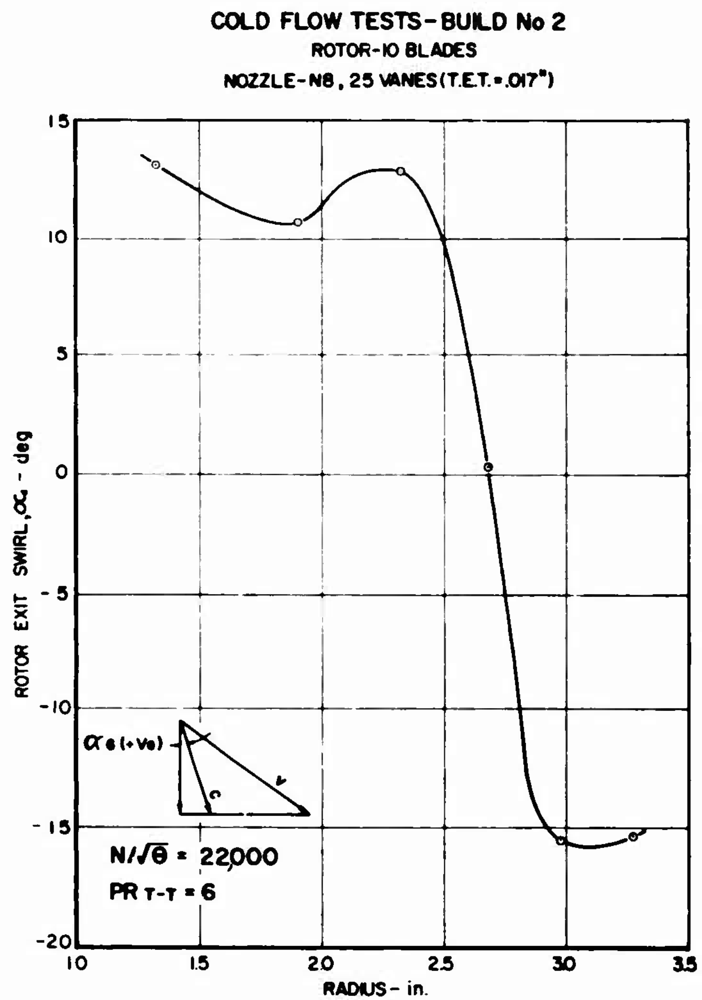

Figure 163. Build 2 - Rotor Exit Swirl vs Radius.

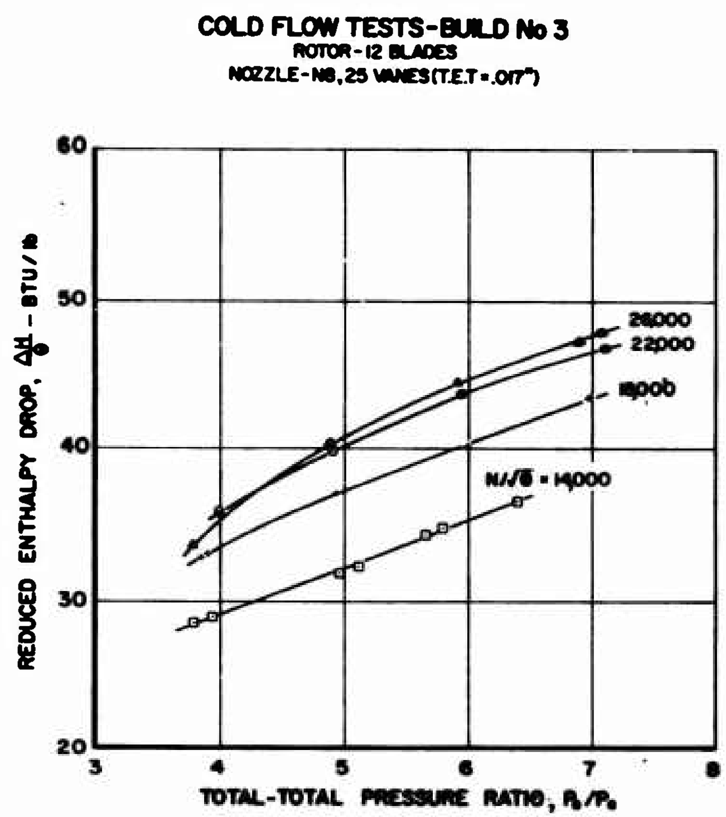

Figure 164. Build 3 - Reduced Enthalpy Drop vs Total-Total Pressure Ratio.

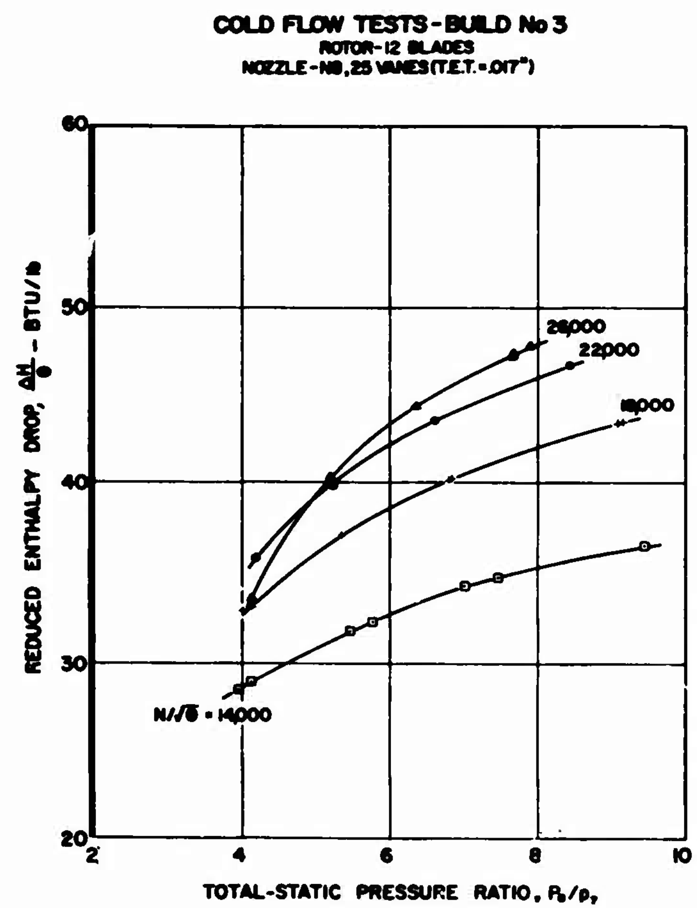

Figure 165. Build 3 - Reduced Enthalpy Drop vs Total-Static Pressure Ratio.

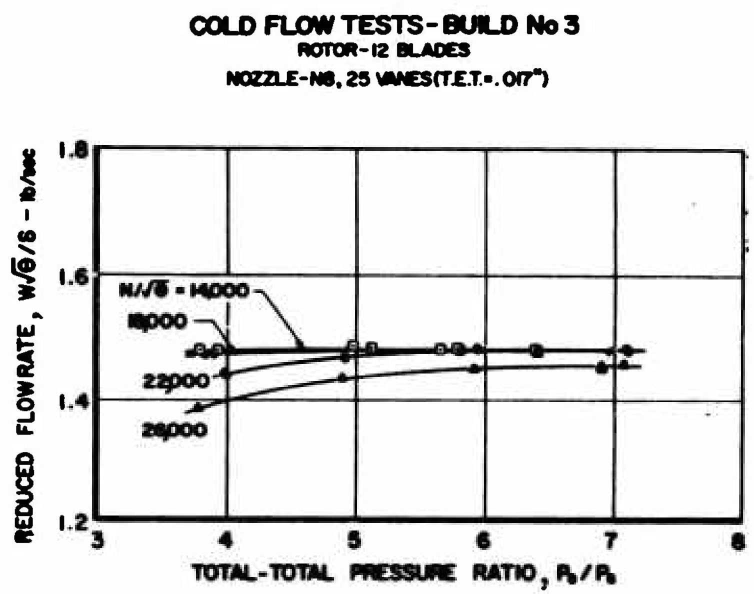

Figure 166. Build 3 - Reduced Flowrate vs Total-Total Pressure Ratio.

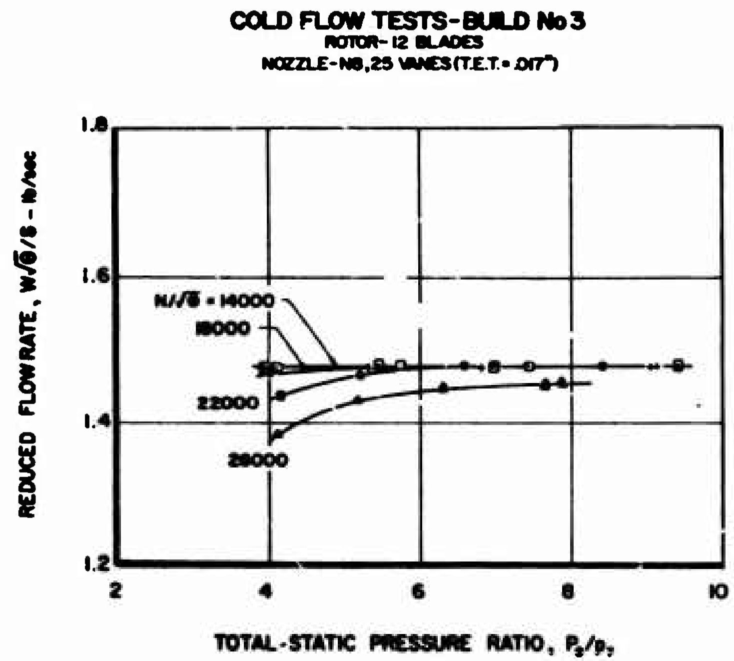

Figure 167. Build 3 - Reduced Flowrate vs Total-Static Pressure Ratio.

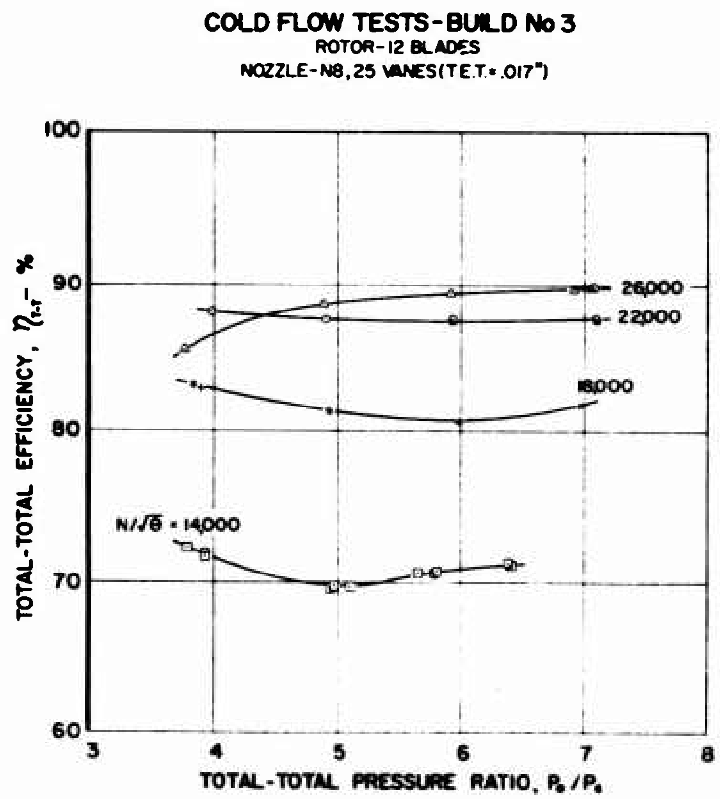

Figure 168. Build 3 - Total-Total Efficiency vs Total-Total Pressure Ratio.

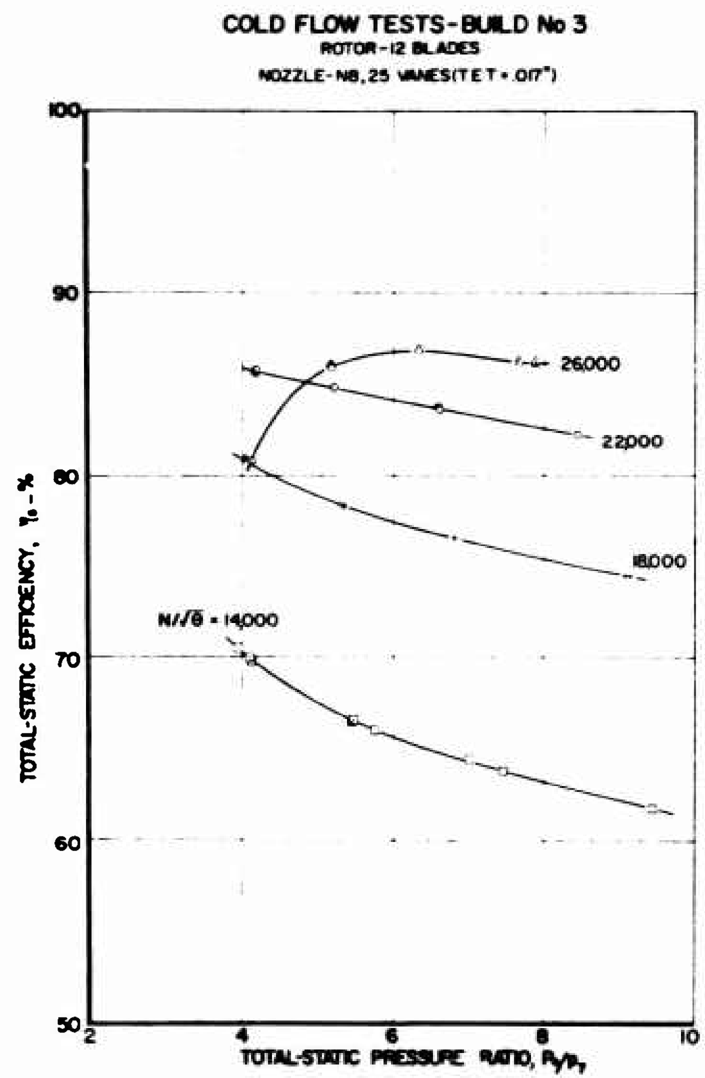

Figure 169. Build 3 - Total-Static Efficiency vs Total-Static Pressure Ratio.

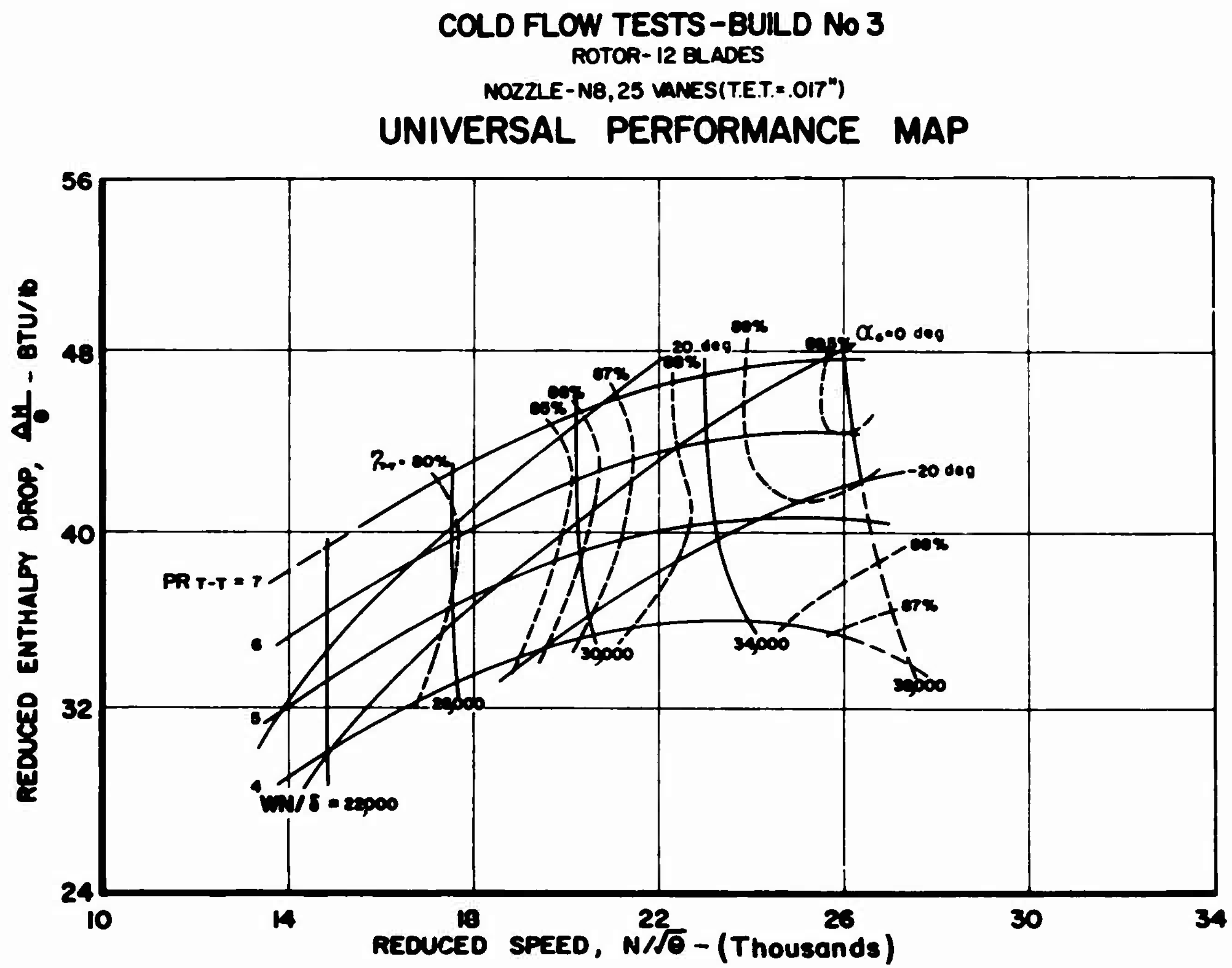

Figure 170. Build 3 - Reduced Enthalpy Drop vs Reduced Speed.

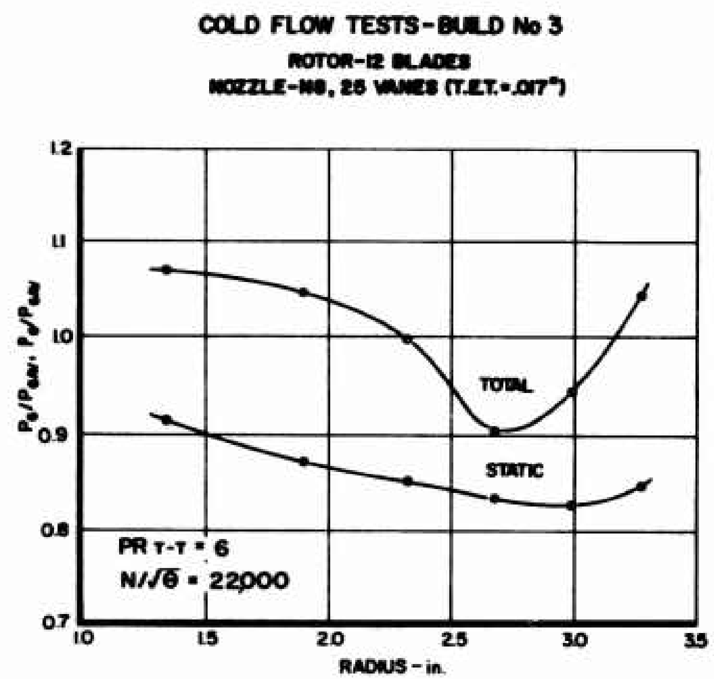

Figure 171. Build 3 - P_6/P_{6AV}, P_6/P_{6AV} vs Radius.

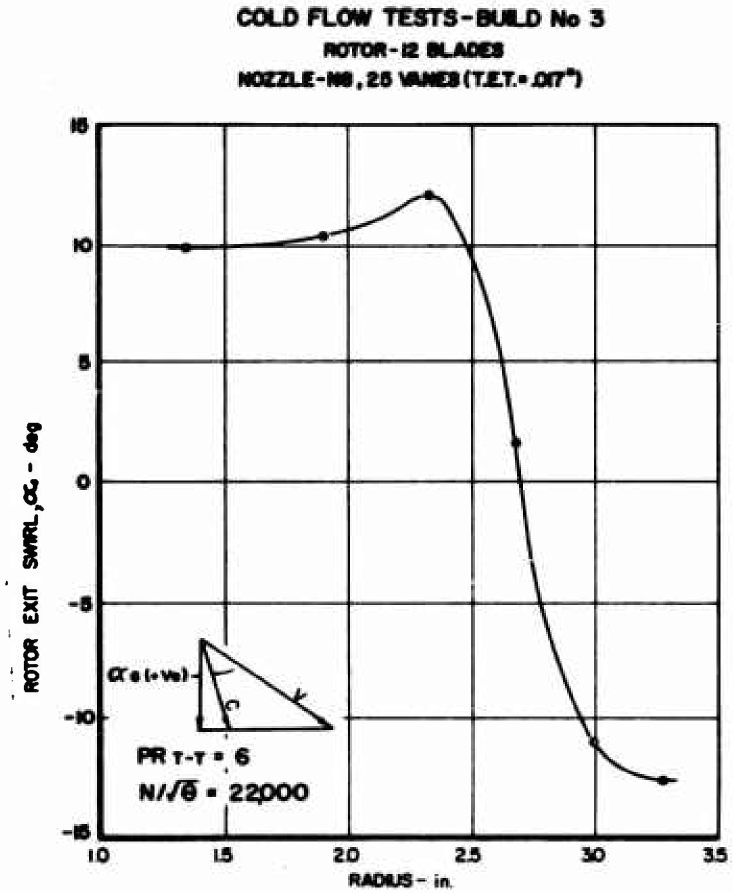

Figure 172. Build 3 - Rotor Exit Swirl vs Radius.

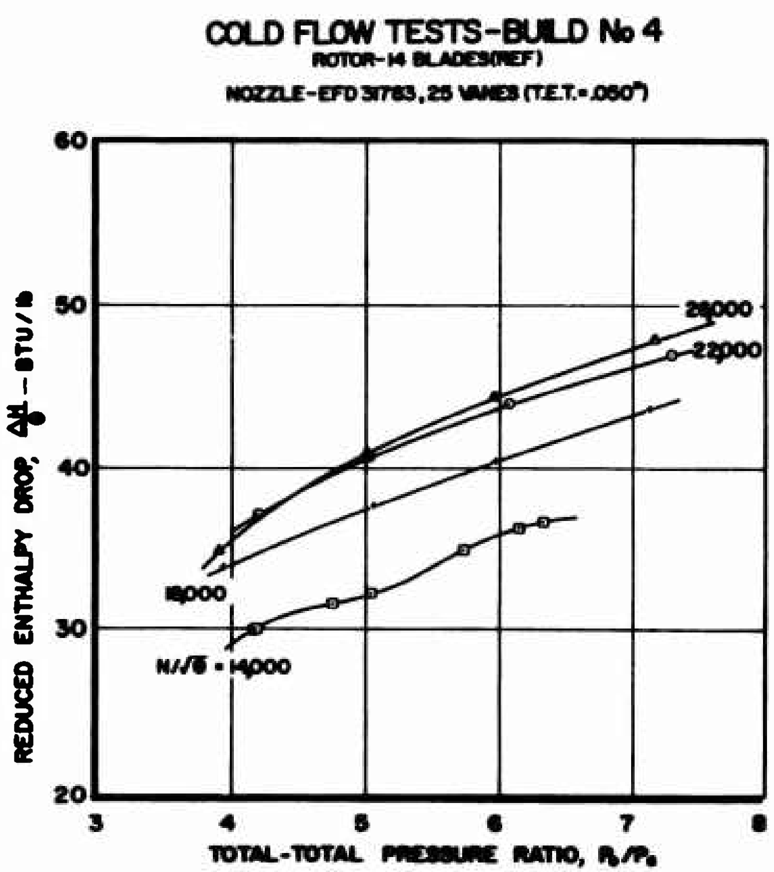

Figure 173. Build 4 - Reduced Enthalpy Drop vs Total-Total Pressure Ratio.

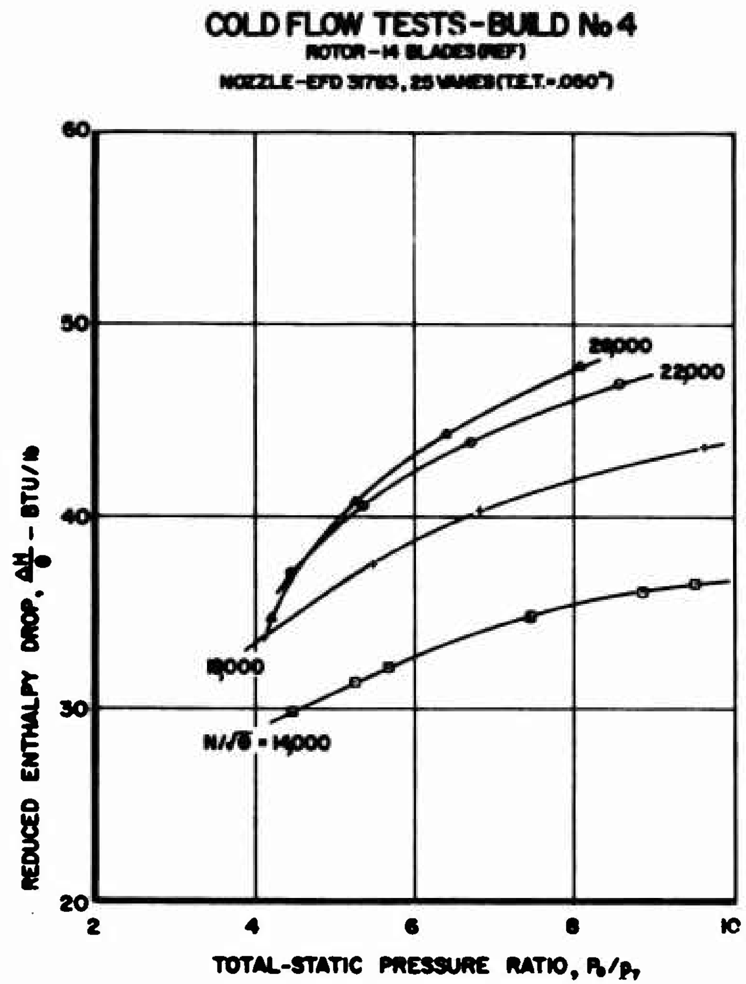

Figure 174. Build 4 - Reduced Enthalpy Drop vs Total-Static Pressure Ratio.

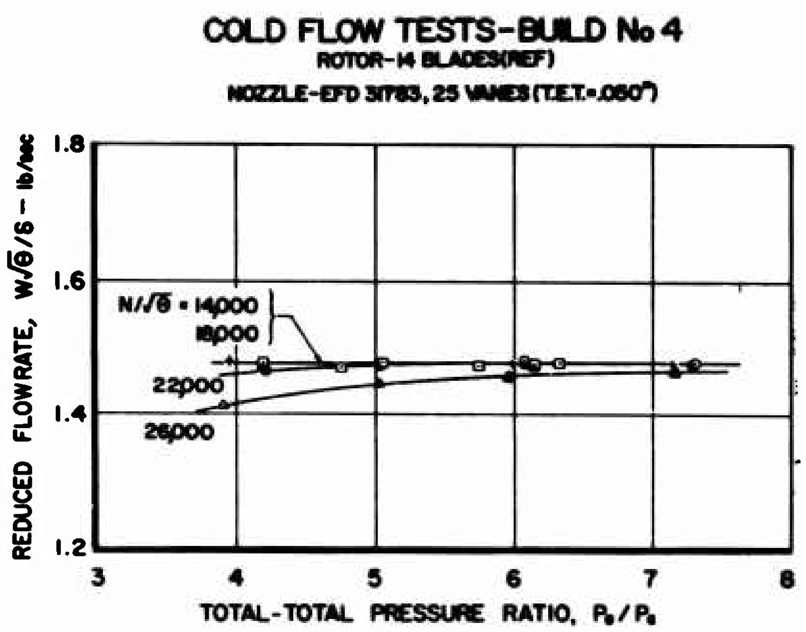

Figure 175. Build 4 - Reduced Flowrate vs Total-Total Pressure Ratio.

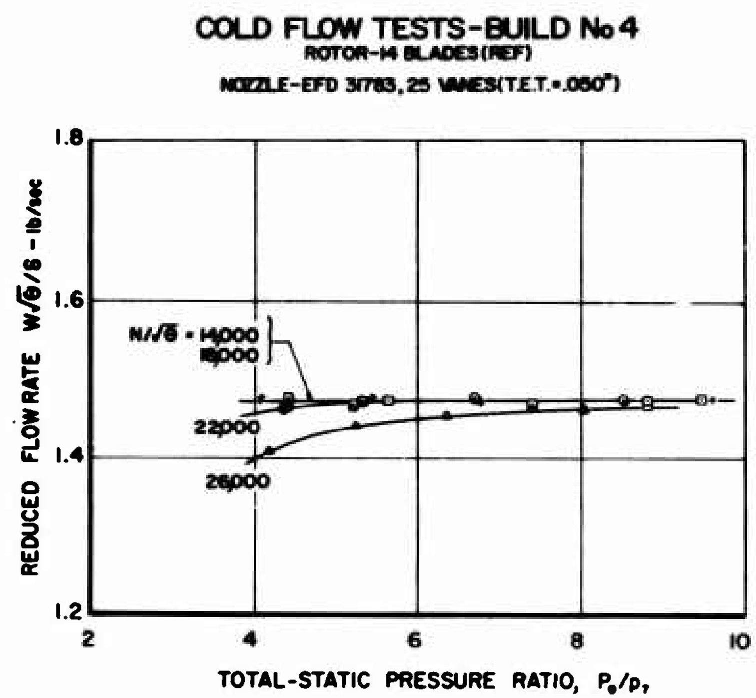

Figure 176. Build 4 - Reduced Flowrate vs Total-Static Pressure Ratio.

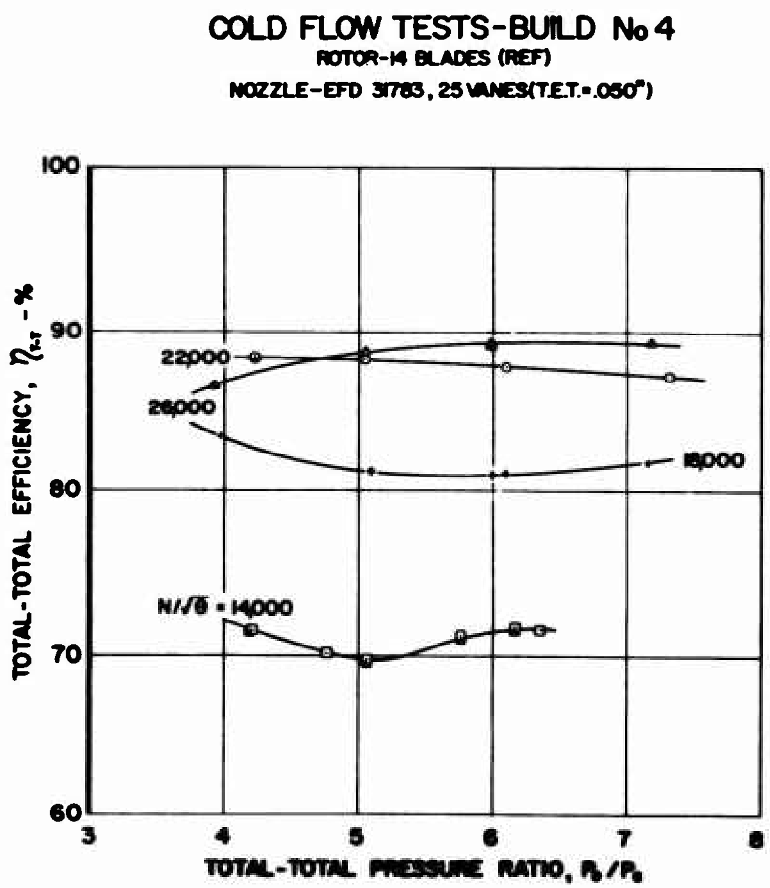

Figure 177. Build 4 - Total-Total Efficiency vs Total-Total Pressure Ratio.

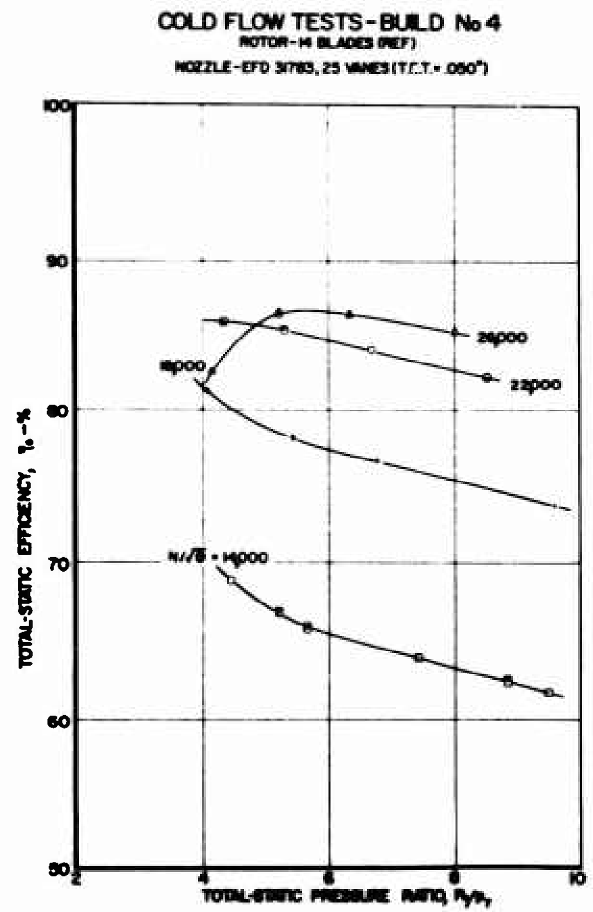

Figure 178. Build 4 - Total-Static Efficiency vs Total-Static Pressure Ratio.

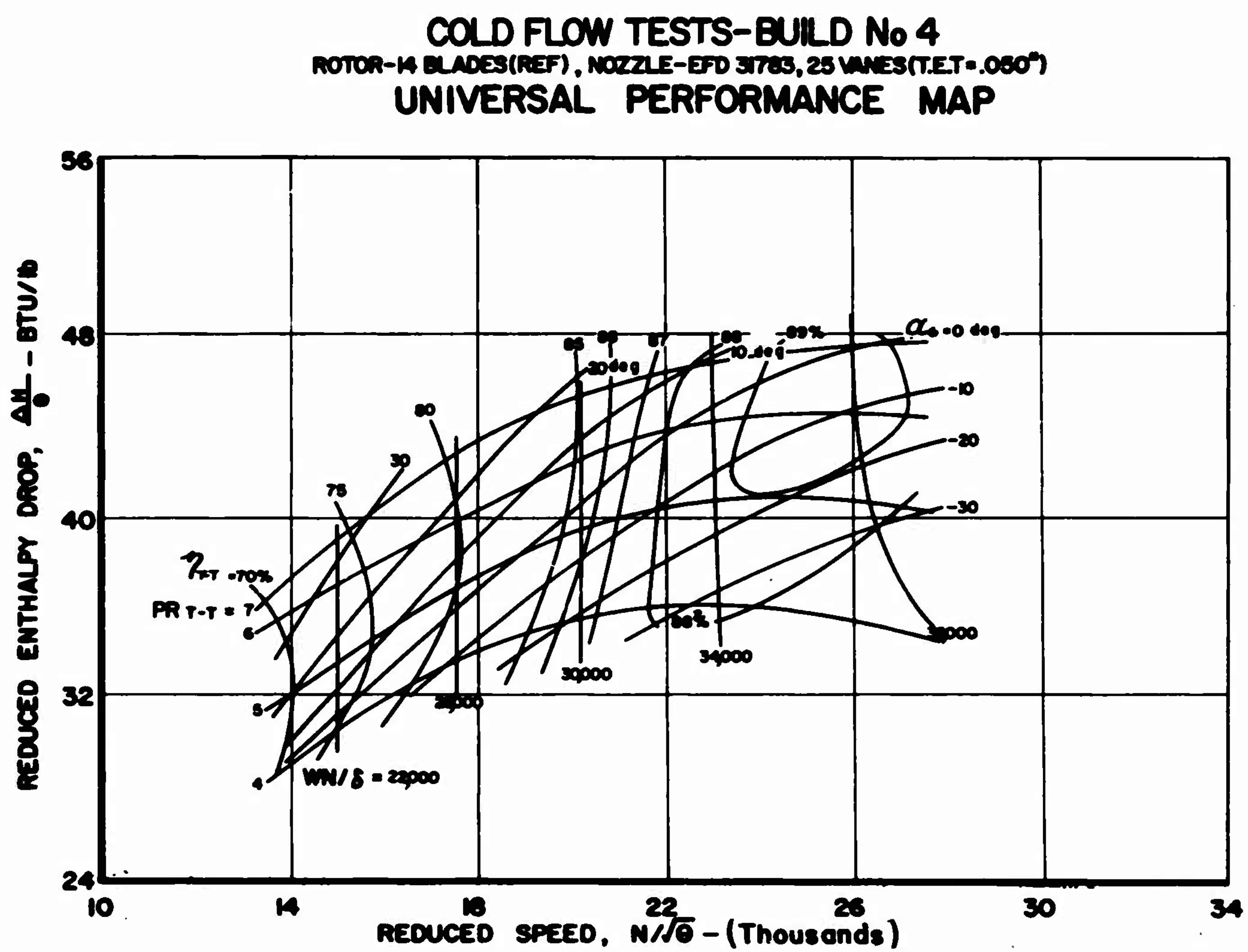

Figure 179. Build 4 - Reduced Enthalpy Drop vs Reduced Speed.

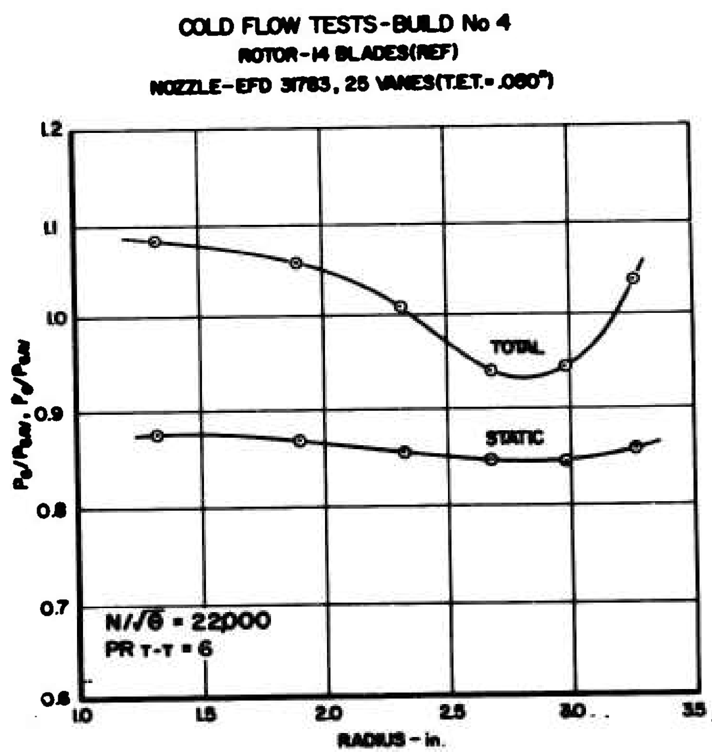

Figure 180. Build 4 - P_6/P_{6AV}, P_6/P_{6AV} vs Radius.

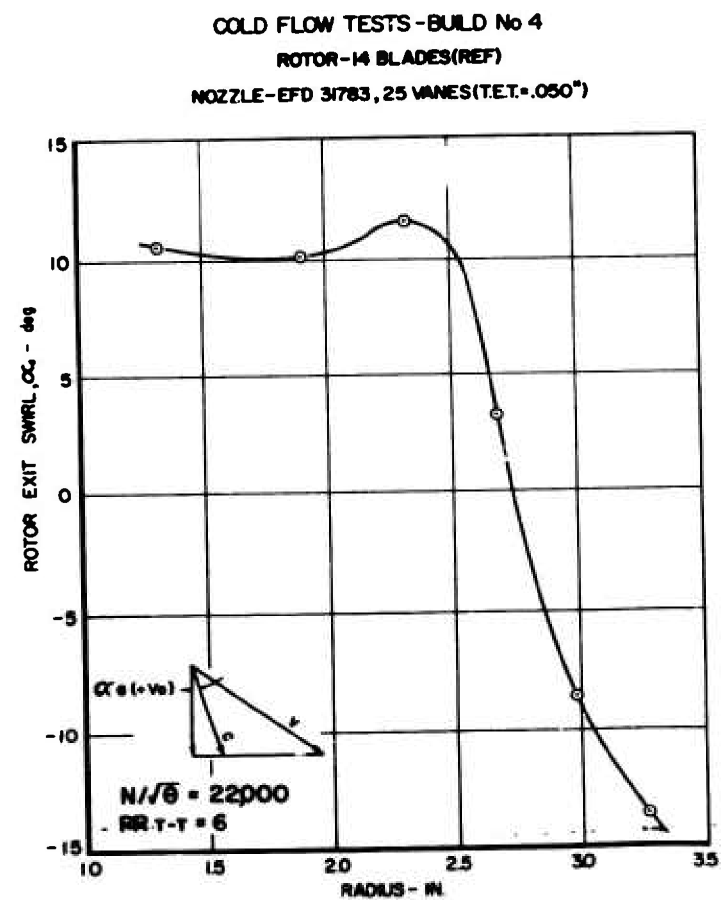

Figure 181. Build 4 - Rotor Exit Swirl vs Radius.

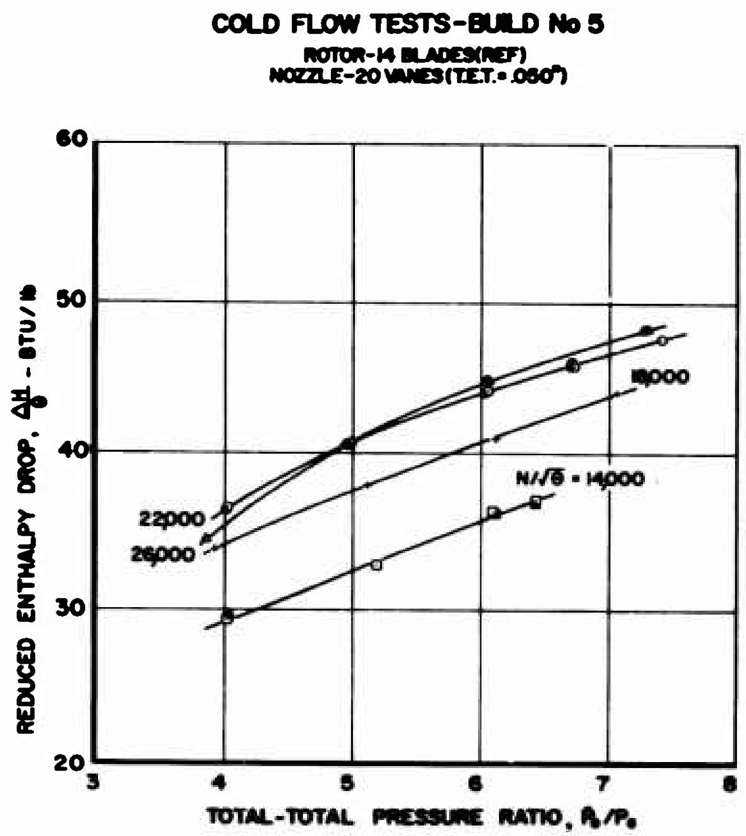

Figure 182. Build 5 - Reduced Enthalpy Drop vs Total-Total Pressure Ratio.

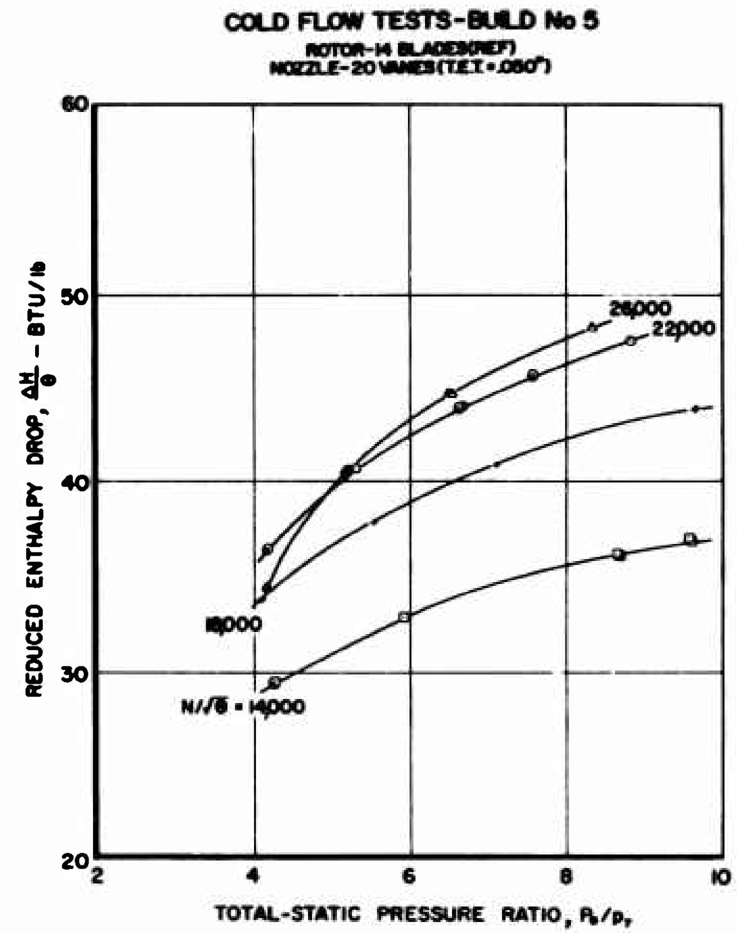

Figure 183. Build 5 - Reduced Enthalpy Drop vs Total-Static Pressure Ratio.

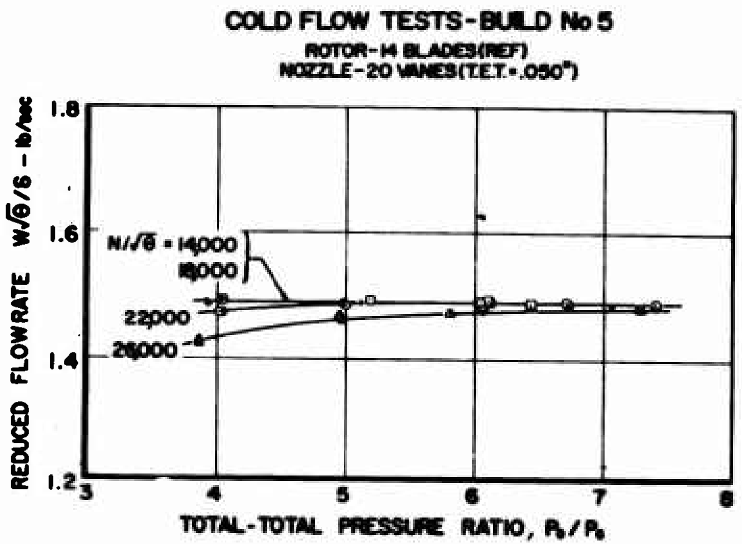

Figure 184. Build 5 - Reduced Flowrate vs Total-Total Pressure Ratio.

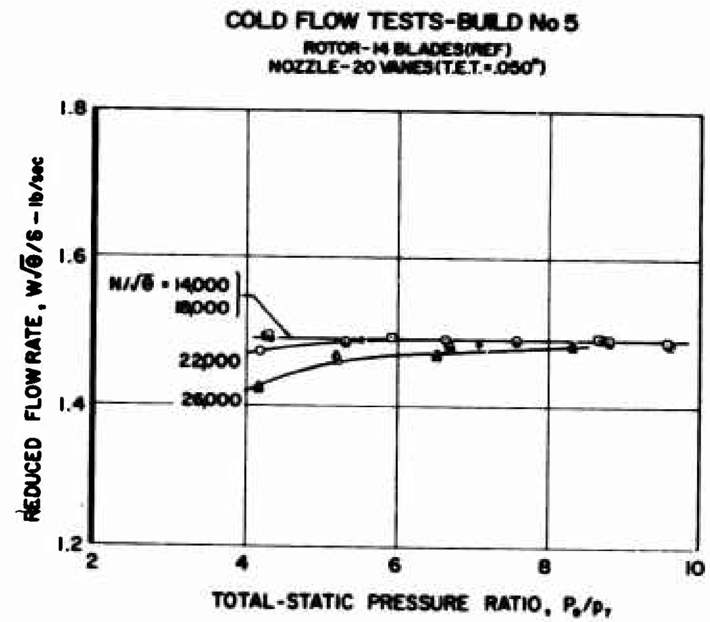

Figure 185. Build 5 - Reduced Flowrate vs Total-Static Pressure Ratio.

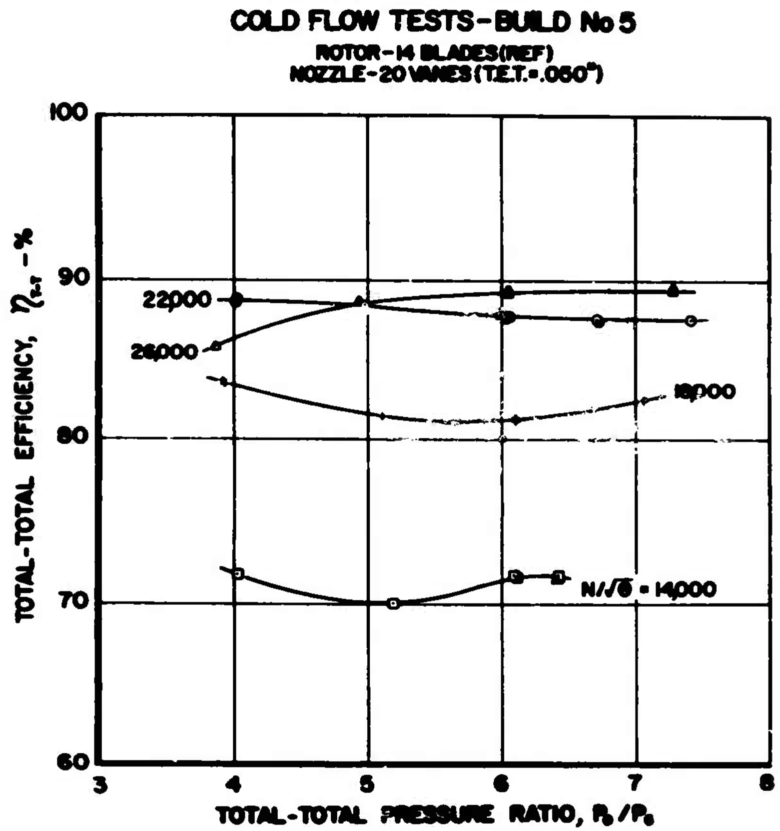

Figure 186. Build 5 - Total-Total Efficiency vs Total-Total Pressure Ratio.

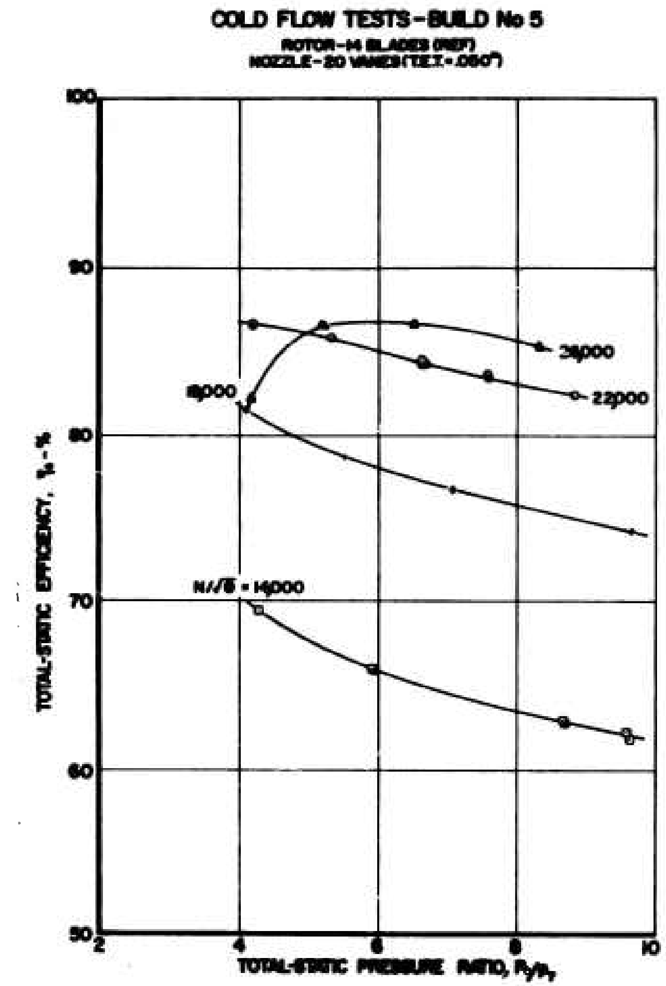

Figure 187. Build 5 - Total-Static Efficiency vs Total-Static Pressure Ratio.

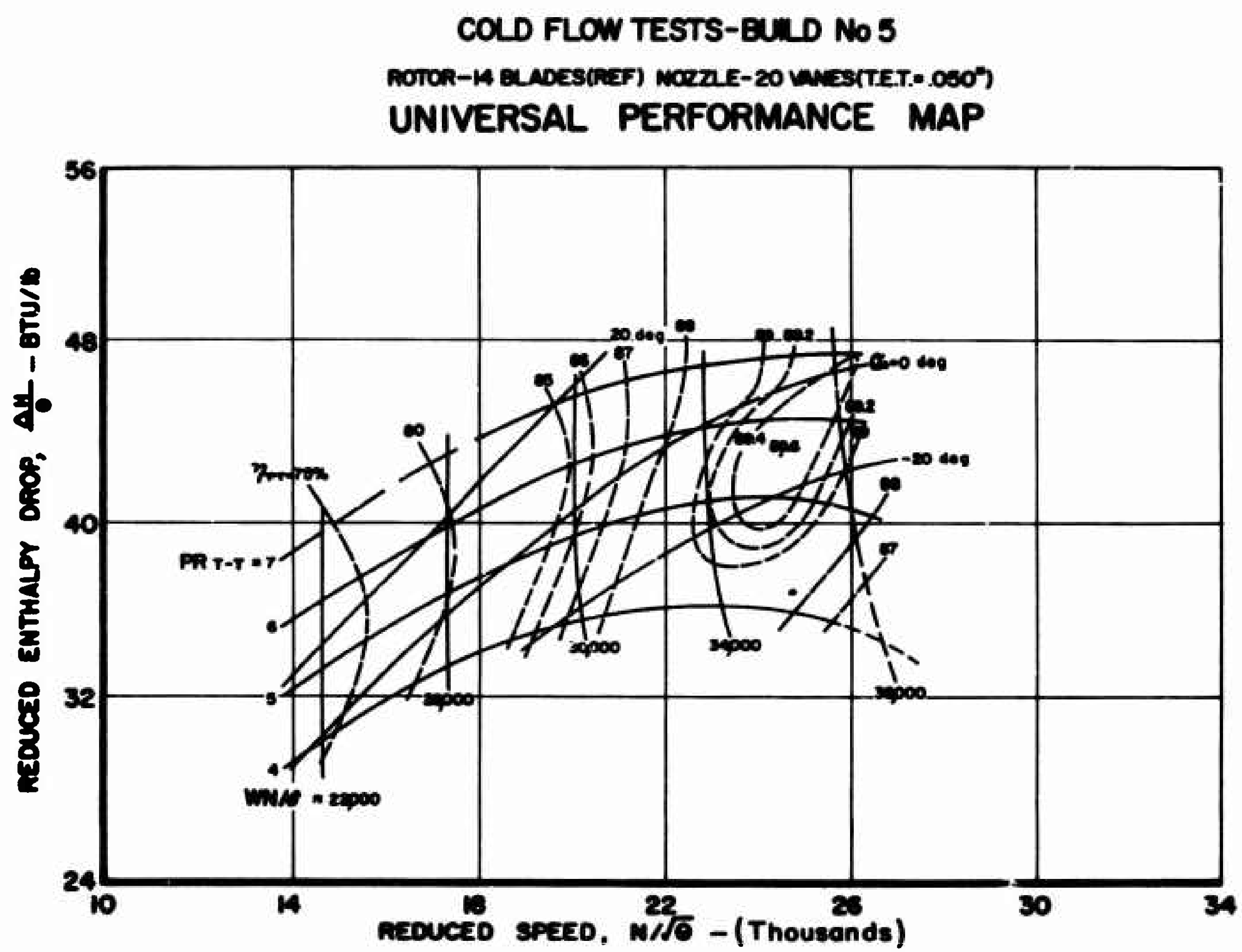

Figure 188. Build 5 - Reduced Enthalpy Drop vs Reduced Speed.

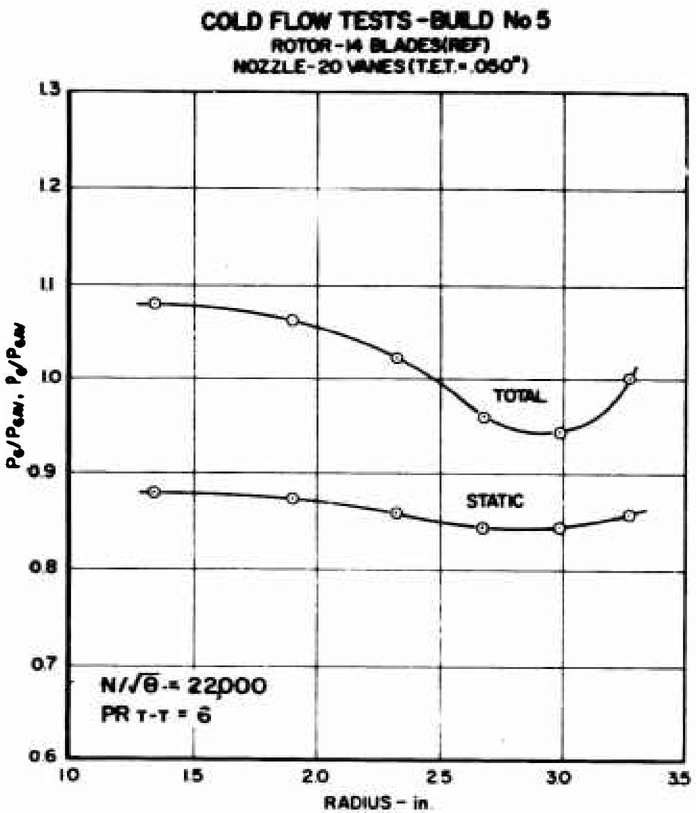

Figure 189. Build 5 - P_6/P_{6AV}, P_6/P_{6AV} vs Radius.

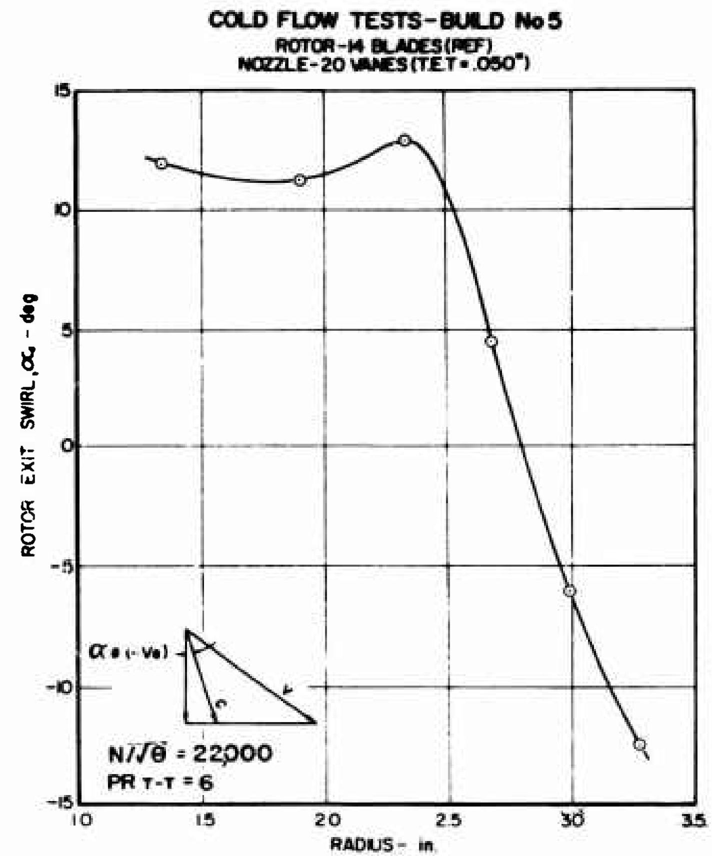

Figure 190. Build 5 - Rotor Exit Swirl vs Radius.

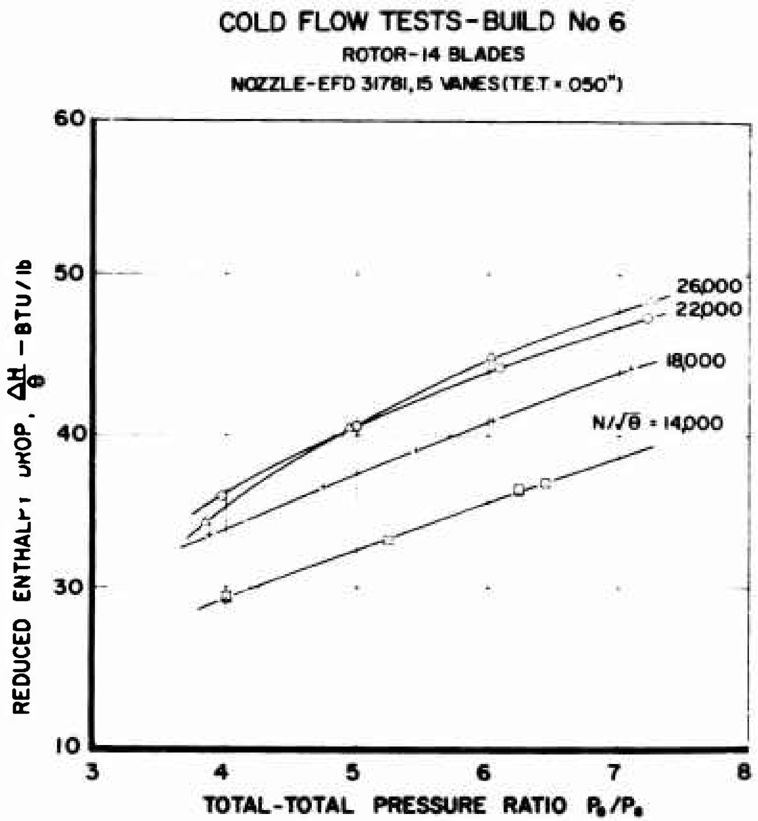

Figure 191. Build 6 - Reduced Enthalpy Drop vs Total-Total Pressure Ratio.

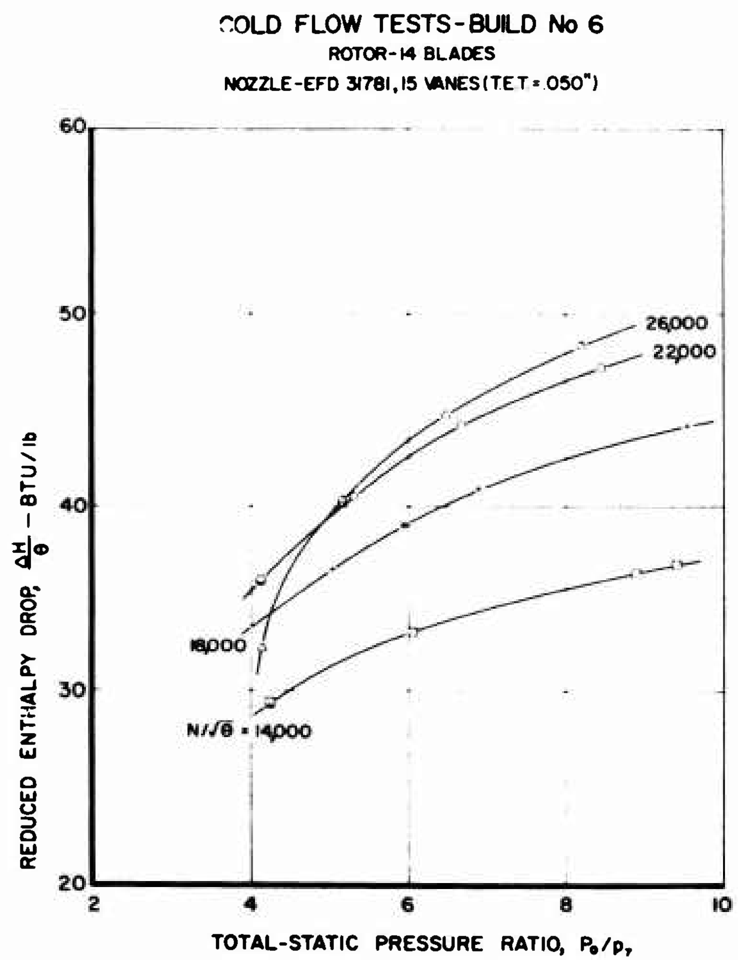

Figure 192. Build 6 - Reduced Enthalpy Drop vs Total-Static Pressure Ratio.

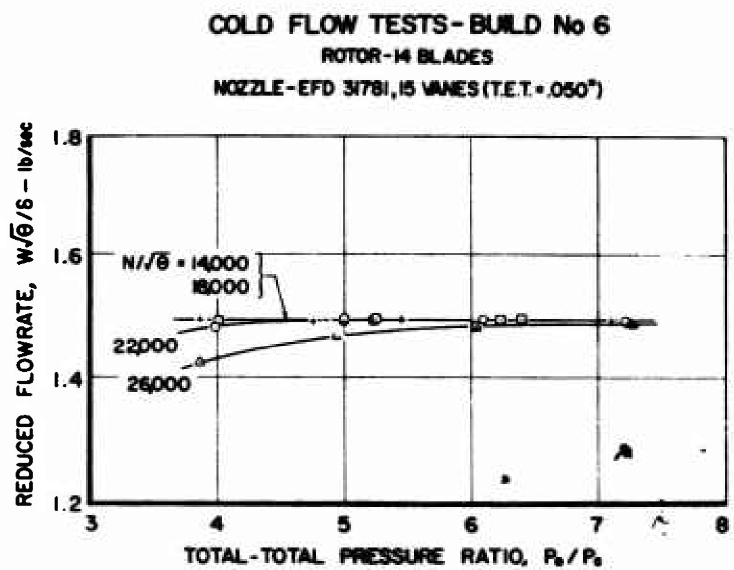

Figure 193. Build 6 - Reduced Flowrate vs Total-Total Pressure Ratio.

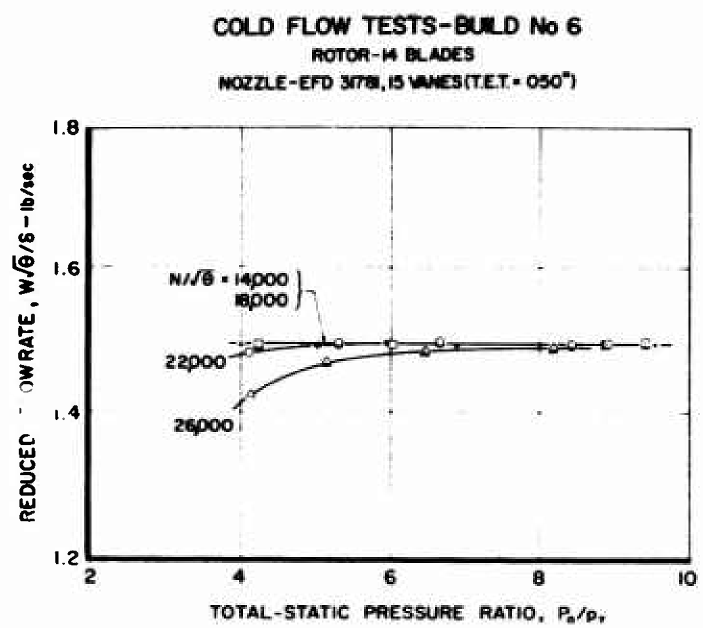

Figure 194. Build 6 - Reduced Flowrate vs Total-Static Pressure Ratio.

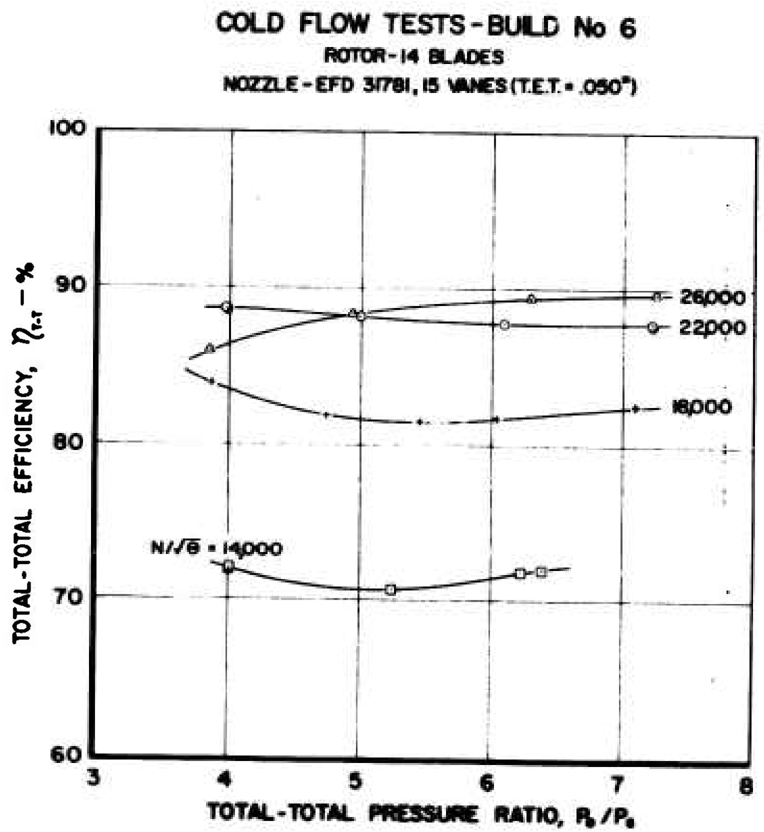

Figure 195. Build 6 - Total-Total Efficiency vs Total-Total Pressure Ratio.

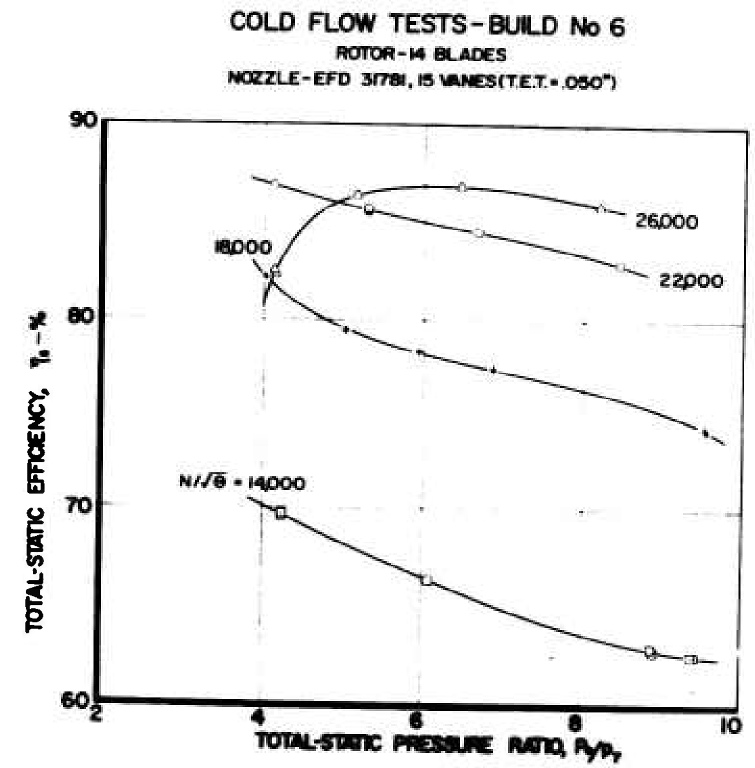

Figure 196. Build 6 - Total Static Efficiency vs Total Static Pressure Ratio

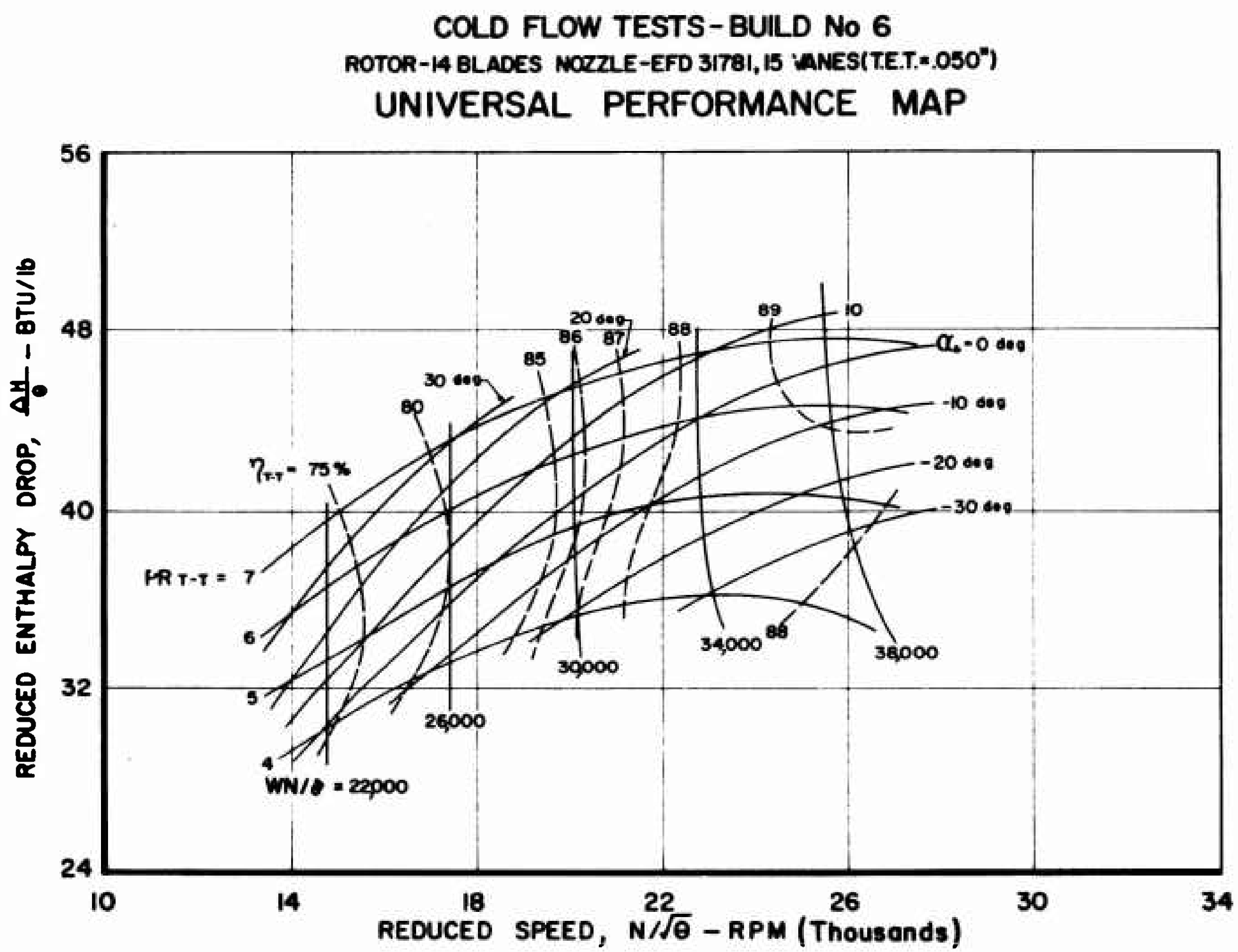

Figure 197. Build 6 - Reduced Enthalpy Drop vs Reduced Speed.

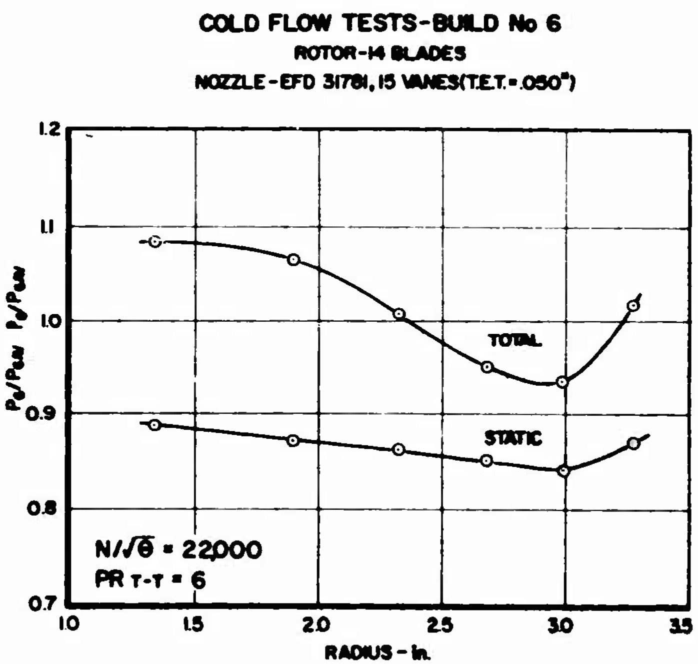

Figure 198. Build 6 - P_6/P_{6AV}, P_6/P_{6AV} vs Radius.

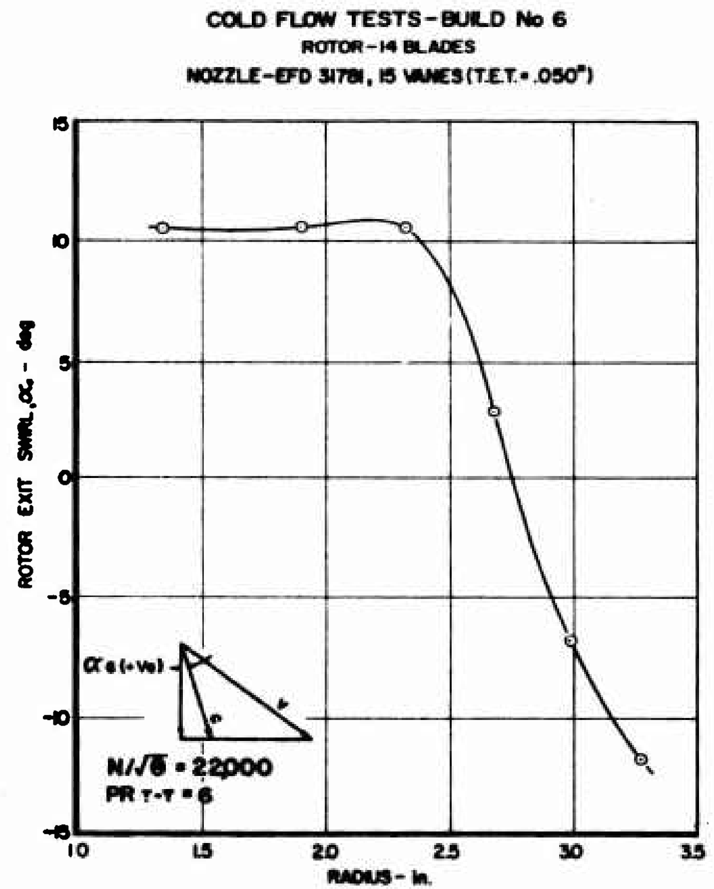

Figure 199. Build 6 - Rotor Exit Swirl vs Radius.

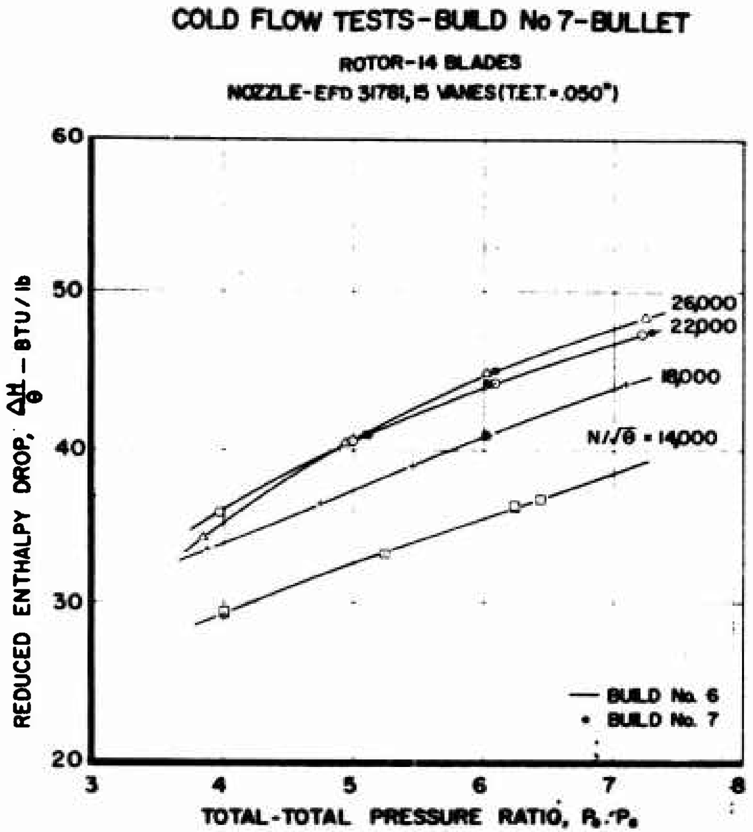

Figure 200. Build 7 - Reduced Enthalpy Drop vs Total-Total Pressure Ratio.

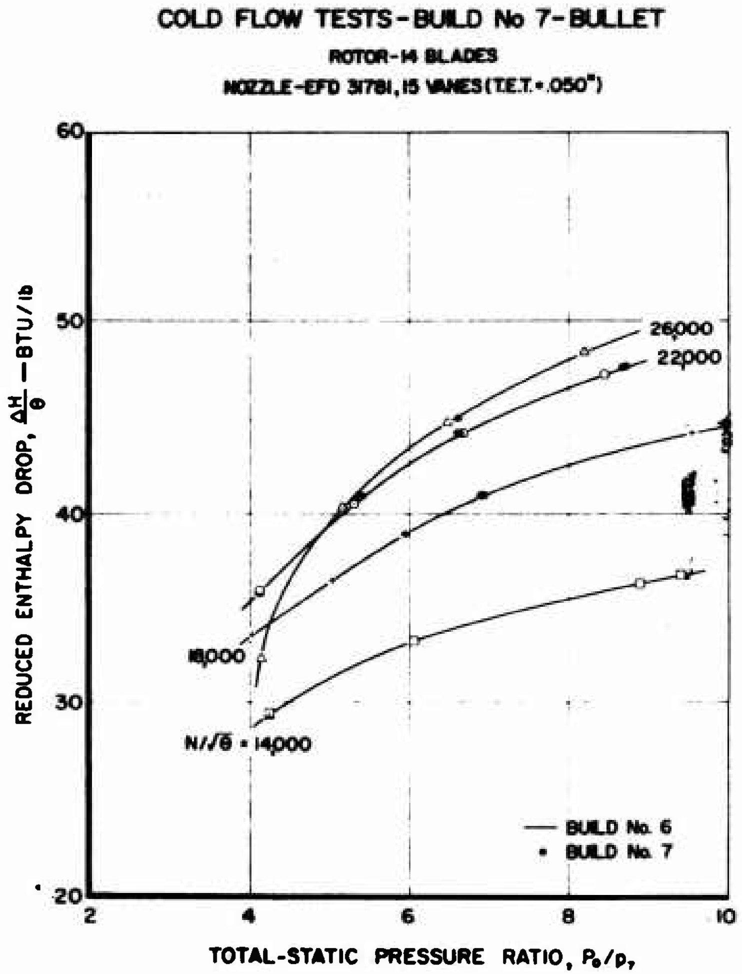

Figure 201. Build 7 - Reduced Enthalpy Drop vs Total-Static Pressure Ratio.

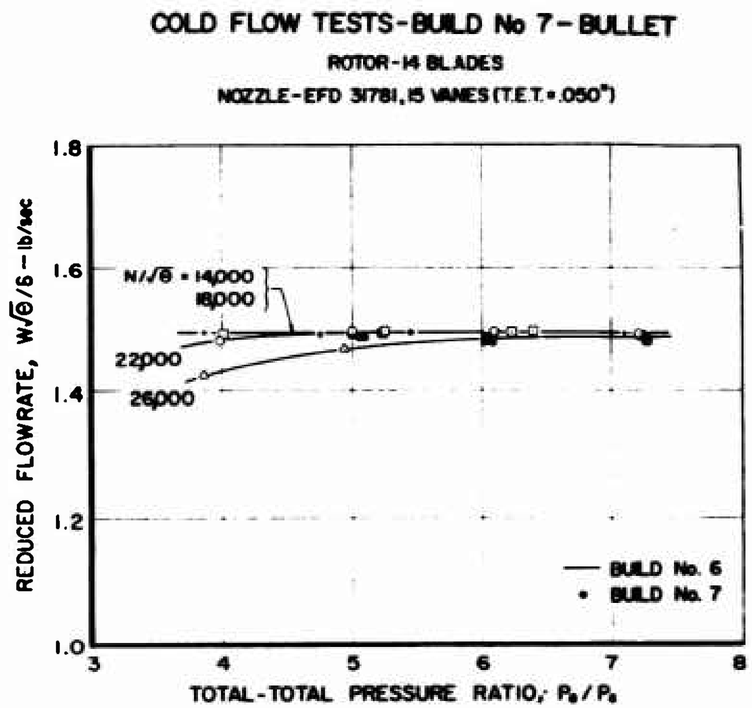

Figure 202. Build 7 - Reduced Flowrate vs Total-Total Pressure Ratio.

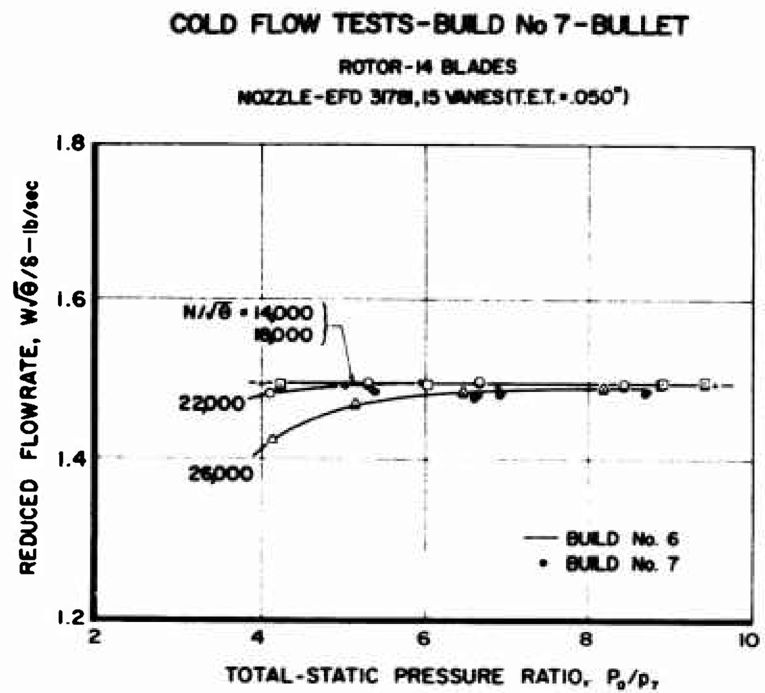

Figure 203. Build 7 - Reduced Flowrate vs Total-Static Pressure Ratio.

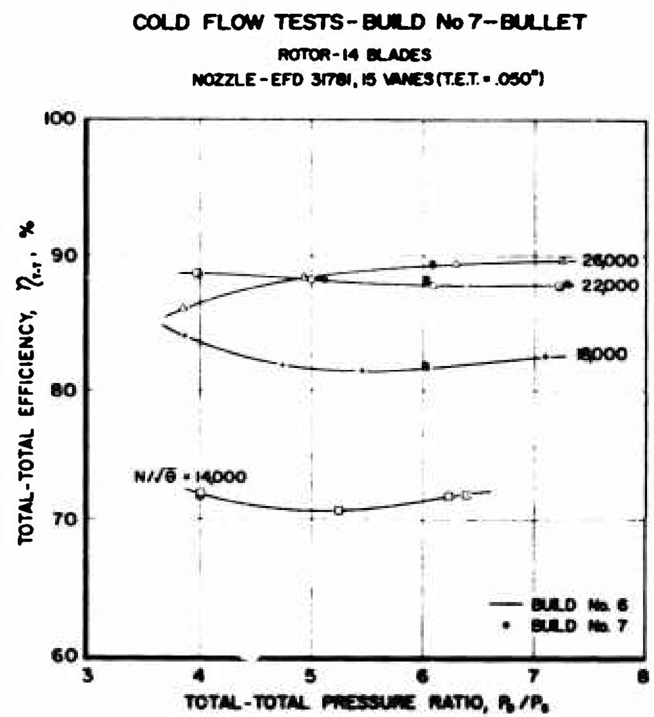

Figure 204. Build 7 - Total-Total Efficiency vs Total-Total Pressure Ratio.

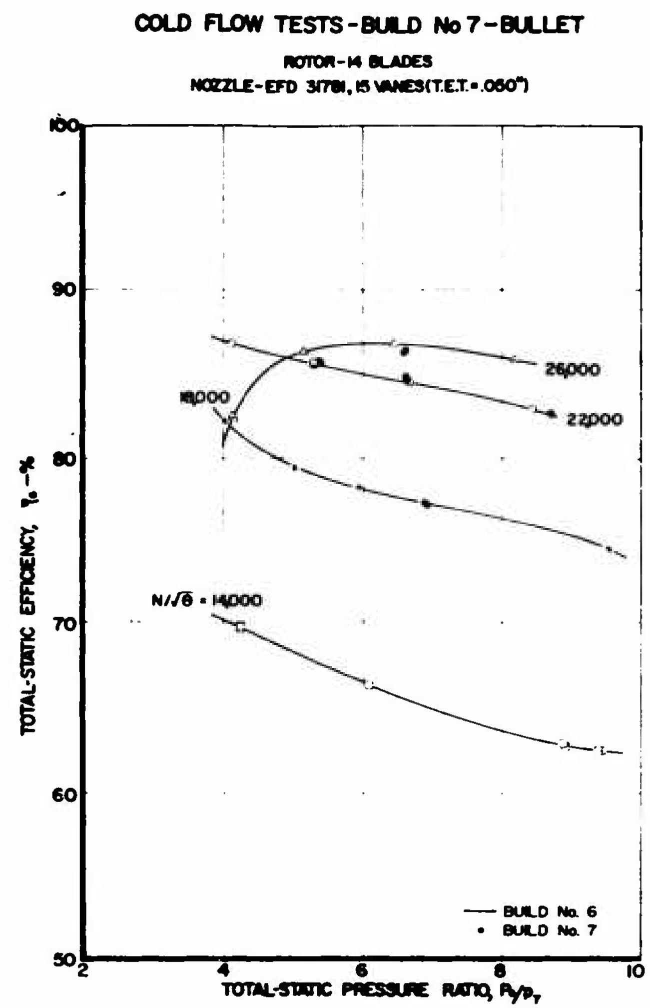

Figure 205. Build 7 - Total-Static Efficiency vs Total-Static Pressure Ratio.

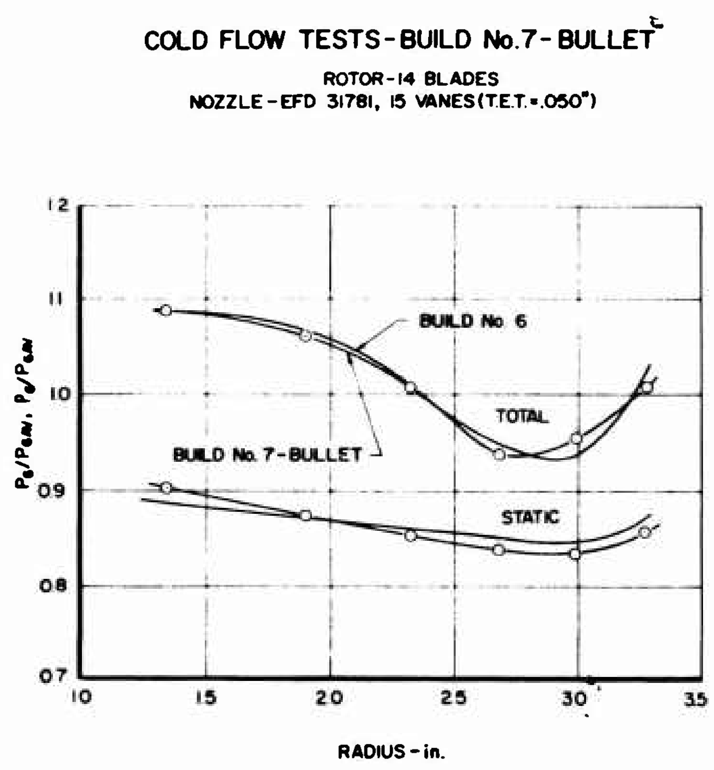

Figure 206. Build 7 - P_6/P_{6AV}, P_6/P_{6AV} vs Radius.

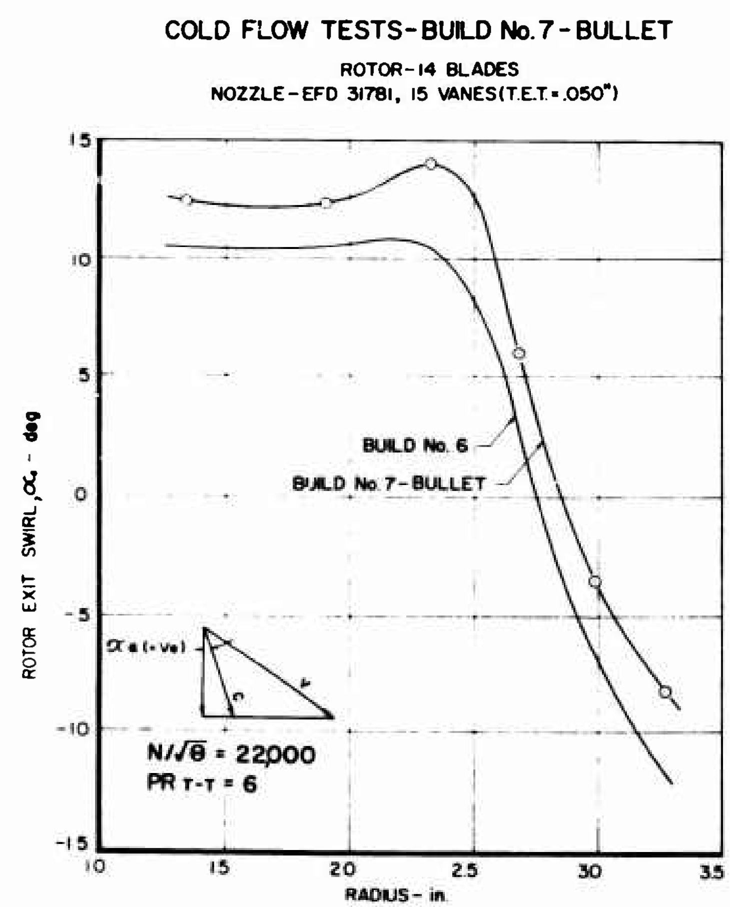

Figure 207. Build 7 - Rotor Exit Swirl vs Radius.

APPENDIX II
COLD-FLOW TEST DATA (TABLES)

TABLE XI. TEST OBSERVATIONS AND RESULTS OF COLD-FLOW TESTS - BUILD NO. 1

Cond No.	N_{mech} (rpm)	P_0 (psia)	T_0 (°R)	P_6 (psia)	P_6 (psia)	P_7 (psia)	T_8 (°R)	W_{actual} (lb/sec)	α_6 (deg)	PR_{T-T}	PR_{T-S}	$N/\sqrt{\theta}$ (rpm)	η_{T-T} (pct)	η_{T-S} (pct)	$W\sqrt{\theta}/\delta$ (lb/sec)	$\Delta H/\theta$ (Btu/lb)	WN/δ (lb/sec x rpm)
1	28,800	29.244	830.9	5.778	5.228	5.438	556.2	2.279	-12.63	5.061	5.378	22,755	89.61	87.07	1.4492	41.44	32,976
2	28,800	29.233	830.9	5.772	-	5.435	556.3	2.278	-	5.064	5.379	22,755	89.54	87.02	1.4492	41.42	32,978
3	28,800	29.150	831.4	4.799	4.118	4.373	533.7	2.298	3.02	6.075	6.666	22,748	89.33	85.98	1.4608	44.87	33,367
4	28,800	29.150	831.0	4.803	-	4.375	533.8	2.298	-	6.070	6.663	22,754	89.26	85.91	1.4661	44.82	33,360
5	28,800	29.098	828.9	4.022	3.062	3.486	512.9	2.301	12.60	7.234	8.348	22,783	88.69	84.23	1.4690	47.77	33,469
6'	28,800	29.098	829.0	4.034	-	3.486	512.9	2.298	-	7.214	8.348	22,781	88.80	84.25	1.4674	47.78	33,429
25	34,600	29.141	833.9	7.633	6.754	6.899	617.1	2.118	-49.84	3.818	4.224	27,289	82.15	77.41	1.3543	32.57	36,958
26	34,600	29.141	833.8	7.636	-	6.901	617.3	2.112	-	3.816	4.223	27,291	82.09	77.35	1.3503	32.54	36,849
27	34,600	29.115	[illegible]	5.982	5.356	5.580	571.1	2.190	-34.03	4.867	5.218	27,289	87.05	84.14	1.4013	39.48	38,240
28	34,600	29.111	[illegible]	5.976	-	5.588	571.1	2.190	-	4.871	5.210	27,284	87.08	84.27	1.4019	39.51	38,249
29	34,600	29.234	834.0	5.066	4.391	4.702	541.7	2.232	-18.17	5.770	6.217	27,287	89.40	86.58	1.4229	43.92	38,828
30	34,600	29.224	833.7	5.065	-	4.702	541.5	2.227	-	5.770	6.215	27,292	89.40	86.60	1.4195	43.92	38,740
31	34,600	29.157	833.5	4.237	3.446	3.732	519.2	2.239	- 4.54	6.882	7.813	27,295	89.43	85.29	1.4303	47.26	39,039
32	34,600	29.132	833.7	4.229	-	3.734	519.1	2.232	-	6.888	7.801	27,292	89.44	85.35	1.4276	47.28	38,964
39	34,570	29.070	830.8	4.256	3.508	3.804	518.5	2.237	- 5.83	6.831	7.642	27,316	89.39	85.69	1.4311	47.10	39,092
40	34,570	29.071	831.0	4.258	-	3.804	518.5	2.238	-	6.827	7.642	27,313	89.44	85.71	1.4320	47.12	39,111

Note: 1. Rotor Exit Pressures and Swirl are Area-Averages.
2. Station 7 is at Diffuser Exit: T-S Conditions Calculated to That Station.

Table XI - Continued

Cond No.	N_{mech} (rpm)	P_o (psia)	T_o (°R)	P_6 (psia)	p_6 (psia)	p_7 (psia)	T_8 (°R)	W_{actual} (lb/sec)	α_6 (deg)	PR_{T-T}	PR_{T-S}	$N/\sqrt{\theta}$ (rpm)	η_{T-T} (pct)	η_{T-S} (pct)	$W\sqrt{\theta}/\delta$ (lb/sec)	$\Delta H/\theta$ (Btu/lb)	WN/δ (lb/sec x rpm)
7	17,300	27.843	830.1	7.085	6.177	6.460	636.3	2.218	2.81	3.930	4.310	13,675	72.50	68.76	1.4807	29.26	20,249
8	17,300	27.846	830.3	7.058	-	6.391	636.5	2.215	-	3.946	4.357	13,674	72.30	68.32	1.4791	29.24	20,224
9	17,300	28.757	829.9	5.805	4.024	4.773	615.2	2.284	23.12	4.953	6.025	13,677	70.86	64.77	1.4762	32.42	20,190
10	17,300	28.765	830.1	5.802	-	4.773	615.3	2.284	-	4.958	6.027	13,675	70.85	64.78	1.4763	32.43	20,188
33	17,300	29.128	[illegible]	5.186	2.733	3.884	607.3	2.316	30.08	5.616	7.499	13,634	70.45	62.64	1.4829	34.20	20,217
34	17,300	29.136	836.1	5.190	-	3.887	607.4	2.320	-	5.613	7.496	13,626	70.62	62.79	1.4859	34.20	20,247
11	17,300	28.818	832.8	5.034	2.841	3.843	603.0	2.291	29.88	5.725	7.499	13,653	70.65	63.36	1.4801	34.27	20,208
12	17,300	28.805	833.7	5.022	-	3.816	599.2	2.293	-	5.736	7.548	13,646	71.94	64.42	1.4829	35.25	20,235
35	17,300	29.108	835.5	4.700	1.358	3.103	596.0	2.312	31.57	6.193	9.382	13,631	70.94	60.94	1.4812	35.92	20,190
36	17,300	29.080	835.4	4.703	-	3.100	596.8	2.311	-	6.183	9.380	13,632	70.71	60.71	1.4819	35.79	20,201
13	23,100	28.732	830.8	7.382	6.862	7.093	606.3	2.272	-17.81	3.892	4.051	18,253	84.40	82.42	1.4704	33.86	26,840
14	23,100	28.730	830.8	7.366	-	7.089	606.4	2.273	-	3.900	4.053	18,252	84.28	82.39	1.4716	33.85	26,860
15	23,100	28.646	831.4	5.862	5.208	5.434	581.6	2.290	- 0.85	4.887	5.272	18,246	82.85	79.86	1.4873	37.65	27,137
16	23,100	28.659	831.5	5.856	-	5.429	581.8	2.289	-	4.894	5.279	18,245	82.73	79.76	1.4862	37.63	27,117
17	23,100	28.593	832.6	4.907	3.875	4.290	563.1	2.285	13.81	5.827	6.665	18,233	82.21	77.73	1.4879	40.56	27,128
18	23,100	28.582	832.3	4.911	-	4.300	562.8	2.287	-	5.820	6.647	18,236	82.28	77.84	1.4895	40.57	27,163
19	23,100	28.343	844.6	4.196	2.493	3.319	533.5	2.266	23.12	6.755	8.540	18,181	82.35	75.59	1.4995	43.20	27,261
20	23,100	28.335	846.8	4.198	-	3.324	555.0	2.265	-	6.750	8.525	18,158	82.35	75.61	1.5007	43.19	27,250
21	23,100	28.125	829.5	4.071	2.221	3.165	539.7	2.245	26.73	6.909	8.886	18,267	82.72	75.64	1.4816	43.82	27,062
22	23,100	28.124	829.7	4.061	-	3.163	539.6	2.242	-	6.925	8.892	18,265	82.72	75.64	1.4816	43.82	27,062
23	28,880	29.225	835.1	7.416	6.835	7.039	595.8	2.245	-31.77	3.941	4.152	22,777	88.84	86.18	1.4326	35.90	32,629
24	28,880	29.222	833.5	7.416	-	7.040	594.8	2.243	-	3.940	4.515	22,799	88.78	86.12	1.4298	35.88	32,599
37	28,880	29.320	832.0	7.464	6.778	7.006	592.1	2.242	-32.97	3.928	4.185	22,804	89.57	86.33	1.4234	36.13	32,458
38	28,880	29.325	829.0	7.465	-	7.016	591.7	2.243	-	3.928	4.180	22,845	88.91	85.76	1.4212	35.87	32,467

Note: 1. Rotor Exit Pressures and Swirl are Area-Averages.
2. Station 7 is at Diffuser Exit; T-S Conditions Calculated to That Station.

TABLE XII. TEST OBSERVATIONS AND RESULTS FOR COLD-FLOW TESTS - BUILD NO. 2

Cond No.	N_{mech} (rpm)	P_o (psia)	T_o (°R)	P_6 (psia)	P_6 (psia)	P_7 (psia)	T8 (°R)	W_{actual} (lb/sec)	α_6 (deg)	PR_{T-T}	PR_{T-S}	$N/\sqrt{\theta}$ (rpm)	η_{T-T} (pct)	η_{T-S} (pct)	$W\sqrt{\theta}/\delta$ (lb/sec)	$\Delta H/\theta$ (Btu/lb)	WN/δ (lb/sec x rpm)
47	17,760	29.065	832.7	7.457	6.813	7.075	641.5	2.299	4.68	3.898	4.108	14,017	71.68	69.49	1.473	28.78	20,645
48	17,760	29.056	832.3	7.431	-	7.082	641.4	2.294	-	3.895	4.103	14,020	71.63	69.47	1.470	28.75	20,604
49	17,760	28.936	832.7	6.108	5.070	5.522	624.8	2.296	17.99	4.737	5.240	14,017	69.92	66.53	1.477	31.28	20,710
50	17,760	28.956	832.5	6.111	-	5.520	624.5	2.293	-	4.738	5.246	14,019	69.98	66.57	1.475	31.31	20,672
51	17,760	29.022	832.8	5.184	3.208	4.169	607.6	2.302	28.95	5.599	6.961	14,017	69.91	63.85	1.481	33.89	20,760
52	17,760	29.026	832.6	5.181	-	4.168	607.4	2.299	-	5.602	6.964	14,018	69.91	63.85	1.475	33.90	20,676
53	17,760	29.060	832.5	4.553	1.925	3.094	592.0	2.316	32.06	6.383	9.391	14,019	70.61	61.41	1.484	36.21	20,803
54	17,760	29.026	832.2	4.554	-	3.097	590.3	2.311	-	6.374	9.373	14,021	71.08	61.81	1.482	36.43	20,778
55	22,840	29.012	831.7	7.451	6.965	7.165	613.2	2.277	-15.39	3.894	4.049	18,037	82.06	80.18	1.460	32.93	26,341
56	22,840	29.007	832.0	7.458	-	7.173	613.3	2.279	-	3.889	4.044	18,034	82.13	80.25	1.463	32.93	26,376
57	22,840	29.065	831.7	6.035	5.403	5.620	591.0	2.303	0.43	4.816	5.172	18,037	80.39	77.62	1.474	36.27	26,594
58	22,840	29.089	831.6	6.041	-	5.620	590.8	2.305	-	4.815	5.176	18,038	80.41	77.60	1.475	36.27	26,601
59	22,840	29.056	831.8	4.970	3.983	4.372	569.4	2.306	14.05	5.847	6.647	18,036	80.02	75.85	1.477	39.54	26,638
60	22,840	29.071	331.9	4.973	-	4.370	569.4	2.308	-	5.846	6.653	18,035	80.03	75.83	1.477	39.55	26,644
61	22,840	29.087	832.6	4.088	2.023	3.050	543.8	2.312	25.44	7.115	9.536	18,027	81.20	73.35	1.480	43.46	26,676
62	22,840	29.092	832.6	4.087	-	3.048	543.8	2.309	-	7.119	9.545	18,027	81.20	73.34	.478	43.47	26,635
63	27,910	29.030	832.4	7.364	6.77	7.070	599.7	2.236	-31.31	3.942	4.106	22,032	86.68	84.63	1.434	35.04	31,595
64	27,910	29.027	832.3	7.376	-	7.085	599.8	2.236	-	3.935	4.097	22,033	86.68	84.66	1.434	35.00	31,594
65	27,910	29.167	831.6	5.921	5.362	5.611	568.8	2.282	-15.50	4.926	5.198	22,043	86.77	84.53	1.456	39.59	32,090
66	27,910	29.172	831.3	5.921	-	5.604	568.7	2.285	-	4.927	5.206	22,047	86.75	84.46	1.457	39.58	32,129
67	27,910	29.065	831.3	4.865	4.179	4.431	544.9	2.303	0.95	5.974	6.560	22,046	86.57	83.27	1.474	43.18	32,506
68	27,910	29.057	831.1	4.864	-	4.436	544.7	2.299	-	5.974	6.551	22,049	86.58	83.32	1.472	43.18	32,456
69	27,910	29.057	831.6	4.132	3.024	3.539	525.3	2.305	13.01	7.032	8.210	22,042	86.64	81.87	1.476	46.17	32,533
70	27,910	29.057	831.4	4.131	-	3.539	525.1	2.303	-	7.033	8.210	22,045	86.63	81.88	1.475	46.17	32,516

Note: 1. Rotor Exit Pressures and Swirl are Area-Averages.
2. Station 7 is at Diffuser Exit: T-S Conditions Calculated to That Station.

TABLE XII.- Continued

Cond No.	N_{mech} (rpm)	P_o (psia)	T_o (°R)	P_6 (psia)	P_6 (psia)	P_7 (psia)	T_R (°R)	W_{actual} (lb/sec)	α_6 (deg)	PR_{T-T}	PR_{T-S}	$N/\sqrt{\theta}$ (rpm)	η_{T-T} (pct)	η_{T-S} (pct)	$W\sqrt{\theta}/\delta$ (lb/sec)	$\Delta H/\theta$ (Btu/lb)	WN/δ (lb/sec x rpm)
71	32,990	29.098	832.2	7.545	6.754	6.902	603.7	2.171	-43.60	3.856	4.216	26,045	86.25	81.86	1.389	34.40	36,179
72	32,990	29.089	832.[illegible]	7.543	-	6.911	603.8	2.171	-	3.857	4.209	26,047	86.19	81.89	1.389	34.38	36,190
73	32,990	29.180	932.4	6.090	5.440	5.701	569.1	2.232	-29.72	4.791	5.118	26,043	88.09	85.27	1.424	39.64	37,076
74	32,990	29.189	832.3	6.084	-	5.702	569.0	2.232	-	4.797	5.119	26,043	88.06	85.28	1.474	39.65	37,085
75	32,990	29.073	832.0	4.836	4.203	4.494	537.0	2.257	-12.94	6.012	6.469	26,048	88.84	86.17	1.445	44.43	37,639
76	32,990	29.059	831.7	4.819	-	4.480	536.9	2.257	-	6.029	6.487	26,053	88.72	86.07	1.445	44.42	37,652
77	32,990	29.057	831.7	4.166	3.382	3.724	517.2	2.277	0.20	6.975	7.802	26,053	89.20	85.56	1.458	47.37	37,989
78	32,990	29.045	831.7	4.172	-	3.729	517.1	2.278	-	6.963	7.789	26,053	89.30	85.65	1.460	47.40	38,025

Note: 1. Rotor Exit Pressures and Swirl are Area-Averages.
2. Station 7 is at Diffuser Exit; T-S Conditions Calculated to That Station.

TABLE XIII. TEST OBSERVATIONS AND RESULTS FOR COLD-FLOW TESTS - BUILD NO. 3

Cond No.	N_{mech} (rpm)	P_o (psia)	T_o (°R)	P_6 (psia)	p_6 (psia)	P_7 (psia)	T_8 (°R)	W_{actual} (lb/sec)	α_6 (deg)	PR_{T-T}	PR_{T-S}	$N/\sqrt{\theta}$ (rpm)	η_{T-T} (pct)	η_{T-S} (pct)	$W\sqrt{\theta}/\delta$ (lb/sec)	$\Delta H/\theta$ (Btu/lb)	WN/δ (lb/sec x rpm)
85	17,760	29.068	831.8	7.657	7.126	7.346	642.2	2.309	2.95	3.796	3.957	14,025	72.30	70.51	1.4785	28.57	20,735
86	17,760	29.070	831.9	7.659	-	7.345	642.1	2.305	-	3.796	3.958	14,024	72.37	70.57	1.4760	28.59	20,698
119	17,760	29.054	832.2	7.388	6.846	7.037	639.8	2.307	4.10	3.933	4.129	14,021	71.77	69.76	1.4781	28.97	20,725
120	17,760	20.059	832.2	7.380	-	7.041	639.2	2.307	-	3.938	4.127	14,021	71.97	70.03	1.4778	29.08	20,720
87	17,660	29.023	831.8	5.833	4.607	5.291	61[illegible].4	2.312	18.78	4.975	5.485	13,946	69.78	66.62	1.4827	31.99	20,679
88	17,660	29.054	832.0	5.848	-	5.307	620.0	2.311	-	4.968	5.475	13,944	69.68	66.54	1.4807	31.93	20,647
121	17,760	29.057	832.7	5.67[illegible]	4.494	5.045	616.9	2.313	20.17	5.123	5.760	14,017	69.80	66.14	1.4820	32.47	20,774
122	17,760	29.069	832.7	5.680	-	5.048	617.1	2.310	-	5.118	5.759	14,017	69.78	66.08	1.4800	32.44	20,745
129	17,760	29.132	831.7	5.151	3.203	4.151	603.4	2.318	28.81	5.656	7.018	14,026	70.65	64.60	1.4806	34.40	20,767
130	17,760	29.144	831.6	5.151	-	4.158	603.4	2.316	-	5.658	7.009	14,026	70.61	64.61	1.4785	34.39	20,737
89	17,760	29.068	832.1	5.013	2.913	3.893	600.8	2.310	29.99	5.799	7.467	14,022	70.74	63.90	1.4795	34.83	20,746
90	17,760	29.096	832.1	5.010	-	3.893	600.5	2.311	-	5.807	7.474	14,022	70.80	63.97	1.4785	34.88	20,731
91	17,760	29.101	832.1	4.543	1.668	3.080	589.2	2.307	32.90	6.406	9.449	14,022	71.22	61.90	1.4759	36.57	20,695
92	17,760	29.086	832.3	4.549	-	3.077	589.3	2.313	-	6.394	9.452	14,020	71.31	61.93	1.4802	36.59	20,753
101	22,840	29.121	832.7	7.587	7.043	7.244	612.7	2.299	-17.09	3.838	4.020	18,027	83.20	80.93	1.4703	33.10	26,504
102	22,840	29.079	832.6	7.595	-	7.259	613.3	2.295	-	3.829	4.006	18,028	83.10	80.87	1.4692	33.01	26,486
93	22,840	29.217	836.9	7.500	7.018	7.214	611.4	2.305	-16.22	3.895	4.050	17,982	84.12	82.20	1.4728	33.77	26,483
94	22,840	29.227	832.1	7.496	-	7.213	611.1	2.307	-	3.899	4.052	18,033	82.89	81.03	1.4690	33.29	26,490
95	22,840	29.186	830.3	5.916	5.309	5.459	583.9	2.318	0.94	4.933	5.346	18,053	81.43	78.35	1.4767	37.18	26,658
96	22,840	29.188	830.8	5.907	-	5.452	584.3	2.322	-	4.942	5.354	18,047	81.35	78.28	1.4797	37.18	26,705
97	22,840	29.013	830.8	4.843	3.816	4.258	563.8	2.304	14.93	5.991	6.814	18,047	80.66	76.52	1.4770	40.28	26,655
98	22,840	29.051	830.9	4.841	-	4.243	563.8	2.308	-	6.000	6.846	18,047	80.72	76.48	1.4780	40.34	26,672
99	22,840	28.999	831.5	4.163	2.201	3.192	543.3	2.302	27.27	6.965	9.085	18,039	81.82	74.46	1.4773	43.44	26,650
100	22,840	28.961	831.1	4.141	-	3.165	542.4	2.303	-	6.994	9.151	18,043	81.88	74.46	1.4793	43.54	26,691

Note: 1. Rotor Exit Pressures and Swirl are Area-Averages.
2. Station 7 is at Diffuser Exit; T-S Conditions Calculated to That Station.

TABLE XIII - Continued

Cond No.	N_{mech} (rpm)	P_o (psia)	T_o (°R)	P_6 (psia)	P_6 (psia)	P_7 (psia)	T_8 (°R)	W_{actual} (lb/sec)	α_6 (deg)	PR_{T-T}	PR_{T-S}	$N/\sqrt{\theta}$ (rpm)	η_{T-T} (pct)	η_{T-S} (pct)	$W\sqrt{\theta}/\delta$ (lb/sec)	$\Delta h/\theta$ (Btu/lb)	WN/δ (lb/sec x rpm)
103	27,910	29.222	832.4	7.326	6.767	6.981	593.9	2.261	-29.53	3.989	4.186	22,032	88.20	85.78	1.4403	35.90	31,731
104	27,910	29.251	833.1	7.328	-	6.979	594.1	2.259	-	3.992	4.191	22,023	88.28	85.83	1.4381	35.95	31,671
105	27,910	29.0	831.6	5.920	5.351	5.558	566.5	2.291	-13.46	4.912	5.233	22,042	87.68	85.04	1.4655	39.95	32,304
106	27,910	29.071	831.7	5.921	-	5.561	566.8	2.291	-	4.910	5.228	22,042	87.61	84.98	1.4665	39.91	32,325
107	27,910	28.864	831.6	4.864	4.172	4.367	542.1	2.295	1.69	5.934	6.610	22,042	87.73	83.89	1.4797	43.63	32,617
108	27,910	28.855	831.6	4.854	-	4.367	542.4	2.293	-	5.944	6.607	22,043	87.57	83.81	1.4785	43.58	32,591
109	27,910	29.109	831.9	4.095	3.078	3.445	520.5	2.311	14.46	7.108	8.449	22,039	87.65	82.36	1.4777	46.90	32,568
110	27,910	29.104	831.8	4.101	-	3.443	520.4	2.313	-	7.097	8.454	22,040	87.71	82.35	1.4789	46.91	32,594
117	32,990	29.080	832.1	7.701	6.926	7.012	608.3	2.162	-46.22	3.776	4.147	26,047	85.59	80.96	1.3842	33.71	36,053
118	32,990	29.080	832.0	7.706	-	7.016	608.2	2.162	-	3.774	4.145	26,048	85.62	80.97	1.3840	33.71	36,051
115	32,990	29.161	832.6	5.964	5.240	5.607	654.4	2.243	-27.83	4.890	5.201	26,039	88.78	86.16	1.4324	40.36	37,299
116	32,990	29.172	832.5	5.973	-	5.605	654.6	2.246	-	4.884	5.205	26,041	88.75	86.04	1.4331	40.32	37,321
113	32,990	29.057	832.3	4.906	4.294	4.576	536.8	2.260	-13.17	5.923	6.350	26,043	89.54	86.94	1.4482	44.49	37,717
114	32,990	20.062	832.4	4.905	-	4.580	536.9	2.265	-	5.924	6.345	26,042	89.53	86.97	1.4509	44.49	37,783
111	32,990	29.055	832.3	4.105	3.389	3.670	513.3	2.271	0.74	7.078	7.917	26,043	89.91	86.27	1.4553	48.03	37,900
112	32,990	29.052	832.4	4.110	-	3.675	513.3	2.275	-	7.069	7.906	26,042	89.96	86.33	1.4578	48.04	37,964
131	32,990	29.157	832.1	4.215	3.509	3.794	516.5	2.281	- 3.32	6.917	7.685	26,047	89.75	86.27	1.4561	47.52	37,928
132	32,990	29.160	832.0	4.215	-	3.794	516.4	2.274	-	6.918	7.686	26,048	89.76	86.29	1.4517	47.53	37,814

Note: 1. Rotor Exit Pressures and Swirl are Area-Averages.
2. Station 7 is at Diffuser Exit; T-S Conditions Caluclated to That Station.

TABLE XIV. TEST OBSERVATIONS AND RESULTS OF COLD-FLOW TESTS - BUILD NO. 4

Cond No.	N_{mech} (rpm)	P_o (psia)	T_o (°R)	P_6 (psia)	P_6 (psia)	P_7 (Psia)	T_8 (°R)	W_{actual} (lb/sec)	α_6 (deg)	PR_{T-T}	PR_{T-S}	$N/\sqrt{\theta}$ (rpm)	η_{T-T} (pct)	η_{T-S} (pct)	$W\sqrt{\theta}/\delta$ (lb/sec)	$\Delta H/\theta$ (Btu/lb)	WN/δ (lb/sec x rpm)
133	17,760	29.372	828.4	7.010	6.321	6.583	631.0	2.324	4.09	4.190	4.462	14,053	71.32	68.89	1.470	29.868	20,654
134	17,760	29.379	830.2	7.003	-	6.581	631.9	2.330	-	4.195	4.464	14,039	71.41	69.01	1.474	29.928	20,696
141	17,760	29.266	834.3	7.010	6.470	6.575	635.6	2.324	3.00	4.175	4.451	14,004	71.42	68.93	1.480	29.849	20,729
142	17,760	29.281	834.4	7.010	-	6.574	635.6	2.331	-	4.177	4.454	14,003	71.42	68.93	1.484	29.858	20,780
173	17,760	29.311	830.6	6.166	5.240	5.597	622.3	2.316	12.95	4.754	5.237	14,035	70.10	66.85	1.469	31.419	20,623
174	17,760	29.316	830.7	6.159	-	5.602	622.2	2.317	-	4.760	5.233	14,034	70.14	66.95	1.470	31.456	20,629
135	17,760	29.366	831.9	5.816	4.680	5.177	618.8	2.335	19.68	5.049	5.672	14,024	69.51	65.84	1.480	32.103	20,757
136	17,760	29.364	832.3	5.816	-	5.182	618.7	2.336	-	5.049	5.666	14,021	69.64	66.00	1.481	32.163	20,767
175	17,760	29.323	833.2	5.096	2.899	3.942	601.8	2.321	30.28	5.754	7.438	14,013	70.95	63.96	1.475	34.813	20,663
176	17,760	29.338	833.4	5.111	-	3.943	601.7	2.321	-	5.740	7.441	14,011	71.09	64.01	1.474	34.844	20,650
137	17,760	29.375	830.5	4.775	1.950	3.318	591.2	2.327	32.41	6.152	8.852	14,036	71.49	62.42	1.473	36.106	20,673
138	17,760	29.346	830.7	4.780	-	3.316	590.8	2.333	-	6.140	8.849	14,034	71.70	62.55	1.479	36.181	20,75[illegible]
139	17,760	29.363	831.5	4.633	1.625	3.090	588.8	2.337	32.69	6.337	9.503	14,028	71.52	61.78	1.481	36.569	20,773
140	17,760	29.370	831.6	4.631	-	3.087	588.7	2.337	-	6.343	9.513	14,026	71.52	61.78	1.480	36.580	20,770
145	22,840	29.238	833.1	7.402	6.947	7.121	609.0	2.324	-13.91	3.950	4.106	18,023	83.27	81.40	1.480	33.703	26,676
146	22,840	29.240	833.7	7.414	-	7.116	609.0	2.330	-	3.944	4.109	18,016	83.52	81.54	1.485	33.774	26,746
143	22,840	29.372	833.2	5.788	5.148	5.365	583.8	2.334	4.80	5.075	5.475	18,021	81.03	78.19	1.486	37.512	26,736
144	22,840	29.379	833.4	5.788	-	5.370	583.4	2.341	-	5.076	5.471	18,019	81.18	78.36	1.484	37.590	26,745
147	22,840	29.333	831.6	4.901	3.894	4.304	563.6	2.332	14.76	5.985	6.815	18,038	80.91	76.72	1.480	40.389	26,689
148	22,840	29.323	831.6	4.901	-	4.307	564.0	2.335	-	5.983	6.808	18,038	80.82	76.65	1.482	40.336	26,734
149	22,840	29.257	832.5	4.100	2.041	3.037	541.5	2.328	25.16	7.136	9.632	18,029	81.75	73.70	1.481	43.810	26,703
150	22,840	29.255	832.4	4.103	-	3.038	541.5	2.327	-	7.129	9.631	18,030	81.76	73.68	1.481	43.797	26,697
151	27,910	29.179	832.4	6.930	6.433	6.636	586.0	2.297	-23.63	4.211	4.397	22,032	88.32	86.23	1.466	37.091	32,289
152	27,910	29.1[illegible]4	832.2	6.933	-	6.639	586.2	2.305	-	4.210	4.396	22,034	88.23	86.15	1.470	37.052	32,394

Note: 1. Rotor Exit Pressures and Swirl are Area-Averages.
2. Station 7 is at Diffuser Exit; T-S Conditions Calculated to That Station

TABLE XIV - Continued

Cond No.	N_{mech} (rpm)	P_0 (psia)	T_0 (°R)	P_6 (psia)	p_6 (psia)	P_7 (psia)	T_8 (°R)	W_{actual} (lb/sec)	α_6 (deg)	PR_{T-T}	PR_{T-S}	$N/\sqrt{\theta}$ (rpm)	η_{T-T} (pct)	η_{T-S} (pct)	$W\sqrt{\theta}/\delta$ (lb/sec)	$\Delta H/\theta$ (Btu/lb)	WN/δ (lb.sec x rpm)
153	27,910	29.132	832.5	5.794	5.249	5.442	562.5	2.307	- 9.77	5.028	5.353	22,031	88.17	85.57	1.475	40.637	32,489
154	27,910	29.115	832.2	5.795	-	5.442	562.3	2.315	-	5.024	5.350	22,034	88.23	85.63	1.480	40.651	32,614
155	27,910	29.163	832.6	4.795	4.111	4.338	539.7	2.318	1.78	6.082	6.722	22,029	87.72	84.20	1.480	44.089	32,603
156	27,910	29.158	832.4	4.796	-	4.341	539.7	2.324	-	6.079	6.717	22,032	87.70	84.19	1.484	44.070	32,692
157	27,910	29.151	832.3	3.998	2.961	3.405	519.6	2.317	14.91	7.291	8.561	22,034	87.15	82.30	1.480	47.080	32,606
158	27,910	29.151	832.2	3.992	-	3.410	519.6	2.300	-	7.302	8.549	22,034	87.10	82.35	1.481	47.081	32,631
159	32,990	29.280	834.6	7.494	6.796	6.958	603.1	2.219	-43.76	3.907	4.208	26,008	86.43	82.78	1.412	34.754	36,734
160	32,990	29.293	834.7	7.507	-	6.966	603.2	2.220	-	3.902	4.205	26,006	86.51	82.83	1.412	34.758	36,734
161	32,990	29.216	834.4	5.814	5.301	5.551	562.1	2.269	-25.32	5.025	5.263	26,010	[illegible]	86.83	1.448	40.904	37,655
162	32,990	29.221	834.4	5.821	-	5.532	562.2	2.267	-	5.020	5.282	26,011	88.77	86.63	1.446	40.880	37,612
163	32,990	29.309	834.4	4.907	4.318	4.584	538.4	2.294	-10.94	5.973	6.394	26,011	89.14	86.63	1.459	44.456	37,942
164	32,990	29.302	834.6	4.906	-	4.584	538.3	2.296	-	5.971	6.392	26,008	89.22	86.70	1.460	44.487	37,982
165	32,990	29.302	834.2	4.085	3.289	3.629	515.0	2.303	3.08	7.173	8.074	26,014	89.30	85.53	1.464	47.949	38,097
166	32,990	29.290	834.2	4.091	-	3.634	515.5	2.307	-	7.160	8.060	26,015	89.23	85.46	1.468	47.877	38,185

Note: 1. Rotor Exit Pressures and Swirl are Area-Averages.
2. Station 7 is at Diffuser Exit; T-S Conditions Calculated to That Station.

TABLE XV. TEST OBSERVATIONS AND RESULTS FOR COLD-FLOW TESTS - BUILD NO. 5

Cond No.	N_{mech} (rpm)	P_o (psia)	T_o (°R)	P_6 (psia)	P_6 (psia)	P_7 (psia)	T_8 (°R)	W_{actual} (lb/sec)	α_6 (deg)	PR_{T-T}	PR_{T-S}	$N/\sqrt{\theta}$ (rpm)	η_{T-T} (pct)	η_{T-S} (pct)	$W\sqrt{\theta}/\delta$ (lb/sec)	$\Delta H/\theta$ (Btu/lb)	WN/δ (lb/sec x rpm)
188	17,760	29.184	834.2	7.226	6.569	6.820	638.4	2.340	0.75	4.039	4.279	14,005	71.72	69.39	1.4944	29.41	20,929
189	17,760	29.164	834.6	7.238	-	6.830	638.9	2.335	-	4.029	4.270	14,001	71.74	69.40	1.4928	29.38	20,900
190	17,760	29.263	834.5	5.631	4.403	4.942	616.1	2.344	21.86	5 197	5.921	14,002	70.03	66.00	1.4930	32.79	20,906
191	17,760	29.262	834.3	5.630	-	4.937	616.0	2.344	-	5.198	5.927	14,004	69.99	65.95	1.4930	32.78	20,908
192	17,760	29.240	834.5	4.782	1.786	3.360	594.2	2.341	33.47	6.114	8.702	14,002	71.65	62.75	1.4920	36.09	20,891
193	17,760	29.240	834.6	4.792	-	3.375	594.1	2.343	-	6.102	8.664	14,001	71.77	62.89	1.4940	36.12	20,918
194	17,760	29.180	832.0	4.537	1.367	3.045	586.9	2.331	32.92	6.432	9.584	14,023	71.78	62.21	1.4866	36.92	20,847
195	17,760	29.186	831.1	4.541	-	3.032	587.5	2.327	-	6.428	9.625	14,031	71.42	61.81	1.4829	6.73	20,806
196	22,840	29.149	830.9	7.411	6.918	7.120	607.3	2.332	-13.45	3.933	4.094	18,046	83.52	81.58	1.4883	33.72	26,857
197	22,840	29.123	831.4	7.423	-	7.121	607.6	2.335	-	3.923	4.090	18,041	83.69	81.67	1.4915	33.74	26,909
186	22,840	29.205	832.8	5.702	5.040	5.287	581.1	2.333	1.49	5.122	5.524	18,026	81.42	78.59	1.4878	37.87	26,819
187	22,840	29.210	832.8	5.709	-	5.295	581.3	2.337	-	5.116	5.517	18,025	81.41	78.59	1.4896	37.84	26,850
198	22,840	29.074	832.6	4.759	3.522	4.104	560.4	2.319	16.30	6.109	7.084	18,028	81.37	76.67	1.4849	40.97	26,770
199	22,840	29.075	831.0	4.758	-	4.102	560.0	2.318	-	6.111	7.088	18,045	81.15	76.46	1.4831	40.87	26,763
200	22,840	29.114	832.9	4.118	1.898	3.014	540.2	2.324	24.42	7.070	9.658	18,025	82.48	74.03	1.4866	44.04	26,796
201	22,840	29.115	831.6	4.119	-	3.020	539.6	2.324	-	7.069	9.642	18,038	82.41	74.00	1.4850	44.00	26,787
202	27,910	29.065	834.1	7.228	6.706	6.938	592.7	2.296	-28.97	4.021	4.189	22,009	88.69	86.63	1.4724	36.27	32,407
203	27,910	29.065	835.3	7.222	-	6.924	592.9	2.296	-	4.025	4.198	21,994	88.86	86.73	1.4732	36.36	32,400
204	27,910	29.061	832.0	5.827	5.291	5.471	562.3	2.321	-10.74	4.988	5.312	22,038	88.46	85.83	1.4867	40.61	32,764
205	27,910	29.057	832.0	5.823	-	5.464	562.3	2.318	-	4.990	5.316	22,038	88.47	85.81	1.4850	40.62	32,725
236	27,910	29.086	834.9	4.817	4.137	4.383	541.4	2.326	3.71	6.038	6.636	21,999	87.93	84.57	1.4907	44.06	32,794
237	27,910	29.081	833.4	4.813	-	4.383	541.3	2.328	-	6.042	6.635	22,019	87.64	84.32	1.4904	43.92	32,828
206	27,910	29.279	832.2	4.828	4.144	4.373	539.2	2.322	3.97	6.064	6.695	22,035	87.89	84.39	1.4765	44.12	32,535
207	27,910	29.283	832.5	4.834	-	4.377	539.9	2.330	-	6.058	6.690	22,031	87.78	84.27	1.4815	44.04	32,640

Note: 1. Rotor Exit Presures and Swirl are Area-Averages
2. Station 7 is at Diffuser Exit; T-S Conditions Calculated to That Station

Cond No.	N_{mech} (rpm)	P_o (psia)	T_o (°R)	P_6 (psia)	P_6 (psia)	P_7 (psia)	T_8 (°R)	W_{actual} (lb/sec)	α_6 (deg)	PR_{T-T}	PR_{T-S}	$N/\sqrt{\theta}$ (rpm)	η_{T-T} (pct)	η_{T-S} (pct)	$W\sqrt{\theta}/\delta$ (lb/sec)	$\Delta H/\theta$ (Btu/lb)	$WN\epsilon$ (lb/sec x rpm)
238	27,910	29.033	834.2	4.316	3.530	3.831	529.3	2.317	10.97	6.727	7.578	22,009	87.45	83.37	1.4871	45.80	32,726
239	27,910	29.023	834.0	4.321	-	3.831	528.7	2.321	-	6.716	7.575	22,011	87.64	83.71	1.4904	45.87	32,804
208	27,910	29.266	833.0	3.946	2.736	3.319	516.2	2.335	19.56	7.416	8.819	22,024	87.66	82.49	1.4860	47.66	32,728
209	27,910	29.266	833.4	3.948	-	3.321	516.5	2.342	-	7.413	8.813	22,019	87.67	82.51	1.4905	47.66	32,819
210	32,990	29.250	834.7	7.564	6.857	7.018	605.8	2.234	-43.77	3.867	4.168	26,007	85.98	82.27	1.4236	34.36	37,023
211	32,990	29.257	834.2	7.567	-	7.021	605.7	2.239	-	3.866	4.167	26,014	85.90	82.21	1.4264	34.32	37,106
212	32,990	29.288	833.9	5.892	5.306	5.614	564.0	2.294	-26.37	4.971	5.217	26,019	88.50	86.46	1.4593	40.56	37,9[illegible]9
213	32,990	29.163	834.0	5.893	-	5.609	564.0	2.298	-	4.949	5.199	26,017	88.69	86.60	1.4681	40.56	38,195
214	32,990	29.295	832.7	4.831	4.226	4.497	535.1	2.314	-10.63	6.064	6.515	26,037	89.23	86.6[illegible]	1.4710	44.79	38,299
215	32,990	29.290	833.2	4.841	-	4.496	535.1	2.314	-	6.051	6.514	26,029	89.40	86.70	1.4715	44.83	38,302
216	32,990	29.253	833.8	4.008	3.198	3.510	512.3	2.326	5.39	7.299	8.335	26,020	89.39	85.24	1.4817	48.31	38,556
217	32,990	29.240	833.6	4.015	-	3.514	512.1	2.329	-	7.283	8.320	26,023	89.50	85.32	1.4837	48.33	38,611

Note: 1. Rotor Exit Pressures and Swirl are Area-Averages
2. Station 7 is at Diffuser Exit; T-S Conditions Calculated to That Station

TABLE XVI. TEST OBSERVATIONS AND RESULTS FOR COLD-FLOW TESTS - BUILD NO. 6

Cond No.	N_{mech} (rpm)	P_o (psia)	T_o (°R)	P_6 (psia)	P_6 (psia)	P_7 (psia)	T_8 (°R)	W_{actual} (lb/sec)	α_6 (deg)	PR_{T-T}	PR_{T-S}	$N/\sqrt{\theta}$ (rpm)	η_{T-T} (pct)	η_{T-S} (pct)	$W\sqrt{\theta}/\delta$ (lb/sec)	$\Delta H/\theta$ (Btu/lb)	WN/δ (lb/sec x rpm)
240	17,760	29.152	833.0	7.274	6.566	6.874	638.2	2.333	3.07	4.008	4.241	14,015	71.79	69.50	1.491	29.308	20,890
241	17,760	29.171	833.4	7.271	-	6.873	637.9	2.312	-	4.012	4.244	14,011	71.99	69.70	1.492	29.404	20,905
242	17,760	29.152	833.0	5.557	4.199	4.825	612.4	2.337	22.50	5.246	6.042	14,014	70.58	66.24	1.493	33.199	20,920
243	17,760	29.149	833.4	5.555	-	4.828	612.4	2.339	-	5.247	6.038	14,012	70.61	66.30	1.495	33.219	20,944
244	17,760	29.150	833.5	4.677	2.005	3.279	591.3	2.340	31.33	6.232	8.890	14,010	71.72	62.87	1.495	36.417	20,950
245	17,760	29.161	833.5	4.678	-	3.269	591.6	2.342	-	6.234	8.920	14,010	71.63	62.73	1.496	36.376	20,963
246	17,760	29.142	833.6	4.560	1.677	3.098	588.5	2.340	33.82	6.391	9.406	14,010	71.82	62.46	1.496	36.850	20,962
247	17,760	29.149	833.5	4.549	-	3.088	588.1	2.342	-	6.407	9.438	14,011	71.84	62.47	1.497	36.898	20,973
248	22,840	29.356	833.8	7.595	7.153	7.333	610.6	2.354	-16.41	3.865	4.003	18,015	83.95	82.21	1.494	33.538	2[illegible],911
249	22,840	29.356	833.7	7.589	-	7.330	610.8	2.352	-	3.868	4.005	18,016	83.83	82.11	1.493	33.504	26,995
278	22,840	29.148	832.7	6.140	5.402	5.791	589.4	2.334	- 3.47	4.747	5.033	18,027	81.73	79.38	1.491	36.604	26,880
279	22,840	29.122	832.7	6.147	-	5.797	589.4	2.329	-	4.737	5.024	18,027	81.84	79.48	1.489	36.517	26,8[illegible]7
250	22,840	29.345	833.8	5.383	4.674	4.940	574.5	2.356	7.08	5.452	5.942	18,015	81.37	78.31	1.496	38.967	26,948
251	22,840	29.332	833.8	5.388	-	4.936	574.2	2.351	-	5.444	5.942	18,015	81.51	78.39	1.493	39.007	[illegible],899
252	22,840	29.332	833.7	4.858	3.806	4.262	561.6	2.350	14.75	6.038	6.883	18,016	81.63	77.39	1.493	40.900	[illegible],898
253	22,840	29.327	833.9	4.863	-	4.264	561.7	2.347	-	6.030	6.878	18,014	81.68	77.42	1.491	40.905	26,865
254	22,840	29.340	833.9	4.130	2.019	3.076	539.9	2.353	26.49	7.103	9.538	18,013	82.59	74.56	1.494	44.182	26,921
255	22,840	29.338	833.9	4.131	-	3.069	540.8	2.352	-	7.101	9.560	18,013	82.36	74.28	1.494	44.052	26,909
256	27,910	29.281	833.4	7.364	6.886	7.114	594.1	2.328	-27.88	3.976	4.116	22,019	88.57	86.81	1.481	35.989	32,605
257	27,910	29.281	833.6	7.370	-	7.114	594.1	2.329	-	3.973	4.116	22,016	88.65	86.84	1.482	36.001	32,626
258	27,910	29.140	833.5	5.832	5.307	5.498	564.1	2.335	-10.09	4.996	5.300	22,018	88.15	85.69	1.493	40.503	32,866
259	27,910	29.132	833.4	5.835	-	5.491	564.3	2.341	-	4.993	5.305	22,018	88.10	85.57	1.497	40.468	32,957

Note: 1. Rotor Exit Pressures and Swirl are Area-Averages.
2. Station 7 is at Diffuser Exit; T-S Conditions Calculated to That Station.

TABLE XVI - Continued

Cond No.	N_{mech} (rpm)	P_0 (psia)	T_0 (°R)	P_6 (psia)	p_6 (psia)	p_7 (psia)	T_8 (°R)	W_{actual} (lb/sec)	α_6 (deg)	PR_{T-T}	PR_{T-S}	$N/\sqrt{\theta}$ (rpm)	η_{T-T} (pct)	η_{T-S} (pct)	$W\sqrt{\theta}/\delta$ (lb/sec)	$\Delta H/\theta$ (Btu/lb)	WN/δ (lb/sec x rpm)
260	27,910	29.202	833.4	4.795	4.140	4.377	539.8	2.352	2.76	6.091	6.672	22,019	87.78	84.55	1.494	44.141	32,895
261	27,910	29.182	833.5	4.794	-	4.379	539.9	2.346	-	6.087	6.664	22,018	87.78	84.58	1.497	44.133	32,970
262	27,910	29.331	833.5	4.059	3.009	3.477	519.5	2.349	15.44	7.227	8.435	22,017	87.69	82.96	1.492	47.218	32,854
263	27,910	29.327	833.6	4.065	-	3.472	519.5	2.353	-	7.214	8.446	22,015	87.76	82.94	1.494	47.225	32,903
296	32,990	29.013	836.1	7.517	6.808	7.021	607.3	2.215	-43.95	3.860	4.132	25,985	85.90	82.52	1.424	34.285	37,014
297	32,990	29.025	836.1	7.520	-	6.994	607.4	2.217	-	3.860	4.150	25,985	85.88	82.27	1.425	34.277	37,025
298	32,990	29.062	836.2	5.883	5.336	5.630	567.2	2.285	-24.95	4.940	5.162	25,982	88.27	86.41	1.467	40.336	38,126
299	32,990	29.075	836.2	5.880	-	5.623	567.0	2.289	-	4.944	5.171	25,983	88.25	86.35	1.469	40.342	38,173
300	32,990	29.008	836.3	4.811	4.206	4.486	537.7	2.304	- 8.64	6.029	6.466	25,982	89.35	86.75	1.482	44.738	38,514
301	32,990	29.007	836.3	4.815	-	4.496	537.7	2.310	-	6.024	6.451	25,982	89.39	86.88	1.486	44.747	38,606
302	32,990	29.019	836.3	3.999	3.227	3.543	513.6	2.318	6.12	7.257	8.191	25,978	89.71	85.87	1.490	48.382	38,719
303	32,990	29.023	836.2	3.994	-	3.543	513.4	2.313	-	7.267	8.192	25,983	89.65	85.85	1.487	48.372	38,646

Note: 1. Rotor Exit Pressures and Swirl are Area-Averages.
2. Station 7 is at Diffuser Exit: T-S Conditions Calculated to That Station.

TABLE XVII. TEST OBSERVATIONS AND RESULTS FOR COLD—FLOW TEST - BUILD NO. 7

Cond No.	N_{mech} (rpm)	P_o (psia)	T_t (°R)	P_6 (psia)	p_6 (psia)	P_7 (psia)	T_8 (°R)	W_{actual} (lb/sec)	α_6 (deg)	PR_{T-T}	PR_{T-S}	$N/\sqrt{\theta}$ (rpm)	η_{T-T} (pct)	η_{T-S} (pct)	$W\sqrt{\theta}/\delta$ (lb/sec)	$\Delta H/\theta$ (Btu/lb)	WN/δ (lb/sec x rpm)
314	22,840	29.107	835.2	4.827	3.814	4.193	562.2	2.314	14.78	6.031	6.941	18,000	81.80	77.26	1.4827	40.96	26,688
315	22,840	29.105	835.2	4.834	-	4.203	562.1	2.311	-	6.021	6.924	18,000	81.88	77.36	1.4805	40.98	26,648
316	27,910	28.998	836.2	5.684	5.190	5.359	563.3	2.306	- 9.09	5.102	5.411	21,982	88.09	85.68	1.4836	40.89	32,612
317	27,910	28.981	836.0	5.718	-	5.379	563.3	2.306	-	5.068	5.388	21,984	88.35	85.83	1.4847	40.88	32,639
310	27,910	29.084	836.5	4.820	4.142	4.373	542.3	2.309	5.51	6.034	6.651	21,978	88.00	84.53	1.4817	44.08	32,564
311	27,910	29.075	837.9	4.820	-	4.387	542.5	2.308	-	6.032	6.627	21,959	88.23	84.63	1.4828	44.19	32,561
312	27,910	29.105	834.8	3.993	2.944	3.340	518.1	2.319	16.68	7.288	8.713	22,000	88.02	82.63	1.4858	47.54	32,686
313	27,910	29.106	834.9	3.990	-	3.349	518.2	2.316	-	7.295	8.691	21,999	87.97	82.68	1.4837	47.54	32,639
318	32,990	29.123	836.9	4.789	4.145	4.407	536.8	2.309	- 8.64	6.081	6.608	25,972	89.41	86.40	1.4801	44.93	38,440
319	32,990	29.113	836.0	4.784	-	4.407	536.6	2.303	-	6.085	6.606	25,986	89.27	86.30	1.4756	44.87	38,346

Note: 1. Rotor Exit Pressures and Swirl are Area-Averages.
2. Station 7 is at Diffuser Exit: T-S Conditions Calculated to That Station.

Unclassified
Security Classification

DOCUMENT CONTROL DATA - R & D

(Security classification of title, body of abstract and indexing annotation must be entered when the overall report is classified)

1. ORIGINATING ACTIVITY (Corporate author) Pratt & Whitney Aircraft Florida Research and Development Center West Palm Beach, Florida	2a. REPORT SECURITY CLASSIFICATION Unclassified 2b. GROUP

3. REPORT TITLE

DESIGN AND EVALUATION OF A HIGH-TEMPERATURE RADIAL TURBINE

4. DESCRIPTIVE NOTES (Type of report and inclusive dates)

Final Report - Phase I 18 July 1967 to 30 May 1968

5. AUTHOR(S) (First name, middle initial, last name)

Glenn S. Calvert
Ulo Okapuu

6. REPORT DATE	7a. TOTAL NO. OF PAGES	7b. NO. OF REFS
January 1969	267	5

8a. CONTRACT OR GRANT NO. DAAJ02-68-C-0003 b. PROJECT NO. 1G162203D14413 c. d.	9a. ORIGINATOR'S REPORT NUMBER(S) USAAVLABS Technical Report 68-69 9b. OTHER REPORT NO(S) (Any other numbers that may be assigned this report) FR 2858

10. DISTRIBUTION STATEMENT

This document has been approved for public release and sale; its distribution is unlimited.

11. SUPPLEMENTARY NOTES	12. SPONSORING MILITARY ACTIVITY
	U.S. Army Aviation Materiel Laboratories Fort Eustis, Virginia

13. ABSTRACT

This report describes the work accomplished in the first phase of a two-phase, two-year program that involves the design and testing of a single-stage, high-work radial inflow turbine. This turbine will be typical of one required for advanced gas turbine engines employing high cycle pressure ratios and high turbine inlet temperatures.

The objectives of Phase I were to establish a preliminary turbine design, to confirm the preliminary design through cold-flow tests, and to conduct a fabrication study. The objectives of Phase II will be to develop a final turbine design and, finally, to fabricate and test the design.

The Phase I final preliminary turbine design is the result of iterative aerodynamic-structural-heat transfer analyses. The final selections of number of nozzle vanes, number of rotor blades and rotor cooling air ejection method were confirmed and supported by cold-flow tests. The fabrication study showed some material property problems which require additional investigation.

DD FORM 1 NOV 65 1473 REPLACES DD FORM 1473, 1 JAN 64, WHICH IS OBSOLETE FOR ARMY USE.

Unclassified
Security Classification

Unclassified
Security Classification

14. KEY WORDS	LINK A		LINK B		LINK C	
	ROLE	WT	ROLE	WT	ROLE	WT
Radial Turbine Turbine Inlet Temperature Aerodynamic Design Creep-Rupture Heat-Transfer						

Unclassified
Security Classification